Functionalized Metal-organic Frameworks: Promising Porous Materials for Chemical Separation

A Thesis
Submitted in Partial Fulfillment of the Requirements
for the Degree of

Doctor of Philosophy

by

Soumya Mukherjee

ID: 20113126

Indian Institute of Science Education and Research (IISER), Pune

2016

Dedicated to

Ma and Baba (My Parents)

Indian Institute of Science Education and Research (IISER), Pune

Certificate

It is hereby certified that the work described in this thesis entitled *"Functionalized Metal-organic Frameworks: Promising Porous Materials for Chemical Separation"* submitted by *Mr. Soumya Mukherjee* was carried out by the candidate, under my supervision. The work presented here or any part of it has not been included in any other thesis submitted previously for the award of any degree or diploma from any other university or institution.

Date: 1st September, 2016

Dr. Sujit K. Ghosh

Research Supervisor

Email: sghosh@iiserpune.ac.in

Contact No.: +91 (20) 25908076

Declaration

I declare that this written submission represents my ideas in my own words and wherever other's ideas have been included; I have adequately cited and referenced the original sources. I also declare that I have adhered to all principles of academic honesty and integrity and have not misrepresented or fabricated or falsified any idea/data/fact/source in my submission. I understand that violation of the above will cause for disciplinary action by the Institute and can also evoke penal action from the sources which have thus not been properly cited or from whom proper permission has not been taken when needed.

Date: 1st September, 2016

Soumya Mukherjee

ID: 20113126

Acknowledgment

At the very outset, I would like to convey my deepest regards to my research supervisor Dr. Sujit K. Ghosh, who has continuously encouraged me in the last five years. I firmly believe that his inspiring guidance has been a key factor behind the wholesome learning process throughout my PhD tenure. Belonging from his third batch of PhD students, I joined the group at a time where our seniors' painstaking research outputs were still to get published from our laboratory, and entire lab was developing from the nascent stage by taking tiny footsteps in the way of cumulatively achieving greater heights of scientific establishment. Learning from my lab seniors Dr. Biplab Joarder, Abhijeet K. Chaudhari, Dr. Biplab Manna, and Dr. Sanjog S. Nagarkar, I was fortunate to get the unique opportunity to witness the setting up of a relatively new lab, almost from scratch. Their diligent efforts and our supervisors confidence on each of us was indeed instrumental behind each and every small success I could achieve, and will undoubtedly remain the prime asset for my future research. I acknowledge Indian Institute of Science Education and Research (IISER), Pune and its director Prof. K. N. Ganesh for providing state-of-the-art research facilities, funding and an excellent interdisciplinary research atmosphere, facilitating thoroughly collaborative research endeavours.

I am also grateful to my Research Advisory Committee (RAC) members Prof. Avinash S. Kumbhar (Professor, University of Pune) and Dr. Nirmalya Ballav (Assistant Professor, IISER Pune) for their invaluable advices and helpful suggestions provided at the annual research advisory committee meetings. I am thankful to Prof. Rajamani Krishna (University of Amsterdam, Netherlands), Prof. Jinkui Tang (Changchun Institute of Applied Chemistry, China), Dr. Ravichandar Babarao (CSIRO Australia), Dr. Arnab Mukherjee (IISER Pune), Prof. Jing Li (Rutgers, USA), Dr. Praveen K. Thallapally (PNNL, USA), Prof. Jin-Chong Tan (University of Oxford, UK), Prof. Parimal K. Bhardwaj (IIT Kanpur) and Dr. Rashmi A. Agarwal (IIT Kanpur) for giving me their collective research inputs, and to allow me to work with them in different collaborative research projects as joint ventures. Because of their immensely helpful suggestions, I gained a lot of working experience in diverse fields of research which indeed proved very helpful in my way of learning. I am also extremely thankful to Prof. M. Jayakanan (Chair, Chemistry department) and all the faculty members of our Chemistry department for their valuable suggestions bestowed on myself, during my research period.

It was indeed a pleasure to work in such an excellent ambience, conducive to new learning and gaining proficient wisdom. I would like to thank all my old school and university teachers for enthusing me in the way of learning, un-learning and re-learning a number of things, even before I started to dream about obtaining a PhD in Chemistry. I strongly believe, PhD is not just receiving yet another academic degree, it is the humongous learning process and the distinctive test of endurance which truly makes the experience of PhD a treasure trove for a lifetime. Among all these teachers, a few of them have made such long-lasting impressions that it would be a form of disregard, if I refrain from mentioning their names in

this piece of document. Mr. Atanu Bhattacharya (Mathematics teacher, Sodepur High School), Mr. Shyamsanatan Santra (Biology teacher, Sodepur High School), Mr. Suddhasattwa Bhattacharya (Geography teacher, Sodepur High School), Late Dr. Arunabha Sen (RKMVC College), Dr. Chandrakanta Bandyopadhyay (RKMVC College), Dr. Subhabrata Banerjee (RKMVC College), Dr. Sujoy Chakroborty (Teacher, Physical chemistry), Dr. Sanjib Ganguly (St. Xavier's College, Calcutta), Dr. Rana Sen, Dr. Debjani Ghosh, Dr. Dinabandhu Kundu (Scottish Church College), Prof. Manas Chakroborty (Bose Institute), Prof. Gautam Chattopadhyay (former Presidency College): all of them are a few of those excellent teachers, I was fortunate to come across as a student. These are the people who will continue to be inspiring figures for myself in the years ahead.

I am grateful to my first research supervisor Dr. Subi Jacob George (Associate Professor, JNCASR), the careful supervision of whom had given me an impeccable research exposure during my M.Sc. days, in the JNCASR summer research fellowship program, 2010. I thank Dr. Umeshareddy Kacherki (deputy librarian) and Anuradha for library support and all other instrument operators (Mr. Parveen Nasa, Ms. Archana, Mr. Nilesh Dumbre, Ms. Swati, Ms. Nayana, Mr. Anil, Mr. Mahesh, Mr. Neeraj Maheshwari, to name a few), as well as all the IISER Pune non-teaching staff members, especially Mr. Mayuresh, Mr. Tushar, Ms. Vrushali, Mr. Suresh, Mr. Prabhas, Mr. Sandeep, Ms. Mariamma John for their generous support at a number of times.

It is my immense pleasure to thank all the lovable and dear members of the "Microporous Materials Lab" team I belong to: the alumni (Dr. Sanjog S. Nagarkar, Dr. Biplab Joarder, Dr. Biplab Manna, Abhijeet K. Chaudhari, Dinesh Mullangi, Amrit K. Singh, Shweta Singh, Naveen Kumar, among many), and the present team (Avishek Karmakar, Aamod V. Desai, Partha Samanta, Dr. Tarak Nath Mandal, Shivani Sharma, Samraj Mallick, Arunava Sen, Subhajit Dutta, Arkendu, Priyangshu, to name a few). Series of long discussion sessions and fun-filled sharing of individual work-experiences combined with assimilation of individual ideas has helped me a lot to expand the horizon of scientific knowledge and have inculcated the ideology to work as an integral team member, and to even rise as a team leader at a few occasions. The innumerable experiences over the years in our esteemed lab-space has taught me to value the importance of a good work atmosphere. Without a few team members (current and alumni), the journey would not have been as exciting as it has been. Thank you Avishek, Aamod, Partha, Abhijeet, Manna, Biplabda, Tarakda and so on..., for making my ride truly special. Bumpy it was at times, but the expedition was worthy because of the unique blend of so many experiences typifying ecstasy and agony.

In these five years, there are three persons who have always stood beside me, irrespective of the situation concerned. Two among them are the ones who were geographically the most distant ones, while the other has always been pretty much in the next laboratory, busy in her day-to-day ordeals as an independent researcher. As a single child, I was unable to do any duty to help my aging parents, who have strongly supported my education, like no one else. Throughout the difficult times, I have found my parents' support and encouragement as the sole saviour, without which I firmly believe, it would not have been possible for myself to

accomplish, whatever tiny footsteps have been taken to move ahead in my career. Apart from my parent's unquestionable role, Arundhati has been the best friend I have been blessed with. I believe, our partnership will continue and we both would be there for each other at all the stages of our future lives.

I would like to thank all my IISER friends specially Arindamda, Koushikda, Abhigyanda, Barun, Arivind Gupta, Sohini, Tanmoy, Sagar, Sunil, Parthada, Sudeb, Abhik, Supratik, Gopal, Shyama, Rajkumar, Maidul, Rahi, Bijoyda, Amit, Rejaul, Chandramouli, Shammi, Palwan, Kriti, Avishikta, Farhan and others. I apologize beforehand for not being able to take all of your names, but am sure, it would not offend you to a great extent. Among all, Barun, Arindamda, Koushikda and Abhigyanda needs special mention, since they helped me in a lot of trivial, yet important aspects of life at IISER.

I would also like to thank American Chemical Society (ACS), Royal Society of Chemistry (RSC), John Wiley & Sons (Wiley-VCH), Elsevier and Springer for publishing a number of my research articles produced during my PhD tenure at IISER Pune. Moreover, I would not miss this opportunity to thank BASF SE (Germany) as well as, BASF India for selecting me to participate in the prestigious 129th International Summer Course held at Ludwigshafen, Germany in August, 2015. The exposure was truly exceptional and it provided me a great to platform to learn about the key transition parameters for an academician before conceiving the colossal leap to the industrial sector. I would also like to thank the sixth European Association for Chemical and Molecular Sciences Chemistry Congress (6th EuCheMS Chemistry Congress) at Seville, Spain (September, 2016) for inviting me to present my work in the form of a poster and parallely, SERB-ITS (DST-India) for generously providing me the requisite travel grant to attend the same. A number of conference organizers including MTIC, ICSIC, SCOMM, NSC, CRSI etc. have provided me ample opportunities to present my research works in the form of oral presentations and poster formats, which have definitively given me a lot of confidence to rely upon my own caliber. IISER Pune, and its director has always remained supportive of such participations, which had further supported my cause, each time I approached.

A number of old friends, Arpan (IIT Bombay), Turbasu (NCL), Suman (HCU), Sanjoy (Purdue), Indranath (Illinois), Suman (Berger India Paints Ltd.) and Subhabrata (IIT Kharagpur): all of them have been special in their individual ways. I would like to express my heartfelt thanks to Ma'am (Dr. Sudarshana Mukherjee) for her friendly advises. My Best wishes to little Suvan for a wonderful life ahead.

Lastly, I would be signing off by saying that like all good things have a definite end, for me, the PhD experience at IISER Pune bound to be over within the next few months, will stay very close to my heart. I will cherish a lot of the moments I have lived in this place, and it has taught me grow as a human being like nothing else could. I will miss this place and that is a certainty.

Soumya Mukherjee.

Contents

1. General Introduction on Functionalized Metal-organic Frameworks Addressing Chemical Separation Challenges

1.1. Metal-organic Frameworks (MOFs): A brief account 1.1-1.2
1.2. Functionalization of MOFs: Immense Role of Crystal engineering 1.2-1.5
1.3. Chemical Separation: The Genesis of the Inexorable Issue of Adsorptive Separation 1.5-1.7
1.4. Functionalization as a Promising Strategy to Achieve Separation 1.7-1.8
1.5. Scopes of work in the current context 1.8
1.6 Overview of the thesis-work 1.9-1.10
1.7. References 1.11-1.14

2. C_8-Alkylaromatic Isomer Species Selective Sorption Analyses on a Dynamic Metal-organic Framework

2.1. Introduction 2.1-2.3
2.2. Experimental Section 2.3-2.7
Section 2A: Framework-Flexibility Driven Selective Sorption of *p*-Xylene over Its Congener Isomers 2.8-2.52
2A.1 Introduction 2.9-2.10
2A.2 Synthetic Protocol 2.11-2.12
2A.3 Result and discussions 2.12-2.20
2A.4 Theoretical Analyses 2.20-2.23
2A.5 Conclusion 2.24
2A.6 Appendix Section 2.25-2.52
Section 2B: Exploiting Framework Flexibility for Selective Adsorption of Styrene over Ethyl benzene 2.53-2.73
2B.1 Introduction 2.54-2.56
2B.2 Synthetic Protocol 2.56
2B.3 Result and discussions 2.57-2.61
2B.4 Conclusion 2.62
2B.5 Appendix Section 2.62-2.73
2.3. References 2.74-2.77

3. Vapor-Phase Selective Benzene Adsorption over Cyclohexane by Dual Coherent Approaches Rationalized on MOFs

3.1. Introduction 3.1-3.3
3.2. Experimental Section 3.3-3.4

Section 3A: A π-electron Deficient Diaminotriazine Functionalized MOF for Selective Sorption of Benzene over Cyclohexane 3.5-3.25
3A.1 Introduction 3.6-3.7
3A.2 Synthetic Protocol 3.7-3.8
3A.3 Result and discussions 3.8-3.12
3A.4 Conclusion 3.12
3A.5 Appendix Section 3.13-3.25
Section 3B: Harnessing Lewis Acidic Open Metal Sites of MOFs: Foremost Route to Achieve Highly Selective Benzene Sorption over Cyclohexane 3.26-3.46
3B.1 Introduction 3.27-3.28
3B.2 Synthetic Protocol 3.28
3B.3 Result and discussions 3.29-3.35
3B.4 Conclusion 3.36
3B.5 Appendix Section 3.36-3.46
3.3. References 3.47-3.52

4. An Ultrahydrophobic Fluorous MOF Derived Recyclable Composite As A Promising Platform to Tackle Marine Oil Spills

4.1. Introduction 4.1-4.3
4.2. Experimental Section 4.3-4.10
4.3. Synthetic Protocol 4.10-4.11
4.4. Result and discussions 4.11-4.19
4.5. Conclusion 4.19
4.6. Appendix Section 4.20-4.34
4.7. References 4.35-4.40

5. **Summary and Perspectives** 5.1-5.2

Synopsis:

This thesis is primarily focused upon comprehensive experimental investigations of suitably functionalized metal-organic frameworks derived from a few strategic design principles, in a way to gain better insights into the structure-property correlation intricacies of such host-guest supramolecular systems. In fact, such targeted approach is aimed at the development of better new-generation sorbent materials for achieving targeted chemical separation challenges. Followed by the syntheses of a number of carboxylate-donor based rigid and dynamic metal-organic frameworks, the purposefully introduced functionalities could lead to anticipated separation applications, markedly promising from the omnipresent energy and environmental perspective. To sum up, we seek to develop novel MOF-functionalization rationales, and therefore coherently synthesize ensuing open framework sorbent MOF materials, which might end up in getting employed for serving a few unrelenting chemical separation demands.

During my entire PhD tenure, a considerable effort has been put upon the design, syntheses and comprehensive experimental investigation of a number of metal-organic frameworks (MOFs) with diverse appended functionality on each of their pore/connolly surface. In the quest of deftly maneuvering such chemical functionalities and their imperative influence on the structure-property correlation-driven attainment of chemical separation features, extensively recorded experimental findings have been methodically analyzed herein, along with correlating them with theoretical insights.

Chapter 1. *General Introduction on Functionalized Metal-organic Frameworks Addressing Chemical Separation Challenges*

Adsorptive separation presents a key challenge in nearly all the industrial processes, especially manufacturing and production plants. In general, the process employs porous solid adsorbent materials such as activated carbons, silica gels, or zeolites. With an ever increasing need for a more energy-saving, and environmentally benign efficient procedures for gas/solvent separation, new-generation adsorbents with designed/tailored architectures and tunable surface attributes must be found. Metal–organic frameworks (MOFs), self-assembled by metal-containing nodes connected via organic bridging blocks, have categorically substantiated their mettle in the last few years as the front-running contenders in the aforementioned domain of

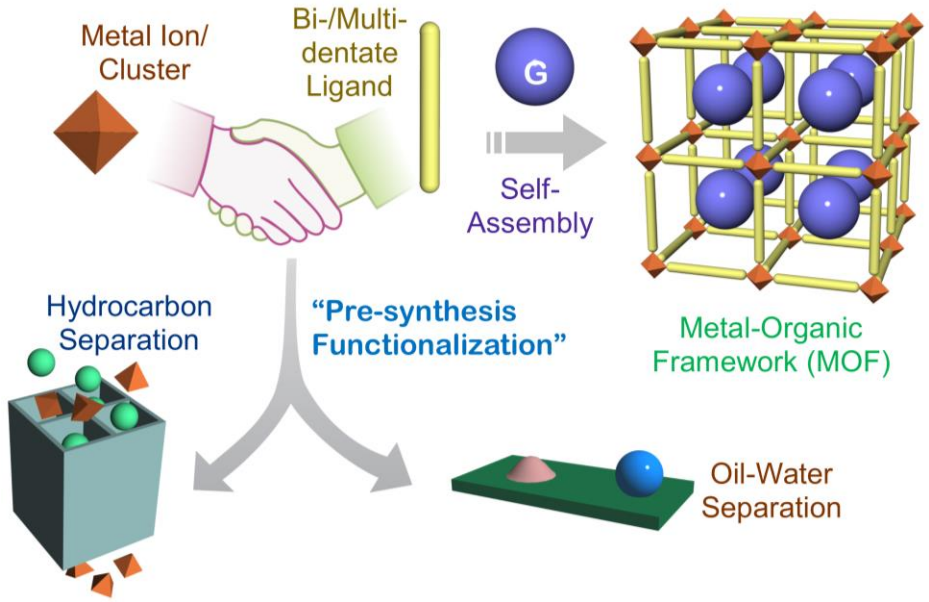

Scheme 1. Schematic representation of the unmatched platform of chemical functionalization, serving as a potential route to achieve key chemical separation-oriented deliverables.

application. They have emerged as one of the most promising class of sorbent materials for chemical separations, particularly gases, owing to their large surface areas, adaptable pore sizes and controllable features, as well as adequate thermal stability.

Chapter 2. *C_8-Alkylaromatic Isomer Species' Selective Sorption Analyses on a Dynamic Metal-organic Framework*

Separation of C_8-alkylaromatic isomeric species prevails to be one of the most important challenges in chemical industry, due to the large amount of commercial usage of *p*-xylene in the production of polyethylene terephthalate (PET) and styrene for polystyrene manufacture units. Isolation of these C_8 species as respective pure feedstock's, however, always suffer from a rather common setback in the terms of high energy penalty drawn in the conventionally adopted separation protocols such as, distillation. Herein, a novel Zn(II)-based dynamic coordination framework (**DynaMOF-100**), stemming from a highly flexible ether-functionalized dicarboxylate linker has been synthesized and extensively characterized. To aptly discuss its applications, the same has been subdivided into two sections: while **Section 2A** covers the remarkably *p*-xylene selective sorption phenomena over its congener C_8-alkyl aromatic isomers at ambient conditions, its ensuing section (**Section 2B**) solely comprises of the unique sorption

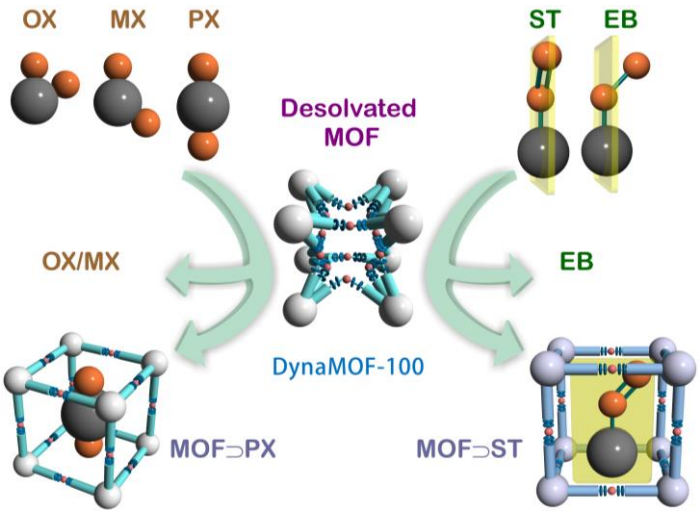

Scheme 2. Schematic illustration of soft porous crystallinity assisted selective sorption/guest-inclusion phenomena: *p*-xylene over its congener isomeric xylenes, as well as styrene over azeotropic congener ethylbenzene (both works described elaborately in distinct sections of chapter 2).

selectivity for styrene vapor over its azeotropic analogue ethylbenzene. In the milieu, the inherent soft porous crystallinity of the concerned ether-functionalized MOF has led to record-breaking selective C_8 isomeric species' sorption performances, following quite an unprecedented fashion. Such kind of reversible framework-breathing and guest-induced solid-state structural transformations with unique sorption selectivity can be purposefully exploited to develop smart functional host materials, capable of industrially important chemical separations.

Publications from this chapter:

1. Framework-Flexibility Driven Selective Sorption of *p*-Xylene over Other Isomers by a Dynamic Metal-Organic Framework
   Soumya Mukherjee, Biplab Joarder, Biplab Manna, Aamod V. Desai, Abhijeet K. Chaudhari and Sujit K. Ghosh
   Sci. Rep. (Nature Publishing Group), **2014**, *4*, 5761.

2. Exploiting Framework Flexibility of a Metal-Organic Framework for Selective Adsorption of Styrene from Mixtures with Ethylbenzene
   Soumya Mukherjee, Biplab Joarder, Aamod V. Desai, Biplab Manna, Rajamani Krishna, and Sujit K. Ghosh
   Inorg. Chem. **2015**, *54*, 4403-4408.

Chapter 3. *Vapor-Phase Selective Benzene Adsorption over Cyclohexane by Dual Coherent Approaches Rationalized on MOFs*

The main challenge lying ahead in C_6 hydrocarbon flow stream separation process encompasses the separation of benzene (Bz) over its azeotropic congener cyclohexane (Cy), since they do possess tantalizingly close physical parameters such as, similar boiling points, related molecular geometry, close Lennard-Jones collision diameters and molecular volumes, in conjunction with low relative volatilities. Adsorptive separation is considered one of the most energy efficient methods in the quest of meting such separation requirements. Herein, in this chapter, two different MOF functionalization approaches have been pursued in way to build up potential strategies targeted at selective sorption based separation deliverable. Alike the last

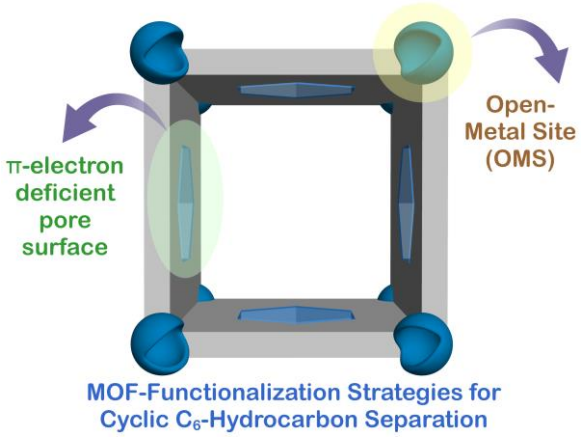

Scheme 3. Schematic illustration of the adopted dual strategies to result in a targeted selective interplay of the respective MOF(s) with Benzene, over its azeotropic congener Cyclohexane.

chapter, here also, there are two chapters which go hand-in-hand; the first one relies on the exploitation of a newly envisaged electron-deficient linker functionality (diaminotriazine) to result in efficient Bz-selective sorption at ambient conditions (for the **DAT-MOF-1** compound), while the latter chapter involves unsaturated metal sites as the responsible functional sites behind yielding the best-till-date Bz sorption selectivity values over Cy for the well-reputed **M-MOF-74** series of compounds.

Publications from this chapter:

1. Harnessing Lewis Acidic Open Metal Sites of Metal-organic Frameworks: The Foremost Route to Achieve Highly Selective Benzene Sorption over Cyclohexane
   Soumya Mukherjee, Biplab Manna, Aamod V. Desai, Yuefeng Yin, Rajamani Krishna, Ravichandar Babarao, and Sujit K. Ghosh
   Chem. Commun. **2016**, *52*, 8215-8218. **(**Selected Back Cover: *Chem. Commun.* Issue**)**

2. A π-electron Deficient Diaminotriazine Functionalized MOF For Selective Sorption of Benzene Over Cyclohexane
   Biplab Manna,[Ŧ] **Soumya Mukherjee**,[Ŧ] Aamod V. Desai, Shivani Sharma, Rajamani Krishna, and Sujit K. Ghosh
   (Ŧ **Equal author contribution declared**)
   Chem. Commun. **2015**, *51*, 15386-15389.

Chapter 4. *An Ultrahydrophobic Fluorous MOF Derived Recyclable Composite As A Promising Platform to Tackle Marine Oil Spills*

To mitigate obnoxious environmental hazards caused by catastrophic marine oil spills, a number of solid adsorbent materials (with high oil absorption capacity) have been developed as a part of the desired greener and economical methods to tackle such ecosystem anomaly. Derived from a tactically nominated hexafluorinated dicarboxylate linker aimed at the designed synthesis of a highly hydrophobic metal−organic framework (MOF), the fluorine-rich nanospace of a new water-stable MOF (**UHMOF-100**) exhibits excellent oil absorption and water repellence features. It registered the highest water contact angle (176°) in the MOF domain, marking the first example of an ultrahydrophobic MOF. Various experimental and theoretical studies reinforce its distinctive water-repellent characteristics, and the conjugation of superoleophilicity and unparalleled hydrophobicity of a MOF material has been coherently exploited to achieve real-time oil/water separation in recyclable membrane form, with significant absorption capacity performance. This also inaugurates reports for a new class of oil/water separating, fluorinated, ultrahydrophobic MOF-based membrane materials, with potential promise for tackling marine oil spillages.

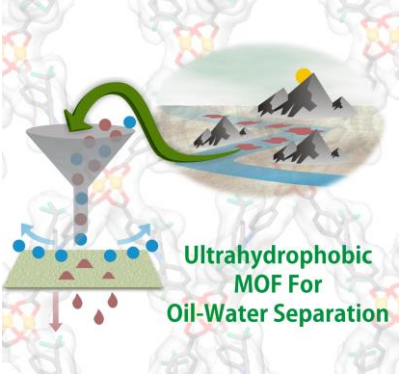

Scheme 4. Schematic illustration of the ultrahydrophobic MOF-derived recyclable composite membrane based oil/water separation application.

Publication from this chapter:

1. An Ultrahydrophobic Fluorous Metal–Organic Framework Derived Recyclable Composite as a Promising Platform to Tackle Marine Oil Spills
   Soumya Mukherjee, Ankit M. Kansara, Debasis Saha, Rajesh Gonnade, Dinesh Mullangi, Biplab Manna, Aamod V. Desai, Shridhar H. Thorat, Puyam S. Singh, Arnab Mukherjee, and Sujit K. Ghosh
   Chem. Eur. J. **2016**, *22*, 10937–10943. (Listed as *top most accessed articles*: July 2016)

Chapter 5. *Summary and Perspectives*

In view of the constantly escalating research efforts put together in the exciting regime of new-generation materials-based permanently porous sorbent materials, there is a definite necessity for the development of coherent strategic design principles for the upcoming scientific research concentrating on the aspects of recyclability and sustainability. Recent years of research on diverse new-generation porous polymers and the enormous development amassed in the field of metal-organic frameworks have markedly focused on the ease of bed regeneration and hydrolytic stability aspects along with the usage of environment-friendly methods for syntheses. Taking into account the rapid growth in this domain, it seems only a matter of time until the crucial aspects of sustainability and energy-economy can be well-addressed. To judiciously tackle the omnipresent situation of carrying out the balancing act amongst energy and economical bottlenecks, it seems vital to move the present research forward in the right direction by adopting the path of using sustainable, energy-economic processes like adsorptive separation and therein, to discover better benchmark sorbents with enhanced efficiency.

Glossary of Acronyms

AcOH	Acetic acid
Anal.	Analysis
Calc	Calculated
CCDC	Cambridge crystallographic data centre
COF	Covalent organic framework
CP	Coordination polymer
CTF	Covalent triazine framework
DFT	Density functional theory
DMF	N, N-Dimethyl formamide
DMSO-d^6	Dimethyl sulphoxide-d^6
EtOAc	Ethyl acetate
EtOH	Ethanol
H-K plot	Horváth-Kawazoe (HK) plot
HOF	Hydrogen-bonded organic framework
FE-SEM	Field emission scanning electron microscopy
FT-IR	Fourier transform infrared-spectra
g	Gram
MeCN	Acetonitrile
MeOH	Methanol
mg	Milligram
MHz	Megahertz
min	Minutes
mL	Mililiter
mL	Micro liter
mM	Micro molar
mmol	Milli moles
MOF	Metal-organic framework
NLDFT	Non-local density functional theory
NMR	Nuclear magnetic resonance
OMS	Open metal sites
PAF	Porous aromatic framework
PCP	Porous coordination polymer
ppm	Parts per million
PPN	Porous polymeric network
POF	Porous organic framework
PSM	Post synthetic modification
PXRD	Powder X-Ray diffraction
RT	Room temperature
SC-SC	Single crystal-to-single crystal
SCXRD	Single crystal X-ray diffraction
TGA	Thermogravimetric analysis
THF	Tetrahydrofuran
UMS	Unsaturated metal sites

Rights and Permissions

Chapter 2:

Section A: Reprinted (adapted) with permission from (*Sci.* Rep. **2014,** *4*, 5761). Copyright 2014 Nature Publishing Group. This work is licensed under a Creative Commons Attribution-NonCommercial-ShareAlike 4.0 International License.

Section B: Reprinted (adapted) with permission from (*Inorg. Chem.* **2015**, *54*, 4403–4408). Copyright 2015 American Chemical Society.

Chapter 3:

Section A: Reprinted (adapted) with permission from (*Chem. Commun.* **2015**, *51*, 15386-15389). Copyright 2015: The Royal Society of Chemistry. This article is licensed under a Creative Commons Attribution 3.0 Unported Licence.

Section B: Reprinted (adapted) with permission from (*Chem. Commun.* **2016**, *52*, 8215-8218). Copyright 2016: The Royal Society of Chemistry.

Chapter 4:

Reprinted (adapted) with permission from (*Chem. Eur. J.* **2016**, *51*, 15386-15389) Copyright 2016: John Wiley and Sons]. Licence number: 4000681003494; dated: Dec 02, 2016.

Research Publications (including Research Articles and Book Chapters)

Included in Thesis

1. Framework-Flexibility Driven Selective Sorption of *p*-Xylene over Other Isomers by a Dynamic Metal-Organic Framework
   Soumya Mukherjee, Biplab Joarder, Biplab Manna, Aamod V. Desai, Abhijeet K. Chaudhari and Sujit K. Ghosh
   Sci. Rep. (Nature Publishing Group), **2014**, *4*, 5761.

2. Exploiting Framework Flexibility of a Metal-Organic Framework for Selective Adsorption of Styrene from Mixtures with Ethylbenzene
   Soumya Mukherjee, Biplab Joarder, Aamod V. Desai, Biplab Manna, Rajamani Krishna, and Sujit K. Ghosh
   Inorg. Chem. **2015**, *54*, 4403-4408.

3. Harnessing Lewis Acidic Open Metal Sites of Metal-organic Frameworks: The Foremost Route to Achieve Highly Selective Benzene Sorption over Cyclohexane
   Soumya Mukherjee, Biplab Manna, Aamod V. Desai, Yuefeng Yin, Rajamani Krishna, Ravichandar Babarao, and Sujit K. Ghosh
   Chem. Commun. **2016**, *52*, 8215-8218. **(Selected Back Cover: *Chem. Commun.* Issue)**

4. A π-electron Deficient Diaminotriazine Functionalized MOF For Selective Sorption of Benzene Over Cyclohexane
   Biplab Manna,[Ŧ] **Soumya Mukherjee**,[Ŧ] Aamod V. Desai, Shivani Sharma, Rajamani Krishna, and Sujit K. Ghosh
   (Ŧ **Equal author contribution declared**)
   Chem. Commun. **2015**, *51*, 15386-15389.

5. An Ultrahydrophobic Fluorous Metal–Organic Framework Derived Recyclable Composite as a Promising Platform to Tackle Marine Oil Spills
   Soumya Mukherjee, Ankit M. Kansara, Debasis Saha, Rajesh Gonnade, Dinesh Mullangi, Biplab Manna, Aamod V. Desai, Shridhar H. Thorat, Puyam S. Singh, Arnab Mukherjee, and Sujit K. Ghosh
   Chem. Eur. J. **2016**, *22*, 10937–10943 (**top most accessed articles for July 2016**).

Not included in Thesis

6. Exploitation of Guest Accessible Aliphatic Amine Functionality of a Metal−Organic Framework for Selective Detection of 2,4,6-Trinitrophenol (TNP) in Water
   Soumya Mukherjee, Aamod V. Desai, Biplab Manna, Arif I. Inamdar and Sujit K. Ghosh
   Cryst. Growth Des. **2015**, *15*, 4627–4634.

7. A Bifunctional Metal–Organic Framework: Striking CO_2-Selective Sorption Features along with Guest-Induced Tuning of Luminescence
Soumya Mukherjee, Aamod V. Desai, Yogeshwar D. More and Sujit K. Ghosh
ChemPlusChem **2016**, *8*, 702-707 (**Selected as Frontispiece: Communications Section**).

8. Structures and Magnetic Properties of Two Analogous Dy_6 Wheels with Electron-Donation and -Withdrawal Effects
Biplab Joarder,† **Soumya Mukherjee**,† Shufang Xue, Jinkui Tang and Sujit K. Ghosh
(†Equal author contribution declared)
Inorg. Chem. **2014**, *53*, 7554–7560.

9. Influence of Tuned Linker Functionality on Modulation of Magnetic Properties and Relaxation Dynamics in a Family of Six Isostructural Ln_2 (Ln=Dy, Gd) Complexes
Soumya Mukherjee, Jingjing Lu, G. Velmurugan, Shweta Singh, G. Rajaraman, Jinkui Tang and Sujit K. Ghosh
Inorg. Chem. **2016**, *55*, 11283–11298.

10. Selective Detection of 2,4,6-Trinitrophenol (TNP) by a π Stacked Organic Crystalline Solid in Water
Soumya Mukherjee, Aamod V. Desai, Arif I. Inamdar, Biplab Manna, and Sujit K. Ghosh
Cryst. Growth Des. **2015**, *15*, 3493-3497.

11. Cadmium Based Catalysts in *Sustainable Catalysis* (**Book Chapter**, Editor: Prof. Michael North)
Book Title: Sustainable Catalysis: With Non-endangered Metals, Part 2, *Chapter 17*.
Soumya Mukherjee and Sujit K. Ghosh
Royal Society of Chemistry, **2015** ISSN: 1757-7039.

12. Recent Progress in the Realm of Homonuclear Ln_6 Single Molecule Magnets: Structural Overview and Synthetic Approaches
(**Review Article***; Special Issue*)
Soumya Mukherjee and Sujit K. Ghosh
Proc. Indian Natl. Sci. Acad. **2015**, *81*, 357-379.

13. Slow Magnetic Relaxation in an Asymmetrically Coupled Heptanuclear Dysprosium(III)-Nickel(II) Architecture
Soumya Mukherjee, Biplab Joarder, Shufang Xue, Jinkui Tang and Sujit K. Ghosh
Proc. Natl. Acad. Sci., India, Sect. A Phys. Sci. **2014**, *84*, 151-156.

14. An Asymmetrically Connected Hexanuclear Dy^{III}_6 Cluster Exhibiting Slow Magnetic Relaxation
Soumya Mukherjee, Abhijeet K. Chaudhari, Shufang Xue, Jinkui Tang and Sujit K. Ghosh
Inorg. Chem. Commun. **2013**, 35, 144-148.

15. Guest-Responsive Function of a Dynamic Metal-Organic Framework with π-Lewis Acidic Pore Surface
Biplab Joarder, **Soumya Mukherjee**, Abhijeet K. Chaudhari, Aamod V. Desai, Biplab Manna and Sujit K. Ghosh
Chem. Eur. J. **2014**, *20*, 15303-15308.

16. Gas Adsorption, Magnetism and Single-Crystal to Single-Crystal Transformation Studies of a Three-Dimensional Mn(II) Porous Coordination Polymer
Rashmi A. Agarwal, **Soumya Mukherjee**, E. Carolina Sanüdo, Sujit K. Ghosh and Parimal K. Bharadwaj
Cryst. Growth Des. **2014**, *14*, 5585–5592.

17. Bi-Porous Metal-Organic Framework with Hydrophilic and Hydrophobic Channels: Selective Gas Sorption and Reversible Iodine Uptake Studies
Abhijeet K. Chaudhari, **Soumya Mukherjee**, Sanjog S. Nagarkar, Biplab Joarder and Sujit K. Ghosh
CrystEngComm **2013**, *15*, 9465-9471.

18. Chiral Biomolecule Based Dodecanuclear Dysprosium(III)-Copper(II) Clusters: Structural Analyses and Magnetic Properties
Biplab Joarder, **Soumya Mukherjee**, Mahendra Patil, Shufang Xue, Jinkui Tang, and Sujit K. Ghosh
Inorg. Chem. Front. **2015**, *2*, 854-859.

19. One Dimensional Coordination Polymers of Cd(II) and Zn(II): Synthesis, Structure, Polar Packing Through Strong Inter-Chain Hydrogen Bonding and Gas Adsorption Studies
Rashmi A. Agarwal, and **Soumya Mukherjee**.
Polyhedron **2016**, *106*, 163-170.

20. Two-Dimensional Flexible Ni(II)-based Porous Coordination Polymer Showing Single-Crystal to Single-Crystal Transformation, Selective Gas Adsorption and Catalytic Properties
Rashmi A. Agarwal, and **Soumya Mukherjee**.
Polyhedron **2016**, *105*, 228-237.

21. Capsule Voided Nanospace Confinement in a π-Stacked Supramolecular Organic Solid
Abhijeet K. Chaudhari, Amitosh Sharma, **Soumya Mukherjee**, Biplab Joarder and Sujit K. Ghosh
CrystEngComm **2014**, *16*, 4691-4695.

22. Highly Selective Detection of Nitro-Explosive by a Luminescent Metal-Organic Framework.
Sanjog S. Nagarkar, Biplab Joarder, Abhijeet K. Chaudhari, **Soumya Mukherjee** and Sujit K. Ghosh
Angew. Chem. Int. Ed. **2013**, *52*, 2881-2885.

23. Structural Dynamism and Controlled Chemical Blocking/Unblocking of Active Coordination Space of a Soft Porous Crystal
Abhijeet K. Chaudhari, Sanjog S. Nagarkar, Biplab Joarder, **Soumya Mukherjee** and Sujit K. Ghosh
Inorg. Chem. **2013**, *52*, 12784-12789.

24. Selective and Sensitive Aqueous Phase Detection of Nitro Explosive by Amine Decorated Nanospace of a Hydrolytically Stable Metal-organic Framework
Biplab Joarder, Aamod V. Desai, Partha Samanta, **Soumya Mukherjee** and Sujit K. Ghosh
Chem. Eur. J. **2015**, *21*, 965 -969.

25. Metal-organic Frameworks: Functional Luminescent Materials for Sensing Applications
William P. Lustig,† **Soumya Mukherjee**,† Nathan D. Rudd, Aamod V. Desai, Jing Li, Sujit K. Ghosh
(†Equal author contribution declared)
Chem. Soc. Rev. Manuscript under preparation (**Review Article**), **2017**.

26. Mechanically Stiff Self-assembled Fluorine-rich Covalent Triazine Frameworks: A New Class of Hard Materials
Soumya Mukherjee, Zhixin Zeng, Abhijeet K. Chaudhari, Mandar M. Shirolkar, Aamod V. Desai, Jin-Chong Tan, and Sujit K. Ghosh
Manuscript Submitted, **2016**.

27. Highly Selective CO_2 Adsorption by an Electron-deficient Linker Based Ultra-microporous Metal-organic Framework
Soumya Mukherjee, Ravichandar Babarao, Aamod V. Desai, Biplab Manna and Sujit K. Ghosh
Cryst. Growth Des. **2017**, *Manuscript under Revision*.

28. A Dynamic Luminescent Coordination Polymer Infused with Pore Surface Functionalization for Recognition of Volatile Aromatics
Biplab Manna, Shivani Sharma, **Soumya Mukherjee**, Aamod V. Desai and Sujit K. Ghosh
Manuscript Submitted, **2016**.

Sum of the Times Cited (as of 01-12-2016): **615**
H-index (as of 01-12-2016): **10**

Chapter 1

General Introduction on Functionalized Metal-organic Frameworks Addressing Chemical Separation Challenges

1.1. Metal-organic Frameworks (MOFs): A brief account

Permanently porous compounds have engrossed a lot of attention among chemists, physicists and materials scientists owing to momentous scientific interest lying behind the creation of nanometer-sized spaces and the observation of a number of unique phenomena therein. Industrial/commercial interest encompasses their diverse focused applications, mainly in the frontiers of storage, separation, and heterogeneous catalysis. Up until the mid-1990s, there were chiefly two kinds of porous materials, viz., inorganic and carbon-based materials. In the case of microporous inorganic solid architectures, the largest two subclasses are the aluminosilicates and aluminophosphates. Among them, the most industrially relevant porous materials, namely zeolites are classified as three-dimensional, crystalline, hydrated alkaline or alkaline earth aluminosilicate materials with an empirical formula $M_{x/n}^{n+}[(AlO_2)_x(SiO_2)_y]^{x-} \cdot wH_2O$.[1, 2] Furthermore, the porous carbons have both the features of high specific surface area and open porosity, but have an entirely disordered amorphous structure, the essential characteristic of which is a twisted network comprising of defective hexagonal carbon layers, cross-linked by aliphatic bridging groups.[3] However, over the years, a number of other porous materials like organic and organic-inorganic hybrid cages (with intrinsic void-space), covalent-organic frameworks (COFs), and hydrogen-bonded organic frameworks (HOFs) have been discovered and have seamlessly assisted exploring the multifaceted array of porous materials (**Scheme 1.1**).

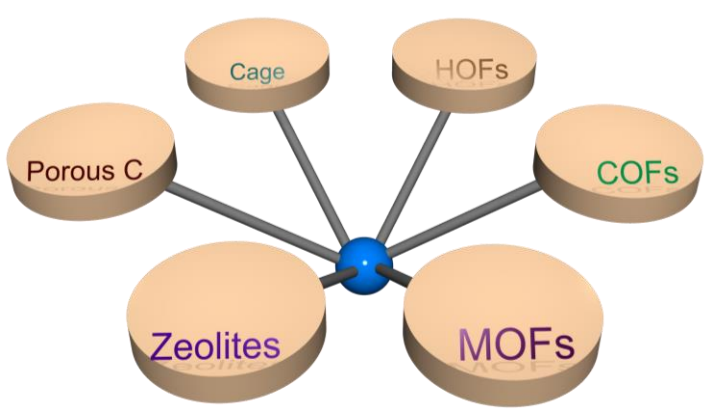

Scheme 1.1. Schematic illustration of the multifaceted array of permanently porous materials.

Among all these different porous materials, metal–organic frameworks (abbreviated as, MOFs), a subset of two-dimensional (2D) or three-dimensional (3D) porous coordination polymers are crystalline open framework compounds with potential voids, based on classical coordination bonds flanked by metal cations and electron donors/ligands such as carboxylates or amines.[4-6] Coordination bond driven self-assembly of the constituent building blocks, typically in solution (mostly providing template effect),[6] often results in the formation of rigid/flexible permanently porous architectures that do not collapse upon removal of the solvent and/or other "guest" molecules occupying the pores following synthesis protocol (as demonstrated in a typical MOF-synthesis scheme: **Scheme 1.2**). The simultaneous presence of both organic and inorganic components allows to impart excellent tailorability attributes to the resultant pore size and chemical environment aimed at achieving explicitly targeted applications. This unmatched facet pertaining to high degree of chemical tuning sets MOFs apart from zeolites (lacking synthetic flexibility) and in fact, lets them score over any other conventional sorbent materials in terms of addressing a particular challenge, in a precisely specific manner.

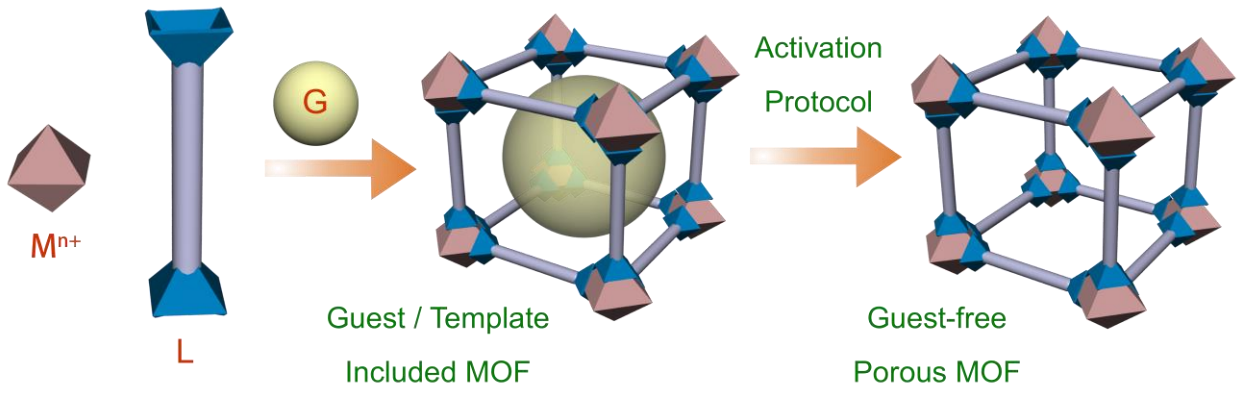

Scheme 1.2. Schematic demonstration of a typical MOF synthesis scheme, resulting in a guest-free porous architecture.

1.2. Functionalization of MOFs: Immense Role of Crystal engineering

Over the last fifteen years, many porous coordination polymers (PCPs) or MOFs have been synthesized, yielding an entire array of properties such as gas/solvent storage, chemical separation, pollutant capture, exchange, heterogeneous catalysis, biomedicines, proton/hydroxide

conduction based fuel cell membranes, thin film/composite material based assorted applications, as well as intriguing magnetic and optical/optoelectronic properties (**Scheme 1.3** shows a few of

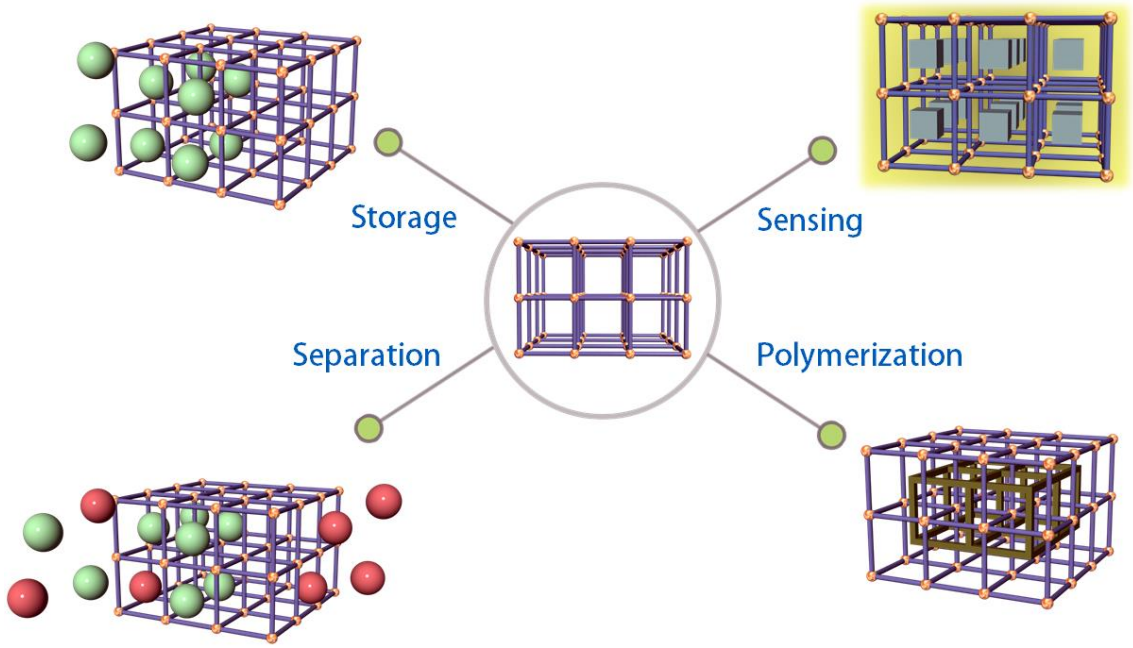

Scheme 1.3. Schematic presentation of a few assorted application regimes, appealingly flourished among the MOF-based research and development endeavors hitherto taken place.

these assortments).[7-21] The differently tailored (synthetically manipulated) nanospaces for such MOFs have inimitable characteristics: regular nanosized porous channels in void-containing framework structures inclusive of excellent long range order and rigidity/flexibility of the channels. Above all, an appropriately designed pore surface, when coupled with these aforesaid attributes can create unprecedented porous functionalities. Adopting diverse pore surface functionalization rationales bring about the culmination of a number of important advantages for this class of coordination framework materials:

a. Ordered crystalline nature
b. High surface area and large pore size
c. Systematically tunable pores
d. Porous channel surface, replete with multiple functional sites
e. Guest-responsive behavior

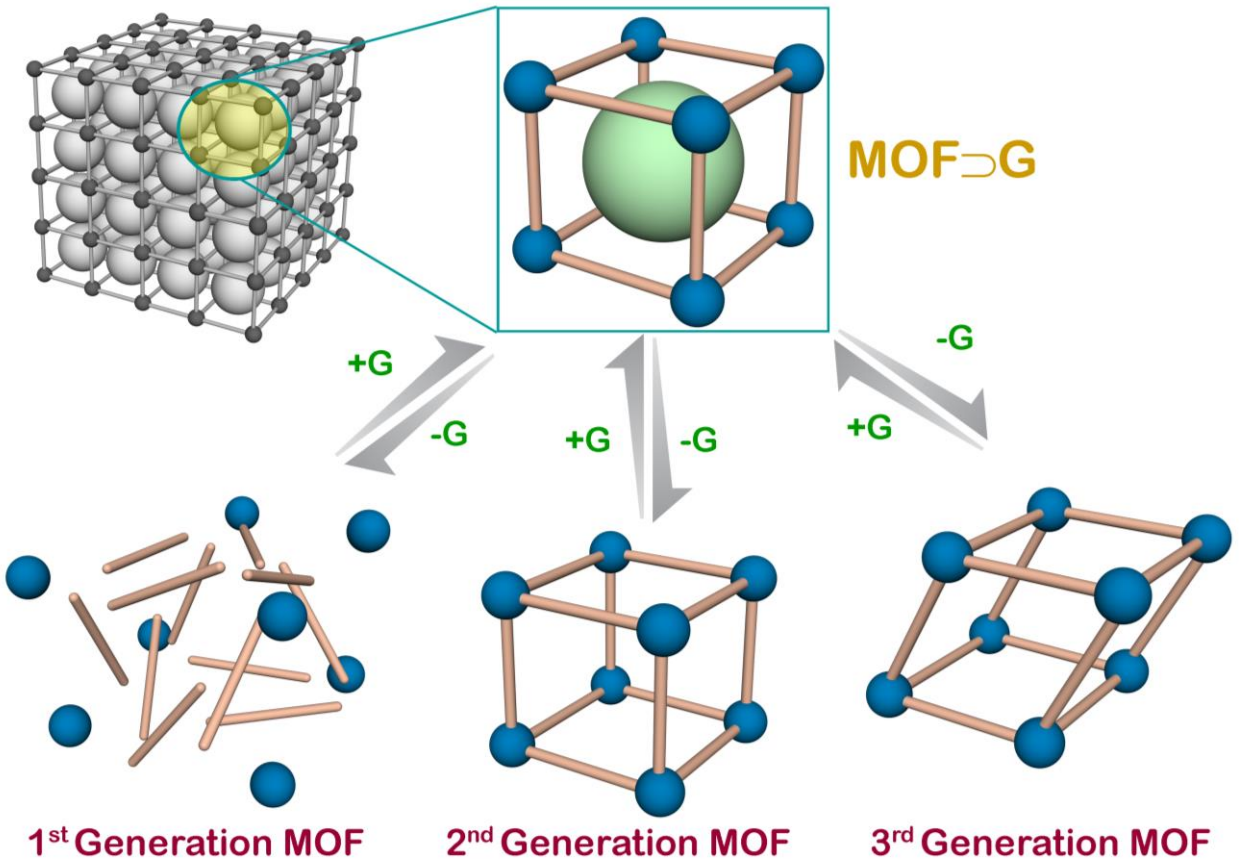

Scheme 1.4. Schematic arrangement of three different kinds of MOF structures: classification based on the structural transformation/sorting features each of such kinds undergo, on applying guest-removing stimulus.

In addition to these frequent characteristics, miscellaneous chemical groups/functionalities can be tactfully grafted onto the pore surface of a number of MOFs by the aid of crystal engineering knowhow.[22] Such appended moieties do not directly ligate/coordinate to the reactive metal centres during the formation of the respective MOF structure(s), but pose as integral parts of the novel host systems suitable for exhibiting a specific function at molecular level. The amenability of such designed host systems to the vast landscape of crystal engineering suggests that the judicious selection of molecular building blocks (MBBs) can systematically facilitate exquisite control over structure with respect to topology and consequently enable fine-tuning with respect to the size and chemistry of their pores.[23] In terms of crystal engineering,[24] certain topologies are readily accessible using the node and linker approach, first outlined by Robson

and co-workers.[25] Among the various aspects controlling the bulk MOF properties, topology plays an important role in the MOF chemistry, since it affords ideal blueprints that enable the design of families of related compounds.[26-28] However, the poor stability of MOFs, resultant of the reversible nature of coordination bonds is generally recognized as the major drawback for their practical applications in most industrial/in-field use.[29, 30] Structural rigidity or flexibility both may lead to significant properties to the resultant guest-free phase and hence both the second and third generations (guest-induced transformation and reformation steps involved, respectively) of MOFs (**Scheme 1.4**) have been found to draw a huge impetus in terms of exhibiting miscellaneous applications.[31-33] Amongst the great amount of research efforts invested to directly construct stable, hydrolytically inert MOFs, a remarkable discovery was the use of Zr-based highly robust secondary building units (SBUs): $Zr_6O_4(OH)_4(CO_2)_{12}$ in UiO-66.[34] To propel the performance of the concerned in-focus systems (for a particular study), we need to combine the key components all together in such an amalgamated fashion, that striking the right chord between stability and efficiency can be delivered by the rationally designed material.[35-37]

1.3. Chemical Separation: The Genesis of the Inexorable Issue of Adsorptive Separation

Commensurate adsorption is a supremely vital phenomenon occurring during adsorption processes, where the molecular shape and size of the adsorbate (guest molecule) lead to an orientation and adsorbed amount (at equilibrium) that is compatible and self-consistent with the pore structure and topology-driven crystal symmetry of the adsorbent.[38, 39] In the chemical, petrochemical and pharmaceutical industries, separation technology acts as a foremost component behind the production of pure compounds. A large chunk of the cumulative production costs are plainly associated with feed purification steps, for instance using solvent extraction, adsorption, crystallization and distillation processes.[40, 41] As of now, distillation itself, accounts for even more than 90% of all the adopted separation methods in any typical chemical industry.[42] Due to the reactive nature-triggered decomposition of certain chemicals, and the high cost-factor related to multiple distillation steps, energy-economic better alternatives are always looked-for, considering the sustainable environment of chemical industry in the future.[43-45]

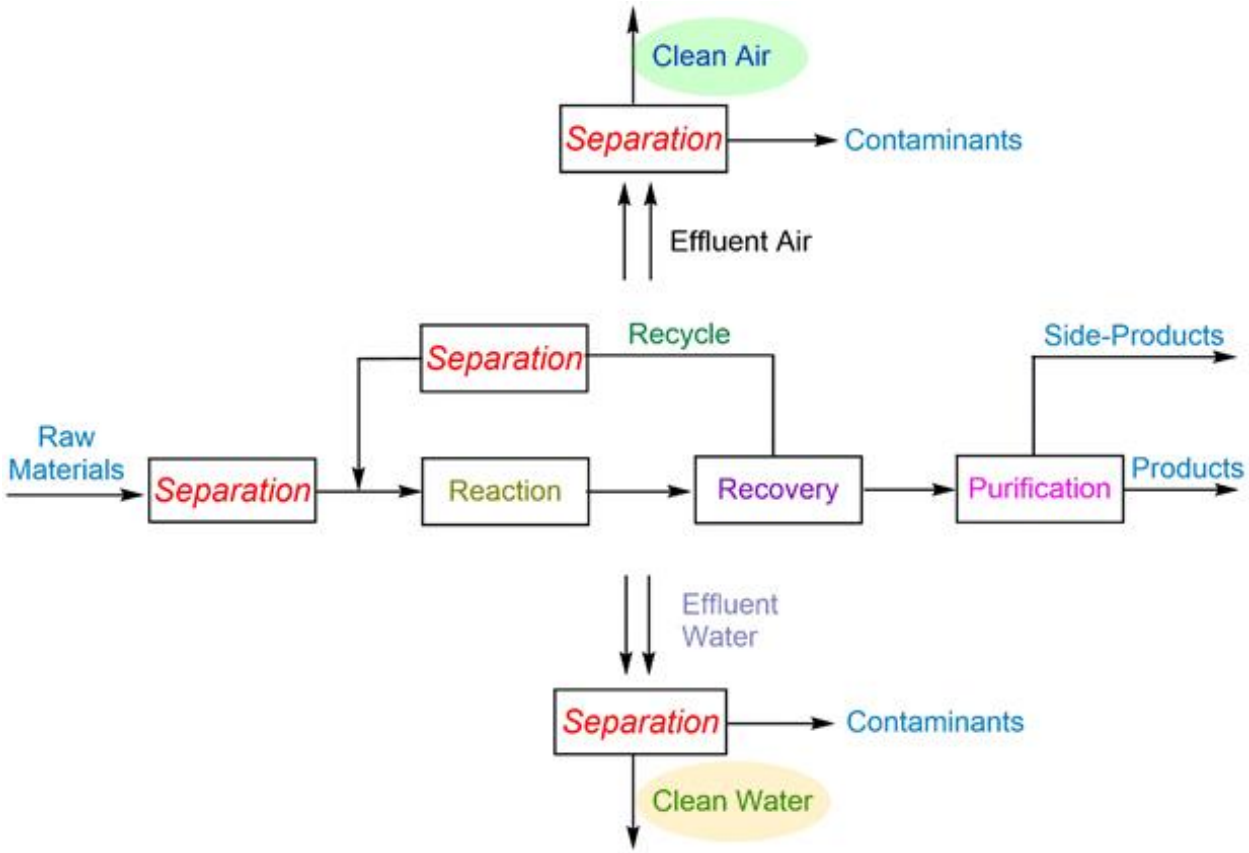

Scheme 1.5. Simplistic flowchart representation of a typical manufacturing production unit, involving multiple chemical separation processes as its integral component.

Adsorptive separation has indubitably emerged as one of the most promising alternative solutions; by now it has already gathered momentum in a multitude of industrial processes today. A solid adsorbent bed is able to separate a mixture of chemicals into its pure constituent compounds, mostly based on differences in the interaction between the adsorbent bed voidage, and constituents of the feed-mixture.[46] The efficacy of separation is therefore strongly dictated by the salient characteristics of the adsorbent. Other microporous materials such as zeolites,[42, 47] activated carbon,[48] aluminophosphates,[49] carbon molecular sieves,[50, 51] polymeric or inorganic resins,[52] and hybrid composite materials[53] have been hitherto analyzed intensively aimed at deriving adsorptive separation based applications. However, with the intention of grasping the challenging separations of future industries and to tackle them in a much improved greener sustainable mode, superior adsorbents are still essential. As depicted in the simplistic

representation of **Scheme 1.5**, at least four separation processes constitute a bare minimum for any manufacturing production plant to optimally operate, for which a huge amount of energy has to be forfeited each passing day. To minimize the same, keeping a close vigil on building up a synergistic approach of energy and environmental key solutions, notwithstanding economic constraints sets a major challenge in terms of the strategic discovery pursued in a specific domain of research, such as chemical separation oriented deliverables encompassing top-notch, new-generation porous materials such as, MOFs.

1.4. Functionalization as a Promising Strategy to Achieve Separation:

Over the last decade, with more and more research on MOFs being focused upon chalking out planned design principles to deduce separation targets in the gas adsorbates' regime, principally concerning the major greenhouse gas CO_2, and the main fuel gases, viz. hydrogen (H_2) and methane (CH_4) as well as, C_2-C_3 hydrocarbon streams (acetylene, propylene over ethylene, ethane and propane).[54-63] Quite a plethora of these principles have convergingly proved that if the chemical functionalities can be optimally and systematically tuned in the coordination nanospace of MOFs, they can assuredly reflect a number of unmatched properties in a systematic and target-oriented fashion. However, a number of approaches are yet to be judiciously evaluated in the arena of solvent vapor sorption based separation phenomena, since it has been observed that albeit the huge research efforts put together in MOF-based storage and separation phenomena for gas adsorbates, analogous liquid vapor adsorbate species' separation could come up with far lesser reports till date.

As a matter of fact, considering the storage and separation frontiers, specifically carbon capture and related applications, a few frequently adopted strategies to enhance efficacy of the concerned sorbent material(s) have been the introduction of lewis basic sites (such as, various amines), open metal sites (OMS)/ unsaturated metal sites (UMS), purposefully involving cationic and anionic ionic species (to render the entire framework cationic or anionic; important for anion capture and sensing applications coupled with propelled CO_2 selective adsorption occurrences), engaging polar groups (such as hexafluorosilicate bearing high F-density, nitro, hydroxyl etc.). These have been extensively covered in the more often reported gas adsorption based separation

instances; however analogous strategies/ design principles manifested in the solvent vapor sorption-mediated chemical separation applications have been scarcely investigated.

1.5. Scopes of work in the current context:

In the quest of realizing benign rationales drawing a rather convergent roadmap in the landscape of new-generation microporous MOF sorbent materials, the first impetus should be specifically emphasized upon the assessment of the present context. Before thriving upon the exact requisite methods to be followed, the first daunting task of prioritizing such an overall assessment calls for quite a tall order. In view of the existent reports, we found that albeit a huge amount of decade-long research efforts has been concentrated on yielding gas-phase selective adsorption based separation phenomena, analogous reports in the vapor sorption regime has been indeed rare. Moreover, chalking out definitive plans for attaining vapor sorption-oriented chemical separation challenges has not been realized in a systematic manner because of the lack of synergistic amalgamation of theoretical/molecular modelling/simulation aided insights with the experimental data-sets on the mentioned forte. While the foremost problems/challenges have been well-asserted, a stern dearth for the actual knowhow of developing the aforementioned understandings was apparent. Herein, we have tried to mitigate this issue by sticking to relatively simple and easily conceivable ideas intended at differential vapor phase sorption attribute based isomeric/azeotropic chemical species' separation phenomena circumventing energy-intensive alternative established protocols, evaluated on deftly functionalized coordination nanospace of MOFs. Apart from this energy-economy related aspect, environmental challenges such as marine oil spillages pose real apprehension to the affected ecosystem, which require smart designed materials as crucial cornerstone sorbents for serving massive cleanup operations. MOFs, wherein, the bulk material property can be astutely tailored, can be considered as ideal porous sorbent prototypes where the inherent porosity (vital for oil capture) can be perfectly exploited along with the concerned materials' other related attributes (such as, hydrophobicity, water and acid/base stability, water repellency etc.), deliberately introduced by firmly adhering to the above-mentioned prefunctionalization or post-synthetic pore surface modification based approaches.

1.6. Overview of the thesis-work:

Herein, the targeted problem frontier mostly pertaining to vapor phase sorption based separation of isomeric and azeotropic industrial feedstock components, a few coherent design principles have been methodically implemented. This has been schematically epitomized in the **Scheme 1.6**. All the four schemes pursued herein, in this thesis, comprises of linker/metal node prefunctionalization based approaches,[64-68] instead of the much lately popular way-out of carrying out post-synthetic modification to MOFs.[69-71] The first of these streamlines the grafting of flexible ether nodes onto the MOF pore surface and consequently render the ensuing dynamic phase inherently soft porous in nature. This in effect, sets off an unprecedented limiting restricted flexibility facet of the framework, instigating the best selective sorption based results recorded for *p*-xylene and styrene (two most important C_8-alkyl aromatic isomeric feedstock's, vital in the manufacture of polyethylene terephthalate (PET) and polystyrene production industries, respectively) in the entire MOF domain. The second approach has been based on the purposeful use of an electron-deficient linker building block to end up with a highly electron-poor MOF pore surface. This has served to trigger off excellent C_6 hydrocarbon vapor selective sorption phenomena, namely benzene over its aliphatic azeotropic congener cyclohexane. On a similar note, the employment of unsaturated metal sites or open metal sites has also upshot the best benzene selective sorption trends for any MOF material hitherto reported, consequently paving new avenues in the cardinal landscape of solvent vapor sorption by appositely functionalized reported porous materials. Lastly, a highly fluorine-rich linker has been engaged to synthesize an ultrahydrophobic, water-repellent MOF with the foremost water contact angle value yet for any porous material. This material has again been proficiently fabricated in the form a recyclable polymer membrane with substantially high oil absorption capacities, with good reproducibility attributes.

The thesis is about to predominantly follow the major outline lucidly discussed in the previous section. Each chapter is divided into two major units: Main content (including figures and schemes therein), and its corresponding appendix section. Apart from this introduction chapter (**Chapter 1**), there are three major work-oriented chapters namely **chapters 2**, **3** and **4** respectively, as focussed discussions addressing different related separation concerns. Each of

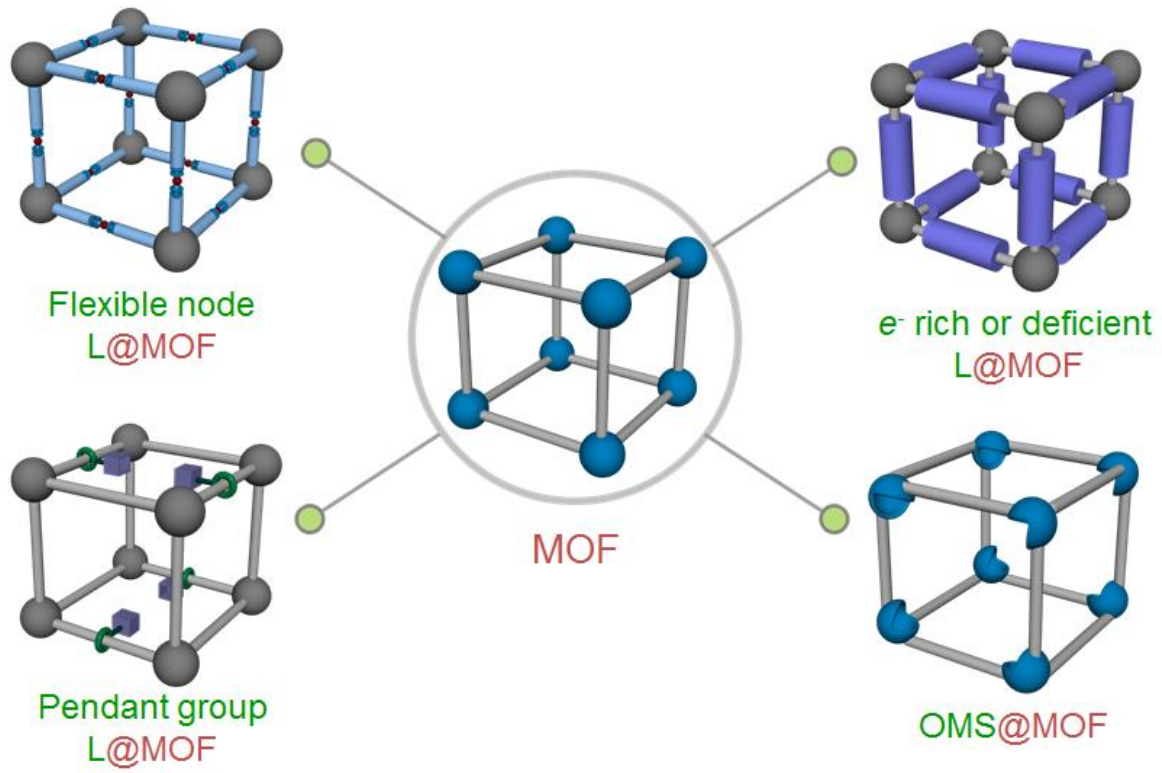

Scheme 1.6. Four diverse strategies pursued in the thesis to achieve chemical separation based deliverables based on MOF materials.

the **chapters 2** and **3** is again sub-classified into two integral sections: **Chapter 2A**, **Chapter 2B**; **Chapter 3A**, **Chapter 3B**, respectively; while, **Chapter 4** stands apart without any subdivision. The last or the concluding chapter (**Chapter 5**) reflects the summary of all the aforementioned focussed discussions and provides an overall outlook to the edifice for this constantly developing regime of research activities. Such definitive design principles, if extrapolated in future with a focus on retaining the stability of the framework material intact (by possible employment of well-documented water-stable SBUs like $Zr_6O_4(OH)_4$ or, decorating the pore/channel surface of the ensuing MOFs with highly polar functional linkers with recognized hydrophobic entities such as, tertiary-butyl, or fluorine-rich pendant substituents might serve as excellent directions to end up with the accomplishment of desired chemical separation challenges based on functionalized MOF-based nanoporous materials.

1.7. References

1. F. Schüth, K.S.W. Sing, J.Weitkamp, Handbook of Porous Solids, vol. 1, VCH, **2002**.

2. D.W. Breck, Zeolite Molecular Sieves, Wiley & Sons, New York, **1984**.

3. Kitagawa, S.; Matsuda, R., *Coord. Chem. Rev.* **2007,** *251*, 2490-2509.

4. Meek, S. T.; Greathouse, J. A.; Allendorf, M. D., *Adv. Mater.* **2011,** *23*, 249-267.

5. Batten, S. R.; Champness, N. R.; Chen, X.-M.; Garcia-Martinez, J.; Kitagawa, S.; Ohrstrom, L.; O'Keeffe, M.; Suh, M. P.; Reedijk, J., *CrystEngComm* **2012,** *14*, 3001-3004.

6. Tanaka, D.; Kitagawa, S., *Chem. Mater.* **2008,** *20*, 922-931.

7. Yaghi, O. M.; O'Keeffe, M.; Ockwig, N. W.; Chae, H. K.; Eddaoudi, M.; Kim, J., *Nature* **2003,** *423*, 705-714.

8. Li, J.-R.; Kuppler, R. J.; Zhou, H.-C., *Chem. Soc. Rev.* **2009,** *38*, 1477-1504.

9. Yang, S.; Ramirez-Cuesta, A. J.; Newby, R.; Garcia-Sakai, V.; Manuel, P.; Callear, S. K.; Campbell, S. I.; Tang, C. C.; Schröder, M., *Nat Chem* **2015,** *7*, 121-129.

10. Banerjee, D.; Cairns, A. J.; Liu, J.; Motkuri, R. K.; Nune, S. K.; Fernandez, C. A.; Krishna, R.; Strachan, D. M.; Thallapally, P. K., *Acc. Chem. Res.* **2015,** *48*, 211-219.

11. Zhang, Y.; Yuan, S.; Feng, X.; Li, H.; Zhou, J.; Wang, B., *J. Am. Chem. Soc.* **2016,** *138*, 5785-5788.

12. Barea, E.; Montoro, C.; Navarro, J. A. R., *Chem. Soc. Rev.* **2014,** *43*, 5419-5430.

13. Shi, P.-F.; Zhao, B.; Xiong, G.; Hou, Y.-L.; Cheng, P., *Chem. Commun.* **2012,** *48*, 8231-8233.

14. Zhu, Q.-L.; Xu, Q., *Chem. Soc. Rev.* **2014,** *43*, 5468-5512.

15. Talin, A. A.; Centrone, A.; Ford, A. C.; Foster, M. E.; Stavila, V.; Haney, P.; Kinney, R. A.; Szalai, V.; El Gabaly, F.; Yoon, H. P.; Léonard, F.; Allendorf, M. D., *Science* **2014,** *343*, 66-69.

16. Li, W.-J.; Tu, M.; Cao, R.; Fischer, R. A., *J. Mater. Chem. A* **2016,** *4*, 12356-12369.

17. Horcajada, P.; Gref, R.; Baati, T.; Allan, P. K.; Maurin, G.; Couvreur, P.; Férey, G.; Morris, R. E.; Serre, C., *Chem. Rev.* **2012,** *112*, 1232-1268.

18. Shimizu, G. K. H.; Taylor, J. M.; Kim, S., *Science* **2013,** *341*, 354-355.

19. Pili, S.; Argent, S. P.; Morris, C. G.; Rought, P.; García-Sakai, V.; Silverwood, I. P.; Easun, T. L.; Li, M.; Warren, M. R.; Murray, C. A.; Tang, C. C.; Yang, S.; Schröder, M., *J. Am. Chem. Soc.* **2016,** *138*, 6352-6355.

20. Kurmoo, M., *Chem. Soc. Rev.* **2009,** *38*, 1353-1379.

21. Brozek, C. K.; Dinca, M., *Chem. Soc. Rev.* **2014,** *43*, 5456-5467.

22. Jiang, H.-L.; Feng, D.; Liu, T.-F.; Li, J.-R.; Zhou, H.-C., *J. Am. Chem. Soc.* **2012,** *134*, 14690-14693.

23. Deng, H.; Grunder, S.; Cordova, K. E.; Valente, C.; Furukawa, H.; Hmadeh, M.; Gándara, F.; Whalley, A. C.; Liu, Z.; Asahina, S.; Kazumori, H.; O'Keeffe, M.; Terasaki, O.; Stoddart, J. F.; Yaghi, O. M., *Science* **2012,** *336*, 1018-1023.

24. Moulton, B.; Zaworotko, M. J., *Chem. Rev.* **2001,** *101*, 1629-1658.

25. Hoskins, B. F.; Robson, R., *J. Am. Chem. Soc.* **1990,** *112*, 1546-1554.

26. O'Keeffe, M.; Peskov, M. A.; Ramsden, S. J.; Yaghi, O. M., *Acc. Chem. Res.* **2008,** *41*, 1782-1789.

27. Li, M.; Li, D.; O'Keeffe, M.; Yaghi, O. M., *Chem. Rev.* **2014,** *114*, 1343-1370.

28. Blatov, V. A.; O'Keeffe, M.; Proserpio, D. M., *CrystEngComm* **2010,** *12*, 44-48.

29. Keskin, S.; van Heest, T. M.; Sholl, D. S., *ChemSusChem* **2010,** *3*, 879-891.

30. Canivet, J.; Fateeva, A.; Guo, Y.; Coasne, B.; Farrusseng, D., *Chem. Soc. Rev.* **2014,** *43*, 5594-5617.

31. Kitagawa, S.; Uemura, K., *Chem. Soc. Rev.* **2005,** *34*, 109-119.

32. Uemura, K.; Matsuda, R.; Kitagawa, S., *J. Solid State Chem.* **2005,** *178*, 2420-2429.

33. Liu, J.; Chen, L.; Cui, H.; Zhang, J.; Zhang, L.; Su, C.-Y., *Chem. Soc. Rev.* **2014,** *43*, 6011-6061.

34. Cavka, J. H.; Jakobsen, S.; Olsbye, U.; Guillou, N.; Lamberti, C.; Bordiga, S.; Lillerud, K. P., *J. Am. Chem. Soc.* **2008,** *130*, 13850-13851.

35. Li, B.; Chrzanowski, M.; Zhang, Y.; Ma, S., *Coord. Chem. Rev.* **2016,** *307, Part 2*, 106-129.

36. Wang, S.; Wang, X., *Small* **2015,** *11*, 3097-3112.

37. Silva, P.; Vilela, S. M. F.; Tome, J. P. C.; Almeida Paz, F. A., *Chem. Soc. Rev.* **2015,** *44*, 6774-6803.

38. Olson, D. H.; Kokotailo, G. T.; Lawton, S. L.; Meier, W. M., *J. Phys. Chem.* **1981,** *85*, 2238-2243.

39. Smit, B.; Maesen, T. L. M., *Nature* **2008,** *451*, 671-678.

40. D. M. Ruthven, Principles of adsorption and adsorption processes, **1984**.

41. R.T.Yang, Adsorbents: Fundamentals and Applications, **2007**.

42. S. Kulprathipanja, Zeolites in Industrial Separation and Catalysis, **2009**.

43. Van de Voorde, B.; Bueken, B.; Denayer, J.; De Vos, D., *Chem. Soc. Rev.* **2014,** *43*, 5766-5788.

44. J. F. Dechow, Separation and Purification Techniques in Biotechnology, Noyes Publications, **1989**.

45. Vitasari, C. R.; Meindersma, G. W.; de Haan, A. B., *Green Chem.* **2012,** *14*, 321-325.

46. Li, J.-R.; Sculley, J.; Zhou, H.-C., *Chem. Rev.* **2012,** *112*, 869-932.

47. De Baerdemaeker, T.; De Vos, D., *Nat Chem* **2013,** *5*, 89-90.

48. Moreno-Castilla, C., *Carbon* **2004,** *42*, 83-94.

49. Hartmann, M.; Kevan, L., *Chem. Rev.* **1999,** *99*, 635-664.

50. Jones, C. W.; Koros, W. J., *Carbon* **1994,** *32*, 1419-1425.

51. Reid, C. R.; O'Koy, I. P.; Thomas, K. M., *Langmuir* **1998,** *14*, 2415-2425.

52. Kirk-Othmer, Separation Technology, John Wiley & Sons, Inc., Hoboken, NJ, 2nd edn, **2008**.

53. Likholobov, V. A.; Fenelonov, V. B.; Okkel, L. G.; Goncharova, O. V.; Avdeeva, L. B.; Zaikovskii, V. I.; Kuvshinov, G. G.; Semikolenov, V. A.; Duplyakin, V. K.; Baklanova, O. N.; Plaksin, G. V., *React. Kinet. Catal. Lett.* **1995,** *54*, 381-411.

54. Broom, D. P.; Webb, C. J.; Hurst, K. E.; Parilla, P. A.; Gennett, T.; Brown, C. M.; Zacharia, R.; Tylianakis, E.; Klontzas, E.; Froudakis, G. E.; Steriotis, T. A.; Trikalitis, P. N.; Anton, D. L.; Hardy, B.; Tamburello, D.; Corgnale, C.; van Hassel, B. A.; Cossement, D.; Chahine, R.; Hirscher, M., *Appl. Phys. A* **2016,** *122*, 1-21.

55. Langmi, H. W.; Ren, J.; North, B.; Mathe, M.; Bessarabov, D., *Electrochim. Acta* **2014,** *128*, 368-392.

56. Gygi, D.; Bloch, E. D.; Mason, J. A.; Hudson, M. R.; Gonzalez, M. I.; Siegelman, R. L.; Darwish, T. A.; Queen, W. L.; Brown, C. M.; Long, J. R., *Chem. Mater.* **2016,** *28*, 1128-1138.

57. Su, N. C.; Sun, D. T.; Beavers, C. M.; Britt, D. K.; Queen, W. L.; Urban, J. J., *Energy Environ. Sci.* **2016,** *9*, 922-931.

58. Pang, J.; Jiang, F.; Wu, M.; Liu, C.; Su, K.; Lu, W.; Yuan, D.; Hong, M., *Nat Commun* **2015,** *6*.

59. Zhang, J.-P.; Chen, X.-M., *J. Am. Chem. Soc.* **2009,** *131*, 5516-5521.

60. Hu, T.-L.; Wang, H.; Li, B.; Krishna, R.; Wu, H.; Zhou, W.; Zhao, Y.; Han, Y.; Wang, X.; Zhu, W.; Yao, Z.; Xiang, S.; Chen, B., *Nat Commun* **2015,** *6*.

61. Thallapally, P. K.; Tian, J.; Radha Kishan, M.; Fernandez, C. A.; Dalgarno, S. J.; McGrail, P. B.; Warren, J. E.; Atwood, J. L., *J. Am. Chem. Soc.* **2008,** *130*, 16842-16843.

62. He, Y.; Zhou, W.; Qian, G.; Chen, B., *Chem. Soc. Rev.* **2014,** *43*, 5657-5678.

63. Mason, J. A.; Oktawiec, J.; Taylor, M. K.; Hudson, M. R.; Rodriguez, J.; Bachman, J. E.; Gonzalez, M. I.; Cervellino, A.; Guagliardi, A.; Brown, C. M.; Llewellyn, P. L.; Masciocchi, N.; Long, J. R., *Nature* **2015,** *527*, 357-361.

64. Furukawa, H.; Cordova, K. E.; O'Keeffe, M.; Yaghi, O. M., *Science* **2013,** *341*.

65. Alaghemandi, M.; Schmid, R., *J. Phys. Chem. C* **2016,** *120*, 6835-6841.

66. Klontzas, E.; Mavrandonakis, A.; Tylianakis, E.; Froudakis, G. E., *Nano Lett.* **2008,** *8*, 1572-1576.

67. Bunck, D. N.; Dichtel, W. R., *Chem. Eur. J.* **2013,** *19*, 818-827.

68. Schneemann, A.; Bon, V.; Schwedler, I.; Senkovska, I.; Kaskel, S.; Fischer, R. A., *Chem. Soc. Rev.* **2014,** *43*, 6062-6096.

69. Burrows, A. D., Metal–Organic Frameworks: Postsynthetic Modification. In *Encyclopedia of Inorganic and Bioinorganic Chemistry*, John Wiley & Sons, Ltd: 2011.

70. Deria, P.; Mondloch, J. E.; Karagiaridi, O.; Bury, W.; Hupp, J. T.; Farha, O. K., *Chem. Soc. Rev.* **2014,** *43*, 5896-5912.

71. Evans, J. D.; Sumby, C. J.; Doonan, C. J., *Chem. Soc. Rev.* **2014,** *43*, 5933-5951.

Chapter 2

C_8-Alkylaromatic Isomer Species' Selective Sorption Analyses on a Dynamic Metal-organic Framework

2.1. Introduction:

During carefully choosing the crucial design protocols aimed at the development of new-generation, functional host adsorbents based on contemporary host–guest systems, it is possible to achieve an excellent synergy between two distinct attributes viz., the amalgamation of crystallinity as well as dynamism (or flexibility). Such bimodal nature of a host framework would offer dual attributes namely, rigid zeolitic features, deftly merged with enzyme-like specificity, consequently leading to smart host crystalline framework-based materials which are guest-responsive in nature, under application of suitable stimuli.[1]

Conventionally, metal-organic frameworks (MOFs) or porous coordination polymers (PCPs) have been classified into three specific categories based on their intrinsic framework characteristics related to stimulus-responsiveness. These pertain to first, second and third generations of MOFs/ PCPs (as illustrated in **Scheme 1.3**).[2] To begin with, the first-generation MOFs involve framework materials whose microporosity undergoes an irreversible collapse on removal of the initially occluded guests; suggesting the irretrievable loss of its permanent porosity. The second generation MOFs possess rigid, stable and quite robust open frameworks, which retain their porous network intact, irrespective of the presence or absence of guest species inside their pores. Depending on individual performances, these second-generation compounds can be used as efficient rigid adsorbents and are regarded as analogous materials to aluminosilicate zeolite sorbents. On the flipside, the third-generation MOFs comprise of a particular kind of dynamic or flexible porous frameworks, which respond to external stimuli in a reversible fashion, chemically as well as, physically. The chemical/structural reversibility observed for the aspect of dynamism between two different yet related phases of the stimulus (/guest inclusion)-responsive supramolecular architecture is indeed an intriguing one because, such two-way breathing/squeezing in solid state crystalline form is not a common phenomenon among other porous platforms.

Soft porous crystalline MOFs are defined as permanent porous bistable or multistable crystalline open framework polymers having the combined facets of highly ordered network and structural transformability.[1] A reversible transformability between two or more states is an essential criterion for such dynamic MOFs.

In recent times, such dynamic MOFs have shown promising signs of pulling off a number of fascinating applications, a number of them primarily focused in the storage, separation and luminescence-based analytes' sensing domains.[3-7] Depending on the pore size, frequently interdigitated channels varying orientation parameters, such breathing systems can act as excellent host receptor units selectively allowing one particular adsorbent species from a mixture feedstock containing a number of mixture adsorbates.[6] Molecular sieving can be a key outcome of such dynamic attributes of the host, resulting into efficient molecular sorting based selective sorption phenomenon for the targeted adsorbent.

Quite a good number of MOFs have been established in the literature to possess the efficacy to effectually separate multifaceted mixture compositions of feedstock gases[8-10] and, less frequently, of liquid hydrocarbons.[11-13] The second one embodies a tangible application for such newly developed and thermally stable hybrid materials, specifically to realize separation protocols that cannot be simply performed using common large-scale separation methods (e.g., ion exchange, column chromatography, fractional distillation).[14] Adsorptive separations using microporous metal-organic frameworks (MOFs) present energy efficient greener alternatives when compared to high energy-consuming separation protocols like, fractional distillation.[15-17] Herein, in this chapter, as an outcome of a novel strategic principle involving flexible ether node-functionality based reversible dynamism of a newly synthesized and characterized MOF (hereafter denoted as DynaMOF-100), two different selective sorption driven separation phenomena has been reported (as illustrated in the **Scheme 2.1**). The chapter is divided into two subsections. The first one (chapter 2A) deals with the selective sorption of *p*-xylene over its congener xylene isomers based on framework flexibility facet, while the second (chapter 2B) would be concentrated on exploitation of the same MOF (soft porosity playing the pivotal role again) to selectively adsorb styrene over ethylbenzene, important for polyethylene terephthalate (PET) and polystyrene manufacture industry, respectively. Both these experimentally validated selective sorption performances have been further comprehensively evaluated by the aid of transient breakthrough simulation-based calculations to gain enhanced insights into the fixed bed adsorber based separation performance for mixture phases of the respective feedstock C_8-alkylaromatic hydrocarbons.

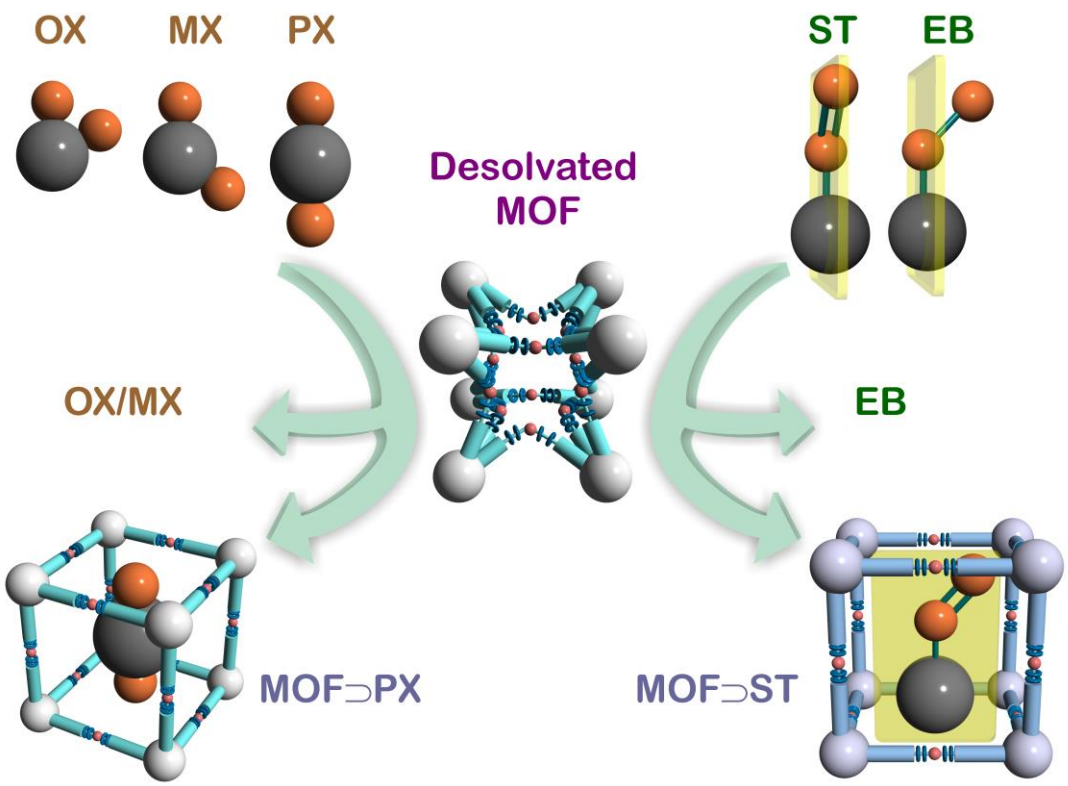

Scheme 2.1. Schematic illustration of soft porous crystallinity assisted selective sorption/guest-inclusion phenomena: *p*-xylene over its congener isomeric xylenes, as well as styrene over azeotropic congener ethylbenzene.

2.2. Experimental Section:

2.2.a. Materials:

All the reagents and solvents were commercially available and used without further purification.

2.2.b. Physical measurements:

Powder X-ray diffraction (PXRD) patterns were measured on Bruker D8 Advanced X-Ray diffractometer at room temperature using Cu-Kα radiation (λ= 1.5406 Å) with a scan speed of 0.5° min^{-1} and a step size of 0.01° in 2 *theta*. Thermogravimetric analysis results were obtained in the temperature range of 30-800 ºC on Perkin-Elmer STA 6000 analyzer under N_2

atmosphere, at a heating rate of 10 ºC min^{-1}, The Fourier transform (FT-IR) infra-red spectra were recorded on NICOLET 6700 FT-IR Spectrophotometer using KBr Pellets.

2.2.c. X-ray Structural Studies:

Single-crystal X-ray data of compound **1⊃G** and **1** (DynaMOF-100) were collected at 200K on a Bruker KAPPA APEX II CCD Duo diffractometer (operated at 1500 W power: 50 kV, 30 mA) using graphite-monochromated Mo Kα radiation (λ = 0.71073 Å), mounting on nylon CryoLoops (Hampton Research) with Paraton-N (Hampton Research) oil. Single-crystal X-Ray data of compound **1⊃PX'** and **1⊃ST'** crystals were collected at 100K on a Bruker KAPPA APEX II CCD Duo diffractometer (operated at 1500 W power: 50 kV, 1 mA) using graphite-monochromated Cu Kα radiation (λ = 1.5418 Å), mounting on nylon CryoLoop (Hampton Research) with Paraton-N (Hampton Research) oil. The data integration and reduction were processed with SAINT[18] software. A multi-scan absorption correction was applied to the collected reflections. The structures were solved by the direct method using SHELXTL[19] and were refined on F^2 by full-matrix least-squares technique using the SHELXL-97[20] program package within the WINGX[21] programme. All non-hydrogen atoms were refined anisotropically. All hydrogen atoms were located in successive difference Fourier maps and they were treated as riding atoms using SHELXL default parameters. The structures were examined using the *Adsym* subroutine of PLATON[22] to assure that no additional symmetry could be applied to the models. **Appendix tables 2A.2, 2A.3 and 2A.4 and 2B.3** contain crystallographic data for the compounds **1⊃G**, **1**, **1⊃PX'** and **1⊃ST'** (CCDC-983317, 983318, 983319, 1035236) respectively. These data can be obtained free of charge from Cambridge Crystallographic Data Centre via www.ccdc.cam.ac.uk/data_request/cif.

2.2.d. Low Pressure Sorption Measurements:

Low pressure gas and solvent sorption measurements were performed using BelSorpmax (Bel Japan). The sorption-recyclability experiments were recorded in BelAqua (Bel Japan). All the gases used were of 99.999% purity. As-synthesized crystals of compound **1⊃G** were heated at 180 °C under vacuum for 24 h, to get guest-free crystals of compound **1**. Prior to adsorption measurement, the guest free sample **1** was pre-treated at 170 °C under vacuum for 2 h, using BelPrepvacII, and purged with N_2 on cooling.

2.2.e. Solvent exposure study:

Crystalline solid powder of compound **1** taken in smaller glass vials were kept open inside larger capped closed glass vials containing different guest solvents (benzene, toluene, cyclohexane, *o*-xylene, *m*-xylene and *p*-xylene, styrene and ethylbenzene respectively) over a period of 48h to allow vapor-phase exposure of solvents and subsequently characterized by PXRD.

2.2.f. GC experiment for comparison of xylene and styrene selectivity:

GC Instrumentation: Materials and Methods:

GC-2014 Shimadzu Gas chromatograph (with AOC-20i Auto Injector) was used with the Column RTX-5 (Length: 30m, Inner diameter: 0.32 mm, Film thickness: 0.25 μm); Injection volume: 1 μL, Injection temperature: 200 °C, Initial Column temperature: 40 °C, Column heating range: 40-70 °C, heating at 1 °C min^{-1}. With this setup, we could not obtain separate retention times for PX and MX, rather both of them were giving GC signal at similar retention times. That is why, to support the observed decrease in the mixed (PX+MX) signal intensity with time when the MOF was immersed in a quaternary mixture of xylenes, two more experiments comprising of ternary combinations of xylenes (one excluding MX, and the other excluding PX) was performed. The results (**Appendices 2A.42-2A.44**) confirm that the observed decline in the signal intensity is solely in the presence of PX. The corresponding uptake times indicate convincingly fast kinetics of the process.

2.2.f.1. Assessment of *p*-xylene selectivity:

Crystalline phase **1** (100 mg) was immersed into mixture solution of xylenes for 1 h according to the following three different combinations, and GC chromatogram were recorded by pipetting out the supernatant solutions (0.123 mL each time) at regular time intervals, and preparing the GC samples in 1.3 mL MeCN in each of the occurrences. (GC parameters employed are mentioned after the description of the three setups.)

Setup A: Quaternary xylene mixture immersion test: 100 mg of **1** was kept immersed in a mixture solution of OX (1 mL), MX (1 mL), PX (1 mL) and EB (1 mL) for 1h, while in the intermediate time intervals 0.123 mL of the supernatant solution were pipetted out for recording the GC chromatogram at those respective times (**Appendix 2A.42**).

As per the literature reported standard GC chromatogram for xylene mixtures,[23] it was found that EB and OX were giving rise to their characteristically separate GC signals, although the retention times for MX and PX coincided to give a mixed intensity signal, owing to their very close characteristic retention times. To check whether the observed decrease in the mixed (PX+MX) signal intensity (for setup A) occurs due to the sole effect or PX only, and not MX, the following two experiments were also performed.

Setup B: Ternary xylene mixture immersion test (excluding PX): 100 mg of **1** was kept immersed in a mixture solution of OX (1 mL), MX (1 mL), MX (1 mL) and EB (1 mL) for 1h, while in the intermediate time intervals 0.123 mL of the supernatant solution were pipetted out for recording the GC chromatogram at those respective times (**Appendix 2A.43**).

Setup C: Ternary xylene mixture immersion test (excluding MX): 100 mg of **1** was kept immersed in a mixture solution of OX (1 mL), PX (1 mL) and EB (1 mL) for 1h, while in the intermediate time intervals 0.123 mL of the supernatant solution were pipetted out for recording the GC chromatogram at those respective times (**Appendix 2A.44**).

2.2.f.2. Assessment of *styrene* selectivity:

Crystalline phase **1** (100 mg) was immersed into singular and/or mixture solutions of styrene/ethylbenzene for 3 h according to the following three different combinations, and GC chromatogram were recorded by pipetting out the supernatant solutions (0.123 mL each time) at regular time intervals, and preparing the GC samples in 1.3 mL MeCN in each of the occurrences.

Setup A: Ethylbenzene immersion test: 100 mg of **1** was kept immersed in a solution of EB (3 mL) for 1h, while in the intermediate time intervals 0.123 mL of the supernatant solution were pipetted out for recording the GC chromatogram at those respective times (**Appendix 2B.14**).

Setup B: Styrene immersion test: 100 mg of **1** was kept immersed in a solution of ST (3 mL) for 1h, while in the intermediate time intervals 0.123 mL of the supernatant solution were pipetted out for recording the GC chromatogram at those respective times (**Appendix 2B.15**).

Setup C: Binary styrene/ethylbenzene (1:1) mixture immersion test: 100 mg of **1** was kept immersed in a mixture solution of ST (1.5 mL) and EB (1.5 mL) for 1h, while in the intermediate time intervals 0.123 mL of the supernatant solution were pipetted out for recording the GC chromatogram at those respective times (**Appendix 2B.16**).

For knowing the composition of the adsorbed MOF during the immersion test of ST/EB, the MOF samples subjected to these experiments viz., setups A, B and C were filtered out from the respective immersion solution(s), on completion of immersion-tenure i.e., 3 hours. These were washed well with MeCN, and then digested in DCl, The DCl solutions were separately analyzed by GC by using the same method file (of GC) used for the supernatant solutions, effective to detect the presence of ST. No ligand peak was seen in the range of 2-40 minutes retention time using the specified scan parameters, mostly due to the highly polar nature of the constituent ligands, unlike to ST and EB.

Section 2A

Framework-Flexibility Driven Selective Sorption of *p*-Xylene over Its Congener Isomers

2A.1. Introduction:

Separation is one of the most important aspects in chemical industry. Xylene isomers separation is one of them, as illustrated by the statistic that only considering the U.S., there have been as many as 130 patents awarded and applied for in the span of 2006-2009.[24] Remarkably, the entire world's mixed xylene production in 2008 was about 39.2 Mt. Among all isomers, *p*-xylene (PX) has the most extensive commercial use with more than 80% of the world production of xylenes being used for the production of PX, because of its expansive commercial usage as a feedstock in manufacture of terephthalic acid, a monomer used in the production of polymer polyethylene terephthalate (PET), widely utilized in the production of beverage bottles, fibres and films.[25] In this context, separation of C_8-alkylaromatic components, specifically the xylene product stream comprising of four isomers: *o*-xylene (OX), *m*-xylene (MX), *p*-xylene (PX), and ethylbenzene (EB) is a pressing issue, since the separation of PX (kinetic diameter ~0.58 nm) from its bulkier *m*- and *o*-isomers (MX and OX; ~0.64 nm and 0.65 nm respectively) is of extreme importance in the petrochemical industry. This is practically infeasible by distillation (closely matched boiling points; 138 °C-144 °C). Among the recognized methods, fractional crystallization and adsorption using zeolites are mostly employed to separate xylene isomers, where adsorption has been markedly proved to be of higher efficiency and gained broader acceptance.[25, 26]

In recent times, few MOFs especially, MIL-47, MIL-53, MIL-125(Ti) have been found appropriate for execution of liquid-phase purifications and separations of xylene isomers.[27-33] These primarily focus on high-temperature vapor-phase and liquid-phase binary breakthrough chromatographic experiments, chiefly by virtue of the molecular sieving phenomena aimed at the simulated moving bed technology employed in industry at around 180 °C and 9 bar. Very few rigid porous MOFs have been reported in the literature exhibiting a clear para preference, which is highly desired for an absorbent to be used for separation of PX from mixture of C_8-alkylaromatic components.[26-36] Notably, no dynamic structure based MOF is reported which shows clear para preference. Framework flexibility and extensive breathing phenomena in MIL-53 (Al) resulted in well-defined two-step adsorption isotherms at 110 °C, although showing similar uptake amounts for all the four isomeric probe adsorptives.[37] The aspect of framework flexibility can be exploited to achieve a clear adsorption-selectivity among xylene isomers at

room temperature to develop smart functional host materials. Although the strategy of pore surface functionalization has been proficiently exploited in rigid frameworks for chemical separation and storage; analogous examples are still scarcely reported for dynamic systems,[1, 38-45] perhaps due to the difficulties in proper strategic design and correlation of structural attributes coupled with dynamic behavior of such materials. The exploration of such kind of systems might serve as a significant way-out for achieving separation of small molecules with structural similarity. With this background, we have synthesized a dicarboxylate ligand, with two ether linkages which can act as flexible nodes. Additionally, Zn(II) is highly accommodative to build dynamic frameworks, since it has versatile coordination chemistry and can readily adopt either of tetrahedral and octahedral geometries with four and six coordination numbers respectively. Construction of an inherently flexible framework essentially involves the cooperative interplay of these two factors. Herein, we report dynamic behavior of a MOF demonstrated by solid state structural transformations between porous and non-porous phases, exhibiting structural flexibility based selective sorption of *p*-xylene over the other xylene isomers in vapor phase at ambient temperature (**Scheme 2A.1**).

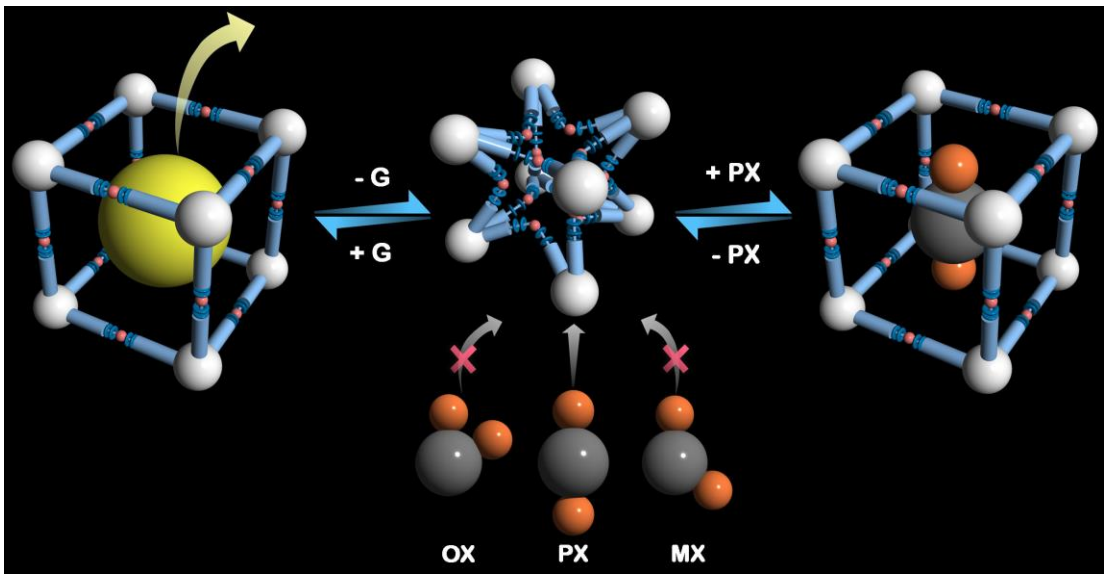

Scheme 2A.1. Schematic illustration of selective guest-responsive framework flexibility driven molecular sieving phenomena prevalent for xylene isomers.

2A.2. Synthetic Protocol:

2A.2.a. Synthesis of Intermediate L':

4-tert-butyl catechol (11 g, 0.0662 mole), 4-fluorobenzonitrile (16.029 g, 0.1324 mole) and potassium carbonate (~27.6 g, 0.2 mole) were refluxed at 180 °C in a mixture of N, N-dimethylformamide (DMF) and *p*-xylene (110 mL/55 ml) for 2days (**Appendix 2A.2**). After cooling the reaction mixture to r.t., it was poured into ~100 mL ice-cold water, followed by acidification with dil. HCl until pH~3. The reaction mixture was evaporated to dryness (maximum amount as possible) by rotary evaporation under reduced pressure, to get a reddish yellow product. This was extracted with Ethyl acetate (2 × 250 mL), washed with brine/water (twice each) and the resultant EtOAc layer was dried over anhydrous Na_2SO_4. Evaporation of this EtOAc layer, followed by drying under high vacuum yielded the intermediate compound L'. Yield: 23.28 g, 95.48%. ^{1}H NMR (400 MHz, $CDCl_3$) δ(ppm): 7.55-7.51 (m, 4H), 7.33 (dd, J=8.24 Hz, J=2.28 Hz, ^{1}H), 7.22 (d, J=2.28Hz, ^{1}H), 7.14 (d, J=8.28Hz, ^{1}H), 6.82-6.77 (m, 4H), 1.34 (s, 9H) ; ^{13}C NMR (100 MHz, $CDCl_3$) δ(ppm) : 161.1, 151.2, 145.2, 143.4, 134.2, 124.21, 122.9, 120.7, 119, 116.8, 106, 35, 31.5 ; HRMS (ESI) Calcd. for $C_{24}H_{20}N_2O_2$ 369.160 [M+H]+, found 369.160 (**Appendices 2A.3**, **2A.4** and **2A.5** respectively).

2A.2.b. Synthesis of Ligand:

A mixture of L' (10g, 0.0271 mole) (**Appendices 2A.1** and **2A.2**) and potassium hydroxide (9.138g, 0.163 mole) was refluxed in 200 mL water/ ethanol (1:1) solvent mixture for 1day. After the reaction mixture was allowed to cool to r.t., it was acidified by dil. HCl keeping on an ice bath till pH~1. The crude material that precipitated out was recrystallized from hot EtOH/water to get colorless crystalline product LH_2. Yield: 9.56 g, 86.66%. ^{1}H NMR (400 MHz, DMSO-d^6) δ(ppm): 7.87-7.84 (m, 4H), 7.36 (dd, J=8.7 Hz, J=2.28 Hz, 1H), 7.30 (d, J=2.28Hz, 1H), 7.22 (d, J =8.68Hz, ^{1}H), 6.87-6.83 (m, 4H), 1.29 (s, 9H); ^{13}C NMR (100 MHz, DMSO-d^6) δ(ppm): 167.1, 161.0, 150, 145.5, 144, 131.9, 125.3, 123.8, 122.6, 120.5, 116.4, 34.8, 31.4 : HRMS (ESI) Calcd. For $C_{24}H_{22}O_6$ 429.131 $[M+Na]^+$, found 429.130 (**Appendices 2A.6**, **2A.7** and **2A.8** respectively).

2A.2.c. Synthesis of $\{[Zn_4O(L)_3(DMF)_2].xG\}_n$ (1⊃G): A mixture of LH_2 (40 mg, 0.1 mmol), $Zn(NO_3)_2.6H_2O$ (29.7 mg, 0.1 mmol), DMF (1 mL) and 1-butanol (1 mL) was placed in a teflon capped glass vial. This was heated at 90 °C for 48h and then cooled to room temperature for 1

day. Growth of colorless block-shaped crystals was observed upon cooling to RT, the desired product **1⊃G** appeared in ~72% yield.

2A.2.d. Synthesis of $[Zn_4O(L)_3]_n$ (1): Shiny single crystals of **1⊃G** were heated at 160 °C under reduced pressure for 8h, to obtain the slightly pale colorless dehydrated crystals of compound **1**.

2A.2.e. Synthesis of Resolvated phase $\{[Zn_4O(L)_3(DMF)_2].(C_8H_{10})\}_n$ (1⊃PX'): Colorless single crystals of **1⊃PX'** were obtained on exposing the crystals of **1** to the vapor of a solution of *p*-Xylene (2 mL) and DMF (1 mL) for 72h, without allowing any disturbance to the system.

2A.3. Result and discussions:

The compound $\{[Zn_4O(L)_3(DMF)_2].xG\}_n$(**1⊃G**) was synthesized by solvothermal reaction of $Zn(NO_3)_2$•$6H_2O$ with newly designed flexible dicarboxylic acid ligand LH_2 (**Figure 2A.1**, **Appendix 2A.1**) in a solvent mixture of DMF/1-butanol (1:1). Single-crystal X-ray diffraction (SC-XRD) studies revealed that the compound **1⊃G** is a porous 2D sheet structure

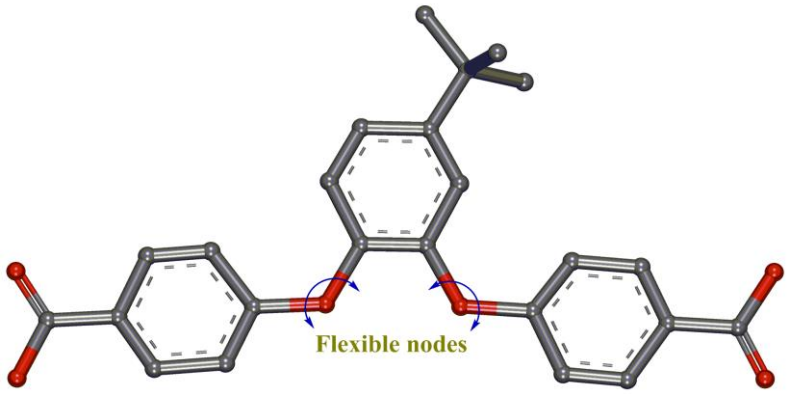

Figure 2A.1. Chemical structure of the designed ligand (LH_2) having two ether linkages as its flexible nodes.

(**Appendices 2A.11-2A.14**), which crystallized in monoclinic centrosymmetric space group *P21/c* (**Appendix table 2A.2**). *Adsym* subroutine of PLATON was applied to check that no additional symmetry could be applied to the model. The asymmetric unit comprises of four Zn(II) units, one central O^{2-}, three L^{2-}, and two N,N'-dimethyl formamide (DMF) molecules, both bound particularly to one of the metal centers (Zn4 centre as shown in **Appendix 2A.9**). Therefore, a $\{Zn_4O(CO_2)_6(DMF)_2\}$ secondary building unit (SBU) is formed by involving six

carboxylates from six different L^{2-} ligand units and two O-atoms of two DMF molecules. The SBU cluster core consists of a single O atom bonded to four Zn atoms, consequently forming regular tetrahedrons for three zinc centers and octahedron for the other zinc. Each Zn_4 cluster is connected to another Zn_4 cluster though two L^{2-} ligand to form a one dimensional (1D) chain. This 1D chain is again connected to similar another two chains on both side via L^{2-} to form the resultant 2D framework. This porous framework comprises of free disordered guest solvent molecules (G). PLATON analysis revealed that the compound **1⊃G** comprises of large voids of 3,441.2 $Å^3$, which represent 34.2% per unit cell volume. PXRD for the bulk phase of this compound **1⊃G** and its simulated pattern matched precisely, indicative of the phase purity (**Appendix 2A.20**), which is also supported by SC-XRD analysis of randomly selected crystals.

Thermogravimetric analyses (TGA) and variable temperature powder X-ray diffraction (VT-PXRD) measurements (**Appendices 2A.15, 2A.19**) were carried out to examine the thermal stability of this framework. The TGA curve for **1⊃G** shows that all the guest molecules present in the voids as well as the coordinated DMF molecules inside the shiny single crystalline phase of **1⊃G** can be removed by heating at 160 °C, to obtain the slightly pale colorless desolvated crystals of compound **1** (**Appendix 2A.10**). Variable temperature PXRD patterns for the compound **1⊃G** also validated this phase transformation. The thermal stability and phase purity of **1** were also confirmed by TGA and PXRD-analysis respectively (**Appendices 2A.15, 2A.20**). Furthermore, TGA plot showed that the sample is stable up to 410 °C. The release of free guest molecules along with the coordinated DMF molecules led to a drastic structural transformation, giving rise to squeezed non-porous framework $[Zn_4O(L)_3]_n$ (**1**), from porous **1⊃G**. As evidenced from the SC-XRD analysis of both the phases, this single-crystal to single-crystal (SCSC) solid state structural transformation (**Figure 2A.2**) is due to the slippage of 2D layers with respect to each other upon guest removal. PLATON analysis for **1** revealed that the ensuing 2D framework [space group $P2_1/c$ (**Appendix table 2A.3**)] underwent considerable squeezing (void volume of 915.8 $Å^3$, 12.8 % per unit cell volume) from **1⊃G** (void volume ~3,441.2 $Å^3$, 34.2% per unit cell volume). The coordination environment for all the four Zn-centers has now become same with tetrahedral geometry (**Appendix 2A.9**). Each of the edges of clusters is again connected to generate the resultant 2D framework. To examine the reversibility aspect of the structural transformation, the bulk crystalline phase 1 was kept immersed in a solution of 1-butanol (1 mL)

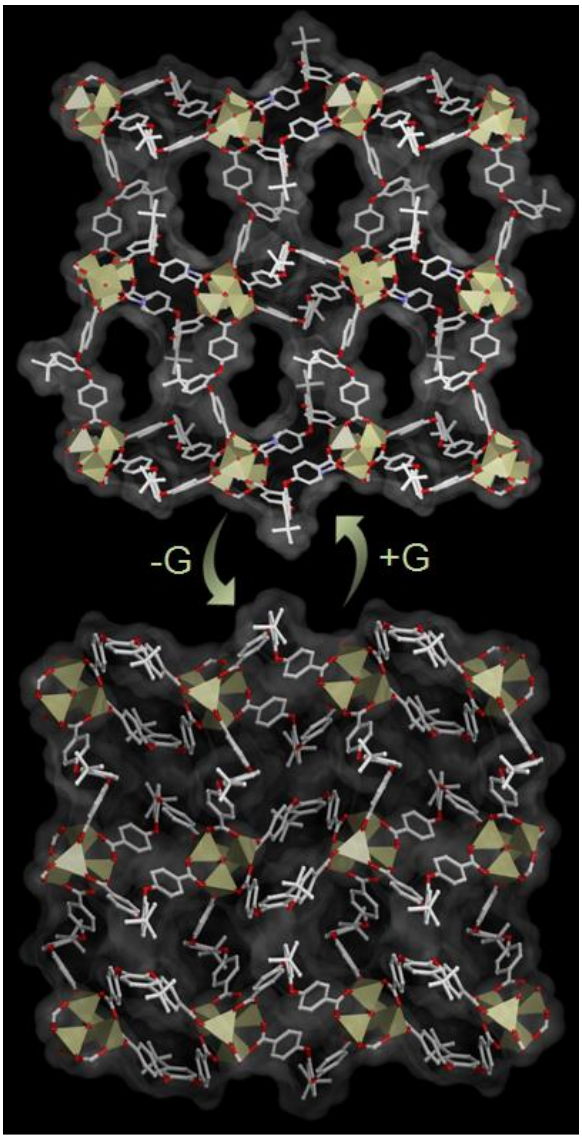

Figure 2A.2. Reversible structural transformation from porous compound **1⊃G** to non-porous **1** viewed along *a*-axis; both orthographic sights (H atoms and free solvent molecules are omitted for clarity).

and DMF (1 mL) for 24 h without any disturbance. PXRD analysis (**Appendix 2A.20**) and SC-XRD analysis of arbitrarily chosen crystals of this resolvated phase **1⊃G'** confirmed about the reversible structural transformations of this dynamic framework.

To examine the permanent porosity and sorption performance for the compound **1**, gas adsorption property of compound **1** was comprehensively investigated. N_2, H_2, Ar, CH_4 and CO_2 sorption experiments were carried out in a relative pressure range from 10^{-4} to 1 atm at 77K (N_2,

H_2 and Ar) and 195 K (CH_4 and CO_2). Compound **1** exhibited differential adsorption behaviour towards CO_2 (195K) as compared to those for N_2 (77K), H_2 (77K), Ar (77K), CH_4 (195K) (**Appendices 2A.25-2A.27**). Gas adsorption measurements were done volumetrically using activated compound **1**. Adsorption analysis of N_2 (77K), H_2 (77K), Ar (77K) and CH_4 (195K) showed only negligible uptake (23, 14, 6.7, 27.65 mLg^{-1} for N_2, H_2, Ar and CH_4 respectively), but notably, significant uptake was observed for CO_2 (114 mLg^{-1}) with a typical Type-1 sorption profile. The H-K (Horvath-Kawazoe) plot for CO_2 sorption at 195K (**Appendix 2A.29**) revealed an effective pore diameter of ~5.1 Å, which is relatively larger than all the probe adsorptive-gases, indicative of the fact that size-selectivity between different probe adsorptive species is not the only deciding factor. This also evidently suggests that the larger quadruple moment of CO_2 (1.34×10^{-39} Cm^2) plays the most crucial role behind the low-temperature CO_2-selective adsorption phenomena,[34-36] since the selective uptake of CO_2 by the dynamic framework **1** can be attributed to the favorable electrostatic interactions with the polar pore surface. Since the adsorption amounts of other gases (H_2, O_2, N_2, Ar, and CH_4) are much negligible compared to that for CO_2, the compound can prove expedient for separation of CO_2 at low temperature.

Microporous and flexible nature of the activated phase **1** with pore diameter close to the kinetic diameter of the xylenes (~0.6 nm), prompted us to investigate the adsorption characteristics for compound **1** systematically, for achieving separation of xylenes having similar physical properties and comparable molecular sizes. The vapor sorption experiments for the π-electron rich solvents like benzene (BZ) and toluene (TL), *p*-xylene (PX), *m*-xylene (MX) and *o*-xylene (OX) were measured along with nonaromatic solvent cyclohexane (CY) at 298K. As an important observation, significant amounts of π-e^- rich guests like benzene, and toluene were adsorbed (98 mLg^{-1} and 73 mLg^{-1} respectively), while as a simultaneous feature, analogous aliphatic guest cyclohexane parallely recorded a high uptake amount (74 mLg^{-1}) at 298K (**Appendix 2A.31**). These sorption profiles reinforced the coexistence of favorable π-π interactions between the π-electron rich polar framework (operative for aromatic guests namely, benzene and toluene) and C-H-π interactions (functional for aliphatic solvent cyclohexane) as the dual crucial influences playing their parts for the respective host-guest interactions. Remarkably, the adsorption isotherms recorded for the three isomers of xylene, *i.e.* PX, MX, OX along with EB at 298K presented selective adsorption of PX over the other three isomers. While the

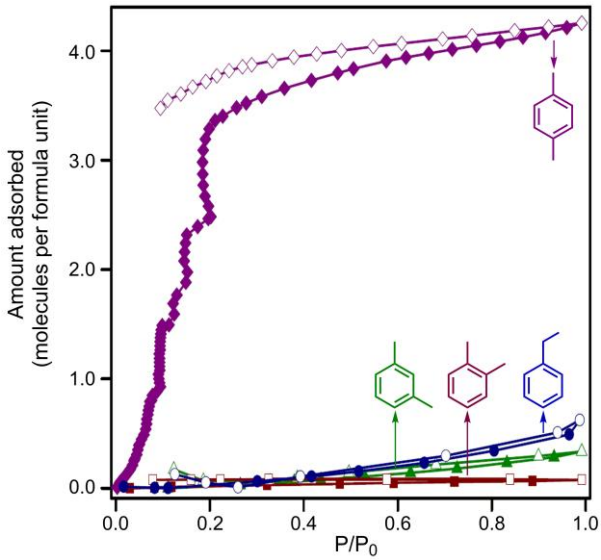

Figure 2A.3. Solvent sorption isotherms for compound **1** at 298K for three of the xylene isomers along with isomeric ethylbenzene. Closed and open symbols denote adsorption and desorption respectively.

adsorption amount for the *p*-isomer was found to be 64 mLg^{-1}, the corresponding uptake amounts for the *m*- and *o*-isomers were surprisingly much lower, 5 mLg^{-1} and 1.15 mLg^{-1} respectively (**Appendix 2A.31**), corresponding to 4 molecules of PX-uptake per formula unit, while only 0.34 and 0.08 molecules uptake for MX and OX respectively (**Figure 2A.3**). EB also recorded a very marginal uptake of only 9.4 mLg^{-1} (0.63 molecules per formula unit). This differential adsorption behavior towards the four constitutional isomers consolidated that the framework flexibility of desolvated phase **1** allow the entry of the linear guest PX but not the bent ones, namely MX and OX, due to steric hindrance that originates in the case of the latter two. Meanwhile, EB possessing the ethyl side group has a minimum dimension of 5.285 Å ('MIN-1', **Appendix table 2A.1**),[37] much higher than the congeners making its entry improbable. 'MIN-1' for all the other three isomers being very similar, the second minimum dimension for molecular orientations that enable a molecule to enter the channel, **'**MIN-2' (**Appendix table 2A.1**) comes into play, which is considerably lower for *p*-xylene (6.618 Å) than the other two (7.269 Å and 7.258 Å for *m*- and *o*-isomers respectively). Interestingly, the effective pore diameter of 5.1 Å, as obtained from HK-pore size distribution plot for the microporous adsorbent host material **1**, is lower than all the three 'MIN-2' values for each of the xylene isomers. This evidently indicates that the strategically achieved framework flexibility feature arising out of the ether-linkage based

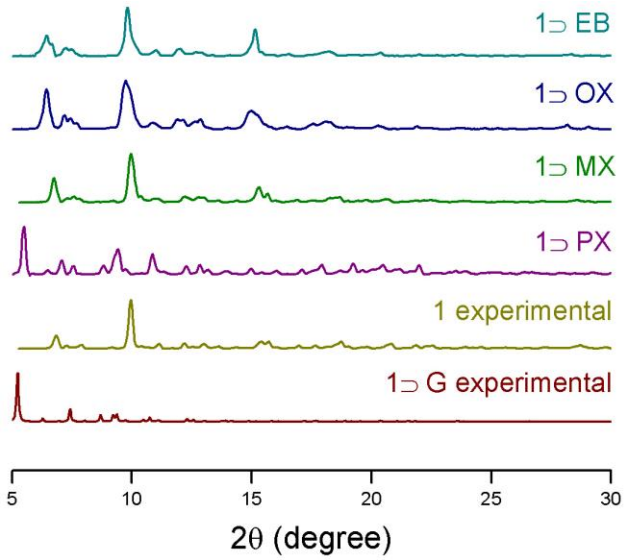

Figure 2A.4. Experimental PXRD patterns of **1⊃G**, **1**, **1⊃PX**, **1⊃MX**, **1⊃OX** and **1⊃EB** compounds.

ligands, make possible the allowance of smaller PX but not the other two, due to limiting restricted flexibility which cannot let the bigger isomers enter inside the porous channels. The small variation in the molecular dimensions between these three isomeric guests might be the only crucial reason in deciding the selective entry of PX, while refusing the flexible framework **1** to open for OX and MX, owing to steric hindrance. Hence, the aspect of size-selectivity proves decisive in determining the observed adsorption-selectivity via guest-inclusion in case of xylene isomers.

To confirm the structural transformations occurring on the interplay of host-guest interactions, TGA plots and PXRD profiles for each of the guest-exposed phases were recorded (**Figure 2A.4**, **Appendices 2A.16-2A.18**, **Appendices 2A.21-2A.22**) which conclusively reaffirmed the results suggested from solvent sorption studies, as MX and OX could do no change to the characteristic PXRD pattern for **1**, while the other solvents were able to mediate the dynamic transformation from **1** to **1⊃G** phases, having similar PXRD forms as for **1⊃G**. TGA results also strengthened this observation since no significant weight loss was observed for the phases **1⊃OX** and **1⊃MX**, but all the other guest solvent vapor-exposed phases revealed considerable loss in %weight within 100 °C, indicative of loss of trapped solvent- guests. To further reinforce the selective interplay of PX with the flexible framework **1** as compared to OX

and MX, PXRD profiles for binary and ternary solvent vapor-exposed phases were recorded (**Appendix 2A.24**), which was reiterated by ^{13}C NMR experiments with the DCl/DMSO-d_6 digested samples after vapor exposure to three different binary mixtures (1:1) of the xylene isomers (**Appendix 2A.33**).

Although the crystals of **1⊃PX** did not diffract while repeated attempts were made to get the crystal structure of the phase **1⊃PX**, a similar resolvated phase **1⊃PX'** (as indicated from the similar PXRD patterns of both) (**Appendix 2A.21**) was obtained on exposing the crystals of **1** to the vapor of a solution of *p*-Xylene (2 mL) and DMF (1 mL) for 72 h. SC-XRD analysis of this new phase **1⊃PX'** (formula: $\{[Zn_4O(L)_3(DMF)_2].(C_8H_{10})\}_n$) revealed that the compound has again transformed to the open phase, having unit cell parameters very similar to the crystals of **1⊃G** and crystallized in monoclinic centrosymmetric space group $P2_1/c$ (**Appendix table 2A.4**). *p*-xylene molecules could actually be located in the SC-XRD structure for this **1⊃PX'** phase crystals, sitting inside the porous channels of the host framework (**Figure 2A.5**), after it could open up the shrinked windows of desolvated phase **1** to get accommodated inside the hydrophobic channels, owing to the inherent dynamism of the framework, arising out of the highly flexible ether nodes. ^{13}CNMR experiment also proved the inclusion of PX (**Appendix 2A.34**). After confirming the phase purity for the new phase **1⊃PX'** from PXRD, both TGA and PXRD analysis for **1⊃PX** and **1⊃PX'** phases confirmed their similar nature (**Appendices 2A.18**, and **2A.21**). To check reversibility of this PX-inclusion, the crystals of **1⊃PX'** were heated at 160 °C under reduced pressure for 4h, to obtain the desolvated phase **1'**. TGA and PXRD profiles (**Appendices 2A.18**, **2A.23**) established the resemblance with the parent desolvated phase **1**, confirming the PX-inclusion reversibility.

To ensure the reproducibility of the xylene adsorbents, reproducing the same isotherm on unchanged desolvated sample **1** was checked ten consecutive times for PX, and three times for each of the other xylene isomers (**Appendices 2A.35-2A.39**). The results reflect excellent repeatability in each case. PXRD patterns recorded for the adsorbent MOF after each of the adsorption-desorption cycles are depicted in **Appendices 2A.40-2A.41**. These patterns are markedly identical to the desolvated adsorbent MOF **1**, which implies that the sample remains intact after each of the sorption cycles.

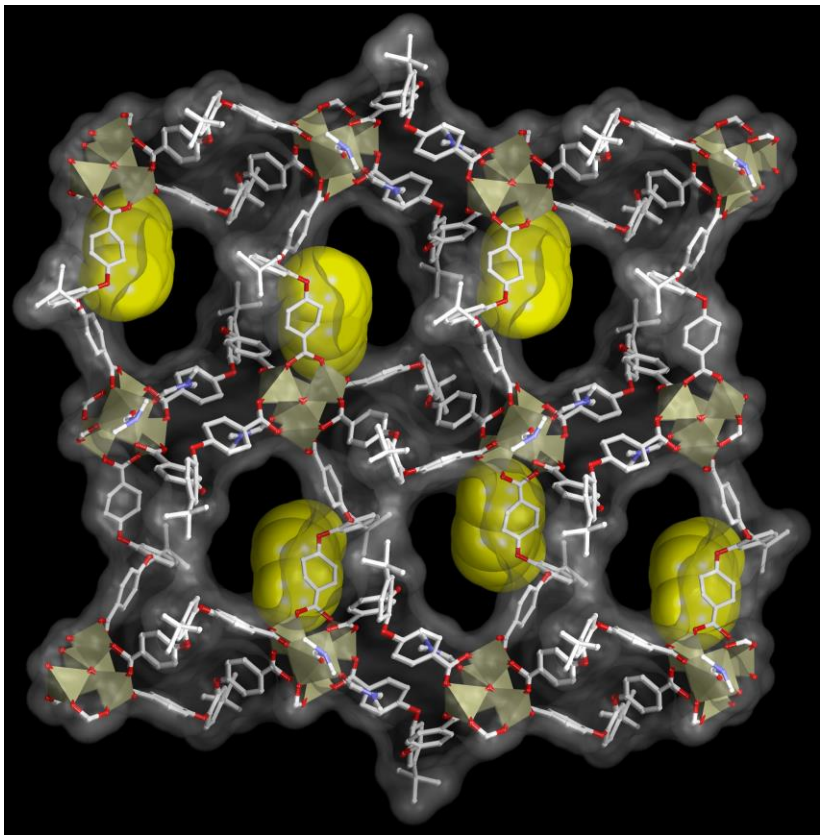

Figure 2A.5. Overall structure of resolvated phase **1⊃PX'** showing free PX molecules in the channels, along *a*-axis (PX molecules shown in spacefill model for clarity): Direct crystallographic evidence of resolvated framework on *p*-xylene accommodation mediated breathing.

To check the practical importance of separation, phase **1** was immersed into ternary and quaternary mixture solution of xylenes for 1 h and the amounts of the non-adsorbed isomers were analyzed by GC in intermediate time intervals. Crystalline phase **1** (100 mg) was immersed into mixture solution of xylenes for 1 h according to the following three different combinations, and GC chromatogram were recorded by pipetting out the supernatant solutions (0.123 mL each time) at regular time intervals, and preparing the GC samples in 1.3 mL MeCN in each of the occurrences (GC parameters employed are mentioned in SI). *Setup A: Quaternary xylene mixture immersion test:* 100 mg of **1** was kept immersed in a mixture solution of OX (1 mL), MX (1 mL), PX (1 mL) and EB (1 mL) for 1h, while in the intermediate time intervals 0.123 mL of the supernatant solution were pipetted out for recording the GC chromatogram at those respective times (**Figure 2A.6a**). As per the literature reported standard GC chromatogram for xylene

mixtures,[38] it was found that EB and OX were giving rise to their characteristically separate GC signals, although the retention times for MX and PX coincided to give a mixed intensity signal, owing to their very close characteristic retention times. To check whether the observed decrease in the mixed (PX+MX) signal intensity (for setup A) occurs due to the sole effect or PX only, and not MX, the following two experiments were also performed. *Setup B: Ternary xylene mixture immersion test (excluding PX):* 100 mg of **1** was kept immersed in a mixture solution of OX (1 mL), MX (1 mL), MX (1 mL) and EB (1 mL) for 1h, while in the intermediate time intervals 0.123 mL of the supernatant solution were pipetted out for recording the GC chromatogram at those respective times (**Figure 2A.6b**). *Setup C: Ternary xylene mixture immersion test (excluding MX):* 100 mg of 1 was kept immersed in a mixture solution of OX (1mL), PX (1 mL) and EB (1 mL) for 1h, while in the intermediate time intervals 0.123 mL of the supernatant solution were pipetted out for recording the GC chromatogram at those respective times (**Figure 2A.6c**). The results (**Figure 2A.6**) confirm that the observed decline in particularly one of the signal intensity is solely in presence of PX.

It is indeed a fascinating observation, that only those guest solvent species which could mediate the SCSC transformation of the desolvated MOF **1** could selectively get adsorbed inside the framework as evidenced from both the PXRD and TGA experiments (also the conclusive SC-XRD structure of resolvated **1⊃PX'**); but the ones which were not capable to affect the PXRD of phase **1** on exposure, did not get adsorbed at all. This conclusively proved the riveting effect of framework flexibility for the present microporous material, allowing the multiple SCSC transformations on guest inclusion due to favorable host-guest interactions. This in effect developed a size-selective adsorption based separation property for *p*-xylene over *m*- and *o*-xylene along with ethylbenzene, by virtue of the restricted limiting allowance principle exhibited by the MOF material, making it a unique dynamic framework functioning as a molecular sieve for xylene isomers.

2A.4. Theoretical Analyses:

Fitting of pure component isotherms for DynaMOF-100

The measured pure component isotherm data for each hydrocarbon exhibit hysteresis effects. For the purpose of analyzing the separation potential, the "adsorption branch" of the isotherms are selectively used, and the "desorption branch" were neglected.

Some of the pure component isotherm data show marked inflections, and in order to correctly capture these inflections the unary isotherm data were fitted with the two-site Langmuir-Freundlich model:

$$q = q_{A,sat}\frac{b_A p^{\nu_A}}{1+b_A p^{\nu_A}} + q_{B,sat}\frac{b_B p^{\nu_B}}{1+b_B p^{\nu_B}} \tag{1}$$

The saturation capacities q_{sat}, Langmuir constants b, and the Freundlich exponents ν, are provided in **Appendix Table 2A.5**. **Appendix 2A.45a** provides a comparison of the experimental isotherm data with the Langmuir-Freundlich fits.

IAST calculations of mixture adsorption equilibrium in DynaMOF-100

The Ideal Adsorbed Solution Theory (IAST) of Myers and Prausnitz[46] is used to determine the adsorption equilibrium for equimolar gas phase four-component equimolar *o*-xylene(1)/*m*-xylene(2)/*p*-xylene(3)/ethylbenzene(4) mixtures; see **Appendix 2A.45b**. We note that for pressures at 100 kPa, the adsorbed phase consists predominantly of *p*-xylene. In current industrial practice, the separation of xylene isomers is conducted with bulk liquid phase mixtures using BaX zeolite; under such conditions the pores of BaX are saturated with guest molecules. For comparison with BaX and other MOFs, let us define the fractional occupancy within the pores, θ_t

$$\theta_t = \sum_{i=1}^{n}\frac{q_i}{q_{i,sat}} \tag{2}$$

where $q_{i,sat} = q_{i,A,sat} + q_{i,A,sat}$, is the sum of the saturation capacities of the two sites A and B in the dual-Langmuir-Freundlich isotherm fits.

Appendix 2A.45c shows the IAST calculations of the fractional occupancy, θ_t, within the pores of DynaMOF-100 as a function of the total gas phase pressure, p_t. We note that the pores are saturated, i.e. $\theta_t \rightarrow 1$, when the total pressure p_t has values exceeding about 4 kPa. **Appendix 2A.45d** shows the IAST calculations of the component loadings as a function of the fractional occupancy, θ_t, within the pores of DynaMOF-100. We note that at pore saturation conditions, i.e. $\theta_t \rightarrow 1$, the pores are predominantly occupied by *p*-xylene.

The adsorption selectivity and *p*-xylene uptake capacities of DynaMOF-100 with BaX and MAF-X8 are also compared herein.

For a binary mixture the adsorption selectivity is defined as follows

$$S_{ads} = \frac{q_1/q_2}{p_1/p_2} \tag{3}$$

For separation of 4-component equimolar *o*-xylene(1)/*m*-xylene(2)/*p*-xylene(3)/ethylbenzene(4) mixtures we adopt the following definition of selectivity that was used in the recent paper of Torres-Knoop *et al.*[47]

$$S_{ads} = \frac{(q_3)/(q_1+q_2+q_4)}{(p_3)/(p_1+p_2+p_4)} = 3\frac{(q_3)}{(q_1+q_2+q_4)} \tag{4}$$

Appendix 2A.46a shows that the adsorption selectivity of DynaMOF-100 is about one to two orders of magnitude higher than that of MAF-X8 and BaX zeolite.

Besides adsorption selectivity, the separation performance is also dictated by the uptake capacity for *p*-xylene. **Appendix 2A.46b** compares the *p*-xylene uptake capacity of MAF-X8 (at 433 K), BaX zeolite (at 393 K, and 453 K), with that of DynaMOF-100 (at 298 K). We note that at pore saturation conditions, that is typical of industrial operations, DynaMOF-100 has a significantly higher uptake capacity than BaX zeolite and MAF-X8.

Transient breakthrough simulations

The separation performance of a fixed bed adsorber (see schematic in **Appendix 2A.48**); is dictated by both adsorption selectivity and capacity. A higher capacity to adsorb *p*-xylene leads to a longer cycle time that is desirable because of this requires less frequent regeneration.

Using the pure component isotherm fits of experimental data, transient breakthrough simulations were carried out, using the methodology described in earlier reports.[48, 49]

The breakthrough characteristics for any component is essentially dictated primarily by the characteristic contact time $\frac{L}{v} = \frac{L\varepsilon}{u}$ between the crystallites and the surrounding fluid phase. It is common to use the dimensionless time, $\tau = \frac{tu}{L\varepsilon}$, obtained by dividing the actual time, t, by the characteristic time, $\frac{L\varepsilon}{u}$ when plotting simulated breakthrough curves.[49] For the breakthrough simulations reported here we use the parameter values: L = 0.3 m; voidage of bed, ε = 0.4; interstitial gas velocity, v = 0.1 m/s; superficial gas velocity, u = 0.04 m/s.

The clearest demonstration of the propensity of DynaMOF-100 to selectively adsorb *p*-xylene is provided by pulse chromatographic simulations; see **Appendix 2A.47a**. The elution sequence of the pulses is ethylbenzene, *m*-xylene, *o*-xylene, and *p*-xylene. The mean times at which the pulses appear are τ = 30 (ethylbenzene, and *m*-xylene), τ = 300 (*o*-xylene), and τ = 10000 (*p*-xylene). The largest time lag between the elution of *o*-xylene and *p*-xylene is a clear indication of the efficacy of separation.

Let us now consider transient breakthroughs with step-input of four-component mixture of C8 hydrocarbons. **Appendix 2A.47b** shows the results of transient breakthrough simulations of a 4-component equimolar *o*-xylene(1)/*m*-xylene(2)/*p*-xylene(3)/ethylbenzene(4) mixtures with step input: p_i = 1 kPa for each hydrocarbon; this choice of partial pressures ensures that the conditions correspond to pore saturation (*cf.* **Appendix 2A.45c**). *o*-xylene, *m*-xylene and ethylbenzene are hardly adsorbed and are rejected into the bulk fluid phase immediately after feed injection.

For comparison with other MOFs, we define the cycle time for *p*-xylene as the dimensionless time, τ_{cycle}, at which the concentration of the gas at the outlet is 99% of the value at the inlet; this approach was used earlier in the comparisons published by Torres-Knoop *et al.*[47] The cycle time τ_{cycle} = 10,186 for DynaMOF-100, as compared to τ_{cycle} = 335 for MAF-X8, and τ_{cycle} = 74 for BaX zeolite. Longer cycle times are desirable because this implies that implies that smaller desorbent-flow rates will be required.

The clean separation achieved with DynaMOF-100 is best illustrated by video animations of the breakthroughs using both step input and pulse input of *o*-xylene/*m*-xylene/*p*-xylene/ethylbenzene mixtures.

2A.5. Conclusion:

In conclusion, a novel dynamic MOF has been successfully synthesized from a strategically designed ligand bearing two ether linkages as its flexible nodes. The resultant MOF showed high degree of framework flexibility owing to the ether linkages actually functioning as the adjustable nodes, accompanying the guest-inclusion mediated solid-state structural transformations. The MOF material presented selective adsorption of *p*-xylene over the other two constitutional isomers, invoking the guest-responsive structural dynamism feature to allow the selective inclusion of the *p*-isomer over the other two sterically bulkier congeners. This kind of guest-selective structural changes occurring in the crystalline state of porous materials can be exploited in future for the targeted application-oriented development of novel functional materials which might result in important industrial applications for chemical separation. The present material might prove to be an excellent candidate to further investigate its sorption kinetics, which will be requisite to evaluate its suitability for practical separations based on this observed ambient temperature PX-selective sorption phenomena.

2A.6. Appendix Section:

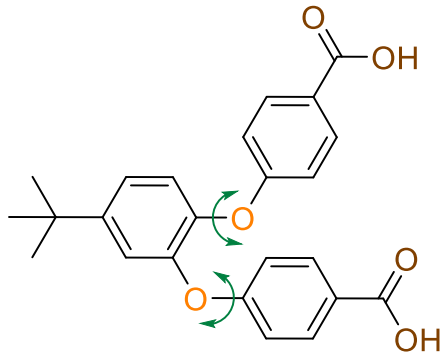

4,4'-((4-(*tert*-butyl)-1,2-phenylene)bis(oxy))dibenzoic acid

Appendix 2A.1. Chemical structure of the ether-functionalized flexible dicarboxylic acid ligand (LH_2) having the *t*-butyl moiety to offer requisite hydrophobicity to the pore channels.

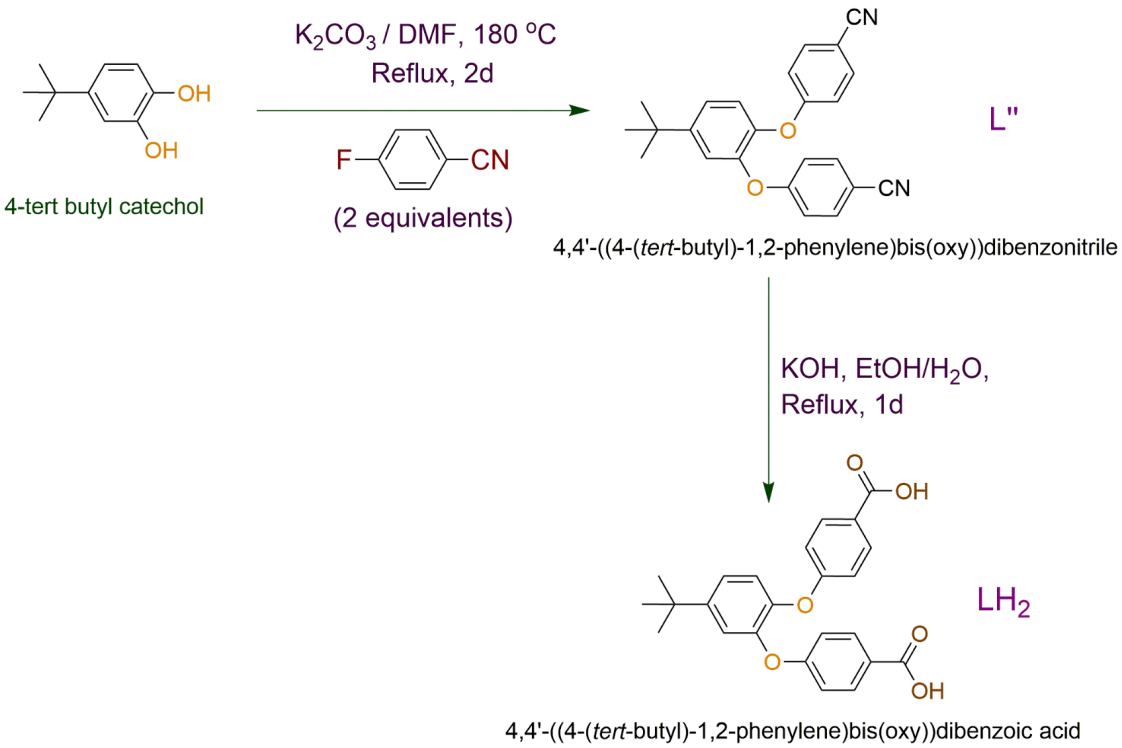

Appendix 2A.2. Synthesis of ligand LH_2 via intermediate L'.

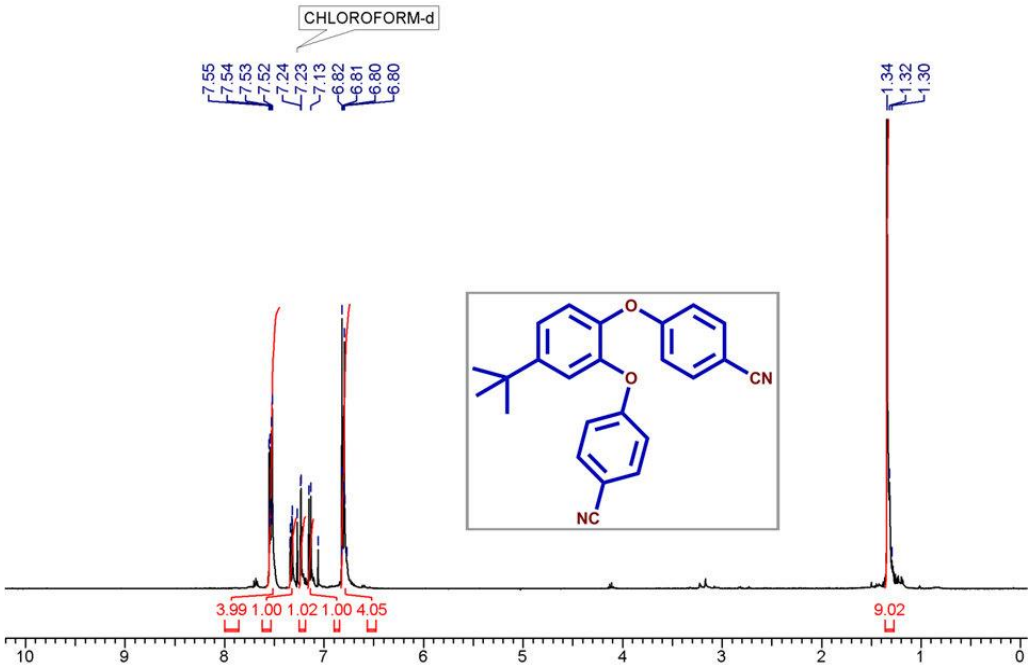

Appendix 2A.3. ^{1}H NMR spectrum of Ligand **L'**.

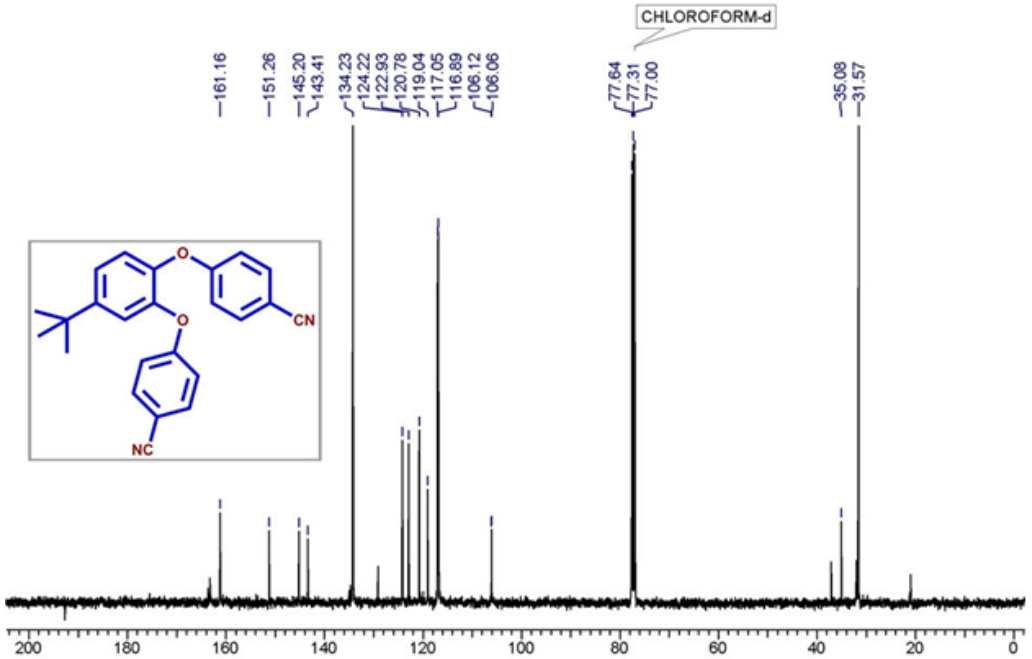

Appendix 2A.4. ^{13}C NMR spectrum of Ligand **L'**.

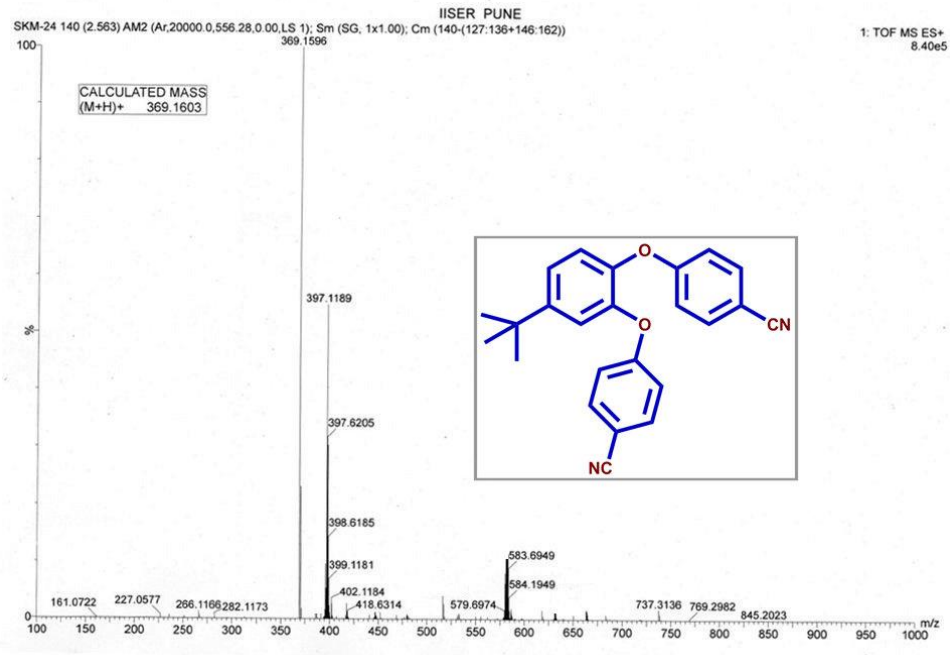

Appendix 2A.5. HRMS spectrum of Ligand **L'**.

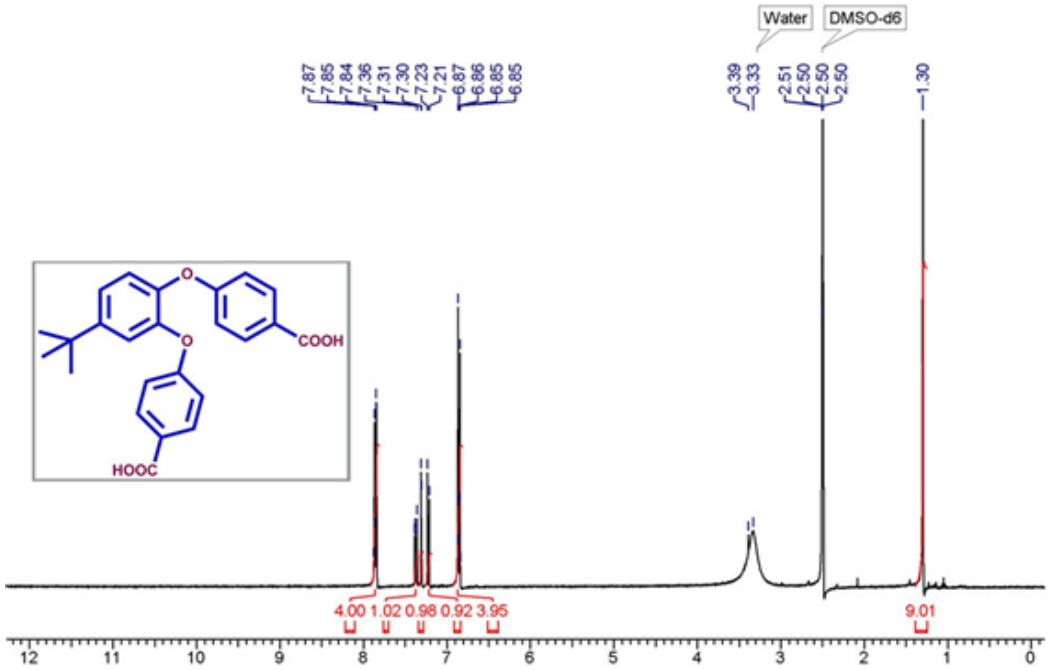

Appendix 2A.6. ^{1}H NMR spectrum of Ligand **LH_2**.

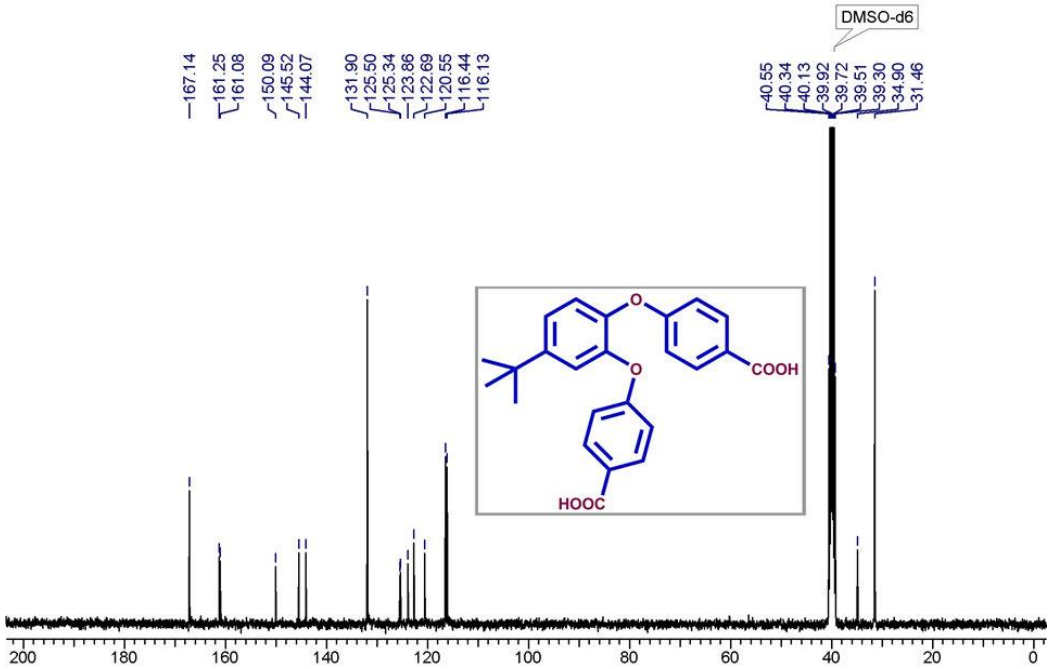

Appendix 2A.7. ^{13}C NMR spectrum of Ligand **LH_2**.

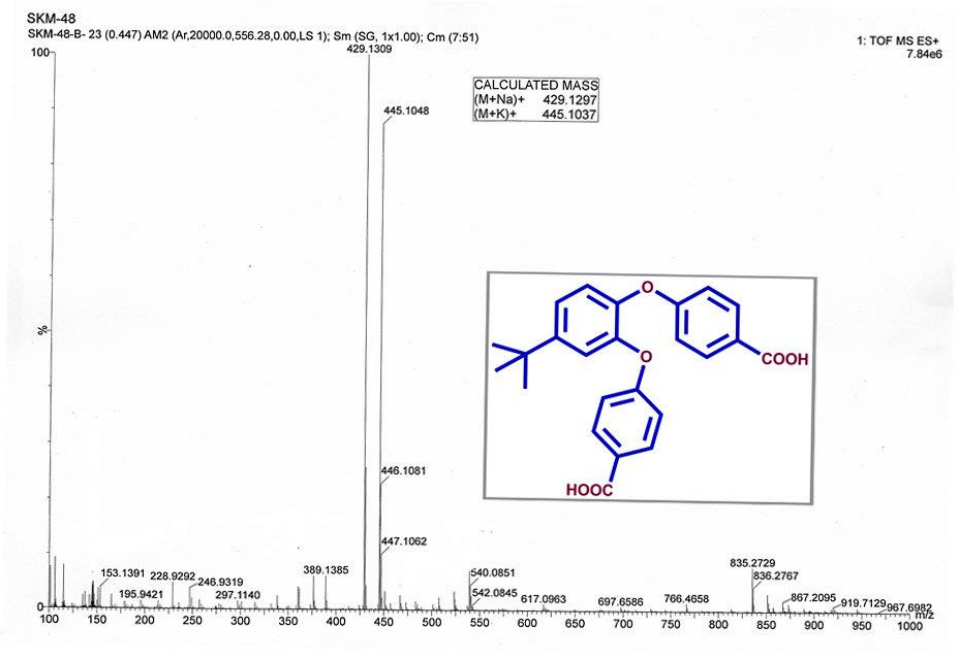

Appendix 2A.8. HRMS spectrum of Ligand **LH_2**.

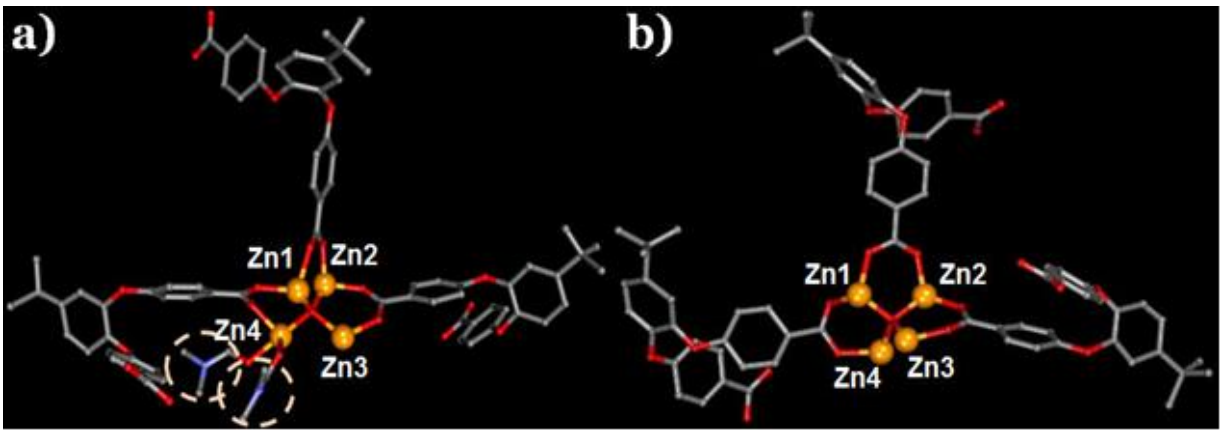

Appendix 2A.9. Asymmetric unit of the two phases: a) as-synthesized phase **1⊃G**; b) desolvated phase **1**; DMF molecules coordinated to Zn4 to make its environment octahedral are shown by dashed circle (water molecules are omitted for clarity for a)).

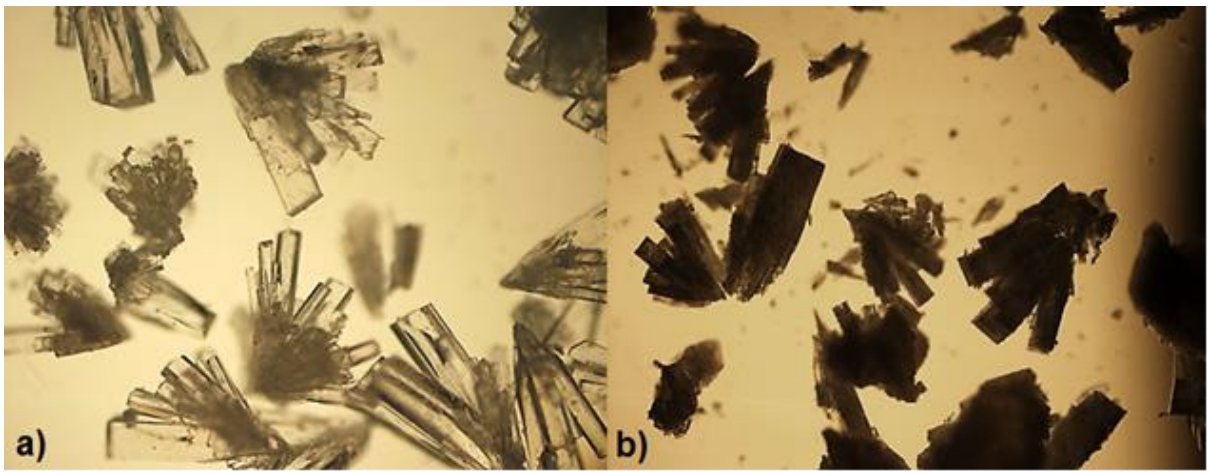

Appendix 2A.10. Microscopy images of the crystals for two different SCSC phases: a) compound **1⊃G** (as synthesized), b) compound **1** (desolvated).

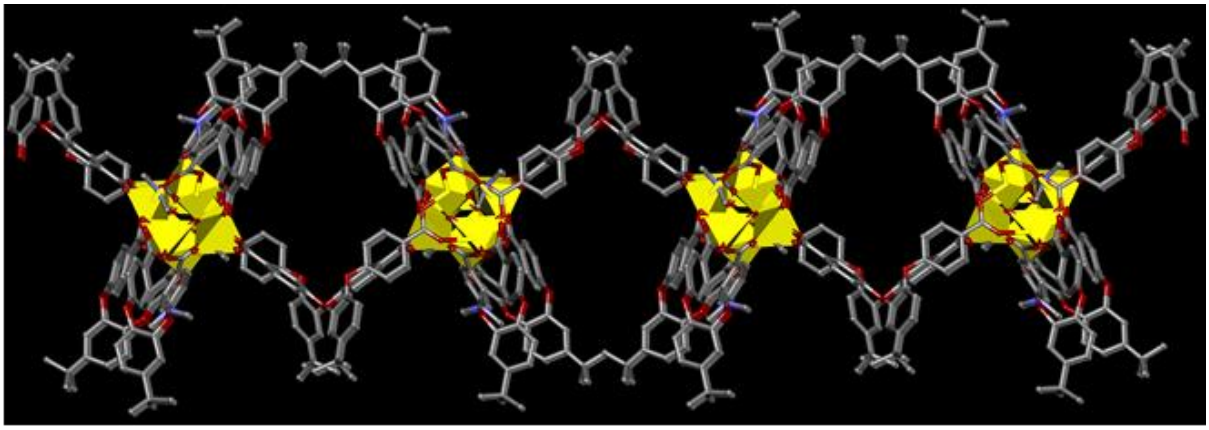

Appendix 2A.11. Progression of a single 2D-sheet (along *c*-axis) for the phase **1⊃G**.

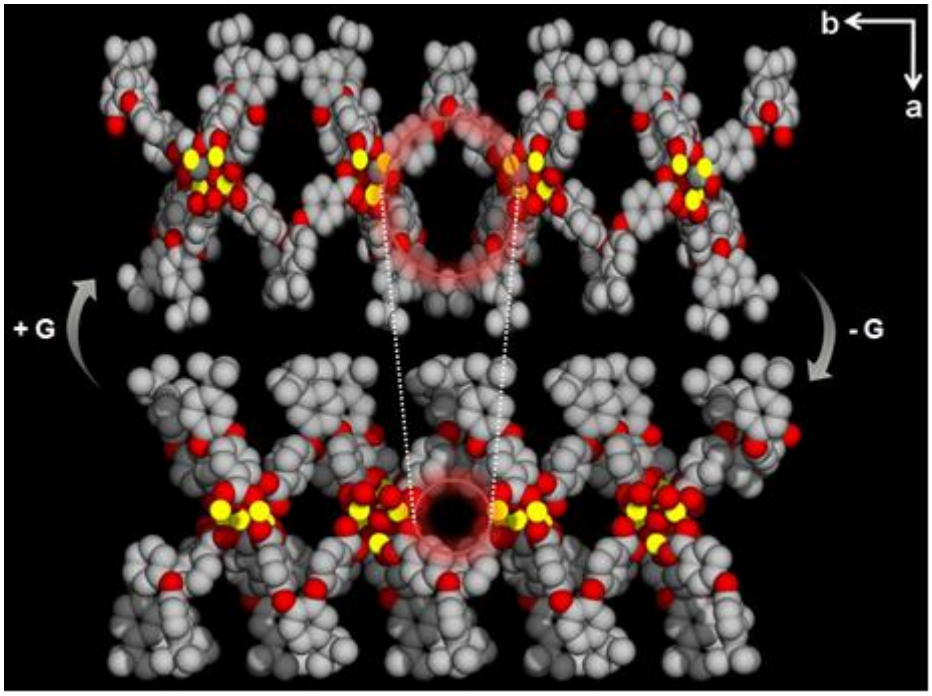

Appendix 2A.12. Squeezing of the channels of the single 2D-sheets (along *c*-axis) for the phases **1⊃G** and **1**.

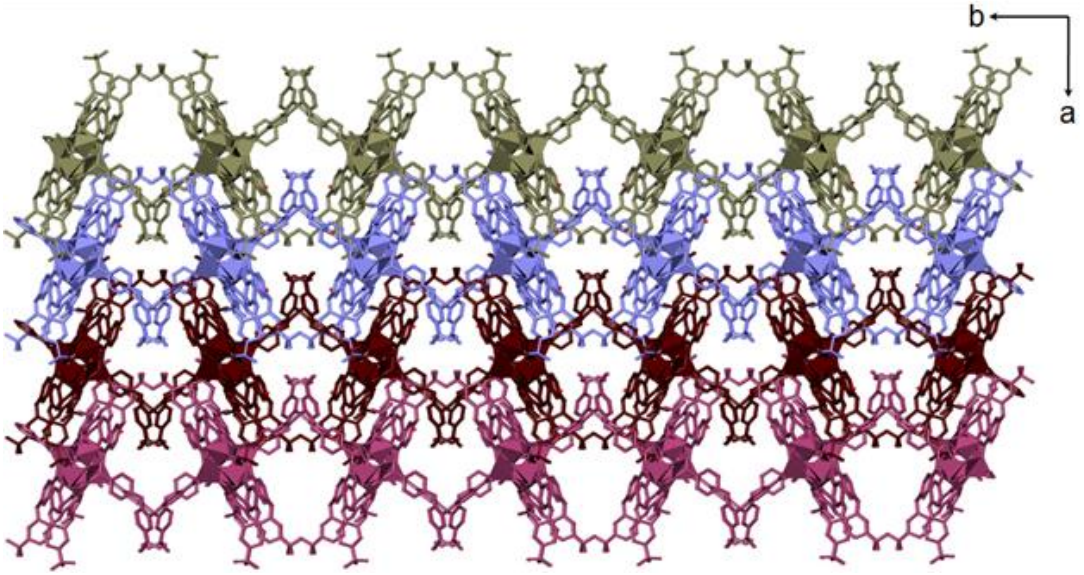

Appendix 2A.13. Perspective view along *c*-axis for the as-synthesized phase **1⊃G** (each color representing a 2D-sheet).

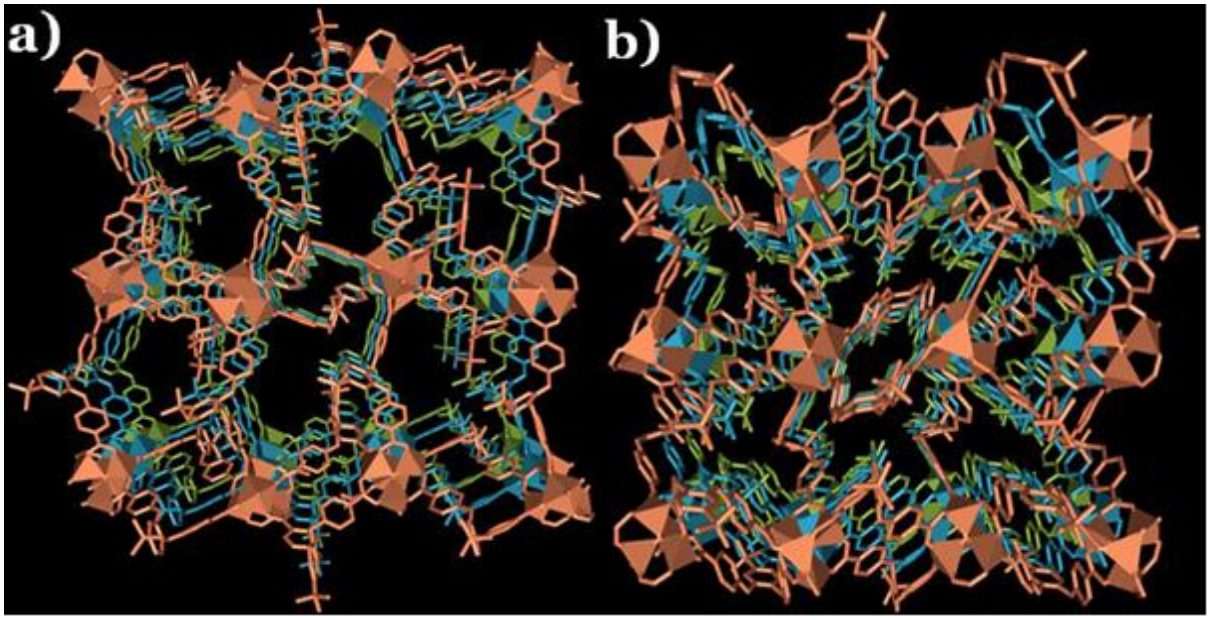

Appendix 2A.14. Perspective view along *a*-axis for the two phases: a) as-synthesized phase **1⊃G**; b) desolvated phase **1** (three nets shown in different colors) (guest molecules omitted for clarity).

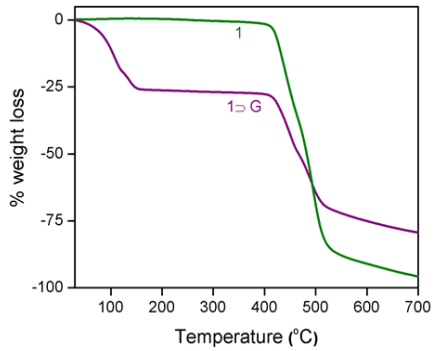

Appendix 2A.15. Thermogravimetric analysis (TGA) plots for the as-synthesized (**1⊃G**; purple color) and desolvated (**1**; olive color) compounds.

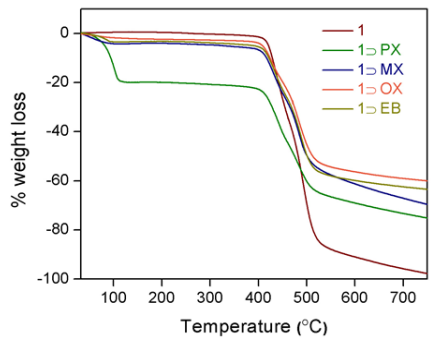

Appendix 2A.16. TGA plots for the guest-exposed phases of **1** (**1⊃ solvent**), compared with that of **1** (wine). Vapor of solvents like ***p*-xylene** (olive), ***m*-xylene** (orange), ***o*-xylene** (navy) and **ethylbenzene** (dark yellow) were exposed.

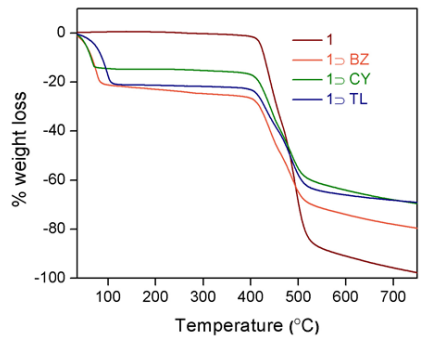

Appendix 2A.17. TGA plots for the guest-exposed phases of **1** (**1⊃ solvent**), compared with that of **1** (wine). Vapor of solvents like **Benzene** (orange), **Toluene** (olive), and **cyclohexane** (royal blue) were exposed.

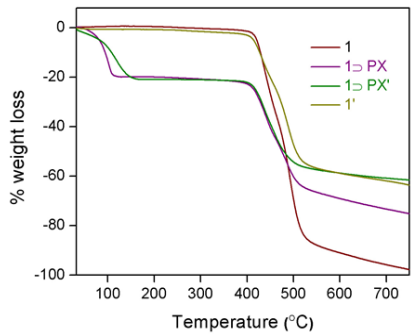

Appendix 2A.18. TGA plots for desolvated phase **1** (wine), compared with that of PX-exposed sample **1⊃PX** (purple), crystals **1⊃PX'**, along with the heated (re-desolvated) phase **1'**.

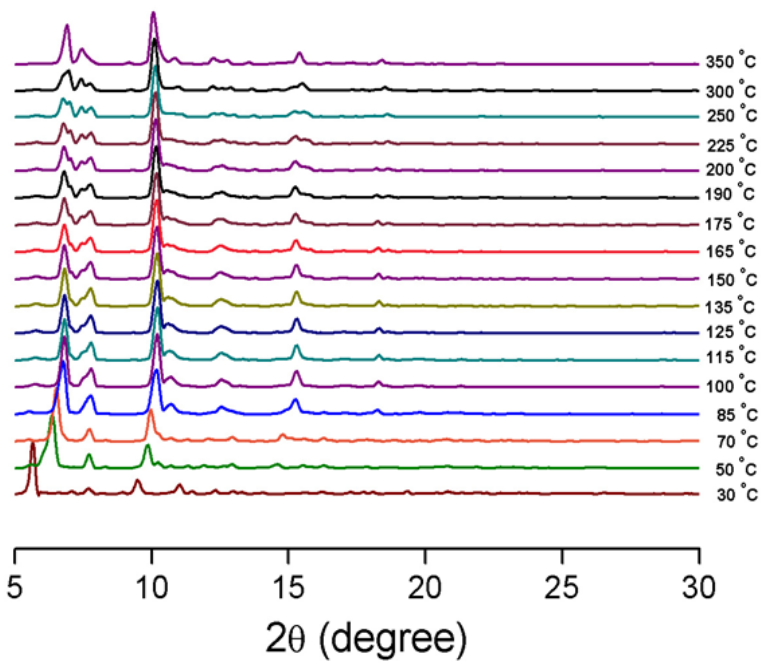

Appendix 2A.19. Variable temperature powder X-ray diffraction (PXRD) patterns of compound **1⊃G**.

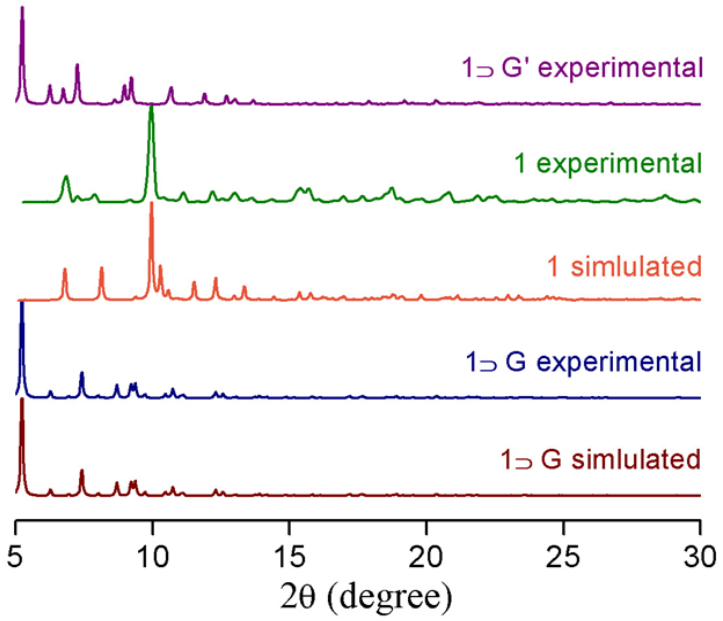

Appendix 2A.20. Powder X-ray diffraction (PXRD) patterns of compounds **1⊃G**, **1** and **1⊃G′**.

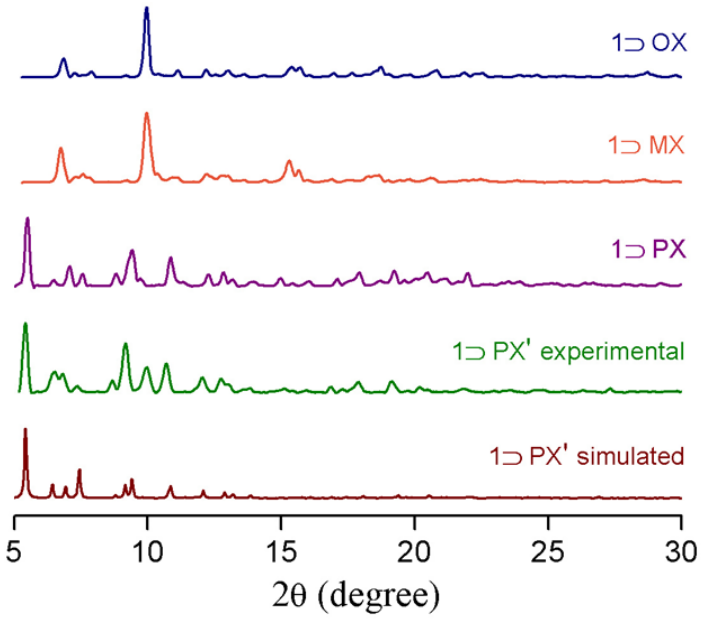

Appendix 2A.21. Simulated and experimental PXRD patterns of **1⊃PX'**, and experimental PXRD patterns for three different solvent exposed samples (**1⊃solvent**): **PX** (*p*-xylene), **MX** (*m*-xylene), **OX** (*o*-xylene).

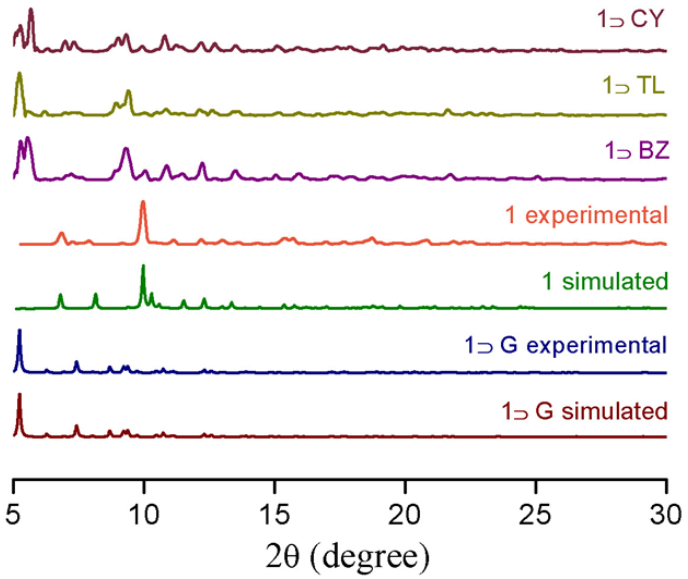

Appendix 2A.22. Simulated and experimental PXRD patterns of **1⊃G** and **1**, and experimental PXRD patterns for different solvent exposed samples (**1⊃solvent**); **BZ** (benzene), **TL** (toluene), and **CY** (cyclohexane).

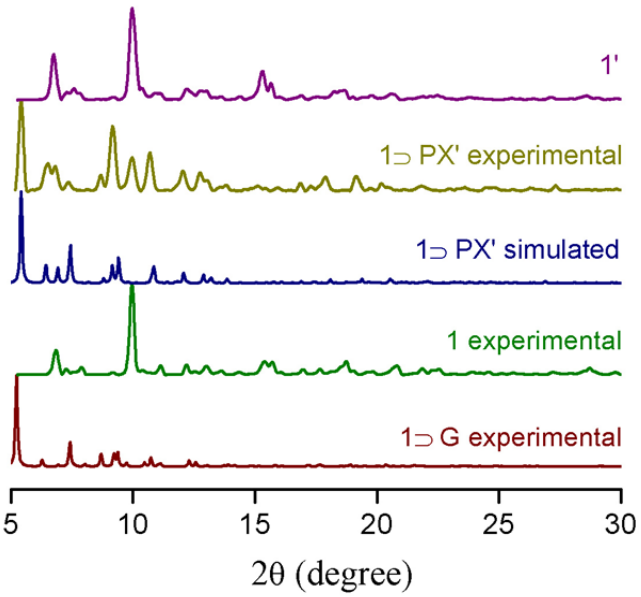

Appendix 2A.23. Powder X-ray diffraction (PXRD) patterns of compounds **1⊃G** (experimental), **1** (experimental), **1⊃PX'** (simulated), **1⊃PX'** (experimental) and **1'**(phase after heating phase **1⊃PX'**).

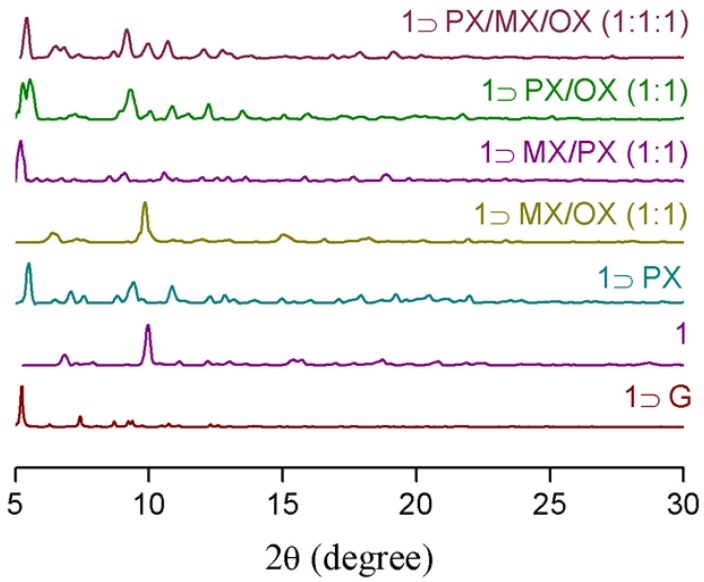

Appendix 2A.24. Experimental PXRD patterns for compounds **1⊃G**, **1**, and the vapor-exposed phases: **1⊃PX** (only PX), **1⊃MX/OX** (binary mixture of 1:1 v/v MX and OX), **1⊃MX/PX** (binary mixture of 1:1 v/v MX and PX), **1⊃PX/OX** (binary mixture of 1:1 v/v PX and OX), **1⊃PX/MX/OX** (ternary mixture of 1:1:1 v/v PX, MX and OX).

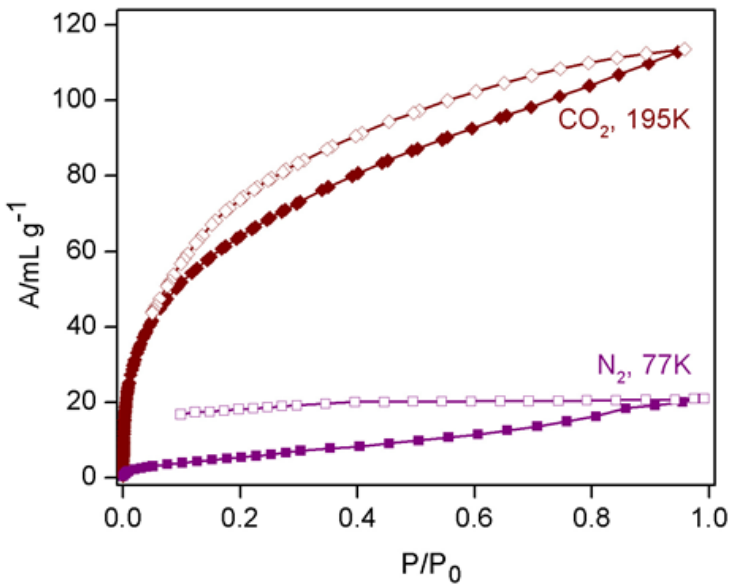

Appendix 2A.25. CO_2 and N_2 sorption isotherms of compound **1** at 195K and 77K respectively. Filled shapes = adsorption, hollow shapes = desorption.

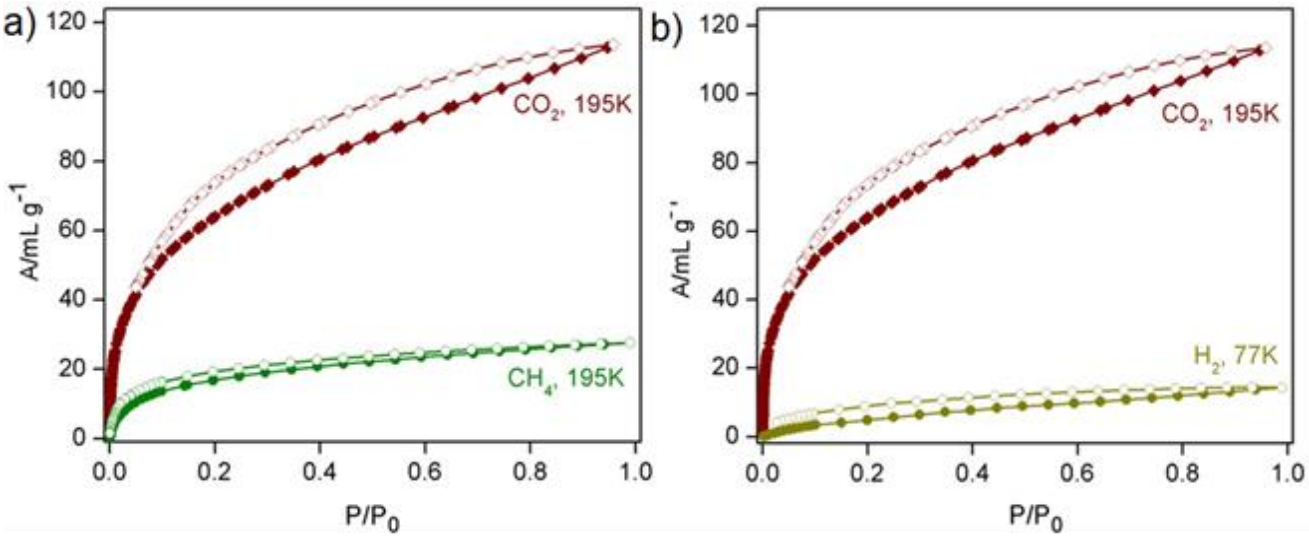

Appendix 2A.26. a) CO_2 and CH_4 sorption isotherms of compound **1** at 195K; b) CO_2 and H_2 sorption isotherms of compound **1** at 195K and 77K respectively. (Filled shapes = adsorption, hollow shapes = desorption).

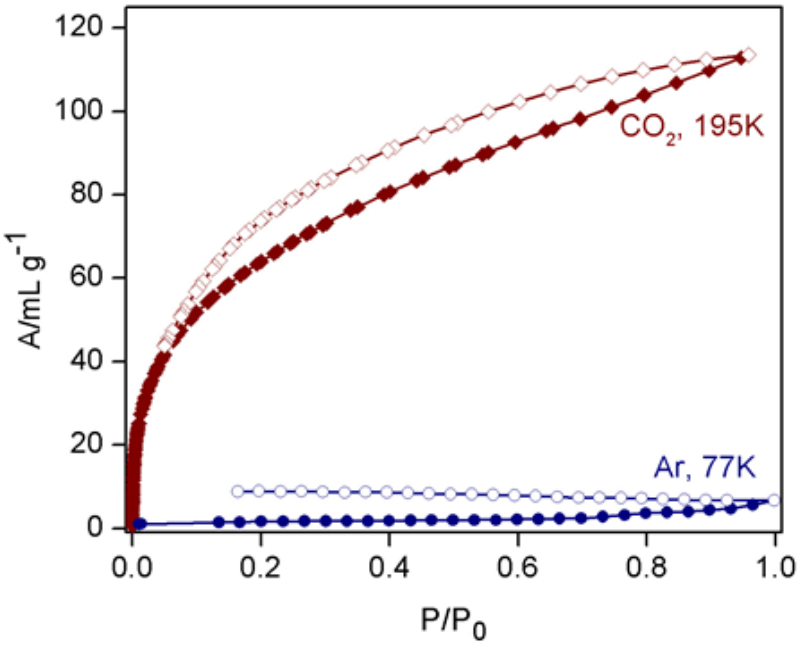

Appendix 2A.27. CO_2 and Ar sorption isotherms of compound **1** at 195K and 77K respectively. Filled shapes = adsorption, hollow shapes = desorption.

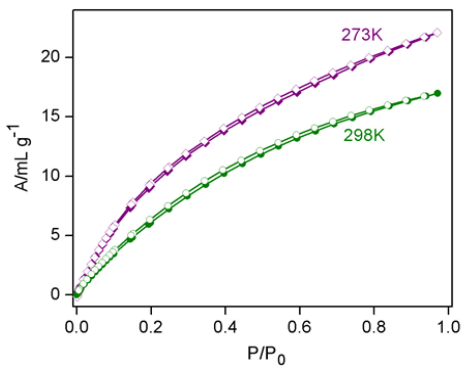

Appendix 2A.28. CO_2 sorption isotherms of compound **1** at 273K and 298K; filled shapes = adsorption, hollow shapes = desorption.

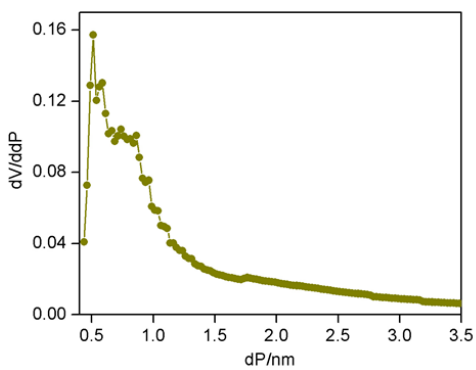

Appendix 2A.29. H-K (Horvath-Kawazoe) plot showing pore size distribution from CO_2 adsorption at 195K.

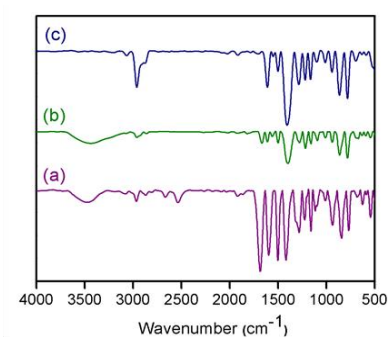

Appendix 2A.30. FT-IR Spectra of (a) H_2L, (b) compound **1⊃G**, and (c) compound **1**.

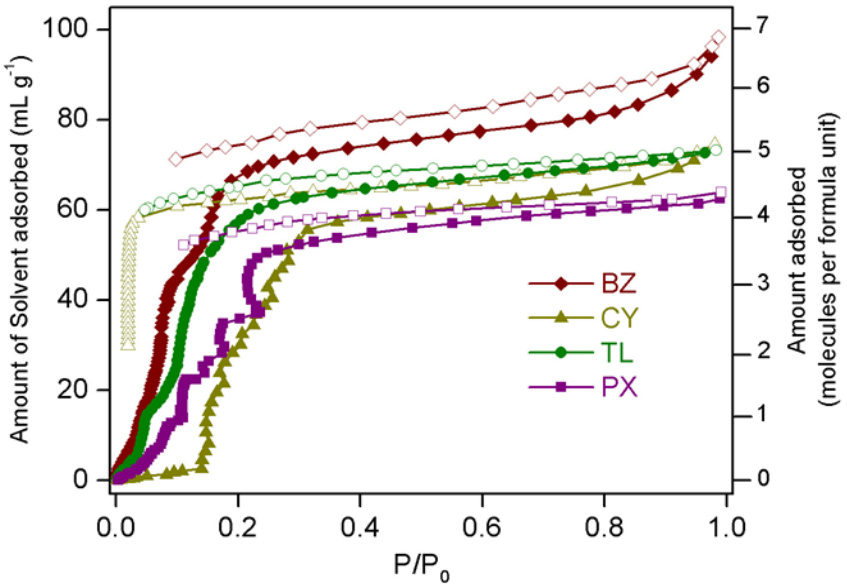

Appendix 2A.31. Solvent sorption isotherms for compound **1** recorded at 298K; color code: Benzene (wine red), toluene (olive), *p*-xylene (purple) and cyclohexane (dark yellow). Filled shapes: adsorption, hollow shapes: desorption.

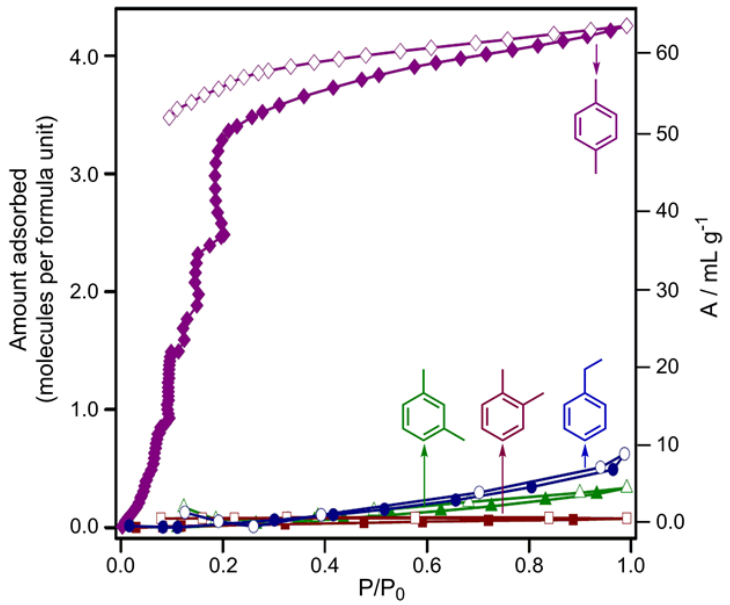

Appendix 2A.32. Solvent sorption isotherms for compound **1** at 298K for three xylene isomers along with isomeric ethylbenzene. Filled shapes: adsorption, hollow shapes: desorption.

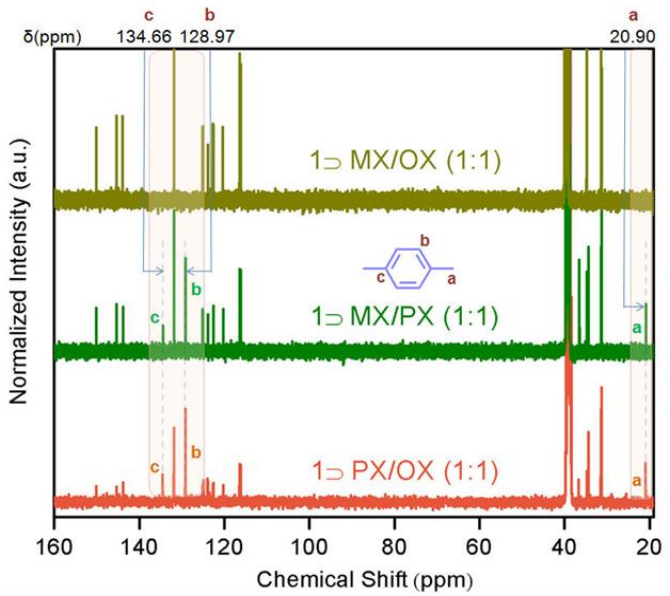

Appendix 2A.33. ^{13}C NMR spectra for different binary-xylene (1:1) mixture vapor-exposed phases of compound **1**. Vapor of each of the binary mixtures (1:1) exposed for 72h to the phase **1** before digesting in DCl/DMSO- d_6.

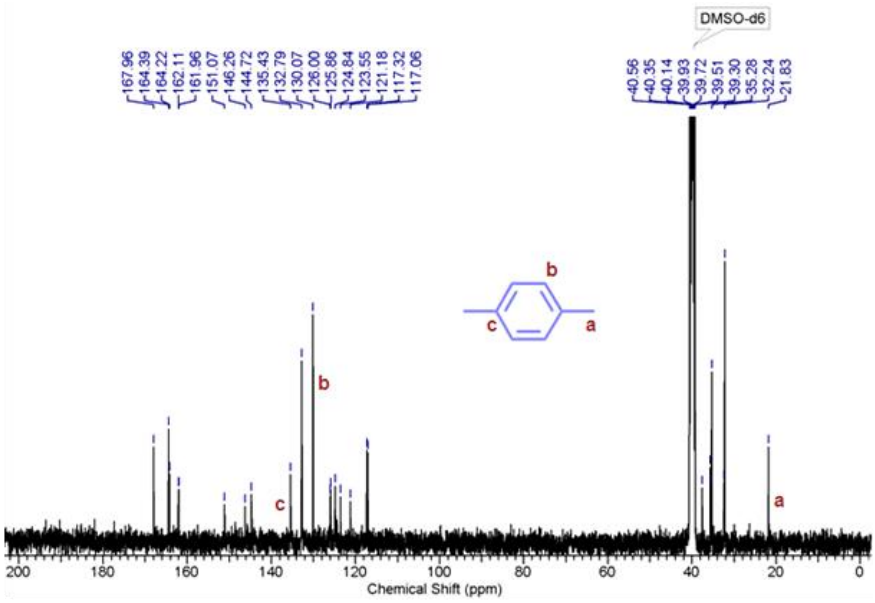

Appendix 2A.34. ^{13}C NMR spectrum of compound **1⊃PX'** digested in DCl/DMSO-d_6.

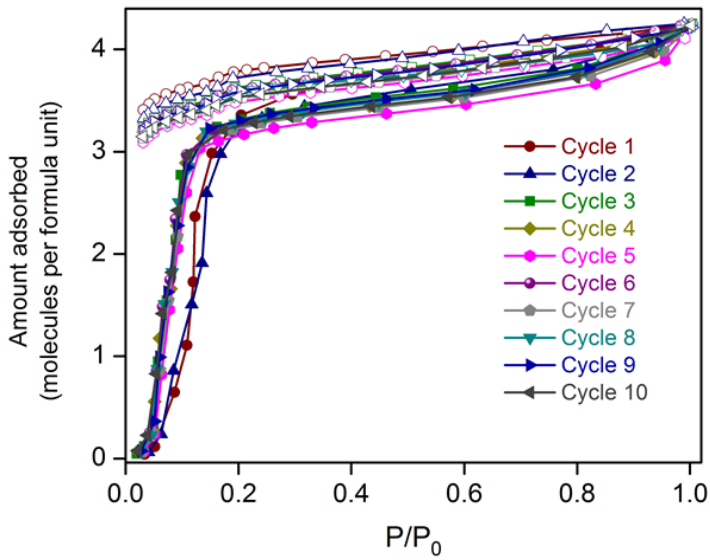

Appendix 2A.35. The recyclability of the PX adsorption behavior was confirmed by reproducing the same isotherm on unchanged desolvated sample **1** for ten consecutive cycles at 298 K. Filled shapes: adsorption, hollow shapes: desorption.

Appendix 2A.36. Bar diagram representation of the recyclability for the PX adsorption behavior as confirmed by reproducing the same isotherm on unchanged desolvated sample **1** for ten consecutive cycles at 298 K. Similar amounts of PX-uptake suggests the PX-sorption's recyclability behaviour for the material **1**.

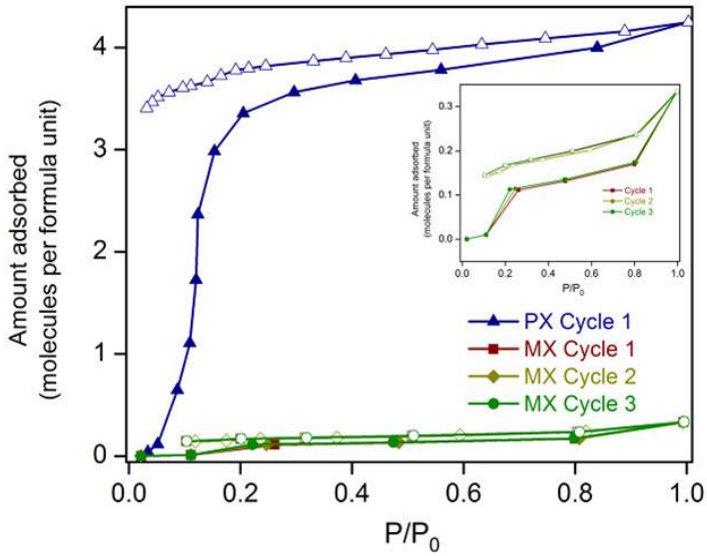

Appendix 2A.37. The recyclability of the MX adsorption behavior was confirmed by reproducing the same isotherm on unchanged desolvated sample **1** for three consecutive cycles at 298 K, as compared to the 'cycle 1' PX-sorption data; Inset: Plots for three consecutive recyclability cycles for MX. Filled shapes: adsorption, hollow shapes: desorption.

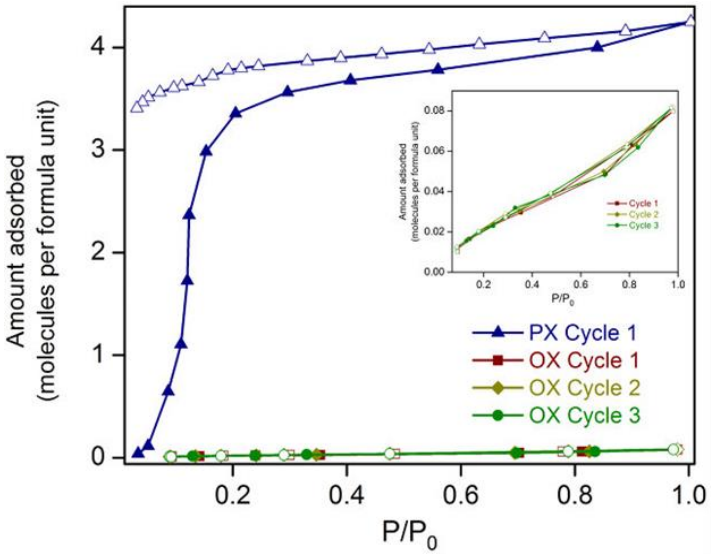

Appendix 2A.38. The recyclability of the OX adsorption behavior was confirmed by reproducing the same isotherm on unchanged desolvated sample **1** for three consecutive cycles at 298 K, as compared to the 'cycle 1' PX-sorption data; Inset: Plots for three consecutive recyclability cycles for OX. Filled shapes: adsorption, hollow shapes: desorption.

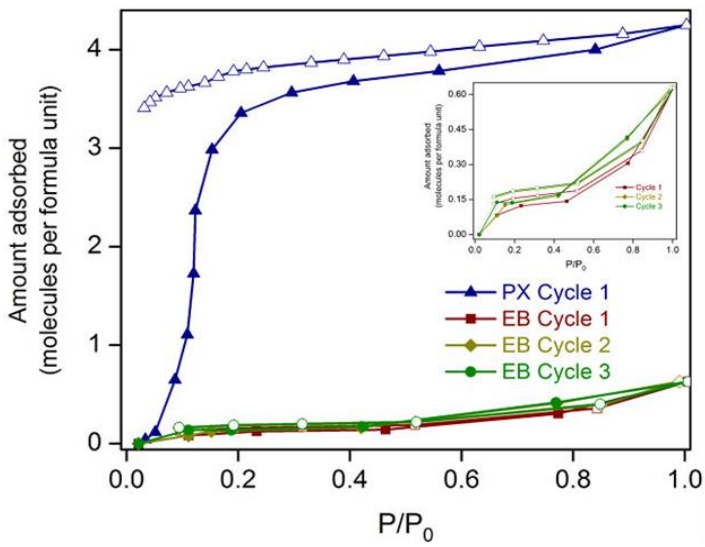

Appendix 2A.39. The recyclability of the EB adsorption behavior was confirmed by reproducing the same isotherm on unchanged desolvated sample **1** for three consecutive cycles at 298 K, as compared to the 'cycle 1' PX-sorption data; Inset: Plots for three consecutive recyclability cycles for EB. Filled shapes: adsorption, hollow shapes: desorption.

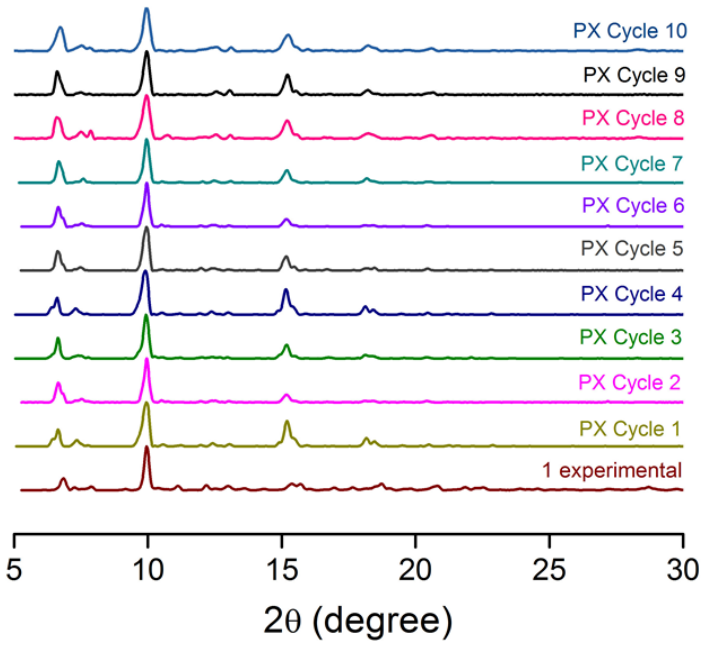

Appendix 2A.40. PXRD patterns for the post-desorption phases of the PX-recyclability experiments, plotted with the experimental PXRD pattern of **1**.

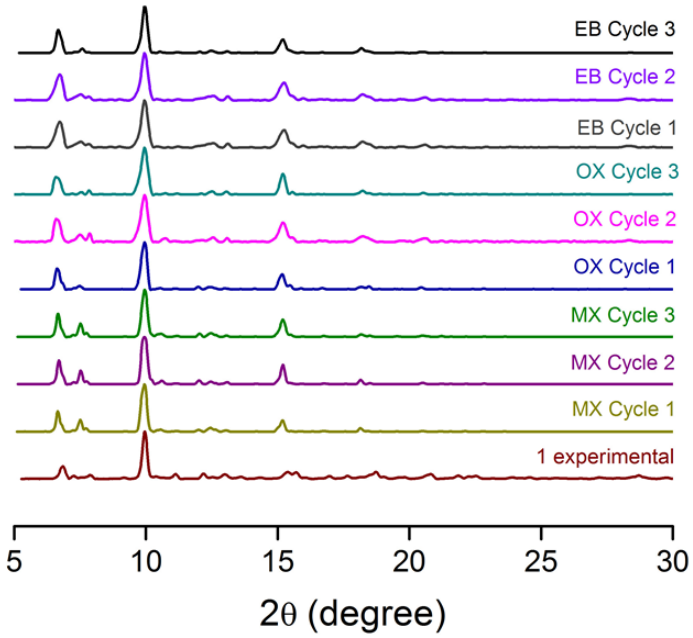

Appendix 2A.41. PXRD patterns for all the post-desorption phases of the MX-recyclability and OX-recyclability experiments, plotted with the experimental PXRD pattern of **1**.

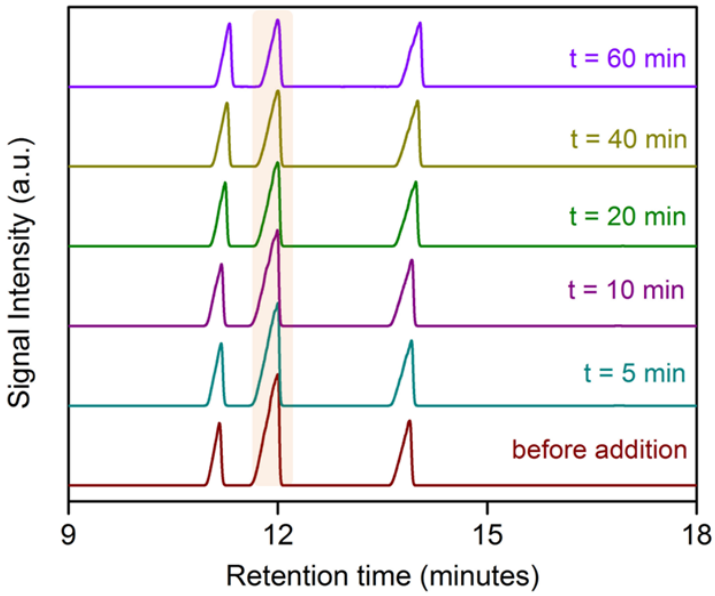

Appendix 2A.42. GC chromatogram of the supernatant solutions recorded at the specified time intervals in the setup A (Quaternary xylene mixture immersion test). Highlighted signals denote the mixed signal for the combined contributions of both MX and PX, intensity of which is getting steadily diminished with increasing time of immersion with MOF.

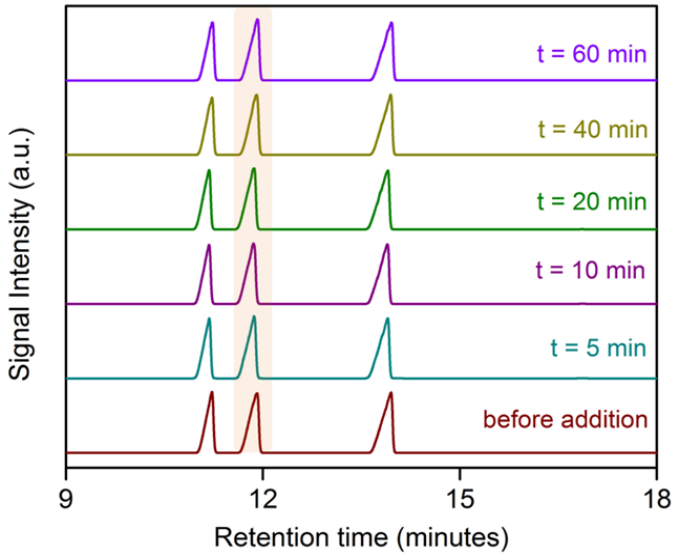

Appendix 2A.43. GC chromatogram of the supernatant solutions recorded at the specified time intervals in the setup B (Ternary xylene mixture immersion test; excluding PX). Highlighted signals denote the individual signal for the contribution of MX only, intensity of which is remaining unchanged with increasing time of immersion with MOF.

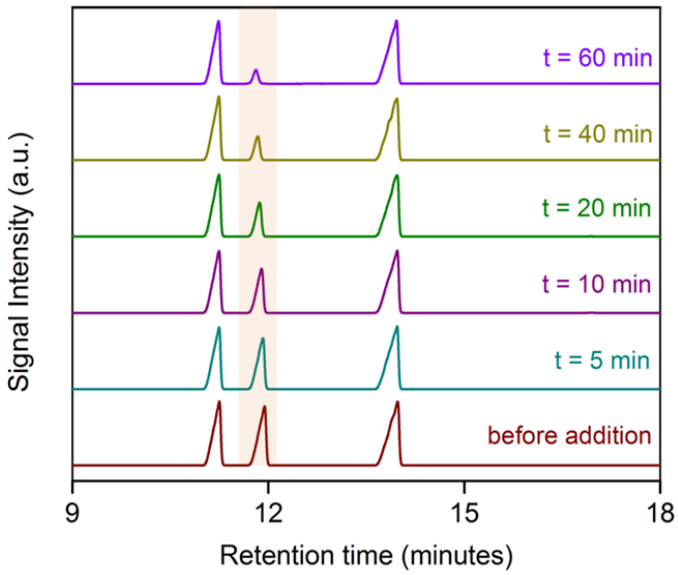

Appendix 2A.44. GC chromatogram of the supernatant solutions recorded at the specified time intervals in the setup C (Ternary xylene mixture immersion test; excluding MX). Highlighted signals denote the individual signal for the contribution of PX only, intensity of which is getting steadily diminished with increasing time of immersion with MOF.

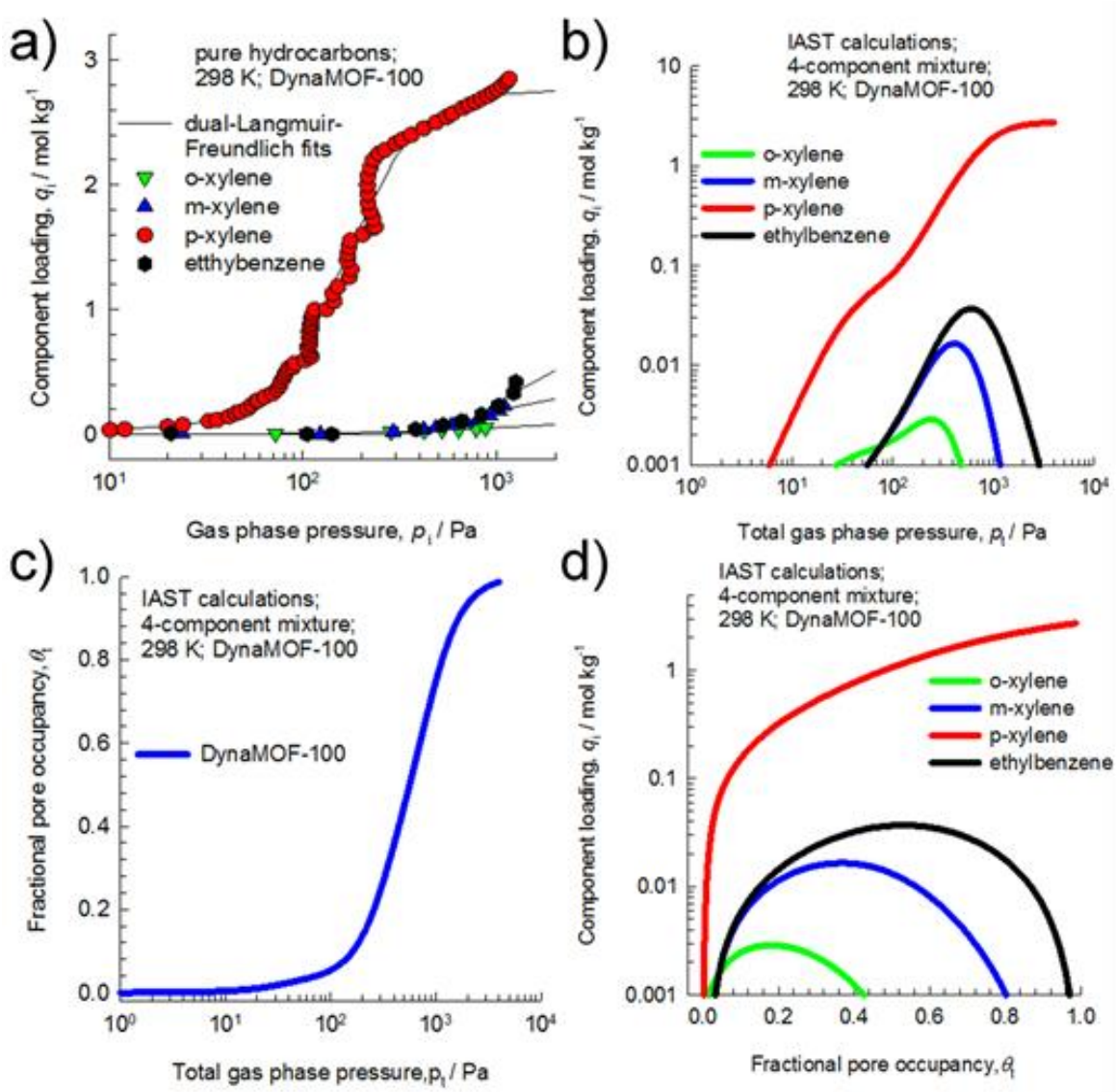

Appendix 2A.45. a) Comparison of experimental data for pure component isotherms in DynaMOF-100 with Langmuir-Freundlich fits (parameters specified in **Appendix Table 2A.5**), that are shown by the continuous solid lines; b) Calculations using the Ideal Adsorbed Solution Theory (IAST) of Myers and Prausnitz[46] to determine the adsorption equilibrium for equimolar gas phase 4-component *o*-xylene/*m*-xylene/*p*-xylene/ethylbenzene mixtures in DynaMOF-100 at 298 K. The *x*-axis is the total gas phase pressure; c) IAST calculations of the fractional occupancy, θ_t, within the pores of DynaMOF-100 as a function of the total gas phase pressure, p_t. The calculations are for equimolar gas phase 4-component *o*-xylene/*m*-xylene/*p*-xylene/ethylbenzene mixtures in DynaMOF-100 at 298 K; d) IAST calculations of the component loadings in equilibrium with equimolar gas phase 4-component *o*-xylene/*m*-xylene/*p*-xylene/ethylbenzene mixtures in DynaMOF-100 at 298 K. The *x*-axis is fractional occupancy, θ_t, within the pores of DynaMOF-100.

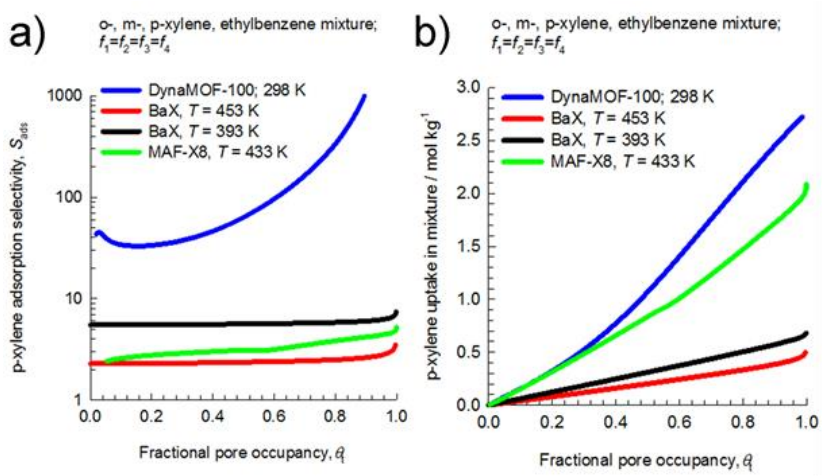

Appendix 2A.46. a) IAST calculations for *p*-xylene adsorption selectivity for 4-component *o*-xylene(1)/*m*-xylene(2)/*p*-xylene(3)/ethylbenzene(4) mixture in MAF-X8 (at 433 K), BaX zeolite (at 393 K, and 453 K), and DynaMOF-100 (at 298 K). The *x*-axis is fractional occupancy, θ_t, within the pores of the MOFs; b) IAST calculations for *p*-xylene uptake capacity for 4-component *o*-xylene(1)/*m*-xylene(2)/*p*-xylene(3)/ethylbenzene(4) mixture in MAF-X8 (at 433 K), BaX zeolite (at 393 K, and 453 K), and DynaMOF-100 (at 298 K). The *x*-axis is fractional occupancy, θ_t, within the pores of the MOFs.

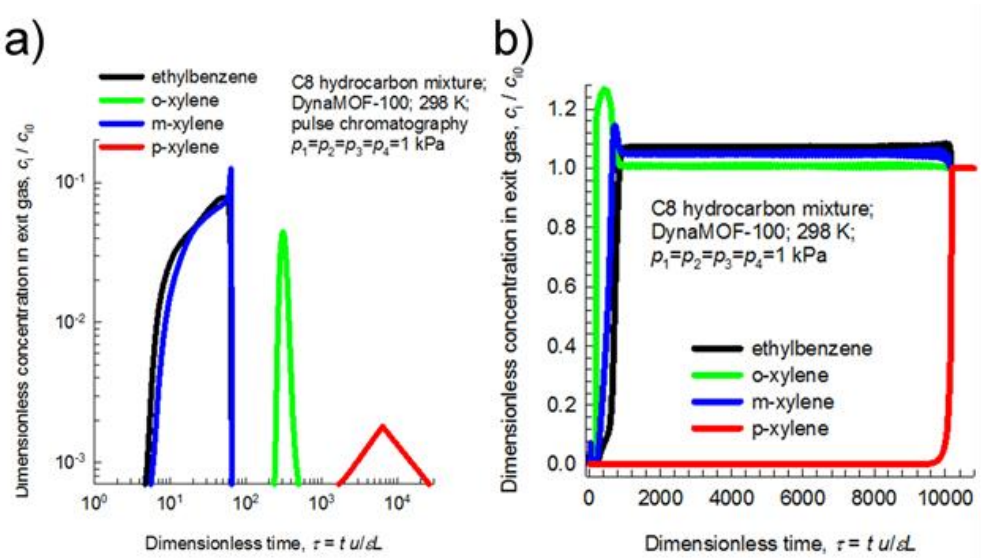

Appendix 2A.47. a) Pulse chromatographic simulations of the breakthrough of 4-component *o*-xylene(1)/*m*-xylene(2)/*p*-xylene(3)/ethylbenzene(4) mixture in packed bed of DynaMOF-100 at 298 K. The inlet gas phase has partial pressures of 1 kPa for each component. The duration of the pulse is 10 s; b) Transient breakthrough simulations for 4-component *o*-xylene(1)/*m*-xylene(2)/*p*-xylene(3)/ethylbenzene(4) mixture in packed bed of DynaMOF-100 at 298 K. The inlet gas phase has partial pressures of 1 kPa for each component.

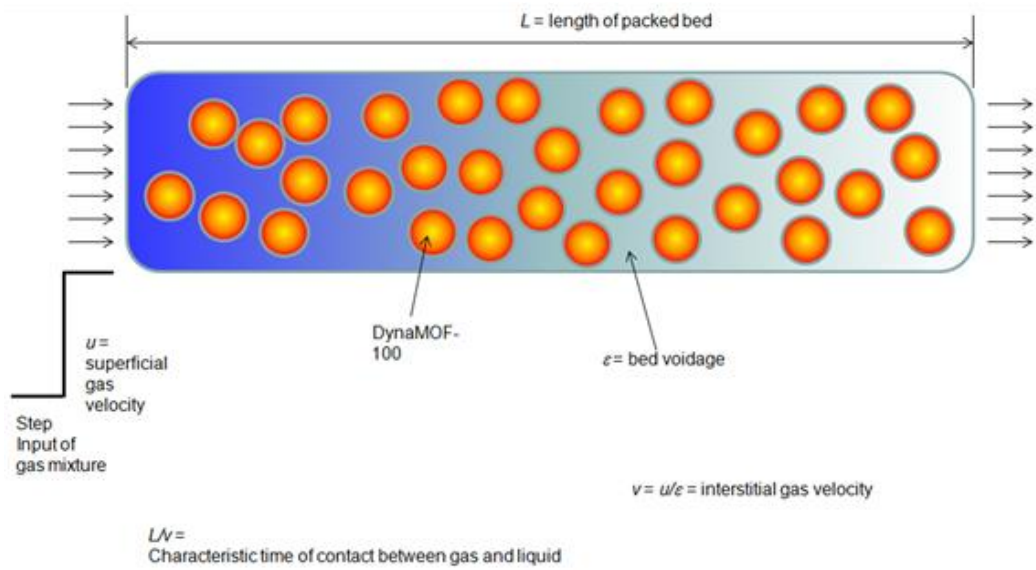

Appendix 2A.48. Schematic of a packed bed adsorber, with DynaMOF-100 adsorbent bed.

Appendix Table 2A.1 Dimensions of Adsorptive molecules (Å)[50] (each atom surrounded by a van der Waals sphere)

	x	*y*	z	MIN-1	MIN-2
BZ	6.628	7.337	3.277	3.277	6.628
TL	6.625	4.012	8.252	4.012	6.625
CY	7.168	6.580	4.982	4.982	6.580
PX	6.618	3.81	9.146	3.81	6.618
MX	8.994	3.949	7.315	3.949	7.258
OX	7.269	3.834	7.826	3.834	7.269
ST	9.721	3.331	6.784	3.331	6.784
EB	6.625	5.285	9.361	5.285	6.625

MIN-1: Size of the adsorptive in the minimum dimension.**MIN-2**: Second minimum dimension for molecular orientations that enable a molecule to enter the channel.

Appendix Table 2A.2: Crystal data and structure refinement for compound **1⊃G**.

Crystal data: Compound **1⊃G** (DynaMOF-100a)	
Chemical formula	$C_{78}H_{78}N_2O_{23}Zn_4$
M_r	1672.90
Crystal system, space group	Monoclinic, $P2_1/c$
Temperature (K)	200
a, b, c (Å)	11.801 (3), 33.733 (10), 25.650 (8)
β (°)	99.893 (6)
V (Å^3)	10059 (5)
Z	4
Radiation type	Mo $K\alpha$
μ (mm^{-1})	1.00
Crystal size (mm)	0.15 × 0.13 × 0.12
Data collection	
Diffractometer	Bruker *APEX*-II CCD diffractometer
Absorption correction	Multi-scan Bruker *SADABS*
T_{min}, T_{max}	0.864, 0.889
No. of measured, independent and observed [$I > 2\sigma(I)$] reflections	28853, 14814, 5030
R_{int}	0.077
$(\sin \theta/\lambda)_{max}$ (Å^{-1})	0.595
Refinement	
$R[F^2 > 2\sigma(F^2)]$, $wR(F^2)$, S	0.079, 0.215, 0.81
No. of reflections	14814
No. of parameters	920
No. of restraints	171
H-atom treatment	H atoms treated by a mixture of independent and constrained refinement
$(\Delta/\sigma)_{max}$	4.358
$\Delta\rho_{max}$, $\Delta\rho_{min}$ (e Å^{-3})	0.63, −0.67

Computer programs: Bruker *SMART*, Bruker *SAINT*, *SHELXL97* (Sheldrick, 2008), Bruker *SHELXTL*.

Appendix Table 2A.3: Crystal data and structure refinement for compound **1**.

Crystal data: Compound **1** (DynaMOF-100)	
Chemical formula	$C_{72}H_{60}O_{19}Zn_4$
M_r	1490.68
Crystal system, space group	Monoclinic, $P2_1/c$
Temperature (K)	200
a, b, c (Å)	12.306 (9), 26.370 (18), 22.124 (16)
β (°)	96.549 (13)
V (Å^3)	7133 (9)
Z	4
Radiation type	Mo $K\alpha$
μ (mm^{-1})	1.40
Crystal size (mm)	0.15 × 0.12 × 0.10
Data collection	
Diffractometer	Bruker *APEX*-II CCD diffractometer
Absorption correction	Multi-scan Bruker *SADABS*
T_{min}, T_{max}	0.818, 0.873
No. of measured, independent and observed [$I > 2\sigma(I)$] reflections	95666, 12514, 3731
R_{int}	0.248
$(\sin \theta/\lambda)_{max}$ (Å^{-1})	0.595
Refinement	
$R[F^2 > 2\sigma(F^2)]$, $wR(F^2)$, S	0.111, 0.331, 0.91
No. of reflections	12514
No. of parameters	865
No. of restraints	78
H-atom treatment	H atoms treated by a mixture of independent and constrained refinement
$\Delta\rho_{max}$, $\Delta\rho_{min}$ (e Å^{-3})	1.00, −0.59

Computer programs: Bruker *SMART*, Bruker *SAINT*, *SHELXL97* (Sheldrick, 2008), Bruker *SHELXTL*.

Appendix Table 2A.4: Crystal data and structure refinement for compound **1⊃PX'**.

Crystal data: Compound **1⊃PX'** (DynaMOF-100⊃PX)	
Chemical formula	$C_{86}H_{84}N_2O_{21}Zn_4$
M_r	1743.03
Crystal system, space group	Monoclinic, $P2_1/c$
Temperature (K)	200
a, b, c (Å)	12.080 (5), 32.556 (5), 25.722 (5)
β (°)	97.830 (5)
V (Å^3)	10022 (5)
Z	4
Radiation type	Mo $K\alpha$
μ (mm^{-1})	1.01
Crystal size (mm)	0.14 × 0.11 × 0.10
Data collection	
Diffractometer	Bruker *APEX*-II CCD diffractometer
Absorption correction	Multi-scan Bruker *SADABS*
T_{min}, T_{max}	0.872, 0.906
No. of measured, independent and observed [$I > 2\sigma(I)$] reflections	28529, 5363, 4639
R_{int}	0.042
θ_{max} (°)	16.8
$(\sin \theta/\lambda)_{max}$ (Å^{-1})	0.407
Refinement	
$R[F^2 > 2\sigma(F^2)]$, $wR(F^2)$, S	0.098, 0.270, 1.04
No. of reflections	5363
No. of parameters	966
No. of restraints	284
H-atom treatment	H atoms treated by a mixture of independent and constrained refinement
	$w = 1/[\sigma^2(F_o^2) + (0.1725P)^2 + 86.6551P]$ where $P = (F_o^2 + 2F_c^2)/3$
$(\Delta/\sigma)_{max}$	0.267
$\Delta\rho_{max}$, $\Delta\rho_{min}$ (e Å^{-3})	1.48, −0.67

Computer programs: Bruker *SMART*, Bruker *SAINT*, *SHELXL97* (Sheldrick, 2008), Bruker *SHELXTL*.

Appendix Table 2A.5. Dual-site Langmuir-Freundlich parameters for aromatic hydrocarbons at 298 K in DynaMOF-100.

	Site A			Site B		
	$q_{i,A,sat}$ mol kg^{-1}	$b_{i,A}$ Pa$^{-\nu_{iA}}$	$\nu_{i,A}$ dimensionless	$q_{i,B,sat}$ mol kg^{-1}	$b_{i,B}$ Pa$^{-\nu_{iA}}$	$\nu_{i,B}$ dimensionless
o-xylene (OX)	0.15	5.57×10^{-4}	1			
m-xylene (MX)	0.3	5.27×10^{-11}	3.5			
p-xylene (PX)	0.06	5.98×10^{-3}	2.3	2.7	4.56×10^{-6}	2.4
Ethylbenzene (EB)	0.56	6.57×10^{-12}	3.7			
Benzene (BZ)	0.3	1.7×10^{-2}	0.86	2.5	6.58×10^{-8}	2.3
Toluene (TL)	1.2	3.26×10^{-3}	0.92	2.1	5.7×10^{-10}	3.5
Cyclohexane (CY)	0.8	4.04×10^{-4}	0.76	2.5	1.06×10^{-22}	6.4
Styrene (ST)	3.9	4.29×10^{-09}	3.7			

Section 2B

Exploiting Framework Flexibility for Selective Adsorption of Styrene over Ethyl benzene

2B.1. Introduction:

Owing to the high reactivity of its vinyl group, styrene (ST) is an important feedstock in the petrochemical industries.[51] Alkylation of benzene with ethylene produces ethylbenzene (EB), which is dehydrogenated to styrene, a monomer used in the manufacture of many commercial polymers and co-polymers. The conversion of ethylbenzene to styrene is only partial, and the reactor product contains a large fraction, in the range of 20%-40%, of unreacted ethylbenzene.[51, 52] Due to the the small (9K) differences in boiling points (ST (b.p. 418.3 K) and EB (b.p. 409.3 K)), the separations are currently achieved in vacuum distillation columns, which are energy-intensive. Adsorptive separations using microporous metal-organic frameworks (MOFs) offer energy efficient alternatives to distillation.[15-17, 28, 29, 53-55] Several MOFs have been demonstrated to offer substantial potential for use in the separation of xylene isomers,[28, 29 30-33, 56, 57] hexane[58-61] or the C_5 fraction-compounds formed by steam crackers, benzene/cyclohexane separation, and removal of heterocyclic aromatic compounds from fuels.[27, 62-66] Flexible MOFs are of particular interest because of their tuneable structural flexibility leading to guest-specific breathing phenomena of the pore windows/ channels.[65, 66] Despite its industrial importance, research on the targeted development of suitable MOFs for ST/EB separations has been rather limited.[67-69] Maes *et al.*[68] and Remy *et al.*[67] have demonstrated that MIL-47 (V) and MIL-53 (Al) are of potential use in the separation of mixtures of styrene and ethylbenzene. However, the adsorption selectivities achieved with these two MOFs are rather low, and fall in the range of 6 – 10.

In the last section of this chapter (Section 2A), we had reported the synthesis of a dynamic structure based MOF compound showing clear *p*-xylene (PX) preference over its congener C_8-alkylaromatic isomers at ambient temperatures by framework-breathing and guest-induced reversible solid-state structural transformations.[33, 57] The structure of this MOF, hereinafter referred to as DynaMOF-100, gets transformed in such a manner as to allow optimal packing of PX within the cavities. The strong sorption selectivity of DynaMOF-100 for PX was established in the previous segment of this chapter (chapter 2A),[57] and the separation performance of this material in comparison to the established MOFs and industrially employed zeolites (BaX) were also included, based on the fixed bed adsorber method governed collaborative theoretical analyses.

In our current investigation, this soft porous crystalline material DynaMOF-100 (compound **1**) has been comprehensively investigated for the targeted separation of EB- and ST-containing feed mixture by exploiting the highly dynamic adaptable feature of the framework. As described, herein the compound **1** (DynaMOF-100) is the desolvated sqeezed 2D phase (of almost non-porous nature; **Figure 2B.1b**, **Appendix 2B.5**) resultant from the porous as-synthesized phase (**1⊃G**), accompanied by the loss of coordinated DMF moleccules and pore-closing event in single-crystal to single-crystal (SCSC) fashion. The prime focus of our current work is to demonstrate the outstanding potential of DynaMOF-100 for selective adsorption of styrene from mixtures containing ethylbenzene (**Scheme 2B.1**). The effective mean pore diameter of 5.1 Å for flexible DynaMOF-100 facilitates selective entry of PX through pore opening but does not respond to the sterically demanding guests OX, MX and EB (dimensional and b.p. closeness: **Appendix 2B.2**).

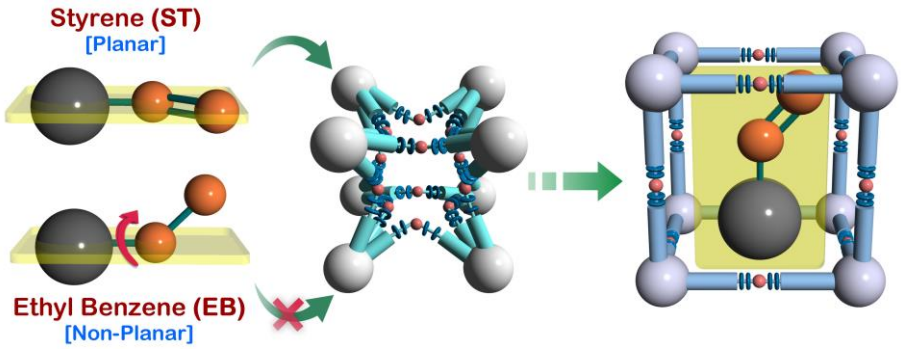

Scheme 2B.1. Schematic illustration of guest-responsive framework flexibility demonstrating selective styrene separation over ethylbenzene.

The salient dimension parameters MIN-1 and MIN-2 (**Appendix table 2A.1**[50]) for ST are intriguingly quite similar to that of PX; with an even lower size of the adsorptive species as its minimum dimension (MIN-1). This factor, coupled with a strikingly close MIN-2 value of ST as compared to the host soft porous adsorbent DynaMOF-100, allows a definite room for restricted limiting allowance principle[57] to operate for the inspected pair ST/EB (**Figure 2B.1a** and **Appendix 2B.3**). This intriguing dimensional compatibility between the probe adsorptive ST and the host adsorbent prompted us to systematically investigate such anticipated selectivity and separation-performance of ST over EB. Styrene is a planar molecule, whereas ethylbenzene is

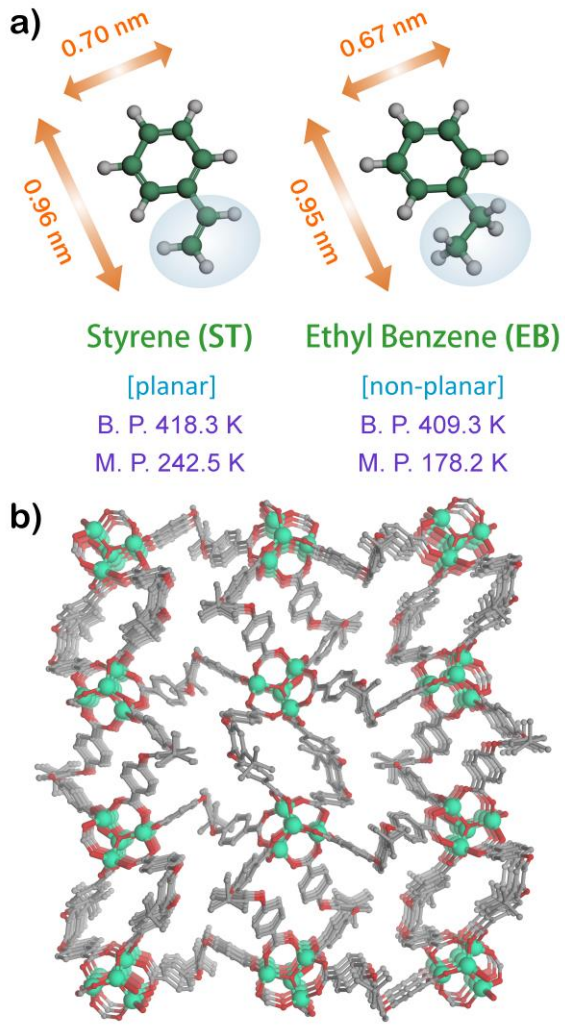

Figure 2B.1. a) Dimensions and relevant physical attributes of ST and EB molecules;[70] b) Overall structure of compound **1** (desolvated squeezed framework) along crystallographic *a*-axis.

non-planar, due to the ethyl group protruded from the planar phenyl ring (**Scheme 2B.1, Figure 2B.1a**). Due to differences in their flatness, styrene may be expected to exert stronger interactions with the framework walls of DynaMOF-100.

2B.2. Synthetic Protocol:

Guest-free probe compound **1** (DynaMOF-100) was prepared according to the previously discussed protocol in this chapter itself (**Chapter 2A.2 section**).

2B.3. Result and discussions:

To verify the respective adsorptive uptake amounts, vapor sorption experiments for both the solvents ST and EB were recorded at 298K. The sorption profile of ST came up with a gradual increase of uptake amount with steadily increasing pressure up to ~6 molecules per formula unit (corresponding to ~86 mLg^{-1}); while on the contrary, EB uptake amount was found to be only 0.63 molecules per formula unit (9.4 mLg^{-1}) (**Figure 2B.2**, **Appendix 2B.10**). The hysteresis in the styrene isotherm, during the adsorption/desorption cycles, is a typical isotherm characteristic observed when guest-induced structural changes occur,[71] and a detailed quantitative analysis, such as that presented by Dubbeldam *et al.* is required for a quantitative understanding of the isotherms.[72]

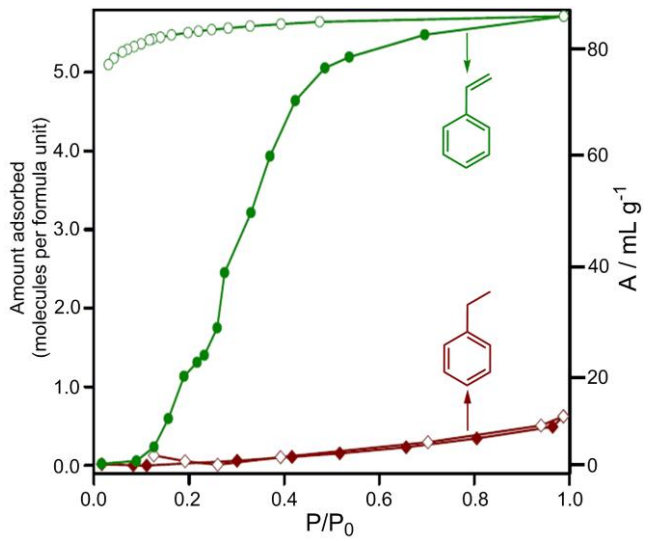

Figure 2B.2. Solvent sorption isotherms for compound **1** recorded at 298K for styrene and ethylbenzene. Closed and open symbols denote adsorption and desorption respectively.

This differential adsorption behavior towards these two related species consolidated that the framework flexibility of desolvated phase 1 allows the entry of the planar guest ST but not the non-planar ones like EB, due to steric hindrance that originates in the case of the latter. The olefin-bond mediated extended conjugation for styrene affords absolute planarity to this molecule, which sterically facilitates the selective uptake of ST. Bed regeneration for this material was verified by performing three consecutive cycles of ST adsorption with the same

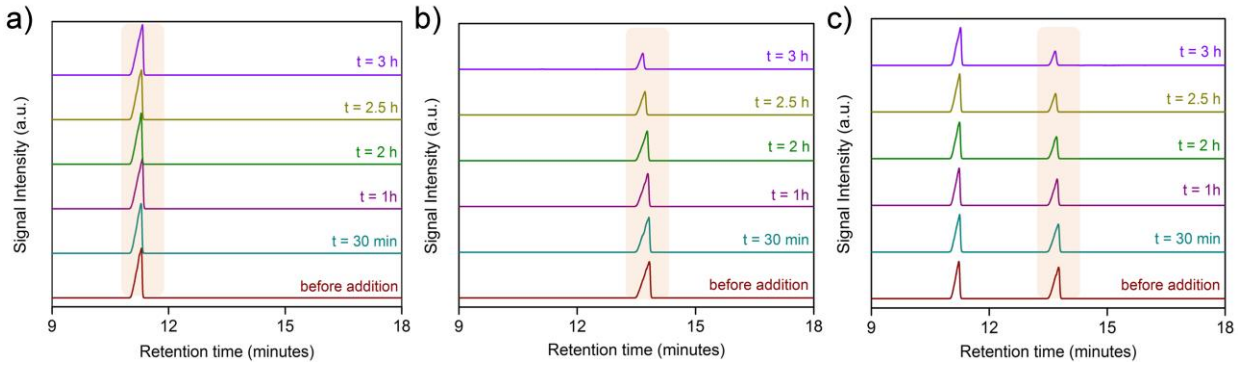

Figure 2B.3. a) GC chromatogram of the supernatant solutions recorded at the specified time intervals in the setup A (ethylbenzene immersion test). Highlighted signals denote the contribution of EB only, intensity of which is remaining unchanged with increasing time of immersion with MOF, b) GC chromatogram of the supernatant solutions recorded at the specified time intervals in the setup B (styrene immersion test). Highlighted signals denote the contribution of ST only, intensity of which is getting steadily diminished with increasing time of immersion with MOF, c) GC chromatogram of the supernatant solutions recorded at the specified time intervals in the setup C (ST/EB mixture immersion test). Highlighted region denotes the individual signal for the contribution of ST only, intensity of which is getting steadily diminished with increasing MOF immersion-time.

desolvated phase **1**, which registered excellent reproducibility features (**Appendices 2B.11, 2B.12**).

The powder X-ray diffraction (PXRD) patterns and thermogravimetric analysis (TGA) profiles for the two phases (**Appendices 2B.6-2B.8**) namely, **1⊃ST** and **1⊃EB** precisely corroborate with the structural transformations occurring on the interplay of host-guest interactions. These results seemed to be in absolute agreement to those obtained from solvent sorption studies, since the characteristic PXRD pattern for **1** remained unaltered in case of **1⊃EB**, while exposure to ST marked a drastic change suggesting a clear phase transition. Interestingly enough, the PXRD pattern of **1⊃ST** registered a striking similarity to the phase **1⊃G**, referring to a breathing phenomenon that might have occurred on ST-exposure. In fact, TGA results simultaneously affirmed this observation, since no significant weight loss accompanied the exposure- mediated phase **1⊃EB**, while **1⊃ST** registered a substantial ~25% weight loss. As an ancillary reinforcement supporting the selective interplay of ST with the flexibleframework **1** as compared to EB, ^{13}C NMR experiments with the DCl/DMSO-d_6 digested samples after vapor exposure to these two different solvent vapors (**Appendix 2B.13**) were performed, which indisputably presented barely the characteristic ST signals.

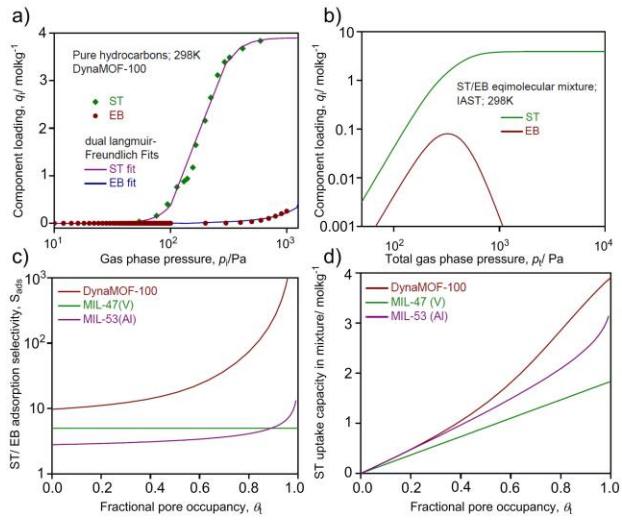

Figure 2B.4. a) Comparison of experimental data for pure component isotherms for ethylbenzene and styrene in DynaMOF-100 with Langmuir-Freundlich fits that are shown by the continuous solid lines; b) IAST calculations for styrene/ethylbenzene adsorption selectivity for equimolar styrene(1)/ethylbenzene(2) mixtures in DynaMOF-100; c) IAST calculations for styrene/ethylbenzene adsorption selectivity for equimolar styrene(1)/ethylbenzene(2) mixtures in MIL-47(V), MIL-53(Al), and DynaMOF-100. The *x*-axis is fractional occupancy, θ_t, within the pores of the MOFs; d) IAST calculations for styrene uptake capacity for equimolar styrene(1)/ethylbenzene(2) mixtures in MIL-47(V), MIL-53(Al), and DynaMOF-100. The *x*-axis is fractional occupancy, θ_t, within the pores of the MOFs.

To verify the separation-viability in actuality, phase **1** was immersed into solvents ST, EB and binary mixture solution of ST/EB (1:1) for 3 h and the respective amounts of the non-adsorbed isomers were scanned by GC at specific intermediate time intervals. The detailed description of the GC experiment with the supernatant solvent(s) is provided in the supporting information. Ensuing results (**Figure 2B.3**, **Appendices 2B.14-2B.17**) evidently authenticate that the observed decline in the characteristic signal intensity is exclusively due to the contribution of ST; the gradually diminishing intensity-trend steadily tell the difference with increasing immersion-time of DynaMOF-100.

We now evaluate ethylbenzene/styrene separations using the ideal adsorbed solution theory (IAST) calculations. **Figure 2B.4a** shows the experimental data for pure component isotherms for ethylbenzene and styrene in DynaMOF-100; the continuous solid lines are Langmuir-Freundlich fits; the parameters are specified in **Appendix table 2A.5**. **Figure 2B.4b** shows IAST calculations for styrene/ethylbenzene adsorption selectivity, S_{ads}, for equimolar styrene(1)/ethylbenzene(2) mixtures in DynaMOF-100.

$$S_{ads} = \frac{q_1/q_2}{p_1/p_2} \qquad (1)$$

We note that for pressures exceeding about 1 kPa, the adsorbed phase contains predominantly styrene. The high styrene/ethylbenzene selectivities as evidenced in **Figures 2B.4b**, and **2B.4c** are caused by better molecular packing of the planar styrene molecules within the MOF channels. The mechanism of separation due to molecular packing effects of mixtures of aromatics is particularly strong for operation under pore saturation conditions, as has been explained in literature.[72] We see from **Figure 2B.4**, that pore saturation is also attained at pressures exceeding 1 kPa and ambient temperatures. It is anticipated that industrial separations in fixed bed adsorbers will operate under conditions approach pore saturation.[73] For this reason we define the fractional occupancy

$$\theta_t = \sum_{i=1}^{n} \frac{q_i}{q_{i,sat}} \qquad (2)$$

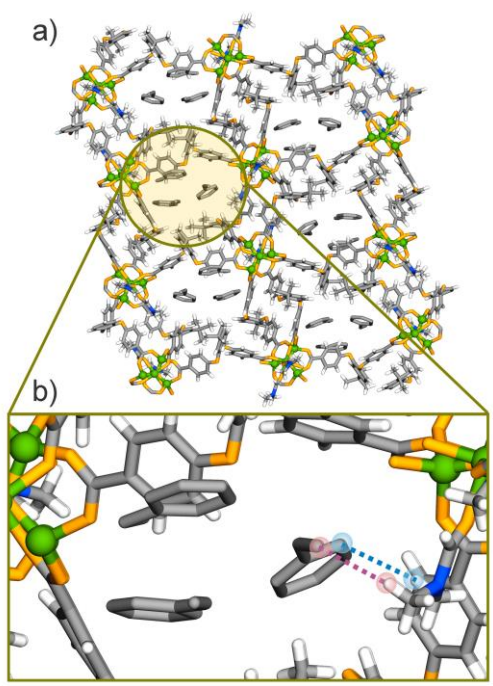

Figure 2B.5. a) Overall structure of resolvated phase **1⊃ST'**, with free guest ST molecular species accommodated inside the channels, along crystallographic *a*-axis; b) Zoomed view of one of these channels showing non-covalent interactions (representative) between the host MOF and guest ST species by dotted lines.

Figure 2B.4c presents a comparison the adsorption selectivities of DynaMOF-100 with MIL-47(V) and MIL-53(Al) as a function of the fractional pore occupancy. We note that the value of S_{ads} for DynaMOF-100 is about one to two orders of magnitude higher than that of MIL-47(V) and MIL-53(Al). **Figure 2B.4d** shows IAST calculations for styrene uptake capacity for equimolar styrene(1)/ethylbenzene(2) mixtures in MIL-47(V), MIL-53(Al), and DynaMOF-100. The uptake capacity of DynaMOF-100 is significantly higher than that of the other two MOFs. Due to the significantly higher adsorption selectivity, and higher capacity, we should expect that sharp separations of styrene(1)/ethylbenzene(2) mixtures is realized in a fixed bed adsorber.

While repeated trials were attempted to obtain the crystal structure of this resolvated phase, an analogous phase **1⊃ST'** (**Appendices 2B.1**, **2B.4**) (as indicated from the exactly alike PXRD patterns for both) (**Appendix 2B.9**) was obtained on exposing the crystals of **1** to the vapor of a binary mixture solution of styrene (2 mL) and DMF (1 mL) for 72 h. SC-XRD analysis of this novel compound **1⊃ST'** (formula: $\{[Zn_4O(L)_3(DMF)_2].(C_8H_8)_3\}_n$ disclosed that the nearly similar unit cell parameters to the crystals of **1⊃G** and crystallized in monoclinic centrosymmetric space group *P21/c* (**Appendix table 2B.3**). As an unambiguous conclusive evidence of selective interplay of ST accompanying this solid-state dynamic structural transformation, styrene molecules could be clearly located in the SC-XRD structure for this **1⊃ST'** phase crystals, residing inside the porous channels of the host framework (**Figure 2B.5**, **Appendices 2B.20** and **2B.21**). This could only be possible after commensurate stacking-mediated accommodation of the planar styrene molecules inside the hydrophobic channels of the shrinked windows of desolvated framework **1**; prominent non-covalent interactions are observed between the host MOF channel and the guest ST, as represented in **Figure 2B.5b**.

Subsequent to the phase purity-confirmation for the new phase **1⊃ST'** from PXRD (**Appendix 2B.9**), both TGA and PXRD analyses for the two phases, namely **1⊃ST** and **1⊃ST'** confirmed their similar nature (**Appendices 2B.7** and **2B.9**). To check reversibility of this ST-inclusion, the crystals of **1⊃ST'** were heated at 160 °C under reduced pressure for 3h, to obtain the desolvated phase **1''** (DynaMOF-100). TGA and PXRD profiles (**Appendices 2B.7** and **2B.9**) confirmed the resemblance with the pristine desolvated phase **1**, confirming the ST-inclusion reversibility.

2B.4. Conclusion:

In the work reported here, the framework flexibility of DynaMOF-100 has been strategically exploited for achieving selective styrene uptake over ethylbenzene. The separation relies on the closeness in the dimensions of the guest styrene molecule and the host material. DynaMOF-100 exhibits significant framework flexibility because of its constituent adjustable ether nodes, which precisely mediates the guest-inclusion, accompanied solid-state structural transformations. IAST calculations for separation of ethylbenzene/styrene mixtures have shown a significant superiority of DynaMOF-100, when compared to the only two reported MOFs namely, MIL-47(V) and MIL-53(Al). Moreover, aimed at potentially significant separation of *o*-xylene/*m*-xylene/*p*-xylene/ethylsbenzene mixtures, DynaMOF-100 is also found to significantly superior to both MAF-X8 and BaX zeolite. The strategy of using guest-selective structural transformations of the MOF frameworks could be proficiently exploited for other industrially important separations of mixtures of aromatic molecules, especially hydrocarbons.

2B.5. Appendix Section:

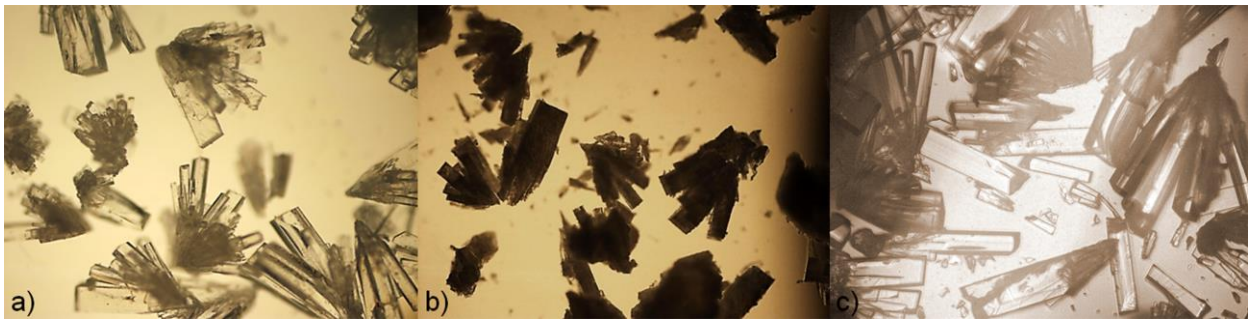

Appendix 2B.1. Microscopy images of the crystals for the different SCSC phases: a) compound **1⊃G** (as-synthesized), b) compound **1** (desolvated), c) compound **1⊃ST'**.

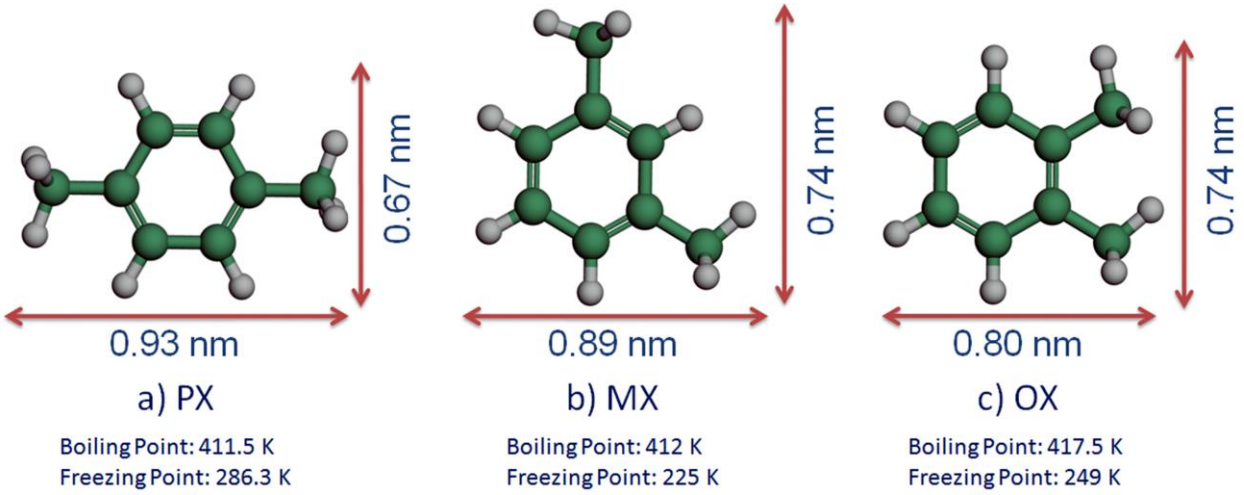

Appendix 2B.2. Dimensions of the C_8-alkyl aromatic xylene isomers (excluding ethylbenzene).

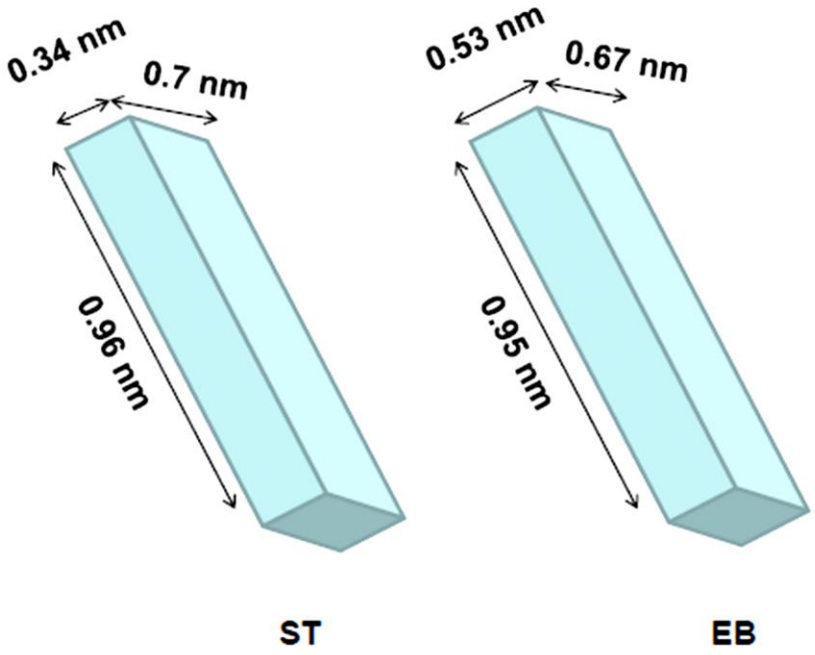

Appendix 2B.3. Box dimensions for ST and EB adsorptive molecules.

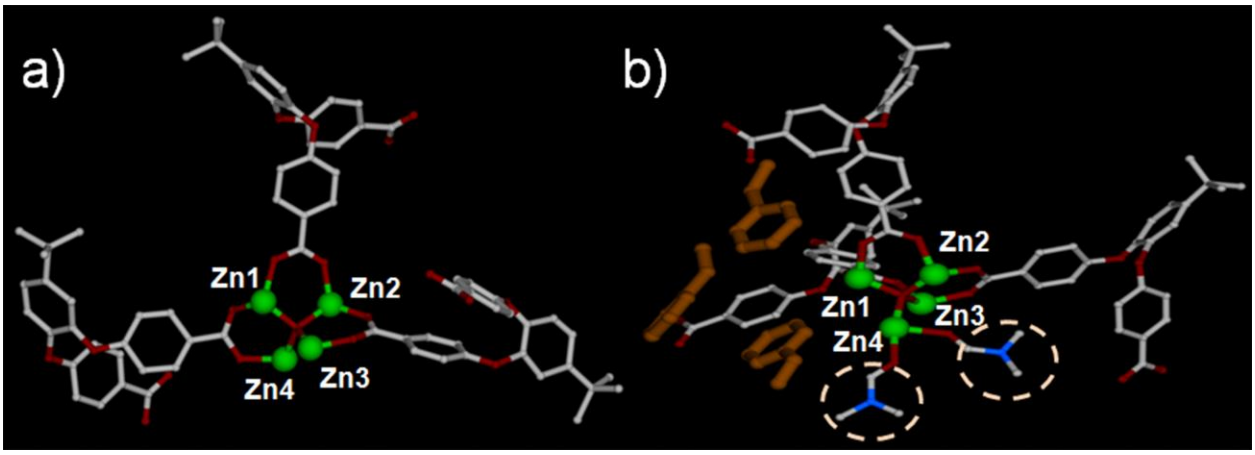

Appendix 2B.4. Asymmetric units for the two phases: a) Compound **1**, and b) Compound **1⊃ST'**; coordinated DMF molecules have been shown using circles (both coordinated to Zn4), with three ST molecules getting accommodated per asymmetric unit (as shown in yellow color for clarity).

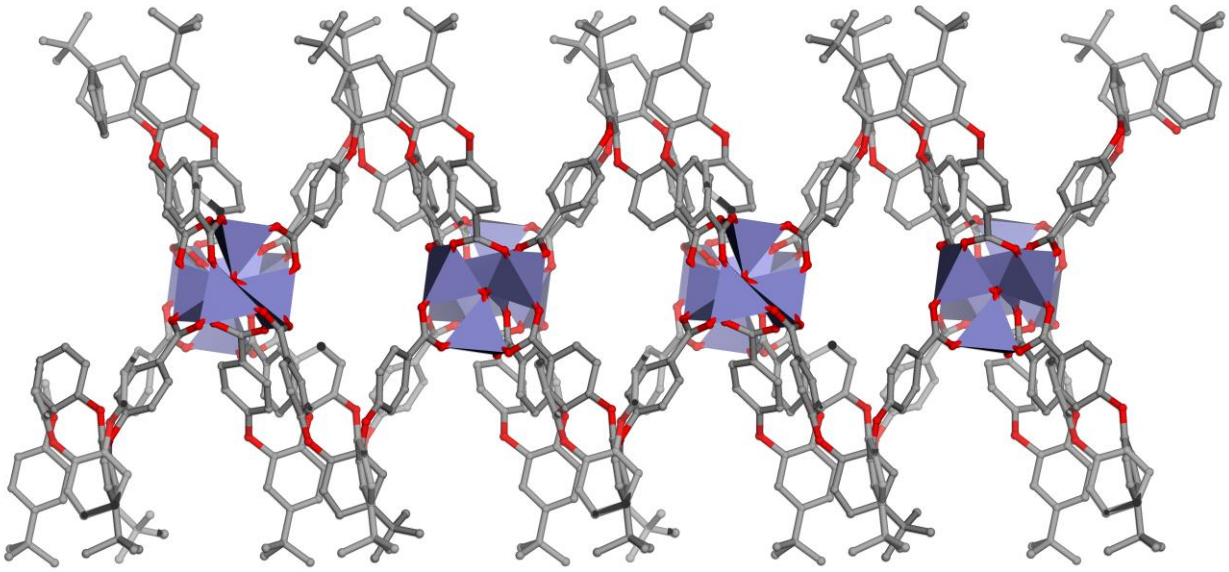

Appendix 2B.5. Progression of a single 2D-sheet (along *c*-axis) for the phase **1**.

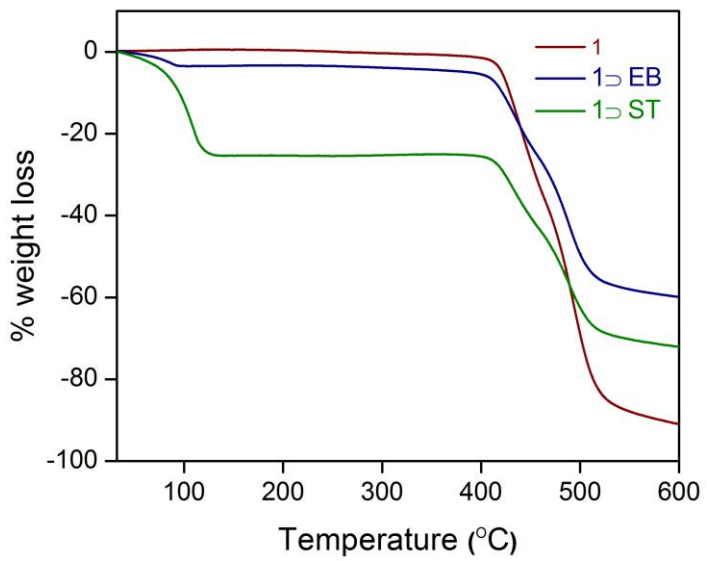

Appendix 2B.6. TGA plots for the guest-exposed phases of **1** (**1⊃ solvent**), compared with that of **1** (wine). Vapor of two solvents namely, **styrene** (olive), and **ethylbenzene** (navy) were exposed to obtain the phases **1⊃ST** and **1⊃EB** respectively.

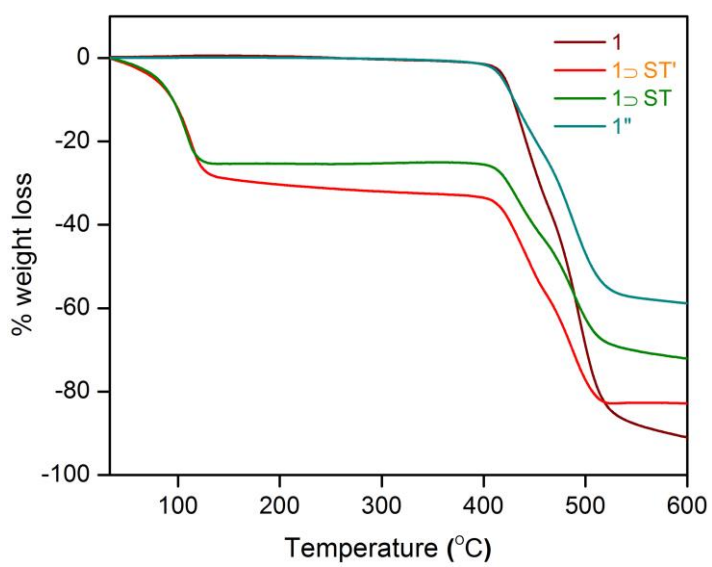

Appendix 2B.7. TGA plots for desolvated phase **1** (wine), compared with that of ST-exposed sample **1⊃ST** (purple), crystals **1⊃ST'**, along with the heated (re-desolvated) phase **1''**.

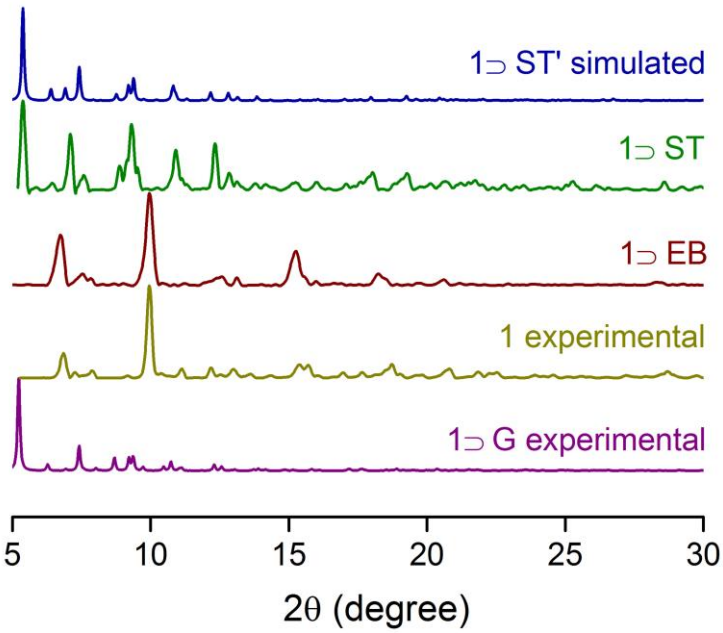

Appendix 2B.8. Experimental PXRD patterns of **1⊃G**, **1**, **1⊃EB, 1⊃ST** plotted with the simulated PXRD pattern of **1⊃ST'**.

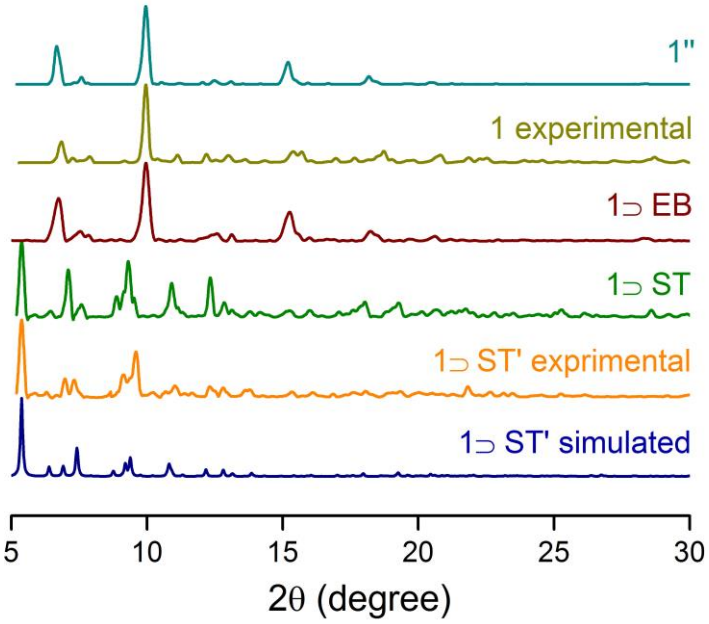

Appendix 2B.9. Powder X-ray diffraction (PXRD) patterns of compounds **1⊃ST'** (simulated), **1⊃ST'** (experimental), **1⊃ST** (experimental), **1⊃EB** (experimental), **1** (desolvated phase' experimental) and **1**".

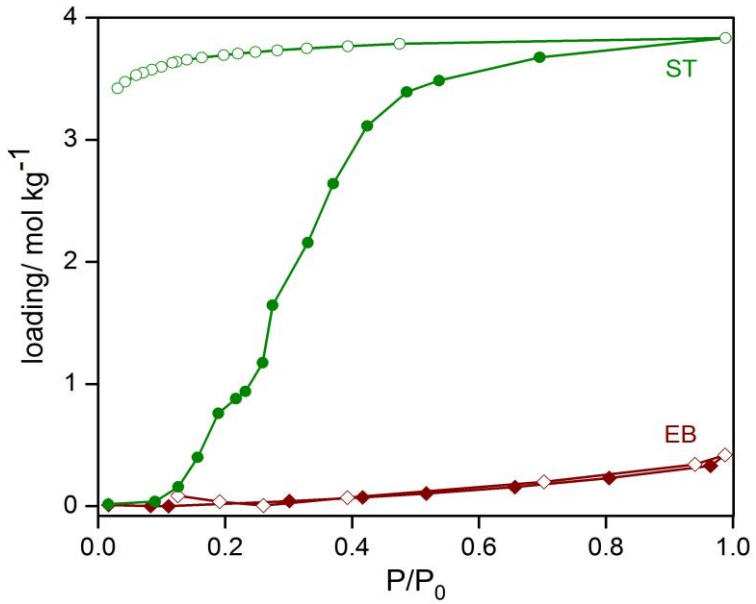

Appendix 2B.10. Single component adsorption isotherms for styrene and ethylbenzene in terms of loading (mol kg^{-1}) against increasing relative pressure.

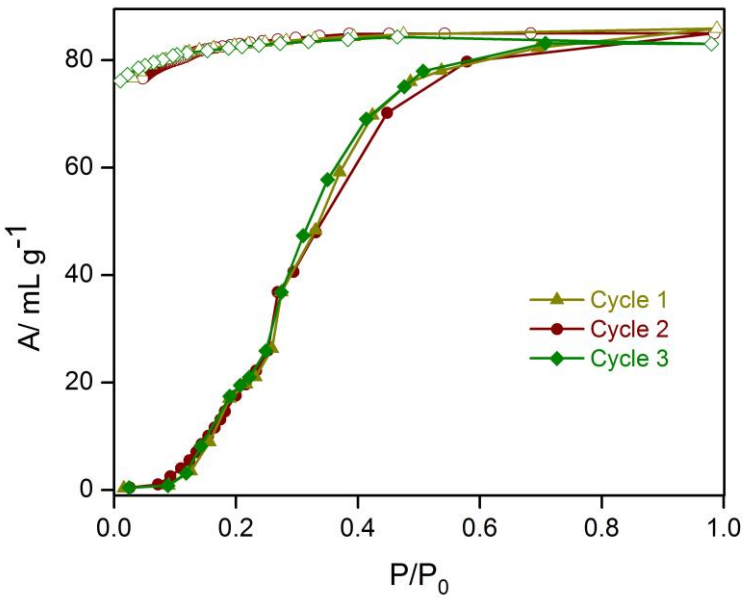

Appendix 2B.11. The recyclability of the ST adsorption behavior was confirmed by reproducing the same isotherm on unchanged desolvated sample **1** for three consecutive cycles at 298 K. Filled shapes: adsorption, hollow shapes: desorption.

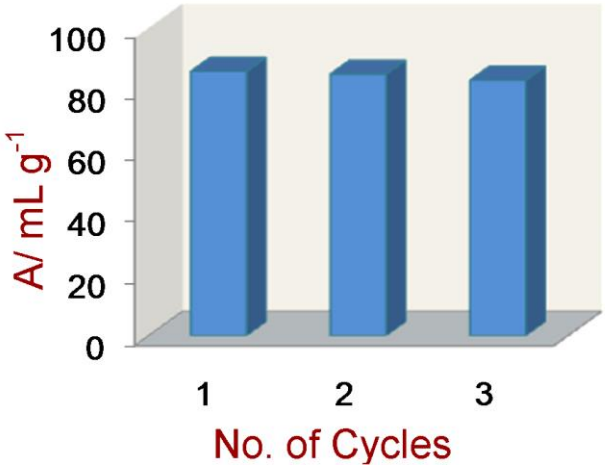

Appendix 2B.12. Bar diagram representation of the recyclability for the ST adsorption behavior as confirmed by reproducing the same isotherm on unchanged desolvated sample **1** for three consecutive cycles at 298 K. Similar amounts of ST-uptake suggests the ST-sorption's recyclability behaviour for the material **1**.

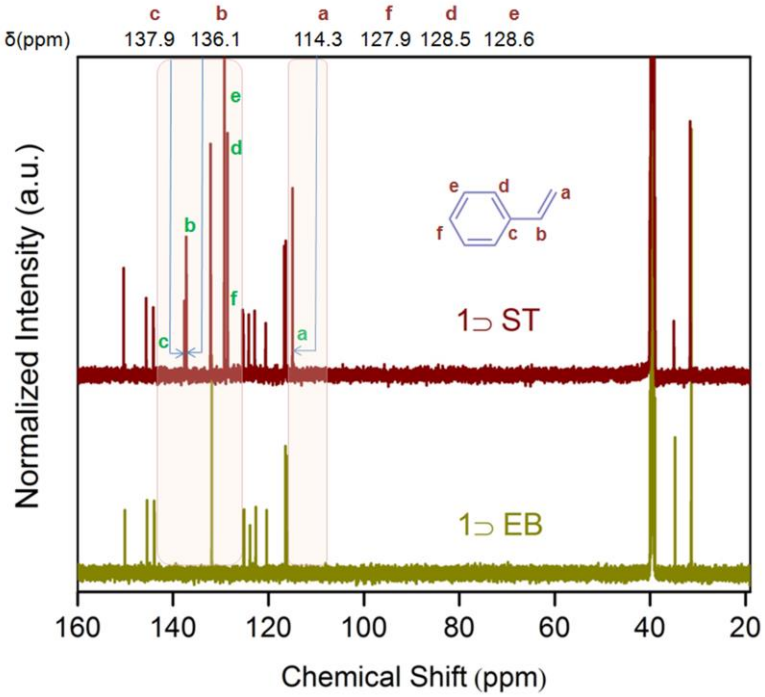

Appendix 2B.13. ^{13}C NMR spectra for styrene and ethyl benzene vapor-exposed phases of compound **1**. Vapor of each of these two solvents were exposed for 48h to the phase **1** before digesting in DCl/DMSO-d_6.

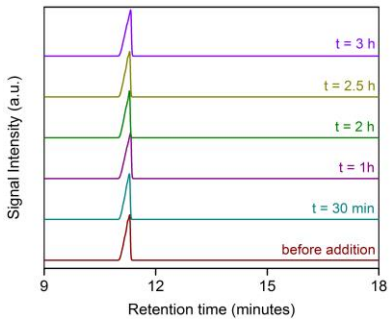

Appendix 2B.14. GC chromatogram of the supernatant solutions recorded at the specified time intervals in the setup A (ethylbenzene immersion test). Signals in each of the cases denote the contribution of EB only, intensity of which is remaining unchanged with increasing time of immersion with MOF.

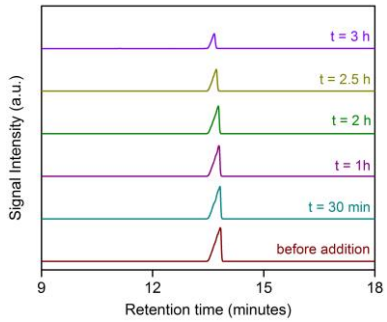

Appendix 2B.15. GC chromatogram of the supernatant solutions recorded at the specified time intervals in the setup B (styrene immersion test). Signals in each of the cases denote the contribution of ST only, intensity of which is getting steadily diminished with increasing time of immersion with MOF.

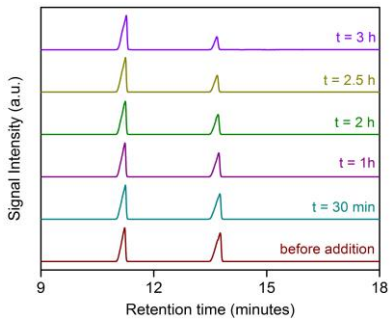

Appendix 2B.16. GC chromatogram of the supernatant solutions recorded at the specified time intervals in the setup C (ST/EB mixture immersion test). Signals in each of the cases denote the individual signal for the contribution of ST only, intensity of which is getting steadily diminished with increasing time of immersion with MOF.

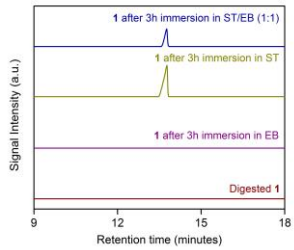

Appendix 2B.17. GC chromatogram of the DCl-digested DynaMOF-100, and all three different immersed MOF-phases after the completion of 3h immersion tenures in the GC experiment setups *a*, *b* and *c* as described above.

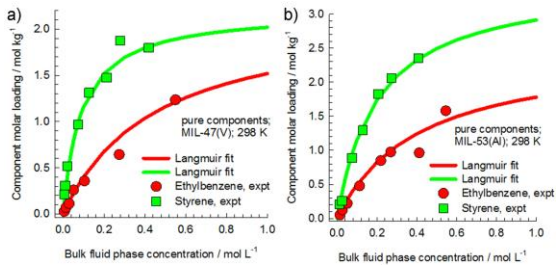

Appendix 2B.18. Comparison of experimental data for pure component isotherms for ethylbenzene and styrene in MIL-47(V) and MIL-53(Al) with Langmuir fits that are shown by the continuous solid lines. The isotherms used in the simulations are the experimental data reported by Maes *et al.*;[68] the Langmuir fit parameters are specified in **appendix tables 2B.1** and **2B.2**.

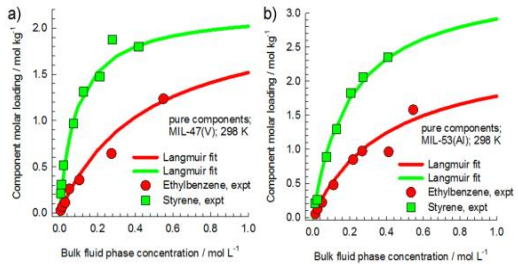

Appendix 2B.19. (a, b) Breakthrough simulations for ethylbenzene/styrene mixtures in (a) MIL-47(V), and (b) MIL-53(Al) at 298 K. The operations are in the liquid phase, with step inputs of feed concentrations c_{i0} = 0.47 mol L^{-1} in both cases. The dotted lines are simulations assuming thermodynamic equilibrium. The continuous solid lines represent breakthrough simulations with inclusion of intra-crystalline diffusion, neglecting thermodynamic coupling. The large symbols are the experimental breakthrough data, scanned from figures 2a and 2b of the paper by Maes *et al.*[68] The isotherms used in the simulations are the experimental data reported by Maes *et al.*;[68] the Langmuir fit parameters are specified in **appendix tables 2B.1** and **2B.2**.

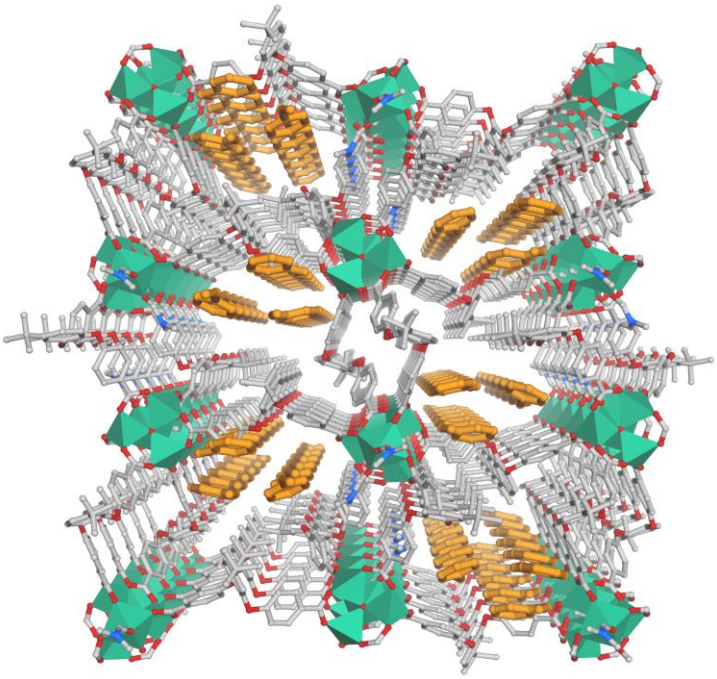

Appendix 2B.20. Resolvated framework on styrene accommodation-mediated breathing phenomenon.

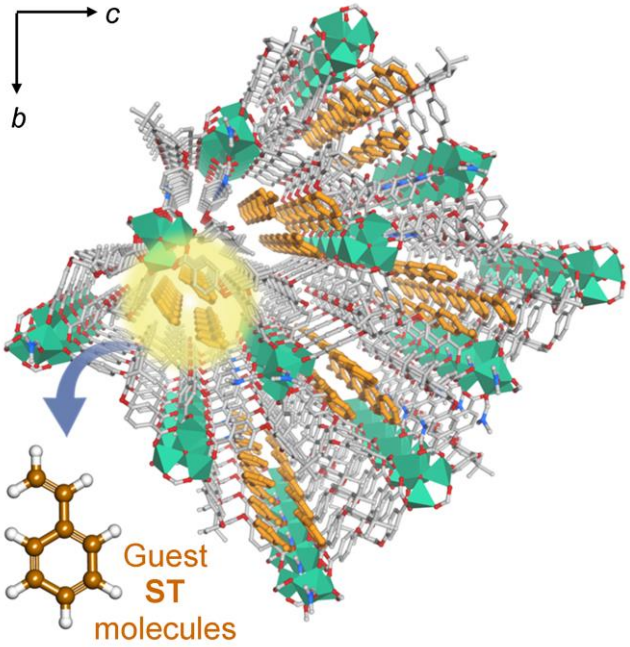

Appendix 2B.21. Perspective view of the resolvated framework, viewed along crystallographic *a*-axis.

Appendix Table 2B.1. Langmuir-Freundlich parameters for ethylbenzene and styrene at 298 K in MIL-47(V). The experimental data are scanned for Figure S1 (supporting information) of Maes *et al.*[68]

$$q = q_{sat}\frac{bc}{1+bc}$$

	q_{sat} mol kg^{-1}	b $[\text{mol L}^{-1}]^{-1}$
ethylbenzene	2.2	2.23
Styrene	2.2	11.15

Appendix Table 2B.2. Langmuir-Freundlich parameters for ethylbenzene and styrene at 298 K in MIL-53(Al). The experimental data are scanned for Figure S2 (supporting information) of Maes *et al.*[68]

$$q = q_{sat}\frac{bc}{1+bc}$$

	q_{sat} mol kg^{-1}	b $[\text{mol L}^{-1}]^{-1}$
ethylbenzene	2.5	2.48
Styrene	3.5	4.96

Appendix Table 2B.3: Crystal data and structure refinement for compound **1⊃PX'**.

Crystal data: Compound **1⊃PX'**	
Chemical formula	$C_{102}H_{98}N_2O_{21}Zn_4$
M_r	1949.11
Crystal system, space group	Monoclinic, $P2_1/c$
Temperature (K)	100
a, b, c (Å)	11.9745 (10), 32.827 (3), 25.847 (2)
β (°)	98.614 (2)
V (Å^3)	10045.6 (15)
Z	4
Radiation type	Mo $K\alpha$
μ (mm^{-1})	1.01
Crystal size (mm)	× ×
Data collection	
Diffractometer	?
Absorption correction	–
No. of measured, independent and observed [$I > 2\sigma(I)$] reflections	181405, 24239, 12947
R_{int}	0.088
$(\sin \theta/\lambda)_{max}$ (Å^{-1})	0.662
Refinement	
$R[F^2 > 2\sigma(F^2)]$, $wR(F^2)$, S	0.109, 0.343, 1.06
No. of reflections	24239
No. of parameters	1049
No. of restraints	135
H-atom treatment	H-atom parameters constrained
$\Delta\rho_{max}$, $\Delta\rho_{min}$ (e Å^{-3})	1.50, −0.65

Computer programs: *SHELXL2014* (Sheldrick, 2014).

2.3. References:

1. Horike, S.; Shimomura, S.; Kitagawa, S., *Nat Chem* **2009,** *1*, 695-704.

2. Kitagawa, S.; Kondo, M., *Bull. Chem. Soc. Jp.* **1998,** *71*, 1739-1753.

3. Maji, T. K.; Matsuda, R.; Kitagawa, S., *Nat Mater* **2007,** *6*, 142-148.

4. Kitaura, R.; Seki, K.; Akiyama, G.; Kitagawa, S., *Angew. Chem. Int. Ed.* **2003,** *42*, 428-431.

5. Kitagawa, S.; Uemura, K., *Chem. Soc. Rev.* **2005,** *34*, 109-119.

6. Shimomura, S.; Higuchi, M.; Matsuda, R.; Yoneda, K.; Hijikata, Y.; Kubota, Y.; Mita, Y.; Kim, J.; Takata, M.; Kitagawa, S., *Nat Chem* **2010,** *2*, 633-637.

7. Ghosh, S. K.; Bureekaew, S.; Kitagawa, S., *Angew. Chem. Int. Ed.* **2008,** *47*, 3403-3406.

8. Li, J.-R.; Sculley, J.; Zhou, H.-C., *Chem. Rev.* **2012,** *112*, 869-932.

9. Li, J.-R.; Kuppler, R. J.; Zhou, H.-C., *Chem. Soc. Rev.* **2009,** *38*, 1477-1504.

10. Zhang, Y.; Yuan, S.; Feng, X.; Li, H.; Zhou, J.; Wang, B., *J. Am. Chem. Soc.* **2016,** *138*, 5785-5788.

11. Wu, H.; Gong, Q.; Olson, D. H.; Li, J., *Chem. Rev.* **2012,** *112*, 836-868.

12. Herm, Z. R.; Bloch, E. D.; Long, J. R., *Chem. Mater.* **2014,** *26*, 323-338.

13. Van de Voorde, B.; Bueken, B.; Denayer, J.; De Vos, D., *Chem. Soc. Rev.* **2014,** *43*, 5766-5788.

14. El Osta, R.; Carlin-Sinclair, A.; Guillou, N.; Walton, R. I.; Vermoortele, F.; Maes, M.; de Vos, D.; Millange, F., *Chem. Mater.* **2012,** *24*, 2781-2791.

15. He, Y.; Krishna, R.; Chen, B., *Energy Environ. Sci.* **2012,** *5*, 9107-9120.

16. Gu, Z.-Y.; Yang, C.-X.; Chang, N.; Yan, X.-P., *Acc. Chem. Res.* **2012,** *45*, 734-745.

17. Bárcia, P. S.; Zapata, F.; Silva, J. A. C.; Rodrigues, A. E.; Chen, B., *J. Phys. Chem. B* **2007,** *111*, 6101-6103.

18. *SAINT Plus*, (Version 7.03); Bruker AXS Inc.: Madison, WI, **2004**.

19. Sheldrick, G. M. *SHELXTL*, *Reference Manual*: version 5.1: Bruker AXS; Madison, WI, **1997**.

20. Sheldrick, G. M. *Acta Crystallogr. Sect. A* **2008**, 112-122.

21. WINGX version 1.80.05 Louis Farrugia, University of Glasgow.

22. Spek, A. L. PLATON, *A Multipurpose Crystallographic Tool*, Utrecht University, Utrecht, The Netherlands, **2005**.

23. Spencer, S. F., *Anal. Chem.* **1963,** *35*, 592-592.

24. http://www.chemsystems.com/about/cs/news/items/PERP%200910_8_Xylenes.cfm

25. Denayer, J. F. M.; De Vos, D.; Leflaive, P., Separation of Xylene Isomers. In *Metal-Organic Frameworks*, Wiley-VCH Verlag GmbH & Co. KGaA: 2011; pp 171-190.

26. Jin, Z.; Zhao, H.-Y.; Zhao, X.-J.; Fang, Q.-R.; Long, J. R.; Zhu, G.-S., *Chem. Commun.* **2010,** *46*, 8612-8614.

27. Alaerts, L.; Kirschhock, C. E. A.; Maes, M.; van der Veen, M. A.; Finsy, V.; Depla, A.; Martens, J. A.; Baron, G. V.; Jacobs, P. A.; Denayer, J. F. M.; De Vos, D. E., *Angew. Chem.* **2007,** *119*, 4371-4375.

28. Finsy, V.; Verelst, H.; Alaerts, L.; De Vos, D.; Jacobs, P. A.; Baron, G. V.; Denayer, J. F. M., *J. Am. Chem. Soc.* **2008,** *130*, 7110-7118.

29. Vermoortele, F.; Maes, M.; Moghadam, P. Z.; Lennox, M. J.; Ragon, F.; Boulhout, M.; Biswas, S.; Laurier, K. G. M.; Beurroies, I.; Denoyel, R.; Roeffaers, M.; Stock, N.; Düren, T.; Serre, C.; De Vos, D. E., *J. Am. Chem. Soc.* **2011,** *133*, 18526-18529.

30. Peralta, D.; Chaplais, G.; Simon-Masseron, A.; Barthelet, K.; Chizallet, C.; Quoineaud, A.-A.; Pirngruber, G. D., *J. Am. Chem. Soc.* **2012,** *134*, 8115-8126.

31. Stylianou, K. C.; Rabone, J.; Chong, S. Y.; Heck, R.; Armstrong, J.; Wiper, P. V.; Jelfs, K. E.; Zlatogorsky, S.; Bacsa, J.; McLennan, A. G.; Ireland, C. P.; Khimyak, Y. Z.; Thomas, K. M.; Bradshaw, D.; Rosseinsky, M. J., *J. Am. Chem. Soc.* **2012,** *134*, 20466-20478.

32. Lusi, M.; Barbour, L. J., *Angew. Chem. Int. Ed.* **2012,** *51*, 3928-3931.

33. Peralta, D.; Chaplais, G.; Paillaud, J.-L.; Simon-Masseron, A.; Barthelet, K.; Pirngruber, G. D., *Microporous Mesoporous Mater.* **2013,** *173*, 1-5.

34. Nicolau, M. P. M.; Bárcia, P. S.; Gallegos, J. M.; Silva, J. A. C.; Rodrigues, A. E.; Chen, B., *J. Phys. Chem. C* **2009,** *113*, 13173-13179.

35. He, Y.; Xiang, S.; Zhang, Z.; Xiong, S.; Fronczek, F. R.; Krishna, R.; O'Keeffe, M.; Chen, B., *Chem. Commun.* **2012,** *48*, 10856-10858.

36. Li, B.; Wang, H.; Chen, B., *Chem. Asian J.* **2014,** *9*, 1474-1498.

37. Finsy, V.; Kirschhock, C. E. A.; Vedts, G.; Maes, M.; Alaerts, L.; De Vos, D. E.; Baron, G. V.; Denayer, J. F. M., *Chem. Eur. J.* **2009,** *15*, 7724-7731.

38. Bradshaw, D.; Warren, J. E.; Rosseinsky, M. J., *Science* **2007,** *315*, 977-980.

39. Zhang, J.-P.; Chen, X.-M., *J. Am. Chem. Soc.* **2008,** *130*, 6010-6017.

40. Chen, C.-L.; Beatty, A. M., *J. Am. Chem. Soc.* **2008,** *130*, 17222-17223.

41. Ghosh, S. K.; Bureekaew, S.; Kitagawa, S., *Angew. Chem.* **2008,** *120*, 3451-3454.

42. Nagarkar, S. S.; Desai, A. V.; Ghosh, S. K., *Chem. Asian J.* **2014,** *9*, 2358-2376.

43. Guillou, N.; Millange, F.; Walton, R. I., *Chem. Commun.* **2011,** *47*, 713-715.

44. Wang, M.; Zhang, X.; Chen, Y.; Li, D., *J. Phys. Chem. C* **2016,** *120*, 5059-5066.

45. Joarder, B.; Chaudhari, A. K.; Nagarkar, S. S.; Manna, B.; Ghosh, S. K., *Chem. Eur. J.* **2013,** *19*, 11178-11183.

46. Myers, A. L.; Prausnitz, J. M., *AIChE J.* **1965,** *11*, 121-127.

47. Torres-Knoop, A.; Krishna, R.; Dubbeldam, D., *Angew. Chem. Int. Ed.* **2014,** *53*, 7774-7778.

48. Krishna, R., *Microporous Mesoporous Mater.* **2014,** *185*, 30-50.

49. Krishna, R.; Long, J. R., *J. Phys. Chem. C* **2011,** *115*, 12941-12950.

50. Webster, C. E.; Drago, R. S.; Zerner, M. C., *J. Am. Chem. Soc.* **1998,** *120*, 5509-5516.

51. *Kirk-Othmer Encyclopedia of Chemical Technology*; John Wiley & Sons, Inc.: New York, **2008**; 1040 pp.

52. *Ullmann's Encyclopedia of Industrial Chemistry*, 6th ed.; John Wiley & Sons, Inc.: New York, **2006**; electronic release.

53. Krishna, R.; van Baten, J. M., *Phys. Chem. Chem. Phys.* **2011,** *13*, 10593-10616.

54. Rowsell, J. L. C.; Yaghi, O. M., *Microporous Mesoporous Mater.* **2004,** *73*, 3-14.

55. Rosseinsky, M. J., *Microporous Mesoporous Mater.* **2004,** *73*, 15-30.

56. Alaerts, L.; Kirschhock, C. E. A.; Maes, M.; van der Veen, M. A.; Finsy, V.; Depla, A.; Martens, J. A.; Baron, G. V.; Jacobs, P. A.; Denayer, J. F. M.; De Vos, D. E., *Angew. Chem. Int. Ed.* **2007,** *46*, 4293-4297.

57. Mukherjee, S.; Joarder, B.; Manna, B.; Desai, A. V.; Chaudhari, A. K.; Ghosh, S. K., *Sci. Rep.* **2014,** *4*, 5761.

58. Herm, Z. R.; Wiers, B. M.; Mason, J. A.; van Baten, J. M.; Hudson, M. R.; Zajdel, P.; Brown, C. M.; Masciocchi, N.; Krishna, R.; Long, J. R., *Science* **2013,** *340*, 960-964.

59. Peralta, D.; Chaplais, G.; Simon-Masseron, A.; Barthelet, K.; Pirngruber, G. D., *Ind. Eng. Chem. Res.* **2012,** *51*, 4692-4702.

60. Finsy, V.; Calero, S.; Garcia-Perez, E.; Merkling, P. J.; Vedts, G.; De Vos, D. E.; Baron, G. V.; Denayer, J. F. M., *Phys. Chem. Chem. Phys.* **2009,** *11*, 3515-3521.

61. Bárcia, P. S.; Guimarães, D.; Mendes, P. A. P.; Silva, J. A. C.; Guillerm, V.; Chevreau, H.; Serre, C.; Rodrigues, A. E., *Microporous Mesoporous Mater.* **2011,** *139*, 67-73.

62. Cychosz, K. A.; Wong-Foy, A. G.; Matzger, A. J., *J. Am. Chem. Soc.* **2009,** *131*, 14538-14543.

63. Gu, Z.-Y.; Yan, X.-P., *Angew. Chem. Int. Ed.* **2010,** *49*, 1477-1480.

64. Alaerts, L.; Maes, M.; Giebeler, L.; Jacobs, P. A.; Martens, J. A.; Denayer, J. F. M.; Kirschhock, C. E. A.; De Vos, D. E., *J. Am. Chem. Soc.* **2008,** *130*, 14170-14178.

65. Joarder, B.; Mukherjee, S.; Chaudhari, A. K.; Desai, A. V.; Manna, B.; Ghosh, S. K., *Chem. Eur. J.* **2014,** *20*, 15303-15308.

66. Shimomura, S.; Horike, S.; Matsuda, R.; Kitagawa, S., *J. Am. Chem. Soc.* **2007,** *129*, 10990-10991.

67. Remy, T.; Ma, L.; Maes, M.; De Vos, D. E.; Baron, G. V.; Denayer, J. F. M., *Ind. Eng. Chem. Res.* **2012,** *51*, 14824-14833.

68. Maes, M.; Vermoortele, F.; Alaerts, L.; Couck, S.; Kirschhock, C. E. A.; Denayer, J. F. M.; De Vos, D. E., *J. Am. Chem. Soc.* **2010,** *132*, 15277-15285.

69. Maes, M.; Vermoortele, F.; Boulhout, M.; Boudewijns, T.; Kirschhock, C.; Ameloot, R.; Beurroies, I.; Denoyel, R.; De Vos, D. E., *Microporous Mesoporous Mater.* **2012,** *157*, 82-88.

70. Torres-Knoop, A.; Heinen, J.; Krishna, R.; Dubbeldam, D., *Langmuir* **2015,** *31*, 3771-3778.

71. Serre, C.; Millange, F.; Thouvenot, C.; Noguès, M.; Marsolier, G.; Louër, D.; Férey, G., *J. Am. Chem. Soc.* **2002,** *124*, 13519-13526.

72. Dubbeldam, D.; Krishna, R.; Snurr, R. Q., *J. Phys. Chem. C* **2009,** *113*, 19317-19327.

73. Krishna, R., *Phys. Chem. Chem. Phys.* **2015,** *17*, 39-59.

Chapter 3

Vapor-Phase Selective Benzene Adsorption over Cyclohexane by Dual Coherent Approaches Rationalized on MOFs

3.1. Introduction:

Over the last few decades, separating benzene (Bz) and cyclohexane (Cy) remains one of the most challenging processes in the petrochemical industry sector. Benzene as a very important chemical, is an ubiquitously recognized volatile organic compound (VOC) of tremendous environmental and industrial significance.[1] Cyclohexane gets produced by the catalytic hydrogenation process of benzene feedstock. The unreacted benzene, present in the reactor's effluent stream must be removed for pure cyclohexane recovery. Now, separation of benzene from cyclohexane is inherently difficult by typical distillation processes, because these components in mixture form close boiling point mixtures, known as azeotropes, at a wide range of their compositions.[2] As of now, extractive distillation and azeotropic distillation are being used for this separation. These two separation processes, however, largely suffer from dual disadvantages namely, high degree of complexity and soaring energy consumption. For these drawbacks and to mitigate the bottlenecks of such energy-intensive azeotropic separation processes,[3] the industry has always been looking forward to the implementation of a feasible alternative to these aforesaid conventional Bz/Cy separation processes.

Over nearly two decades of its discovery-led existence, majority of the research and development endeavour in the domain of porous MOF adsorbent materials have been focused on molecular adsorption and separation applications; particularly, related to gas storage and chemical separation.[4] In principle, MOFs score over traditional adsorbents like zeolites owing to their unmatched chemical tailorability trait, which propel them in order to selectively absorb one of the azeotropic component vapor (herein, benzene) in a selective fashion over its competing adsorbate (like cyclohexane in this case). While significant development has taken place in the regime of selective gas adsorption phenomena based separation applications namely, CO_2 over N_2 (postcombustion), CO_2 over CH_4 (natural gas purification), CO_2 over H_2 (precombustion), and CO_2/O_2 (air separation);[4-8] analogous applications in the selective adsorption driven solvent vapor separation frontiers have only been quite a few in number (excluding quite a noteworthy work performed in the domain of MOF-based liquid phase separation[9]). Furthermore, vapor-phase adsorptive separation based on MOF adsorbents is regarded as a much more energy-efficient approach when compared to alternate routes such as azeotropic/extractive distillation, fostering the need behind the designed syntheses

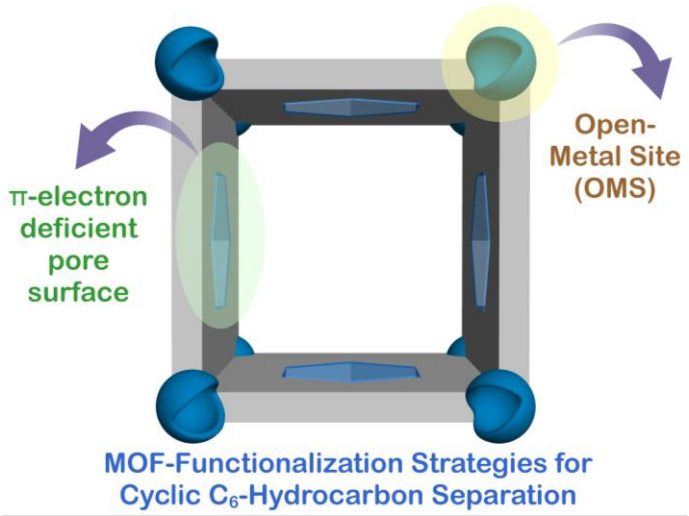

Scheme 3.1. Schematic illustration of the two pursued strategies in this chapter, in the way of leading to targeted selective interplay of the MOF(s) with Benzene, over its azeotropic congener Cyclohexane.

of new kinds of MOF adsorbents with improved efficiency, in a way to mitigate the prevailing bottlenecks.

Herein, in this chapter, two entirely different pre-functionalization approaches have been pursued in the quest of discovering highly efficient benzene-selective MOF sorbent materials which might end up showing good potential to separate benzene from a mixture of the two azeotropic species namely, benzene and cyclohexane. Unlike the last chapter, where a single MOF compound (DynaMOF-100) was comprehensively analyzed both experimentally and by theoretical simulation methodologies to explore its proficient dual separation performances (viz., *p*-xylene over its congener isomers and styrene over ethylbenzene), here in this chapter, two entirely different MOF systems with two diverse chemical functionalization's have been chosen for systematic evaluation in relevance to exhibiting a single focused application that is, Bz/Cy separation mediated by selective sorption of Bz (Scheme 3.1). Henceforth, the ensuing chapter is also divided into two subsections. The first one (chapter 3A) will be focused upon a linker functionalization based approach where highly electron-deficient diaminotriazine core grafted as the responsive functional core turns out the newly designed/synthesized MOF (**DAT-MOF-1**) to be a selective benzene vapor-adsorbent at room temperature and ambient pressure. On the other hand, unsaturated metal sites (UMS)/open metal sites (OMS) have been envisaged upon as the

crucial functionality behind the revelation of excellent Bz/Cy separation performance in the next section (chapter 3B), for an isostructural series of renowned MOF family *viz.* **M-MOF-74** (M: Mg, Mn, Fe, Co, Ni, Cu, Zn).

3.2. Experimental Section:

3.2.a. Materials:

All the reagents and solvents were commercially available and used without further purification.

3.2.b. Physical measurements:

Powder X-ray diffraction (PXRD) patterns were measured on Bruker D8 Advanced X-Ray diffractometer at room temperature using Cu-Kα radiation (λ= 1.5406 Å) with a scan speed of 0.5° min^{-1} and a step size of 0.01° in 2 *theta*. Thermogravimetric analysis results were obtained in the temperature range of 30-800 ºC on Perkin-Elmer STA 6000 analyzer under N_2 atmosphere, at a heating rate of 10 ºC min^{-1}, The Fourier transform (FT-IR) infra-red spectra were recorded on NICOLET 6700 FT-IR Spectrophotometer using KBr Pellets. The morphological features and compositional analyses of the crystalline materials were recorded with Zeiss Ultra Plus field-emission scanning electron microscopy (FESEM)-Ultra Plus Field Emission Scanning Electron Microscope with integral charge compensator and embedded EsB and AsB detectors [Oxford X-max instruments 80mm^2. (Carl Zeiss NTS, Gmbh), Imaging conditions: 2 kV, WD = 2mm, 200 kX, Inlens detector], as well an EDXS attachment (for recording Energy-dispersive X-ray spectroscopy (EDXS) analysis data-sets.

3.2.c. X-ray Structural Studies:

Single-crystal X-ray data of **DAT-MOF-1a** was collected at 150 K on a Bruker KAPPA APEX II CCD Duo diffractometer (operated at 1500 W power: 50 kV, 30 mA) using graphite-monochromated Mo Kα radiation (λ = 0.71073 Å). Crystal was mounted on nylon CryoLoops (Hampton Research) with Paraton-N (Hampton Research) oil. The data integration and reduction were processed with SAINT software.[10] A multi-scan absorption correction was applied to the collected reflections. The structure was solved by the direct method using SHELXTL[11] and was refined on F^2 by full-matrix least-squares technique using the SHELXL-97[12] program package

within the WINGX[13] program. All non-hydrogen atoms were refined anisotropically. All hydrogen atoms were located in successive difference Fourier maps and they were treated as riding atoms using SHELXL default parameters. The structures were examined using the *Adsym* subroutine of PLATON[14] to assure that no additional symmetry could be applied to the models.

3.2.d. Low Pressure Gas and Solvent Sorption Measurements:

Low-pressure solvent (Benzene and Cyclohexane) sorption measurements were performed using BelAqua (Bel Japan). Low pressure gas adsorption measurements were performed using BelSorpmax (Bel Japan). All the gases used were of 99.999% purity. As-synthesized crystals of compound **DAT-MOF-1a** were exchanged thrice each day over a period of five days with fresh batches of lower-boiling solvent acetone, before heating it under vacuum to end up with guest-free crystalline phase **DAT-MOF-1**. As-synthesized **M-MOF-74** compounds (as prepared by the reported protocols)[15-18] were exchanged thrice each day over a period of seven days with fresh batches of dry methanol, before heating each at 210 °C under vacuum to end up with guest-free, activated crystalline phases, suitable for sorption analysis.

3.2.e. Solvent exposure study:

Crystalline solid powder of respective probe MOF compounds were taken in smaller glass vials were kept open inside larger capped closed glass vials containing two different guest solvents (benzene, and cyclohexane respectively) and their 1:1 mixture (separately), over a period of 72h to allow vapor-phase exposure of solvents and characterized by PXRD.

3.2.f. Electron density plot:

Electrostatic potential surface calculation was performed with the Gaussian09 Rev D program suite using Density functional theory (DFT) with Becke's three-parameter hybrid exchange functional and the Lee-Yang-Parr correlation functional (B3LYP) and 6-31G(d,p) basis set.

Section 3A

A π-electron Deficient Diaminotriazine Functionalized MOF for Selective Sorption of Benzene over Cyclohexane

3A.1. Introduction:

Metal–organic frameworks (MOFs), constituted of the coordination chemistry-assisted self-assembly process of organic linkers and metal ions have evolved as one of the most preferred new-generation materials, owing to their superlative potential in multifarious fields, such as gas storage, chemical separation, sensing, drug delivery, and catalysis.[19-28] These crystalline materials score over the other classes of functional materials because of a few unique advantages, such as their unique periodical structures with long-range order, excellent porosity, framework flexibility, and tunable pore surface functionalization, which endow them with promising storage and separation applications.[29-33] Among the diverse porous adsorbent materials utilized for serving efficient separation of flue gas and hydrocarbons, MOFs have established themselves as a uniquely promising class of functional adsorbents owing to the unmatched unison of their aforementioned characteristics.[34-39]

From the application-perspective, the separation of liquid phase hydrocarbons, especially those having similar physical properties and comparable molecular sizes is highly challenging for industrial applications. In this context, the industrially crucial separation of benzene (Bz) and cyclohexane (Cy) poses as a challenging one. The recognized difficulty behind this C_6 hydrocarbon stream separation originates as a consequence of the unavoidable production of cyclohexane during the catalytic hydrogenation of benzene in the benzene/cyclohexane miscible system and also due to their considerably close boiling points (benzene, 353.25 K; cyclohexane, 353.85 K: **Appendix table 3A.1**), similar molecular volumes, comparable Lennard-Jones collision diameters along with low relative volatilities.[40-43] While close proximity in their boiling points (difference: 0.6 K) rules out conventional fractional distillation methods, specialized distillation protocols such as azeotropic and extractive distillation methods employed with entrainer species such as sulpholane, dimethylsulfoxide, N-methylpyrrolidone, and N-formylmorpholine involve high energy-intensive requirements. On the contrary, adsorptive separations offer an energy-efficient alternative to extractive distillation, especially for Bz/Cy mixtures containing small percentages of benzene, as is commonly encountered.

Interestingly enough, these two analogous species have distinct spatial configurational orientations; benzene is a planar π-cloud entity, while aliphatic cyclohexane exists in either chair or boat configurations (**Appendix 3A.1**). This inherent dissimilarity might seem to be the

imperative key-factor behind efficiently separating the duo (**Scheme 3A.1**). The favourable role of π-complexation with benzene behind the selective sorption-mediated Bz/Cy separation was explored in cation-exchange Faujasite-type zeolites Na-Y, Pd-Y, Ag-Y, and FAU-type zeolite membranes;[44-46] while recent years have witnessed some porous MOF materials being used for the targeted selective sorption based separation of Bz/Cy.[41, 42, 47-55] However, ligand design-strategy derived achievement of such separation performance is indeed scarce.[41, 52]

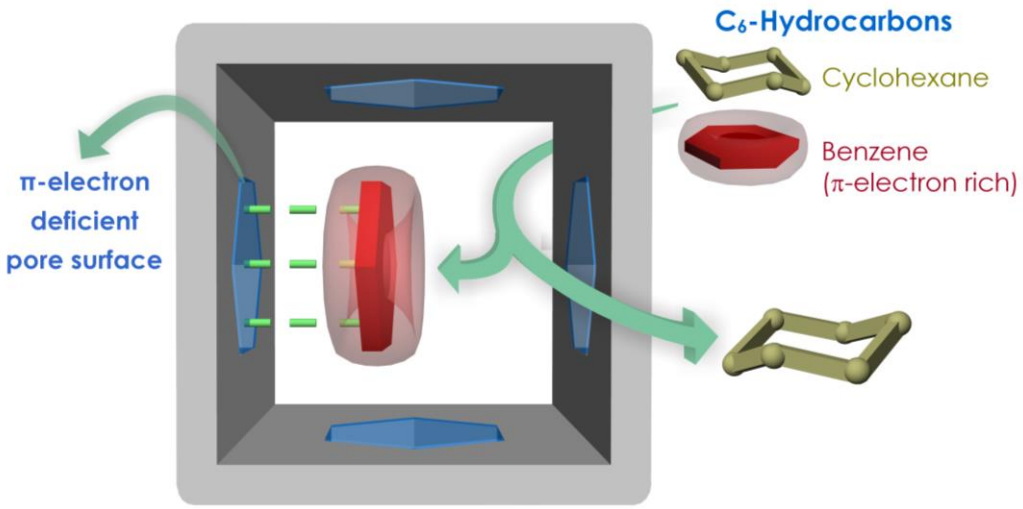

Scheme 3A.1. Schematic representation of the strategic employment of π-electron deficient diaminotriazine (DAT)-functionalized pore surface for exhibiting selective interplay with Benzene over Cyclohexane.

Ligand functionalization based attainment of excellent separation performance by MOFs has witnessed remarkable upsurge in recent times, markedly motivated by the pioneering work of Chen *et al.*[56-58] Over the years, triazine core has been quite well-harnessed chiefly by Zhou *et al.*, as constituent linkers in the MOF domain for presenting excellent adsorption features with concomitant thermal robustness of the materials.[59-62] Under this backdrop, we intended to achieve Bz/Cy separation by the favourable π–π stacking driven interplay of π-electron deficient triazine core of the employed rigid carboxylate linker functionalized MOF pore surface and π-rich guest species benzene.[63]

3A.2. Synthetic Protocol:

3A.2.a. Synthesis of Ligand (LH):

4-cyano benzoic acid (5g, 33.98 mmol) and dicyanamide (4.1619 g, 49.49 mmol) were added to a stirring solution of potassium hydroxide (2.772, 49.5 mmol) in 2- methoxy ethanol (100 mL) (**Appendix 3A.3**) in a round bottomed flask. Resulting mixture was refluxed at 423K for 30 h. This mixture was subsequently cooled down to room temperature. The solution was neutralized using dilute HCl until the pH of reaction mixture was ~7 to get white precipitate. Then the resulting solution was filtered off, dried under vacuum to get white powder. The compound was characterized using ^{1}H NMR, ^{13}C NMR and HRMS (**Appendices 3A.4-3A.6**). ^{1}H NMR (400 MHz, DMSO-d_6): δ 8.3 (td, *J* = 1.6, 8.8 Hz, 2H); 8.0 (td, *J* = 2.0, 8.8 Hz, 2H), 6.8 (S, 4H); ^{13}C NMR (100 MHz, $CDCl_3$): δ 169.4, 167.4, 167.1, 141.0, 133.1, 129.2, 127.7; HRMS (Appendix section): Calc. for $C_{10}H_{10}N_5O_2$ $[M+H]^+$: 232.083; Found: 232.083.

3A.2.b. Synthesis of DAT-MOF-1a:

Single crystals of **DAT-MOF-1a** were synthesized by reacting $Cu(NO_3)_2.3H_2O$ (0.012 g, 0.05 mmol), LH (0.0231 g, 0.1 mmol) in DMF (2 mL) and MeOH (1 mL) in a 5 mL screw-capped vial (**Appendix 3A.7**; Crystallographic data table: **Appendix table 3A.2**). The vial was heated to 90 °C for 48h under autogenous pressure and then cooled to RT over 12 h. The green block shaped single crystals of **DAT-MOF-1a** were obtained with ∼50% yield. Anal. found (elemental analysis) for **DAT-MOF-1a** (%): C, 46.92; H, 5.23; N, 22.88.

3A.3. Result and discussions:

Herein, for the first time, electron deficient diaminotriazine (DAT) core of a new-fangled rigid monocarboxylic acid linker (**Figure 3A.1**) has been proficiently exploited for imparting essential *π*-electron deficiency to the ensuing new MOF (**DAT-MOF-1**) for achieving the targeted selective sorption-based separation of benzene over cyclohexane at ambient temperature (298K) and pressure (1 atm). The electrostatic surface potential (ESP) plot (**Appendix 3A.2**) for the conceived linker was verified to have significant *π*-electron deficiency, which makes its choice strategically triggered. Upon reaction of ligand (LH) (**Appendix 3A.3**) and $Cu(NO_3)_2.3H_2O$ under solvothermal conditions in the binary solvent system DMF/ MeOH (1:1), block shaped green shiny single crystals of compound **DAT-MOF-1a** $[\{Cu(L)_2\}.xG]_n$ (G refers

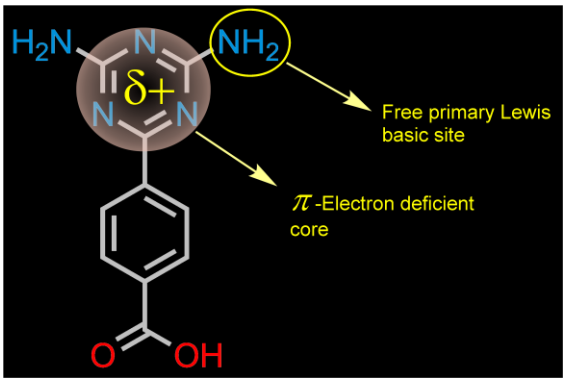

Figure 3A.1. Structure of the π–e$^-$ deficient triazine (DAT) core based linker (LH), with lewis basic primary amino groups, imparting framework functionalization.

to disordered guest molecules) are obtained (**Appendix 3A.7**). A single-crystal x-ray diffraction (SC-XRD) study of the compound showed the formation of a two-dimensional (2D) network, which on further hydrogen bond formation with similar 2D networks in proximity, gave rise to intermolecular hydrogen bonded three-dimensional (3D) supramolecular network (**DAT-MOF-1a**) (**Figure 3A.2**), crystallized in orthorhombic space group P*bnb*. The *Adsym* subroutine of PLATON was applied to confirm that no additional symmetry could be applied to the model. The asymmetric unit contains one Cu(II) center and two monocarboxylate DAT (deprotonated form of LH) linkers. Nearly five guest DMF molecules detected by the combined inputs of elemental analysis, IR spectral investigation and thermogravimetric analysis (**Appendices 3A.8 and 3A.17**), could not be located in the asymmetric unit from Fourier maps in the refinement cycles, because of high extent of disorder for these moieties in the crystal. The phase purity for the as-synthesized phase was confirmed from the PXRD analyses (**Appendix 3A.18**) coupled with the SC-XRD-based unit cell analysis of arbitrarily chosen crystals from the bulk phase.

As observed from the perspective view of the supramolecular H-bonded 3D-framework, the pores along *a*-axis (**Appendices 3A.11-3A.14**) of dimension ~6.71 x 7.08 Å^2 are well-decorated with lewis basic pyridyl and primary amine functionalities, which should ideally facilitate strong interactions with polar guest species CO_2 (owing to the latter's high quadruple moment (-13•4 × 10^{-40} Cm^2)[64] over its congener flue gases.[19, 65-69] The anticipated CO_2-selective adsorption feature was indeed verified for the activated form of **DAT-MOF-1a**, namely **DAT-MOF-1**, as evident from the single component gas adsorption isotherms recorded at low

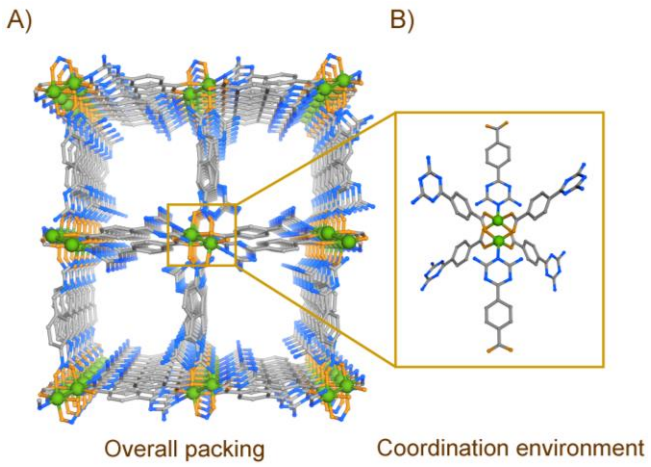

Figure 3A.2. a) Perspective view of the overall packing of **DAT-MOF-1a** (guest molecules and H atoms are omitted for clarity); b) Lewis basic N-rich π-electron deficient coordination environment constructing **DAT-MOF-1a**, rendering the channel functionalization.

temperatures (77K and 195K). Exclusively for CO_2, there was a distinct two step-mediated adsorption uptake observed with noteworthy hysteresis (typical signature of dynamic frameworks) (**Appendix 3A.20**), owing to the concomitant host-guest interactions-driven dynamic structural transformations or breathing phenomena, accompanying the CO_2 vapor sorption process.[70-72] The prominent two-step sorption profile and the observed hysteretic desorption can be attributed to structural transitions between relatively open and closed framework structures as CO_2 adsorptive gets adsorbed with substantial hysteresis consequential from the metastability of the more open structure, similar to the previous reports on breathing phenomena exhibited by soft porous crystalline frameworks.[70, 71, 73, 74] On the flipside, no such steps were observed for the CO_2 sorption isotherm at 298 K over similar pressure range (**Appendix 3A.21**), validating the dependency factor of the structural transitions accompanying sorption process on the low temperature-mediated specific interactions of the host framework with guest CO_2 molecules. The guest–free nature and excellent crystalline features of the activated phase **DAT-MOF-1** once confirmed from the thermogravimetric analyses (TGA) and Powder X-ray Diffraction (PXRD) profiles respectively (**Appendices 3A.17 and 3A.18**), the same was harnessed for the targeted selective vapor sorption based separation studies of benzene/cyclohexane.

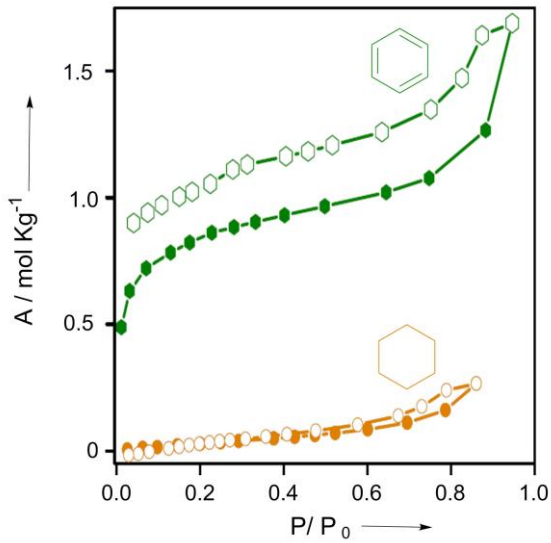

Figure 3A.3. Solvent sorption isotherms for compound **DAT-MOF-1** recorded at 298 K for Bz and Cy. Closed and open symbols denote adsorption and desorption, respectively.

Substantiating the anticipated selective interplay of Bz with **DAT-MOF-1**, the single component vapor sorption experiments for both the solvents Bz and Cy when measured at 298 K, the striking difference between their respective uptake amounts (1.5 molKg^{-1} for Bz, while only ~0.2 molKg^{-1} for Cy) were revealed (**Figure 3A.3**, Appendix 3A.22). ^{13}C NMR studies performed with the DCl/DMSO-d_6 digested samples after vapor exposure to the Bz and Cy solvent vapors and their 1:1 equimolar mixtures indubitably revealed exclusive Bz-selectivity (**Appendix 3A.23**).

We evaluate Bz/Cy separation by utilizing the Ideal Adsorbed Solution Theory (IAST) calculations. **Figure 3A.4a** shows the experimental data for pure component isotherms of Bz and Cy in **DAT-MOF-1**; the continuous solid lines are Langmuir-Freundlich fits (the fit parameters being specified in **Appendix table 3A.3**). For fitting purposes, the sorption branches of the isotherms were solely considered. **Figure 3A.4b** shows IAST calculations of Bz uptake capacity for equimolar Bz/Cy mixtures in **DAT-MOF-1**. Notably, for pressures exceeding about 1 kPa, the adsorbed phase contains predominantly of Bz. **Figure 3A.4c** presents IAST calculations for adsorption selectivity, S_{ads}, for equimolar Bz/Cy mixtures with value in excess of about 200, suggesting viability of the present MOF material for vapor phase selective

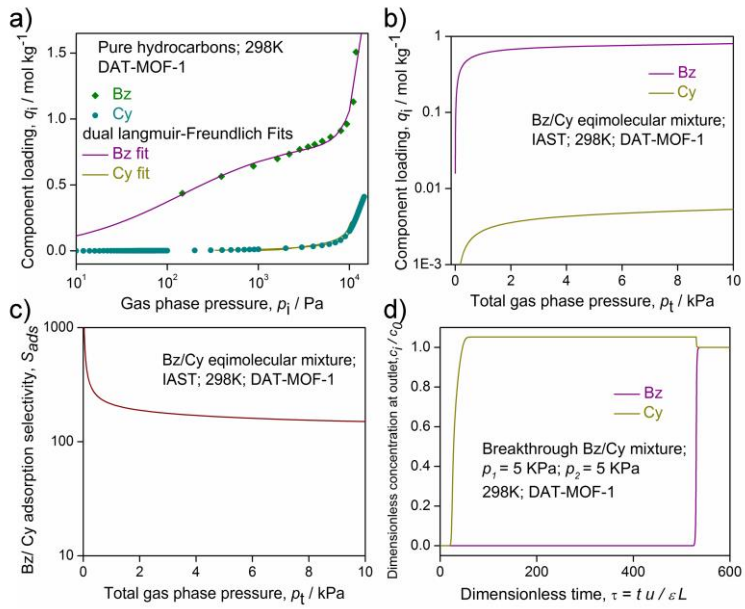

Figure 3A.4. a) Comparison of experimental data for pure component isotherms for Bz and Cy in **DAT-MOF-1** with dual-Langmuir-Freundlich fits that are shown by the continuous solid lines; b) IAST calculations for Bz uptake capacity for equimolar Bz/Cy mixtures in **DAT-MOF-1**; c) IAST calculations of adsorption selectivity for equimolar mixtures equimolar Bz/Cy in **DAT-MOF-1**; d) Breakthrough simulations for Bz/Cy in fixed bed of **DAT-MOF-1** at 298 K.

sorption based Bz/Cy separation at 298 K. Transient breakthrough simulations, using the established methodology described in earlier work,[75] confirm that sharp separations are obtained in a fixed bed adsorber; see **Figure 3A.4d**. The video animation-illustration accompanying the publication,[13] evidently demonstrate that **DAT-MOF-1** has both significantly higher selectivity and uptake for Bz over Cy.

3A.4. Conclusion:

In a nutshell, as a first-of-its kind convergent approach, the triazine core's π-electron-deficiency coupled with the mutual attendance of amino moieties for the reported **DAT-MOF-1** has been strategically exploited for the achievement of selective benzene sorption over its aliphatic analogue cyclohexane. Further examinations to consolidate its practical applications in terms of realistic industrial separation scenario are currently underway. This might indeed help to develop functional porous materials by virtue of their tunable functionalities; immensely important for exhibiting industrially crucial hydrocarbon separation features.

3A.5. Appendix Section:

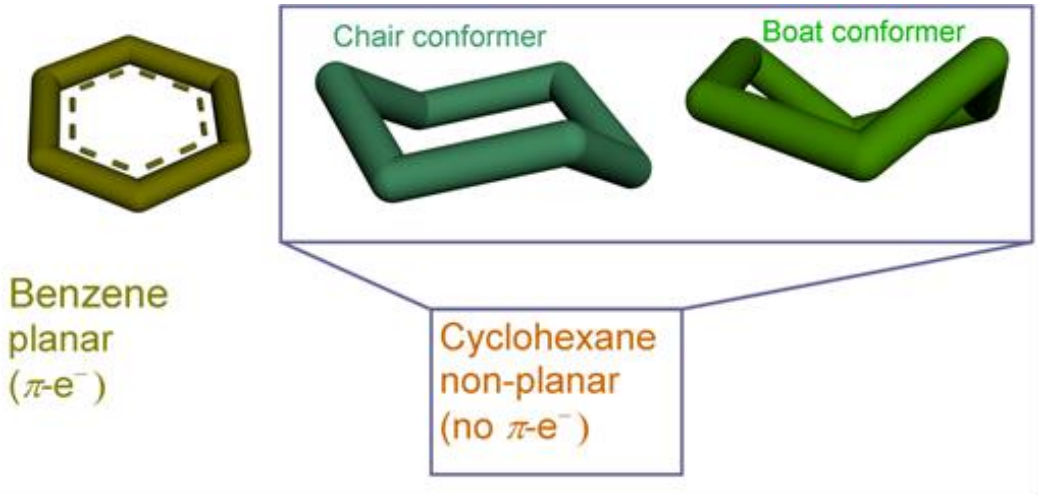

Appendix 3A.1. General conformations of planar aromatic Benzene (Bz) (left) and non-planar aliphatic Cyclohexane (Cy) (right).

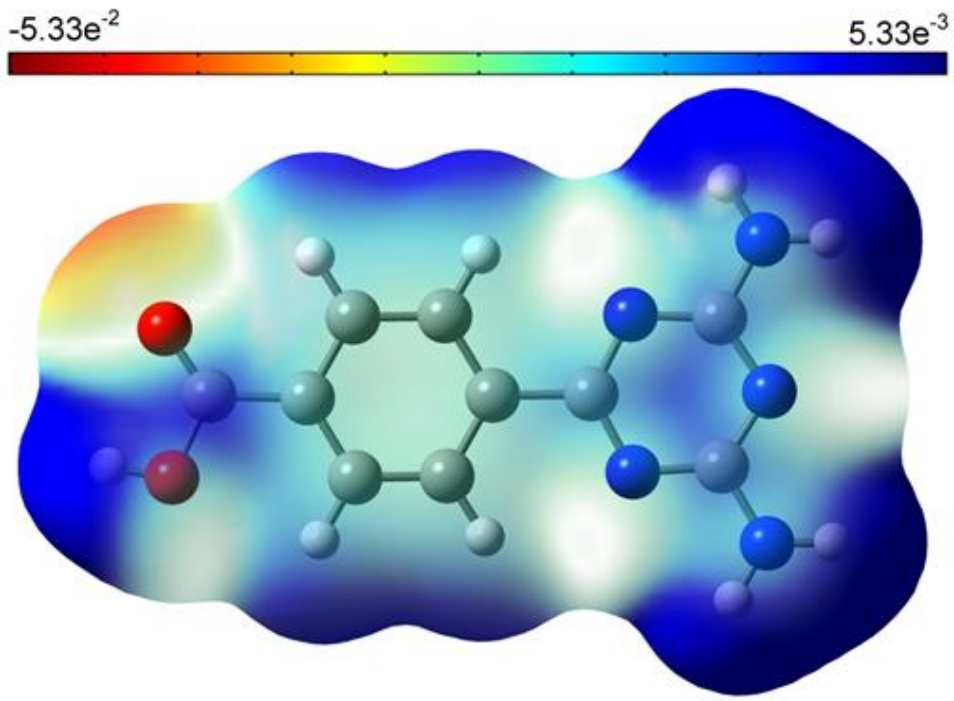

Appendix 3A.2. Electrostatic potential surface for the ligand (LH) representative of the electron density map.

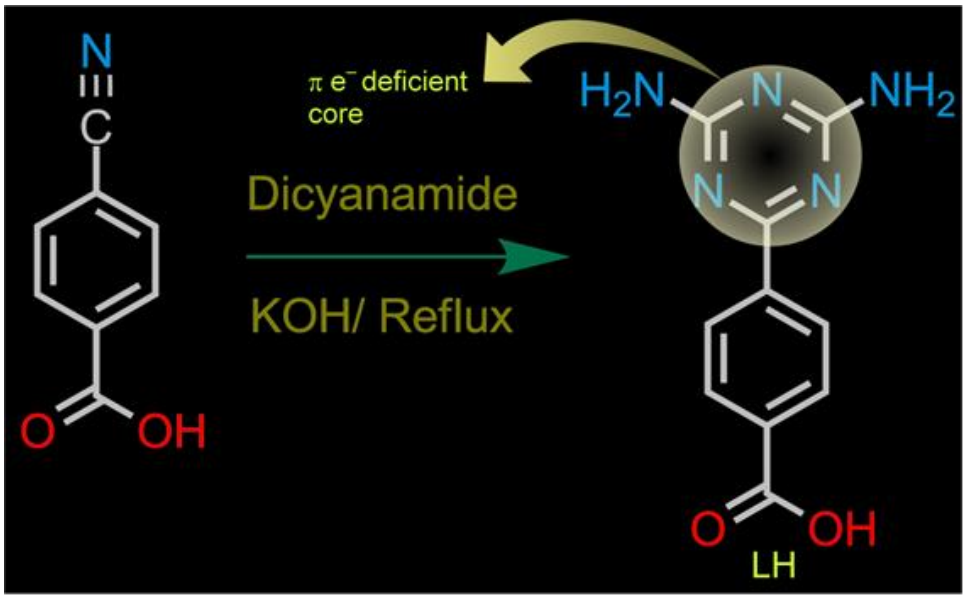

Appendix 3A.3. Ligand (LH) synthesis protocol.

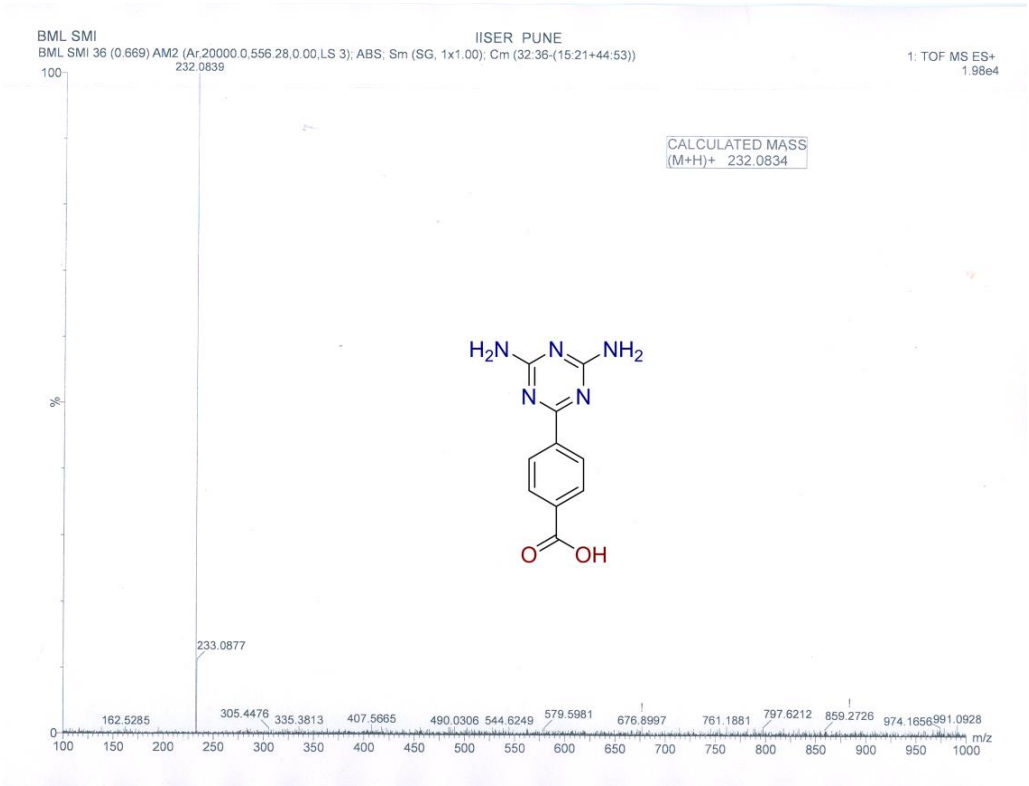

Appendix 3A.4. HRMS spectra of ligand (LH).

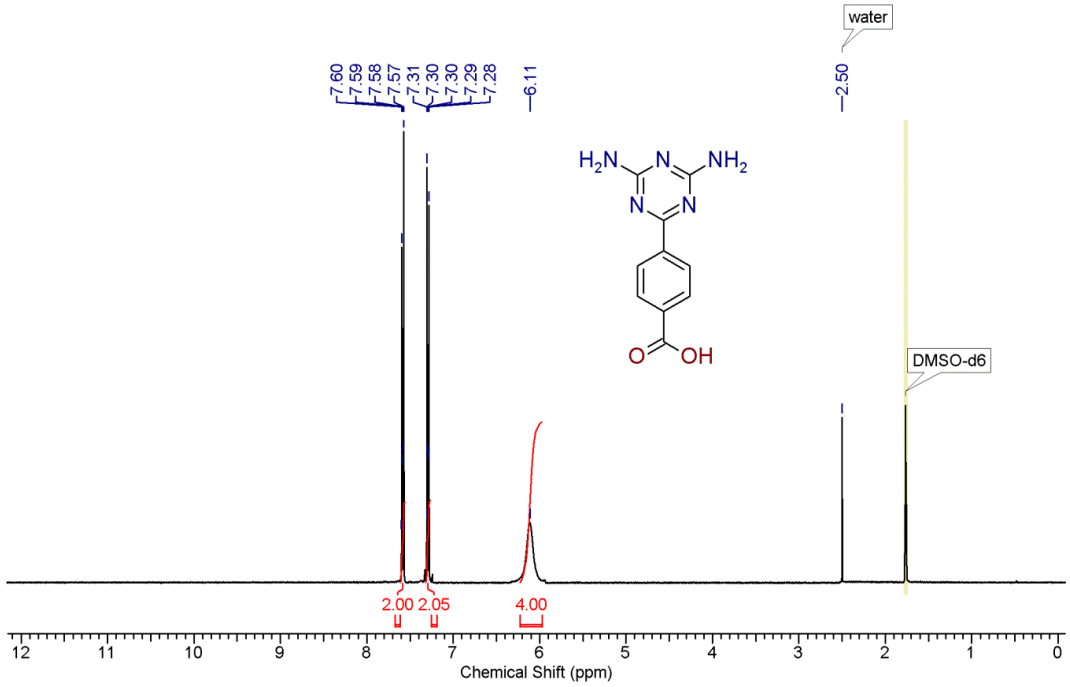

Appendix 3A.5. ^{1}H NMR spectra of ligand (LH).

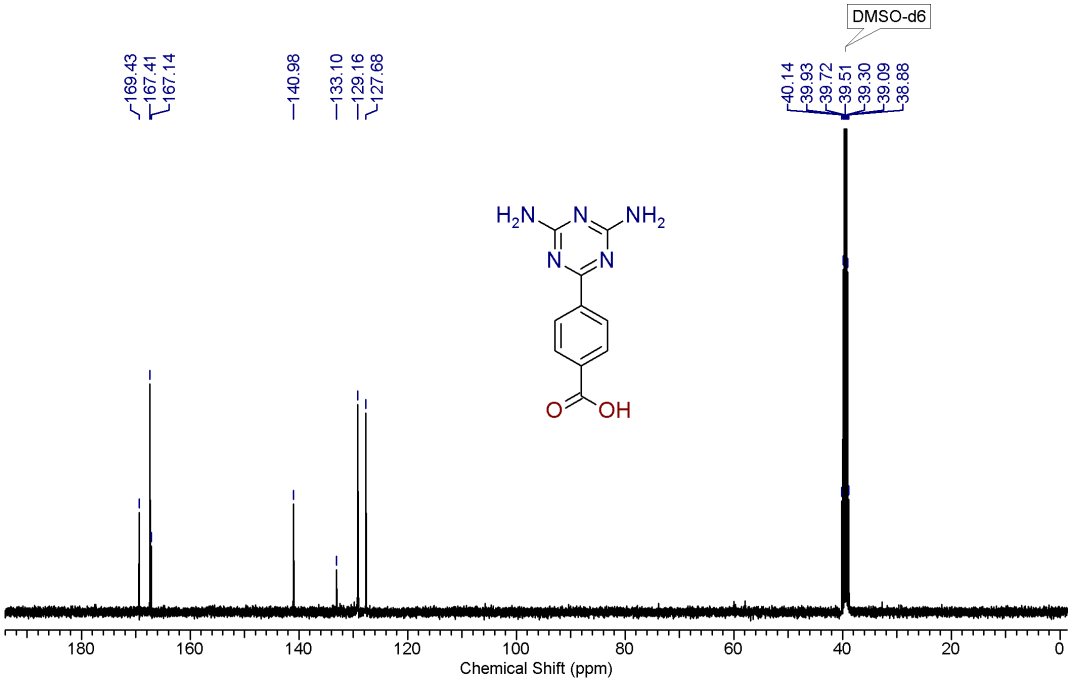

Appendix 3A.6. ^{13}C NMR spectra of ligand (LH).

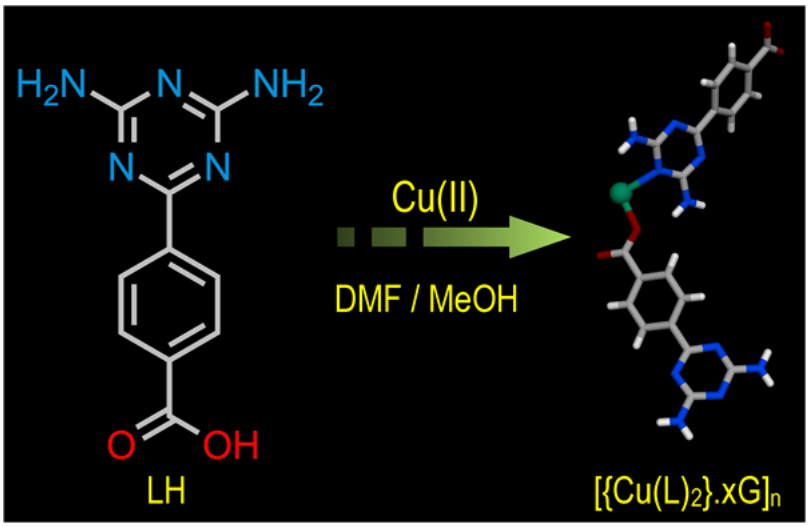

Appendix 3A.7. Synthetic scheme of **DAT-MOF-1a**.

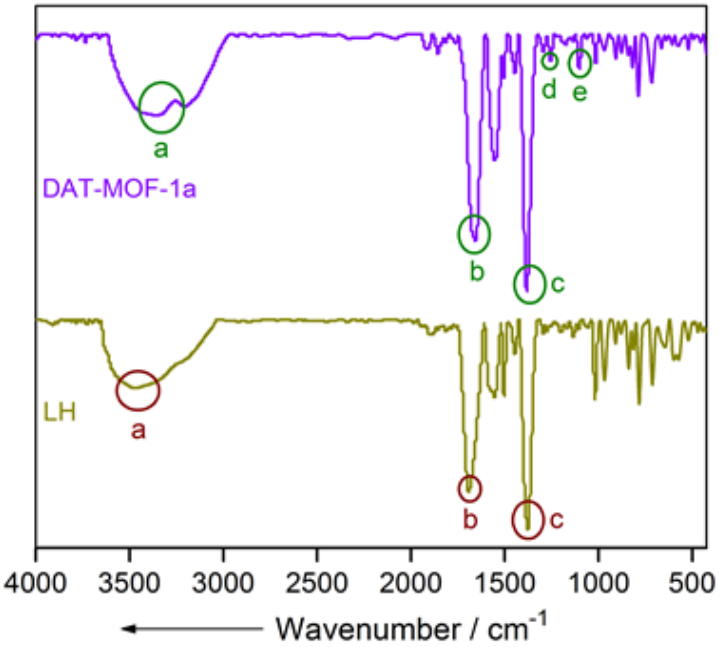

Appendix 3A.8. IR spectra of **DAT-MOF-1a** and the monocarboxylic acid ligand (LH), wherein the labelled peaks refer to the presence of N,N-dimethyl formamide (DMF) molecules within **DAT-MOF-1a**, present in addition to the coordinated monocarboxylate diaminotriazine linker L. *a*: N-H stretching (also in DMF); *b*: C-O stretching (also in DMF); *c*: C-H stretching (also in DMF); *d*: C-N stretching (DMF); *e*: C-H rocking (in DMF, $-CH_3$).

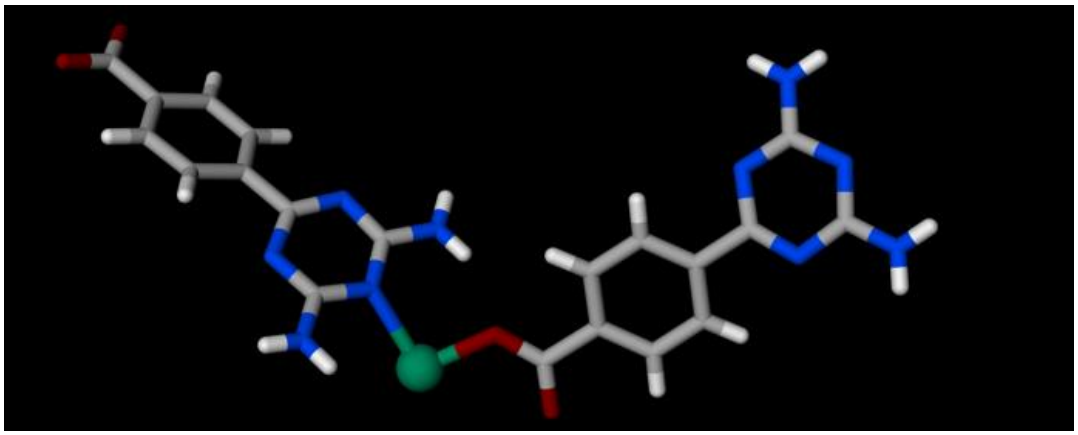

Appendix 3A.9. Asymmetric unit of **DAT-MOF-1a** (Color code: Carbon: grey, oxygen: red, nitrogen: blue, copper: deep green).

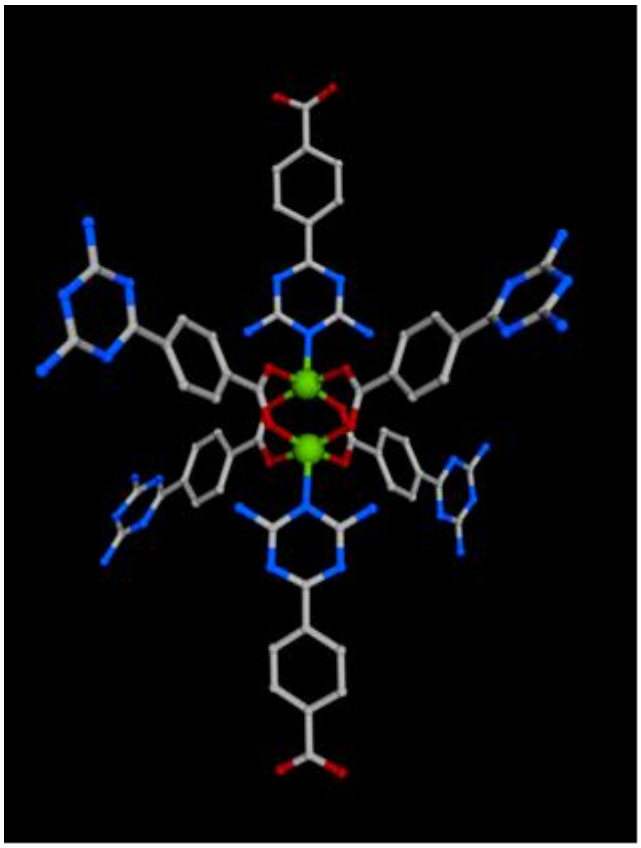

Appendix 3A.10. Coordination environment around the metal centre of **DAT-MOF-1a** (Color code; Carbon: grey, oxygen: red, nitrogen: blue, copper: green).

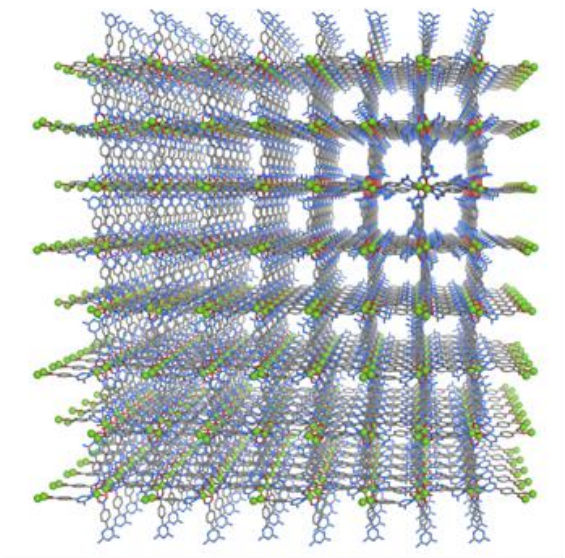

Appendix 3A.11. Perspective view of overall packing of **DAT-MOF-1a** along *a*-axis (free guests have been omitted for clarity) (Color code; Carbon: grey, oxygen: red, nitrogen: blue, copper: green).

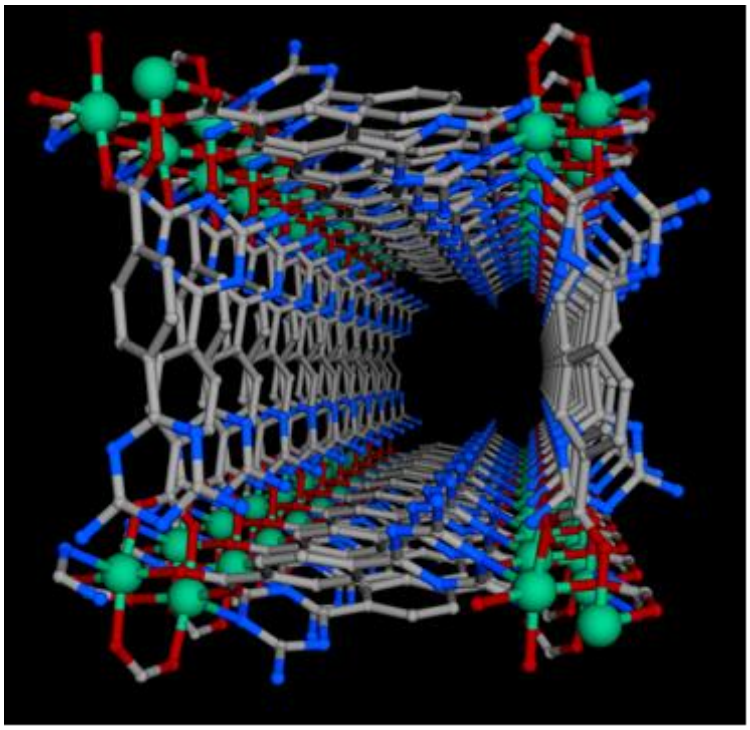

Appendix 3A.12. Perspective view of a single pore of **DAT-MOF-1a** along *a*-axis (free guests have been omitted for clarity) (Color code; Carbon: grey, oxygen: red, nitrogen: blue, copper: green).

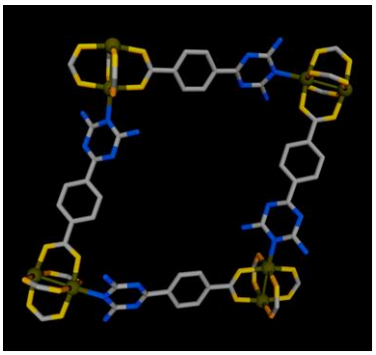

Appendix 3A.13. Single 2D net of **DAT-MOF-1a** *a* axis (Color code; Carbon: grey, oxygen: pale orange, nitrogen: blue, copper: dark yellow).

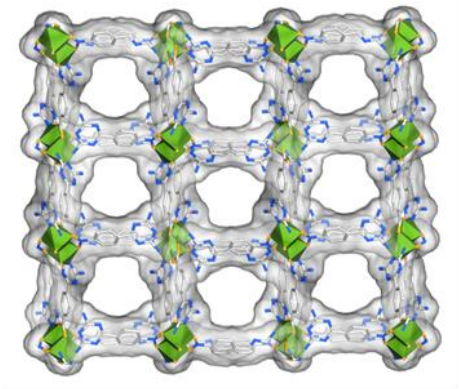

Appendix 3A.14. Pore surface of **DAT-MOF-1a** along *a*-axis (Color code; Carbon: grey, oxygen: pale orange, nitrogen: blue, copper: green polyhedral).

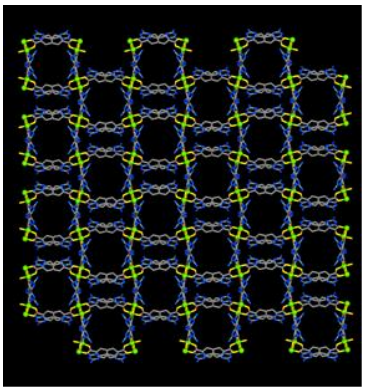

Appendix 3A.15. Overall packing along *b*-axis of **DAT-MOF-1a** (free guests have been omitted for clarity) (Color code; Carbon: grey, oxygen: pale orange, nitrogen: blue, copper: green ball).

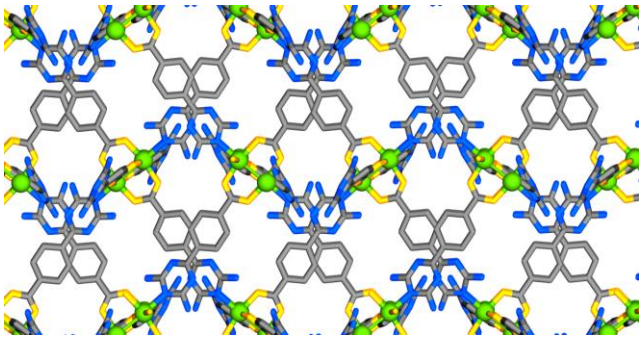

Appendix 3A.16. Overall packing along *b* axis of **DAT-MOF-1a** (free guests have been omitted for clarity) (Color code; Carbon: grey, oxygen: pale orange, nitrogen: blue, copper: green ball).

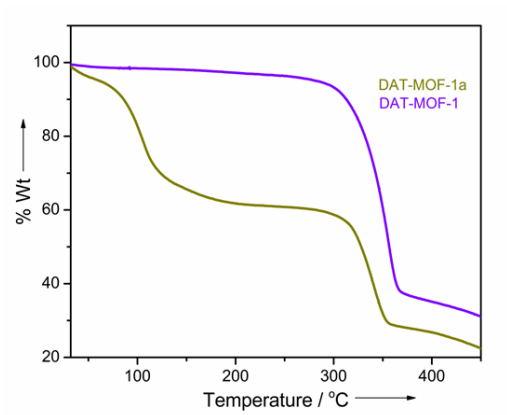

Appendix 3A.17. TGA plot of as-made and desolvated phases of **DAT-MOF-1a**.

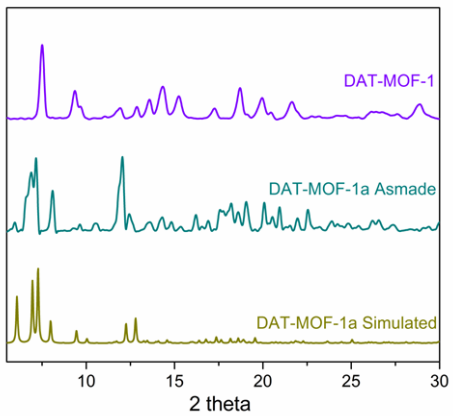

Appendix 3A.18. PXRD patterns of simulated, as-made and desolvated phases of **DAT-MOF-1a**.

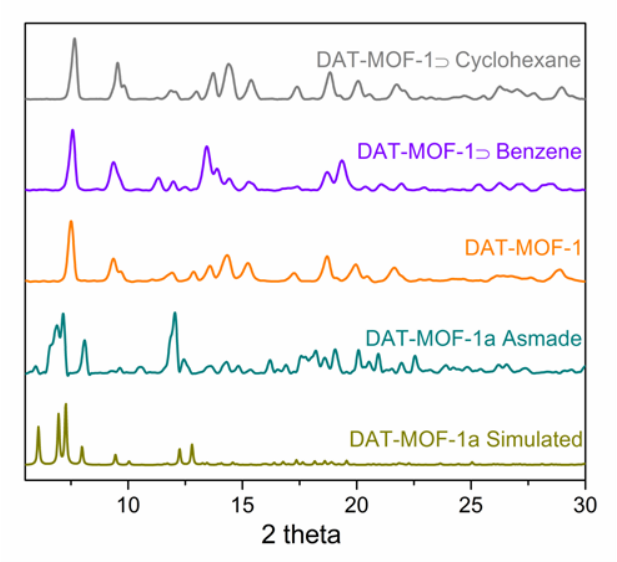

Appendix 3A.19. PXRD patterns for the Bz and Cy-vapor exposed phases of **DAT-MOF-1**, when compared together with the simulated and as-made patterns for **DAT-MOF-1a**.

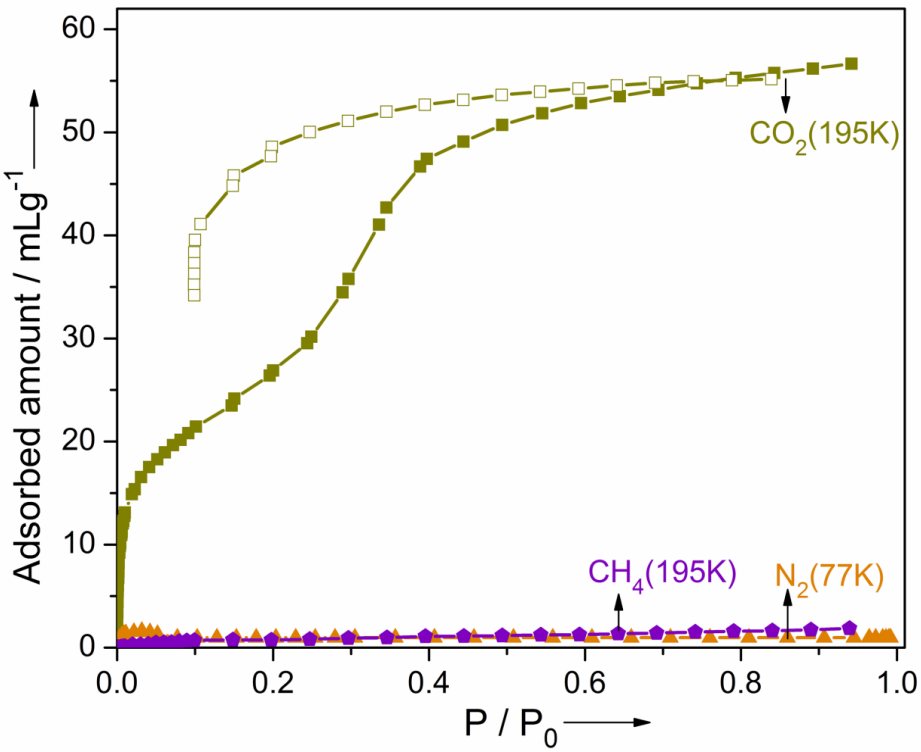

Appendix 3A.20. Low-temperature gas adsorption isotherms for **DAT-MOF-1**.

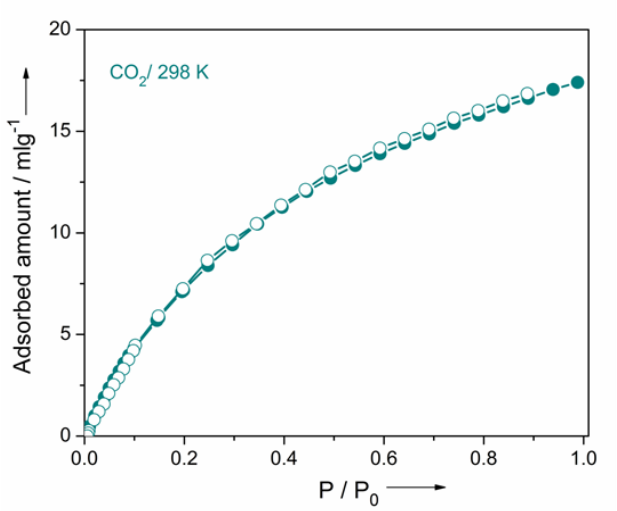

Appendix 3A.21. Room temperature CO_2 adsorption isotherms for **DAT-MOF-1**.

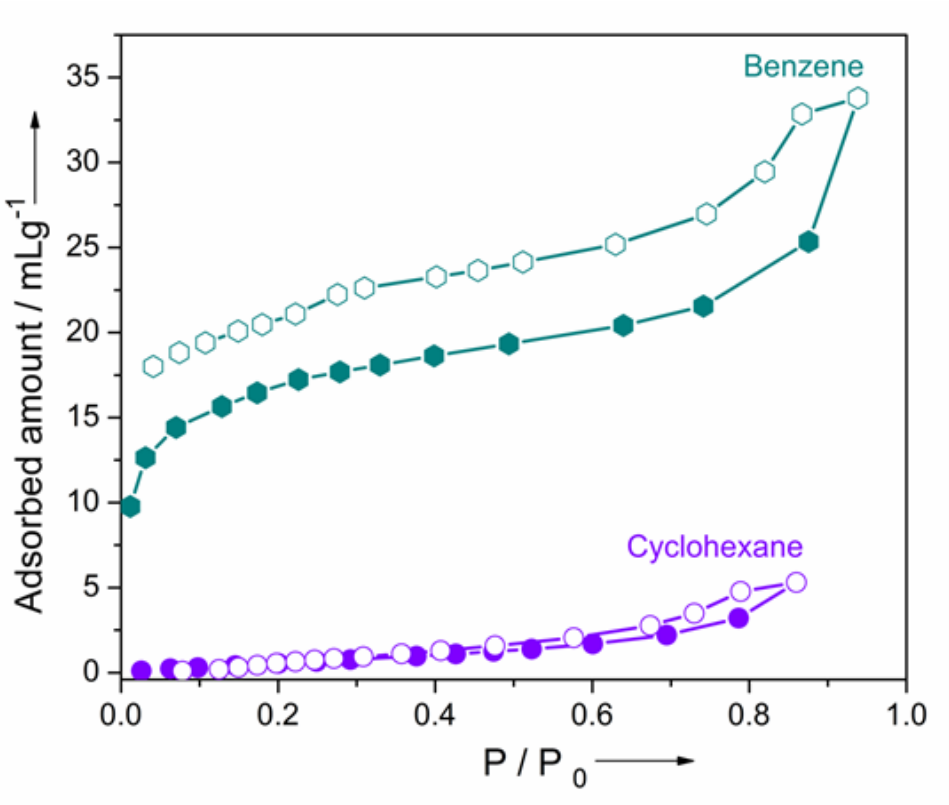

Appendix 3A.22. Benzene and Cyclohexane sorption isotherms for the desolvated phase **DAT-MOF-1** recorded at 298K and 1atm.

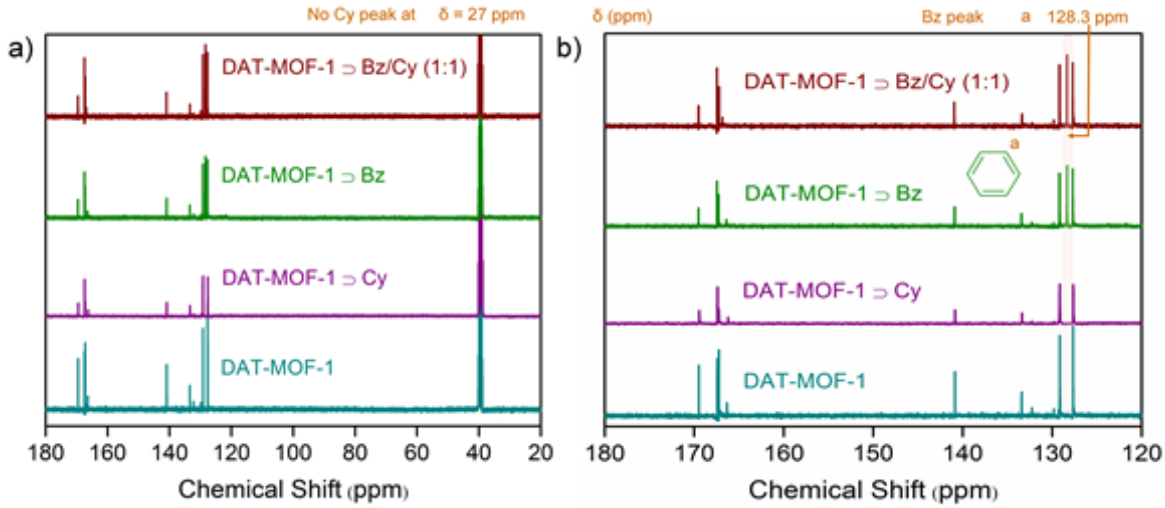

Appendix 3A.23. ^{13}C NMR spectra for Bz and Cy vapor-exposed phases of compound DAT-MOF-1, as compared to the desolvated phase itself. Vapor of each of these two solvents were exposed for 48h to the phase DAT-MOF-1 before digesting in DCl/DMSO- d_6. a) Extended ^{13}C NMR view showing no Cy peak at the characteristic cyclohexane region (δ = 27 ppm); while b) zoomed ^{13}C NMR view presenting Bz peaks for the Bz and Bz/Cy (1:1) vapor exposed phases observed at Bz characteristic region (δ = 128.3 ppm).

Appendix Table 3A.1: Physical Properties of C_6 adsorptive species.

Dimensions of Adsorptive molecules (Å)[76] (each atom surrounded by a van der Waals sphere)						Boiling and Freezing Points		Conformers
Dimensional Closeness								
	x	***y***	**z**	**MIN-1**	**MIN-2**	**B.P.**	**F.P.**	**Type(s)**
Bz	6.628	7.337	3.277	3.277	6.628	353.3 K	278.7 K	Planar
Cy	7.168	6.580	4.982	4.982	6.580	353.9 K	279.6 K	Non-planar: Boat and Chair

MIN-1: Size of the adsorptive in the minimum dimension.

MIN-2: Second minimum dimension for molecular orientations that enable a molecule to enter the channel.

Appendix Table 3A.2: Crystal data and structure refinement for compound **DAT-MOF-1a**.

Crystal data: Compound **DAT-MOF-1a**	
Chemical formula	$C_{20}H_{16}CuN_{10}O_4$
M_r	523.97
Crystal system, space group	Orthorhombic, *Pbnb*
Temperature (K)	100
a, *b*, *c* (Å)	17.7157 (6), 22.1231 (8), 25.3814 (9)
V (Å^3)	9947.6 (6)
Z	8
Radiation type	Mo *K*α
μ (mm^{-1})	0.46
Crystal size (mm)	0.15 × 0.11 × 0.10
Data collection	
Diffractometer	Bruker *APEX*-II CCD
Absorption correction	Multi-scan multi-scan absorption correction
T_{min}, T_{max}	0.934, 0.955
No. of measured, independent and observed [$I > 2\sigma(I)$] reflections	163610, 9132, 7528
R_{int}	0.092
$(\sin \theta/\lambda)_{max}$ (Å^{-1})	0.604
Refinement	
$R[F^2 > 2\sigma(F^2)]$, $wR(F^2)$, S	0.066, 0.165, 0.96
No. of reflections	9132
No. of parameters	316
H-atom treatment	H-atom parameters constrained
	$w = 1/[\sigma^2(F_o^2) + (0.0808P)^2 + 14.5162P]$ where $P = (F_o^2 + 2F_c^2)/3$
$\Delta\rho_{max}$, $\Delta\rho_{min}$ (e Å^{-3})	1.27, −0.31

Computer programs: Bruker *SAINT*, *SHELXS97* (Sheldrick 2008), *SHELXL2013* (Sheldrick 2013), Bruker *SHELXTL*.

Appendix Table 3A.3: Dual-site Langmuir-Freundlich parameters for aromatic hydrocarbons at 298 K in **DAT-MOF-1**.

	Site A			Site B		
	$q_{i,A,sat}$ mol kg^{-1}	$b_{i,A}$	$\nu_{i,A}$ dimensionless	$q_{i,B,sat}$ mol kg^{-1}	$b_{i,B}$	$\nu_{i,B}$ dimensionless
Bz	0.85	3.1×10^{-2}	0.7	3	3.7×10^{-16}	3.6
Cy	0.5	9.55×10^{-5}	0.8	0.5	2.01×10^{-25}	6

Section 3B

Harnessing Lewis Acidic Open Metal Sites of MOFs: Foremost Route to Achieve Highly Selective Benzene Sorption over Cyclohexane

3B.1. Introduction:

Metal–organic frameworks (MOFs), self-assembled from metal ions/clusters along with multidentate organic linkers,[77] have emerged as one of the most promising new-generation materials, from the standpoint of exhibiting miscellaneous applications.[20, 23, 78-80] Considering miscellaneous porous adsorbent materials manifested behind efficient separation of flue gas and industrially relevant hydrocarbons, recent years have witnessed the explicit upsurge of MOFs getting established as an inimitably riveting class of functional adsorbents, mainly because of the consummate blend of functionalities, derived from tailor-made strategic design principles.[37, 81]

Focusing on the application-frontier, separation of liquid phase hydrocarbons, particularly those with cognate physical properties and comparable molecular sizes ubiquitously remain a pressing concern for industrial applications. Under this backdrop, industrially essential separation of benzene (Bz) and cyclohexane (Cy) is an exigent one. The genesis of such identified intricacy lying behind C_6 hydrocarbon stream separation is the inevitable production of Cy accompanying the catalytic hydrogenation protocol of Bz in the Bz/Cy miscible system, coupled with their markedly similar boiling points (Bz, 353.3 K; Cy, 353.9 K: **Appendix Table 3A.1**), related molecular geometry, close Lennard-Jones collision diameters and molecular volumes, in conjunction with low relative volatilities.[42] Conventional fractional distillation methods remaining ineffective, specialized distillation protocols, *viz.* extractive and azeotropic distillations as well as pervaporation, encompass energy-intensive requisites.[82, 83] In contrast to these energy-intensive routes, adsorption-based separations present an energy-efficient alternative, particularly for Bz/Cy mixtures comprising of small percentages of Bz, as generally detected in the C_6 flow stream.[44] Focusing on the sorption-targeted porous material domain comprising of MOF adsorbents,[58] igand prefunctionalization based design principle derived Bz/Cy separation has been only recently revealed,[41, 49] while any other potential alternative rationale is yet to be discovered in the entire MOF regime, particularly with reasonable aqueous stability of the adsorbent.

Notably, the spatial configurational orientations for Bz and Cy involves distinct signatures; aromatic Bz molecule possessing a planar π-cloud entity, in stark contrast to the chair

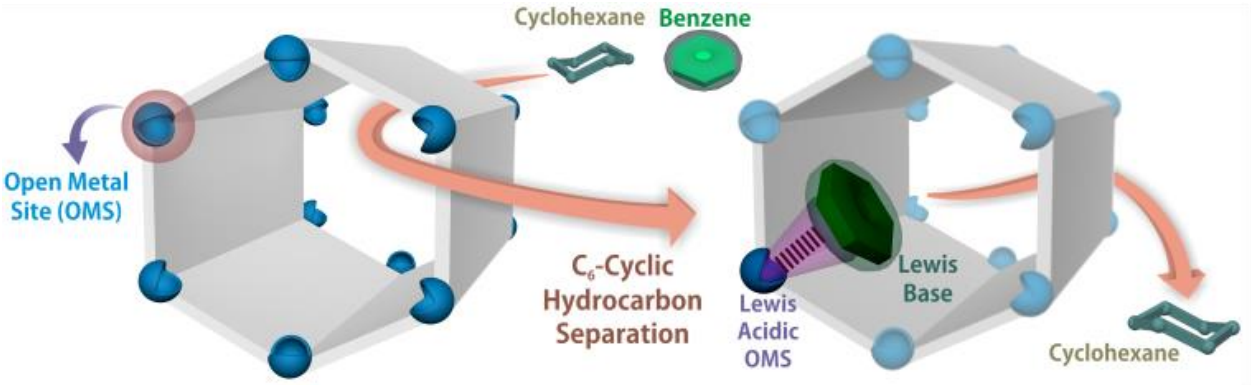

Scheme 3B.1. Schematic representation of the pursued strategy: exploiting Lewis acidic coordinatively unsaturated sites of an OMS-rich MOF platform, to exhibit selective interplay with aromatic, planar Lewis base benzene over its aliphatic, non-planar C_6-analogue cyclohexane.

or boat configurations adopted by aliphatic Cy (**Appendix 3B.1**). Herein, we have foreseen this intrinsic disparity to play the key role behind their desired efficient separation (**Scheme 3B.1**). As a potential strategy, herein, we have envisioned π-complexation triggered facile lewis acid-base interactions between the OMS-sites of a suitably porous MOF and the targeted adsorptive Bz, to play the pivotal role behind the latter's selective interplay.

Keeping in mind the desired amalgamation of the dual facets of OMS-profusion and water-stability, as a first-of-its kind approach, coordinatively unsaturated sites or OMS-rich nanospace of a series of seven isostructural, water-stable metal-organic frameworks (**M-MOF-74**) has been exploited behind the purposeful manifestation of selective Bz sorption over its aliphatic analogue, Cy.

3B.2. Synthetic Protocol:

As-synthesized **M-MOF-74** compounds (as prepared by the reported protocols)[15-18] were exchanged thrice each day over a period of seven days with fresh batches of dry methanol, before heating each at 210 °C under vacuum to end up with guest-free, activated crystalline phases, suitable for sorption analysis.

3B.3. Result and Discussions:

Last decade has witnessed the syntheses and subsequent revelation of fascinating sorbent characteristics for a family of isostructural compounds, namely, **M-MOF-74**, alternatively known as M_2(dobdc) (dobdc^{4-} = 2,5-dioxido-1,4-benzenedicarboxylate) or CPO-27-M or M_2(dhtp) (dhtp = 2,5-dihydroxyterephthalate), where M = Mg, Mn, Fe, Co, Ni, Cu, Zn.[15, 84-88] The 3D honeycomb like network of **M-MOF-74** features helical 1D metal oxide $[O_2M_2](CO_2)_2$ chains which stay connected by the benzene units from dobdc^{4-} linkers, to constitute a hexagonal

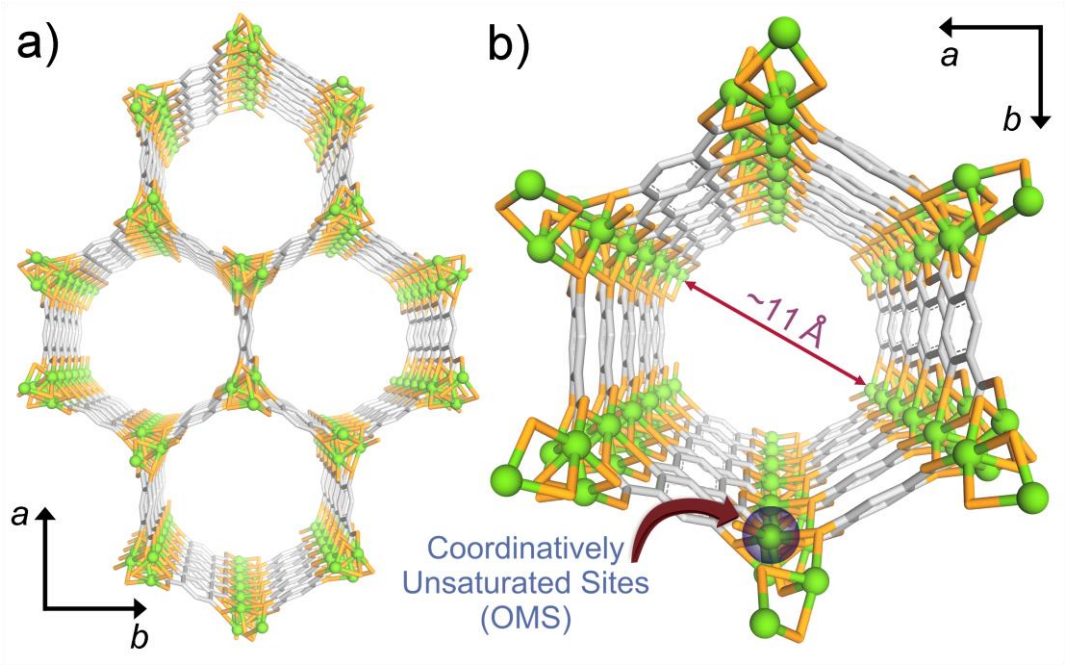

Figure 3B.1. a) Perspective representation of the **M-MOF-74** honeycomb 3D architecture presenting 1D hexagonal porous channels along crystallographic c-axis; b) zoomed view of guest-accessible cylindrical 1D pore (dimension ~11 Å) decorated with cavity-facing OMS (green spheres represent the metal centers while, oxygen and carbon atoms are shown by orange and grey sticks respectively; H-atoms and non-coordinated solvents omitted for clarity).

array of cylindrical channels, with window size ~11 Å, propagating across crystallographic *c*-axis (**Figure 3B.1**, **Appendix 3B.2**); providing an ample guest-accessible BET surface area ~1,500-1,600 m^2g^{-1}.[86, 87, 89] The high negative charge residing on the compact dobdc^{4-} ligand leads to a superior metal cation density as compared to most MOFs with such large pores. Presence of a high concentration of coordinately unsaturated metal cations (~4.5 sites/nm^3),[90]

which pose as the primary interaction sites for adsorptives, has been recently exploited behind serving a number of gaseous species' separation purpose.[91-93] Appropriate activation protocol to this material releases the coordinated water molecules from each metal center, rendering the square pyramidal metal cations with open coordination sites directed into the porous nanospace.[90] Such presence of extremely reactive metal sites decorating the connolly surface has posed as an effectual route to infuse framework selectivity for selective guest adsorption, and to enhance the surface packing density of adsorbates.[93] Therefore, based on exploiting the presumably facile interactions between π-cloud of adsorptive Bz with the OMS-rich pores of water-stable **M-MOF-74** framework via Lewis acid-base type π-complexation interactions,[16, 94, 95] the aforementioned series has been rationally chosen for comprehensive Bz/Cy selectivity analyses.

All the seven analogous compounds pertaining to **M-MOF-74** series (where M = Mg, Mn, Fe, Co, Ni, Cu and Zn) were synthesized.[15-18] While powder X-ray diffraction (PXRD) analyses confirm phase purity and isostructural framework nature of the studied guest-free phases (**Appendix 3B.3**), elemental mapping (EDX) for the seven different compounds shows that the respective metals are homogeneously spread out within the areas spanned across by corresponding crystallites (**Appendix 3B.4**).

In order to validate the anticipated selective interaction of adsorbate Bz with **M-MOF-74** compounds, single component vapor sorption experiments for both the solvents Bz and Cy were measured at 298 K for the entire series of MOFs. The contrasting nature of profiles between the said pair of measurements for any of the **M-MOF-74** analogues gets reflected in their differential saturation uptake amounts (**Mn-MOF-74**: 9.38 mmolg^{-1} for Bz, while only 0.25 mmolg^{-1} for Cy) (**Figure 3B.2**, **Appendices 3B.6-3B.9**, **Appendix table 3B.1**). All the seven congener MOFs register high uptake amount-indicative Bz sorption profiles of similar nature, with the saturation amounts presenting the following decreasing trend: **Mn-MOF-74** > **Ni-MOF-74** ≈ **Mg- MOF-74** > **Cu-MOF-74** > **Zn-MOF-74** > **Co-MOF-74** > **Fe-MOF-74** (precisely identical order with the involved metal ions' corresponding ionic potentials' decreasing sequence).[96, 97] Ethyl benzene (dimension-wise larger than Cy) sorption profile for **Co-MOF-74** registered Type-1 isotherm with high (~4.74 mmolg^{-1}) uptake amount (**Appendix 3B.10**), which served as a testimony of the

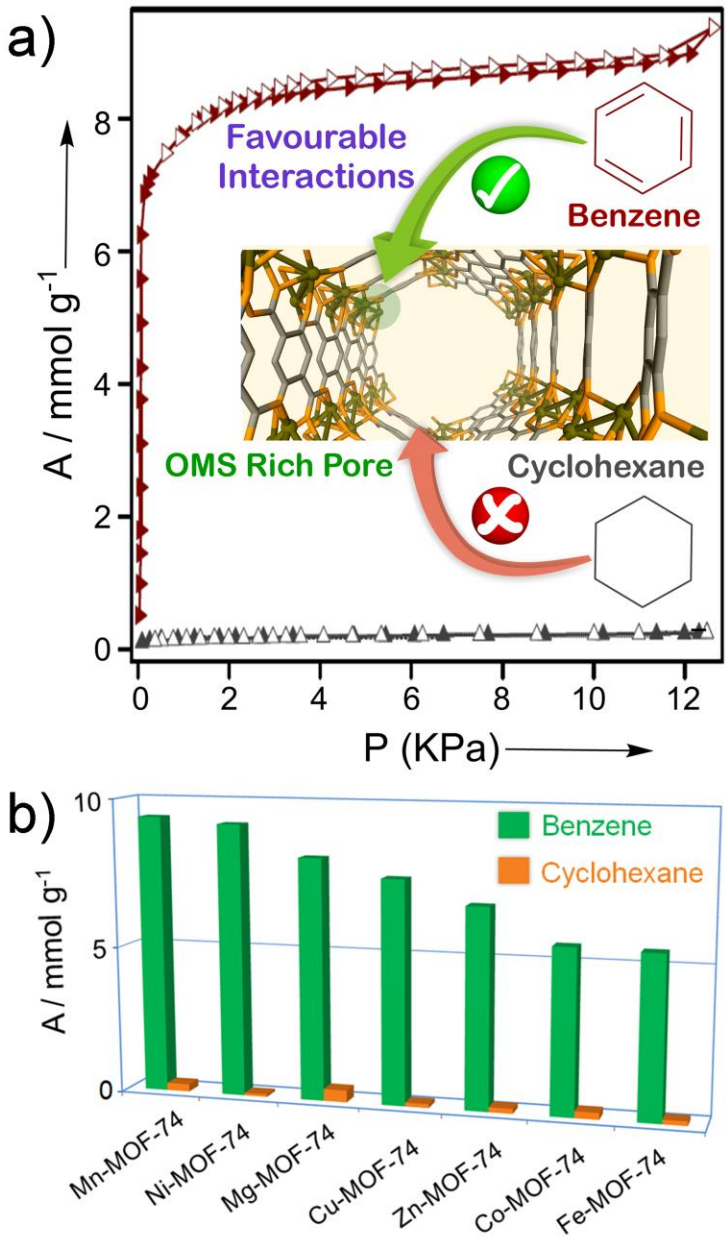

Figure 3B.2. a) Contrasting Bz and Cy solvent sorption isotherms for one of the representatives, **Mn-MOF-74**, recorded at 298 K. Filled and open markers denote adsorption and desorption, respectively; b) Bz and Cy sorption amount uptakes recoded for the entire series of **M-MOF-74** (M= Mg, Mn, Fe, Co, Ni, Cu, Zn) compounds.

framework's discriminating interplay with π-rich adsorbates like ethyl benzene, Bz etc., while emphasizing its non-interactive response to aliphatic guests like Cy, albeit the latter's smaller size.[76]

To verify the separation-viability in solution, a representative (**Mg-MOF-74**) was probed by ^{13}C NMR studies. Solvent vapor of Bz and Cy were separately exposed to the guest-free phase of **Mg-MOF-74** before digesting in DCl/DMSO-d_6. Only characteristic Bz peaks (δ = 128.3 ppm) could be noted for both Bz and Bz/Cy (1:1) vapor exposed phases (**Appendices 3B.11**, **3B.12**), suggesting exclusive interplay with Bz.

To elucidate the different behaviour of Bz adsorption in **M-MOF-74** analogues, both NVT Monte Carlo simulations and density functional theory calculations were further performed. Based on NVT simulated annealing method,[32] we observe that Bz

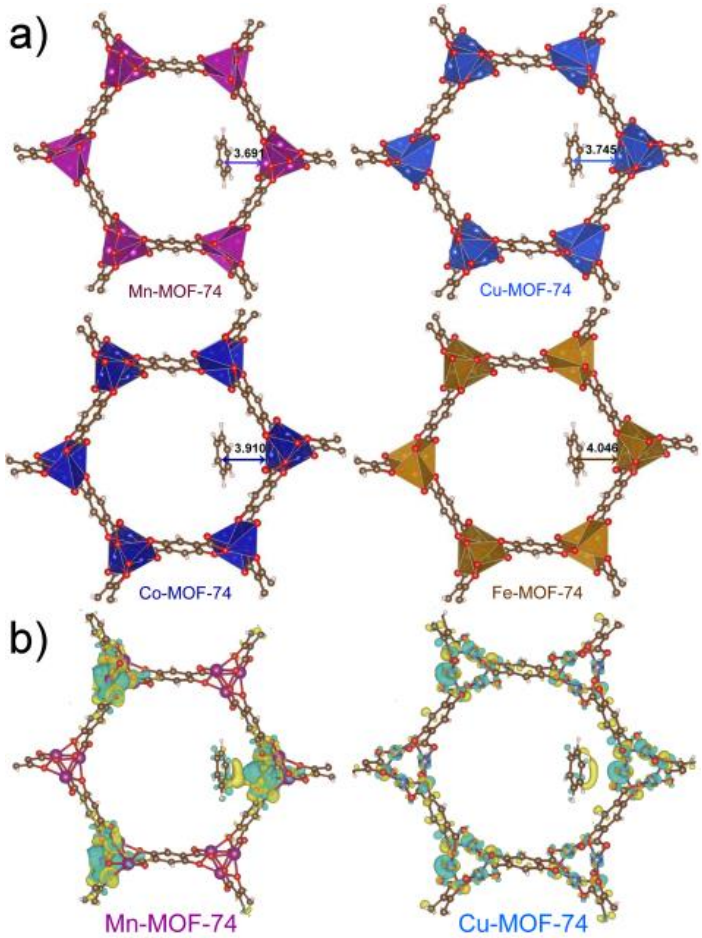

Figure 3B.3. a) DFT optimized location of Bz in different **M-MOF-74** analogues. The distance between the center of Bz molecule and the transition metal is shown in angstroms; b) Distribution of charge density difference for single molecular Bz adsorption on **M-MOF-74**. Yellow and cyan isosurfaces indicates the accumulation and depletion electrons at a level of 0.0005 e/Å^3, respectively.

molecule explicitly interacts with the Lewis acidic transition metal centers.[98, 99] Further, DFT calculations were performed based on the initial geometry obtained from NVT method to determine the binding energies of Bz with different **M-MOF-74** analogues. Dispersion interactions are included by employing a nonlocal van der Waals density functional, vdW-DF.[32] In all **M-MOF-74** analogues, Bz molecule interacts with the transition metal ions in such a way that the sp^2 hybridized carbon atoms are located close to the metal ions. **Figure 3B.3a** and **Appendix 3B.14** show the DFT optimized location of Bz molecule in different **M-MOF-74** analogues. The binding energies (**Appendix table 3B.2**) calculated based on vdW-DF functional; do not show a large difference among **M-MOF-74** analogues, with **Ni-MOF-74** exhibiting higher binding energy with Bz molecule followed by **Mn**-, **Zn**-, **Mg**-, **Cu**-, **Co**- and **Fe-MOF-74**. However, Bz interacts slightly weaker with **Co** and **Fe-MOF-74** compared with the other **M-MOF-74** analogues. This is somewhat consistent with the trend observed in the sorption isotherms of Bz with different **M-MOF-74** analogues (**Figure 3B.2b** and **Appendix 3B.8**).

To quantify the charge transferred from the transition metal ion to ion to adsorbed Bz molecule (π-back-bonding),[100, 101] we calculated the magnitude of net charge transfer using Bader charge population analysis.[102] Except for Co and Fe-MOF-74, the net charge transfer from metal ion to Bz follows the order **Mn-MOF-74** (0.0549) > **Ni-MOF-74** (0.0303) > **Mg-MOF-74** (0.0290) > **Cu-MOF-74** (0.0213) > **Zn-MOF-74** (0.0116), which is consistent with the increase in corresponding ionic potentials of the metal ions. Next, we calculate the distribution of the charge density difference for adsorption of single Bz molecule considering **Mn-MOF-74** and **Cu-MOF-74** as representative and are shown in **Figure 3B.3b**. The charge density difference ($\Delta\rho$) is calculated by, $\Delta\rho = \rho_{(M-MOF-74+Bz)} - \rho_{(M-MOF-74)} - \rho_{Bz}$, where $\rho_{M-MOF-74+Bz}$, ρ_{M-MOF} and ρ_{Bz} are electronic charge densities of the adsorbed **M-MOF-74**/Bz system, isolated **M-MOF-74** and Bz, respectively. We can observe significant charge redistribution upon Bz adsorption on **M-MOF-74**. As the charge transfer from **M-MOF-74** to Bz increases, charge redistribution becomes more concentrated around benzene and metal atoms.

Bz/Cy separation efficiency of **M-MOF-74** series of compounds was evaluated by employing the Ideal Adsorbed Solution Theory (IAST) calculations.[103] Unary isotherms for Bz in **M-MOF-74**, were fitted with the three-site Langmuir-Freundlich isotherm model (**Appendix section**); (fit parameters: **Appendix table 3B.3**). For fitting purposes, only the adsorption branches of isotherms were considered. The unary isotherms for Cy in

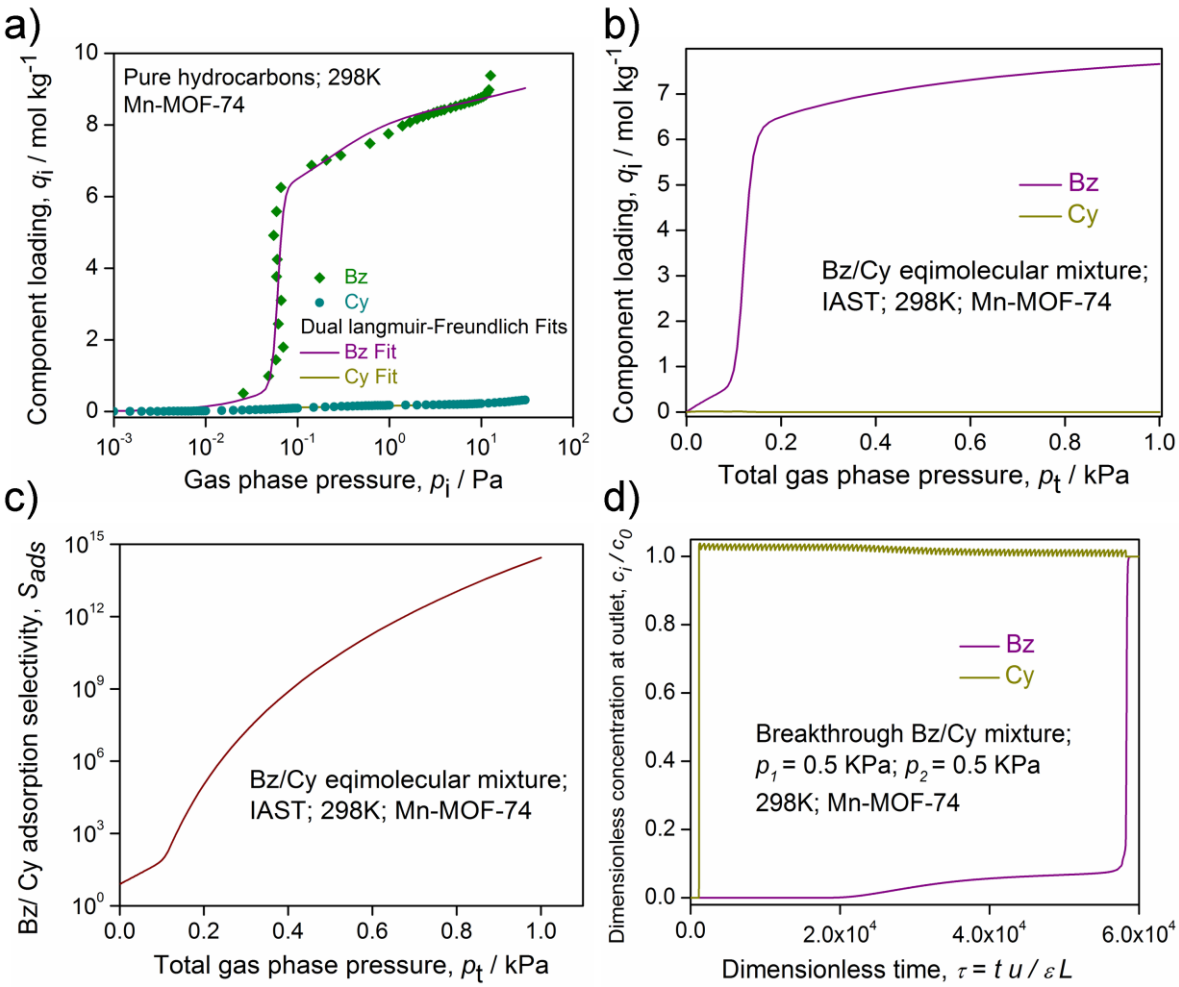

Figure 3B.4. a) Comparison of experimental data for pure component isotherms for Bz and Cy in **Mn-MOF-74** with dual-Langmuir-Freundlich fits, which are shown by the continuous solid lines.; b) IAST calculations for Bz uptake capacity for equimolar Bz/Cy mixtures in **Mn-MOF-74**; c) IAST calculations of adsorption selectivity for equimolar mixtures equimolar Bz/Cy in **Mn-MOF-74**; d) Breakthrough simulations for equimolar Bz/Cy in fixed bed of **Mn-MOF-74** at 298 K (total pressure at the inlet is 1 KPa).

M-MOF-74 were fitted with the dual-site Langmuir-Freundlich isotherm model (appendix section); (fit parameters: **Appendix table 3B.4**). In order to demonstrate the

goodness of the fitted isotherms, **Figure 3B.4a** shows the experimental and fitted data of pure component isotherms for Bz and Cy in **Mn-MOF-74**. Fits for all other **M-MOF-74** materials were also reasonably ideal. **Figure 3B.4b** shows IAST calculations for Bz uptake capacity of equimolar Bz/Cy mixtures in **Mn-MOF-74**. We note that for pressures exceeding about 0.2 kPa, the adsorbed phase contains predominantly of Bz, while the amount of Cy adsorbed is negligibly small. This indicates excellent separation characteristics. **Figure 3B.4c** shows IAST calculations for adsorption selectivity, S_{ads}, for equimolar Bz/Cy mixtures with exceedingly high values in excess of about 10^5 in case of **Mn-MOF-74**.

In fact, the selectivity values propel this benchmark series of compounds as the top-notch Bz/Cy separating porous MOF material reported till date.[13] Since, the selectivities with **Mn-MOF-74** are very high, the separation performance of different **M-MOF-74** materials is simply dictated by the uptake capacity of pure Bz. On the basis of the pure component uptakes of Bz at 1 kPa, we conclude that the separation performance of Bz/Cy mixtures will follow the hierarchy **Mn-MOF-74** > **Mg-MOF-74** ≈ **Ni-MOF-74** > **Cu-MOF-74** > **Zn-MOF-74** > **Co-MOF-74** > **Fe-MOF-74**. The three best MOFs for the targeted Bz/Cy separation are **Mn-MOF-74**, **Ni-MOF-74** and **Mg-MOF-74**.

Transient breakthrough simulations,[75] show that strikingly clear separations of equimolar Bz/Cy mixtures are achievable with **Mn-MOF-74** (**Figure 3B.4d**). It is evidently noted that Cy gets rejected almost immediately into the bulk fluid phase, and practically no cyclohexane is adsorbed, while precisely contrasting behaviour is manifested for Bz; indicative of fixed bed adsorber based sharp Bz/Cy separation signatures. The video animation (ESI)[32] clearly illustrate**s** that **Mn-MOF-74**: a representative of the **M-MOF-74** series possesses both significantly higher selectivity and uptake capacity for Bz over Cy.

3B.4. Conclusion:

In summary, as an archetypal modus operandi, presence of open metal sites acting as Lewis acidic centres could be proficiently exploited behind the realization of highly selective benzene sorption over its aliphatic, azeotropic analogue cyclohexane. This marks the first report of tactically utilizing coordinatively unsaturated sites of a microporous MOF material in course to culminate an excellent selective interplay with the π-cloud of adsorptive benzene. Additional assessments aimed at serving industrial purpose are presently underway. Such novel approach might indeed expand the horizons of strategic development lying behind superior functional porous materials of future, imperative for exhibiting industrially challenging hydrocarbon separation signatures.

3B.5. Appendix Section:

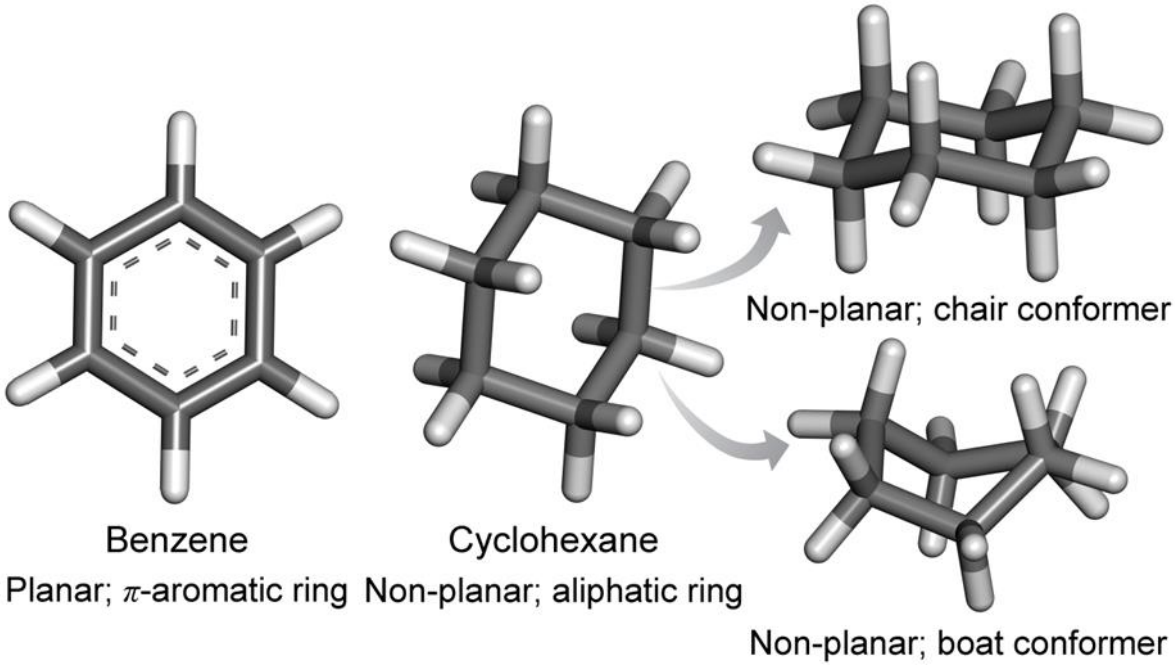

Appendix 3B.1. General conformations of planar aromatic π-ring Benzene (Bz) (left) and non-planar aliphatic congener Cyclohexane (Cy) (middle): chair (top right) and boat (bottom right) conformers.

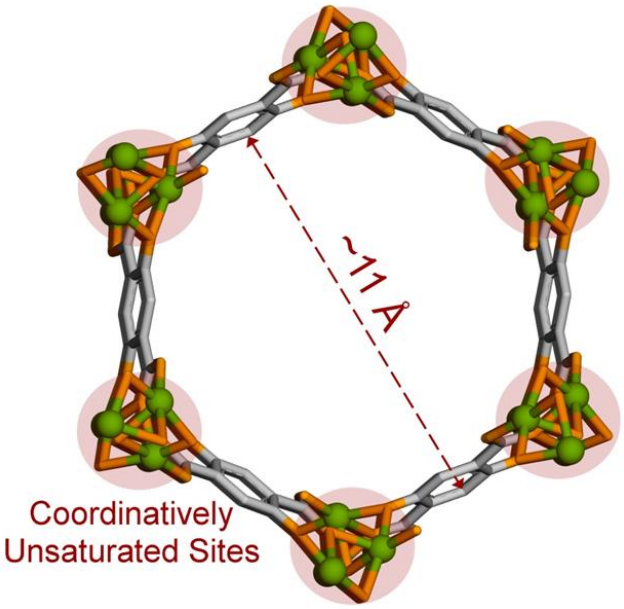

Appendix 3B.2. Orthographic view of a single pore of **M-MOF-74** network, along crystallographic *c*-axis; the pore being decorated with open metal sites or coordinatively unsaturated metal centres, with a window size ~11 Å.

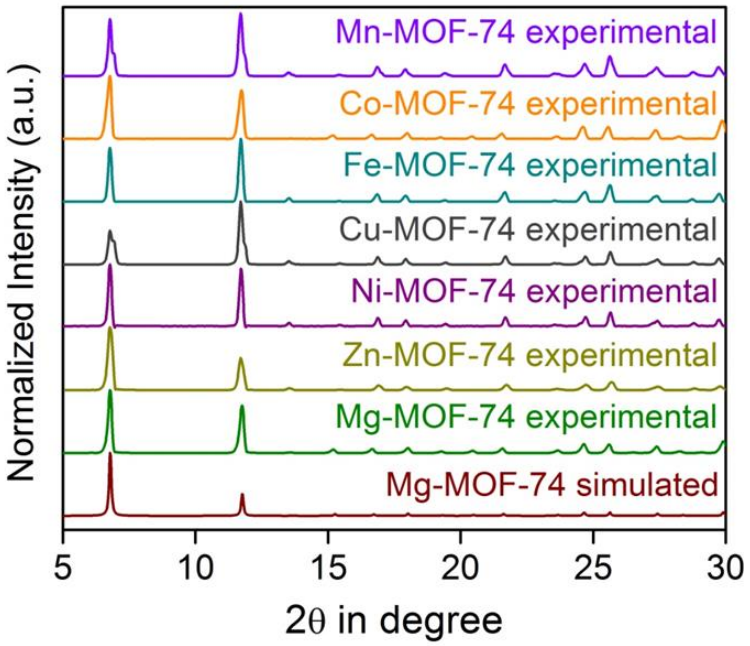

Appendix 3B.3. Similar experimental PXRD profiles for all the seven **M-MOF-74** analogous compounds, plotted relative to the simulated pattern of **Mg-MOF-74**.

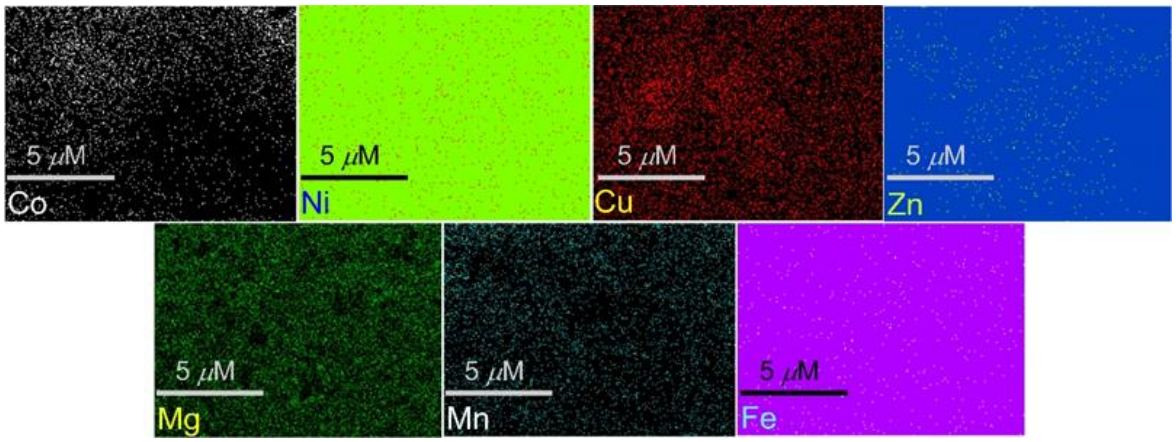

Appendix 3B.4. Elemental mapping (EDX) images of the different metals in cases of the seven **M-MOF-74** compounds.

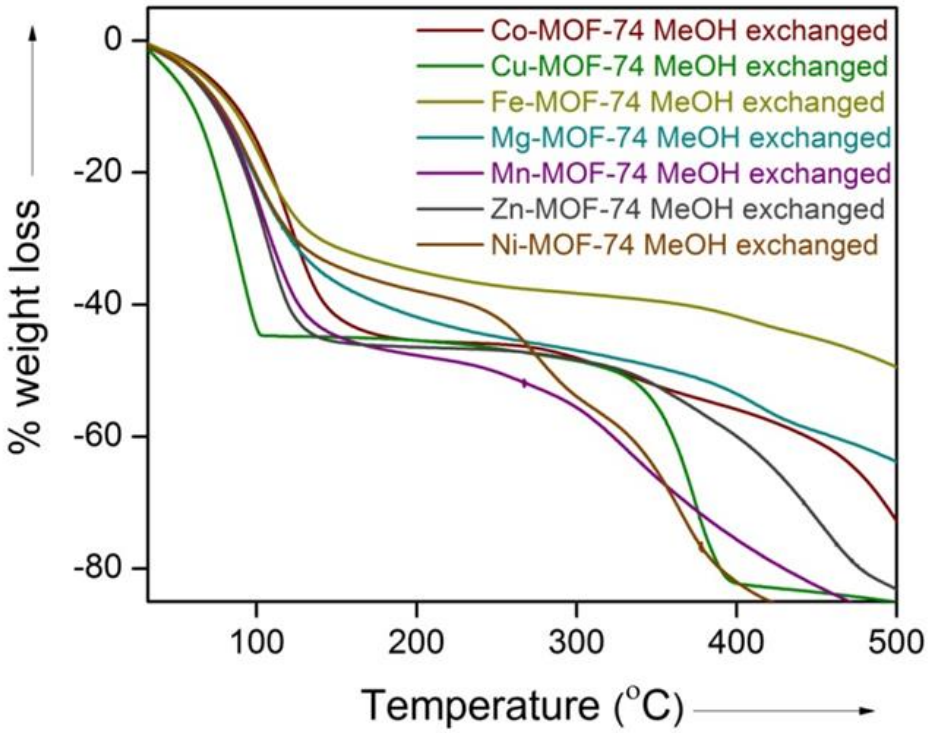

Appendix 3B.5. Thermogravimetric analysis profiles for the MeOH-exchanged phases of **M-MOF-74** compounds.

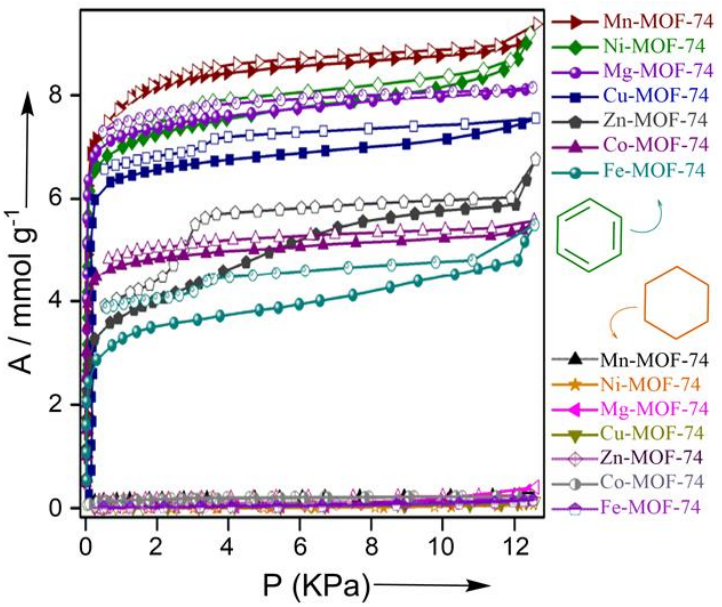

Appendix 3B.6. Single component solvent sorption isotherms (Bz and Cy) for the series of **M-MOF-74** (M= Mg, Mn, Fe, Co, Ni, Cu, Zn) compounds recorded at 298 K (in terms of mmol per g versus P in KPa). Filled and open markers denote adsorption and desorption, respectively.

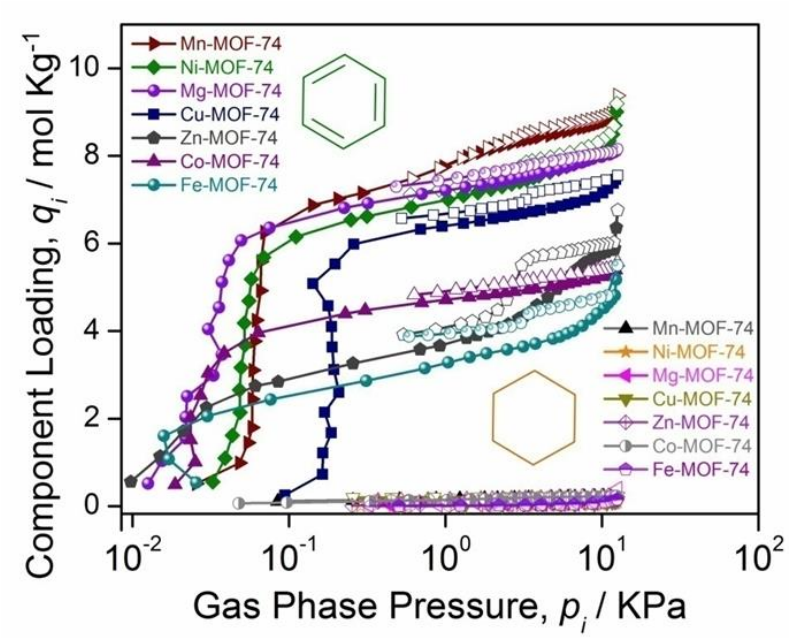

Appendix 3B.7. Comparison of unary benzene isotherms in **M-MOF-74** at 298 K.

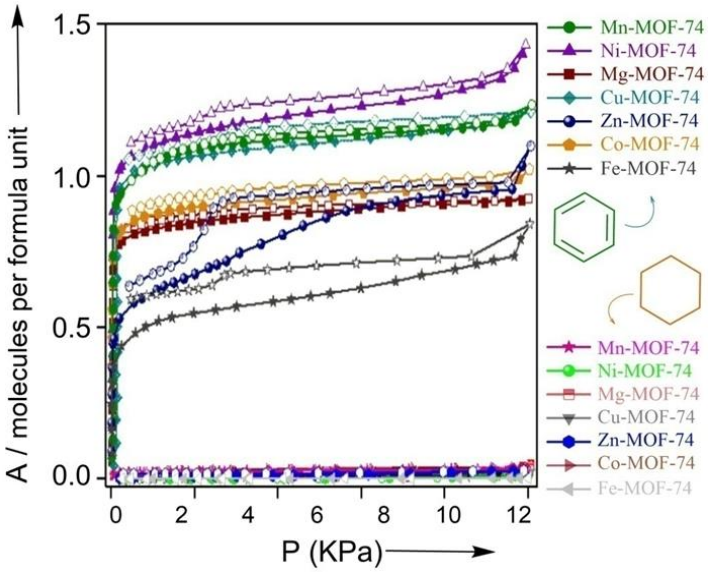

Appendix 3B.8. Single component solvent sorption isotherms (Bz and Cy) for the series of **M-MOF-74** (M= Mg, Mn, Fe, Co, Ni, Cu, Zn) compounds recorded at 298 K (in terms of molecules per formula unit versus P in KPa). Filled and open markers denote adsorption and desorption, respectively.

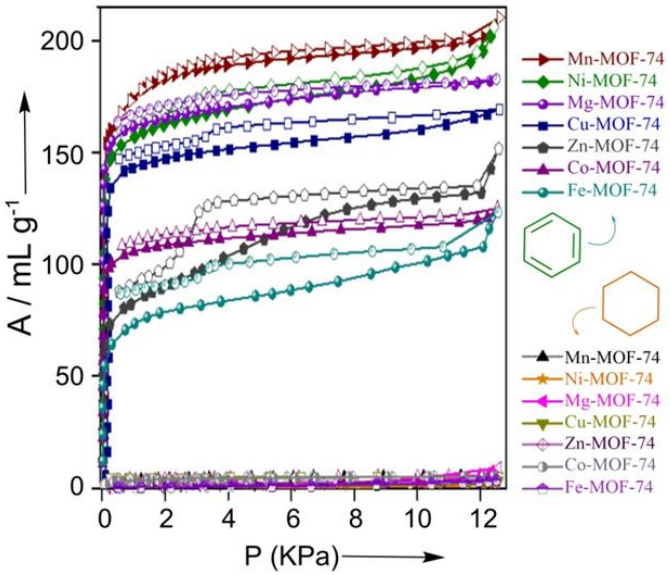

Appendix 3B.9. Single component solvent sorption isotherms (Bz and Cy) for the series of **M-MOF-74** (M= Mg, Mn, Fe, Co, Ni, Cu, Zn) compounds recorded at 298 K (in terms of mL per gram versus P in KPa). Filled and open markers denote adsorption and desorption, respectively.

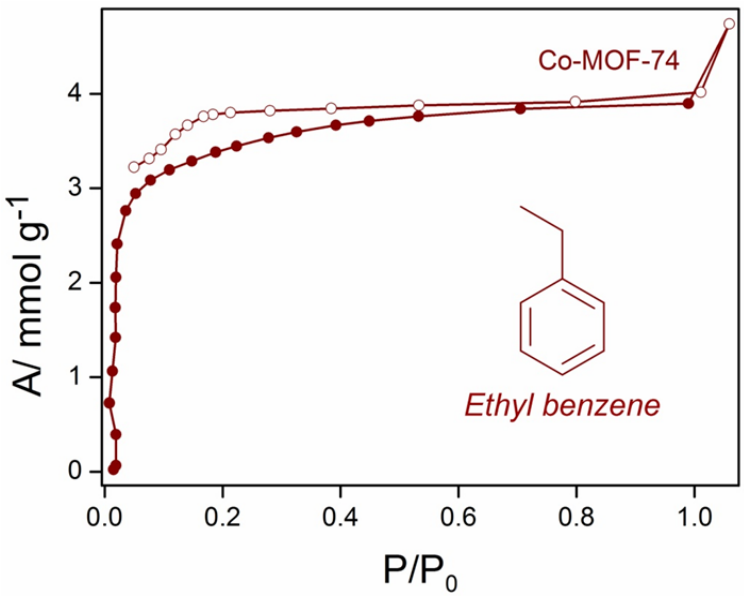

Appendix 3B.10. Single component ethyl benzene sorption isotherm for **Co-MOF-74** (one representative among the series of **M-MOF-74**), recorded at 298 K (in terms of mmol per gram versus P/P_0). Filled and open markers denote adsorption and desorption, respectively.

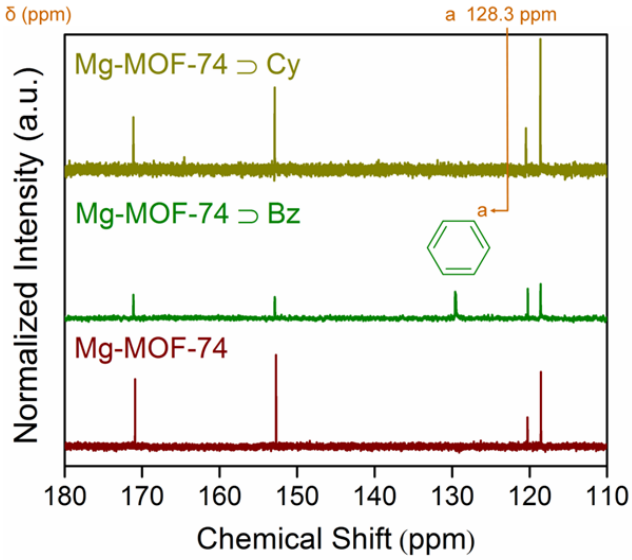

Appendix 3B.11. ^{13}C NMR spectra for Bz and Cy vapor-exposed phases of compound **Mg-MOF-74**, as compared to the desolvated phase itself.

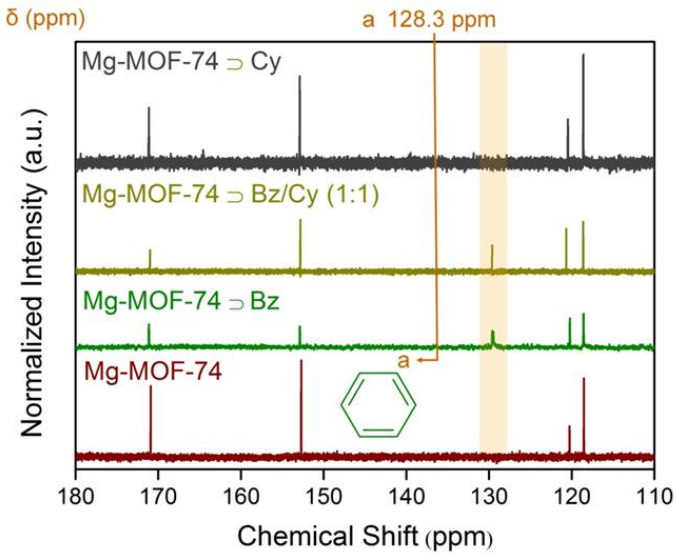

Appendix 3B.12. ^{13}C NMR spectra for 1:1 equimolar mixtures of Bz/Cy exposed phase of **Mg-MOF-74**, as compared to the Bz and Cy vapor-exposed phases of compound **Mg-MOF-74**, and the one for desolvated phase itself.

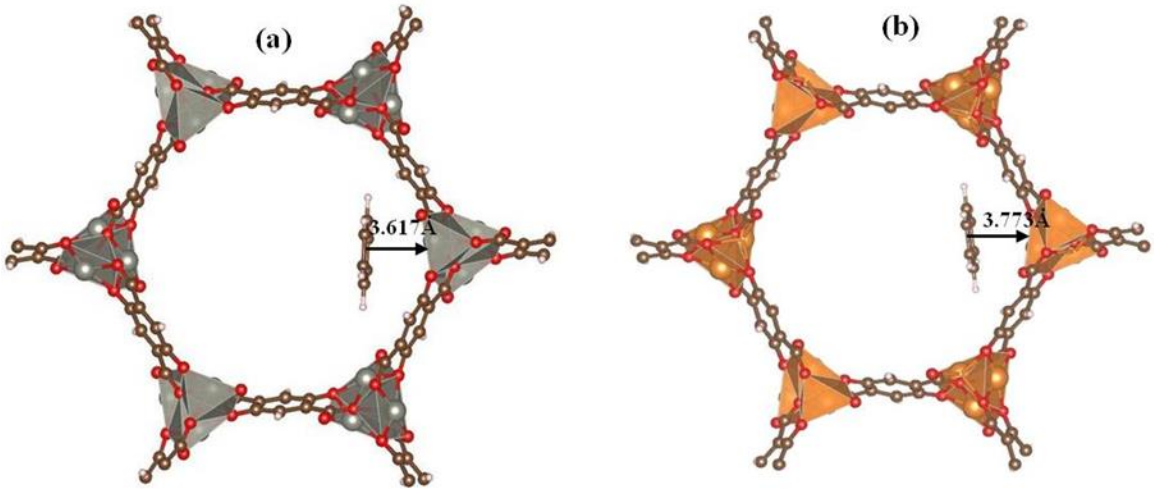

Appendix 3B.13. Location of benzene in (a) **Zn-MOF-74**, and (b) **Mg-MOF-74** identified from NVT simulated annealing method. For clarity the hexagonal cell is cleaved from the supercell to represent the location of guest molecule. The distance between the centriod of benzene and metal ion is shown in angstroms. Similarly for other **M-MOF-74** analogues, we obtained the lowest energy configuration of benzene using simulated annealing method.[32]

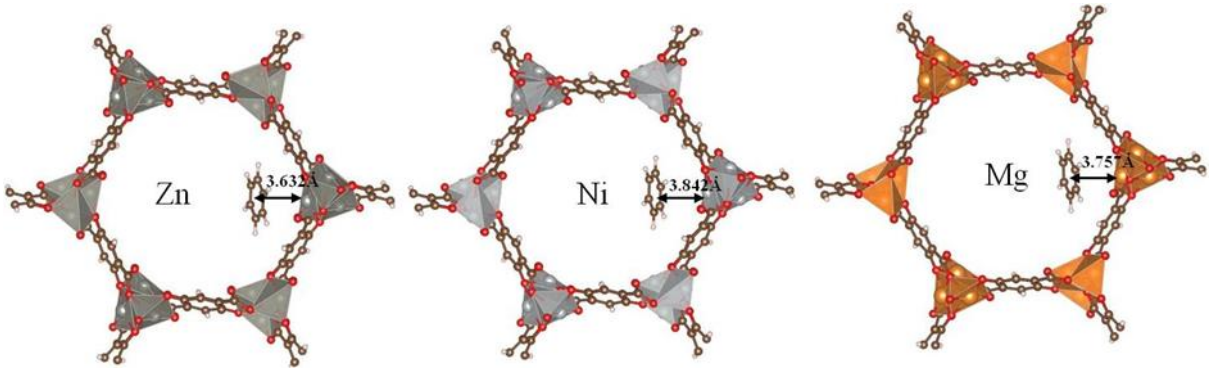

Appendix 3B.14. Optimized location of benzene based on van der Waals density functional in **M-MOF-74** analogues. The distance between the centre of the benzene molecule and the transition metals are shown in angstroms.

Appendix Table 3B.1: Comparative analysis of the saturation uptake amounts recorded for the C_6-hydrocarbon pair Benzene and Cyclohexane in case of all the seven **M-MOF-74** compounds.

Compound	Bz Saturation Uptake Amounts (12.5 KPa) ($mmolg^{-1}$)	Cy Saturation Uptake Amounts (12.5 KPa) ($mmolg^{-1}$)
Mg-MOF-74	8.15	0.40
Mn-MOF-74	9.38	0.25
Fe-MOF-74	5.50	0.15
Co-MOF-74	5.57	0.23
Ni-MOF-74	9.19	0.09
Cu-MOF-74	7.55	0.13
Zn-MOF-74	6.76	0.17

Appendix Table 3B.2: Vdw-DF calculated adsorption energies (in kJ/mol) of a single benzene molecule in **M-MOF-74** analogues.

M-MOF-74	ΔE[a]
Ni-MOF-74	-71.77
Mn-MOF-74	-68.09
Zn-MOF-74	-68.95
Mg-MOF-74	-67.57
Cu-MOF-74	-66.86
Co-MOF-74	-65.49
Fe-MOF-74	-65.31

[a] ΔE refers to the static 0 K adsorption energy.

Appendix Table 3B.3: Three-site Langmuir-Freundlich parameters for adsorption of benzene in **M-MOF-74** at 298 K.

$$q = q_{A,sat}\frac{b_A p^{\nu_A}}{1+b_A p^{\nu_A}} + q_{B,sat}\frac{b_B p^{\nu_B}}{1+b_B p^{\nu_B}} + q_{C,sat}\frac{b_C p^{\nu_C}}{1+b_C p^{\nu_C}}$$

For a binary mixture the adsorption selectivity is defined as follows

$$S_{ads} = \frac{q_1/q_2}{p_1/p_2}$$

	Site A			Site B			Site C		
	$q_{A,sat}$ mol kg^{-1}	b_A $Pa^{-\nu_A}$	ν_A dimensionless	$q_{B,sat}$ mol kg^{-1}	b_B $Pa^{-\nu_B}$	ν_B dimensionless	$Q_{C,sat}$ mol kg^{-1}	b_C $Pa^{-\nu_C}$	ν_C dimensionless
Mn	1	0.00004	1	5.5	1E-25	14	3	0.005	1
Ni	0.5	0.00004	1	4.65	1.2E-25	15	3.2	0.005	1
Mg	0.4	0.00004	1	5.5	1.2E-25	18	2.3	0.005	1
Cu	0.4	0.00001	1	5.1	1E-33	14.5	2.2	0.001	1
Zn	2.3	0.00001	1	2.5	1E-07	6	2.5	0.001	1
Co	0.4	0.00004	1	3.5	1.2E-25	18	1.5	0.005	1
Fe	2.2	0.00001	1	2.3	1E-07	6	2	0.001	1

Appendix Table 3B.4: Two-site Langmuir-Freundlich parameters for adsorption of cyclohexane in **M-MOF-74** at 298 K.

$$q = q_{A,sat}\frac{b_A p^{\nu_A}}{1+b_A p^{\nu_A}} + q_{B,sat}\frac{b_B p^{\nu_B}}{1+b_B p^{\nu_B}}$$

	Site A			**Site B**		
	$q_{A,sat}$ mol kg^{-1}	b_A $Pa^{-\nu_A}$	ν_A dimensionless	$q_{B,sat}$ mol kg^{-1}	b_B $Pa^{-\nu_B}$	ν_B dimensionless
Mn	0.19	0.01	1	0.3	2E-08	1.7
Ni	0.7	0.000001	1	0.2	1E-29	7
Mg	1	0.00001	1	1	1E-46	11
Cu	5	0.000001	1	1	1E-34	8
Zn	0.15	0.0002	1	0.1	0.00004	1
Co	0.14	0.01	1	0.1	0.0002	1
Fe	5	0.000001	1	1	1E-34	8

3.3. References:

1. Reusser, D. E.; Istok, J. D.; Beller, H. R.; Field, J. A., *Environ. Sci. Technol.* **2002,** *36*, 4127-4134.

2. Silva, L. M. C.; Mattedi, S.; Gonzalez-Olmos, R.; Iglesias, M., *J. Chem. Thermodyn.* **2006,** *38*, 1725-1736.

3. Conti, J. J.; Othmer, D. F.; Gilmont, R., *J. Chem. Eng. Data* **1960,** *5*, 301-307.

4. Li, J.-R.; Kuppler, R. J.; Zhou, H.-C., *Chem. Soc. Rev.* **2009,** *38*, 1477-1504.

5. Caro, J., *Curr. Opin. Chem. Biol.* **2011,** *1*, 77-83.

6. Qiu, S.; Xue, M.; Zhu, G., *Chem. Soc. Rev.* **2014,** *43*, 6116-6140.

7. Li, B.; Wang, H.; Chen, B., *Chem. Asian J.* **2014,** *9*, 1474-1498.

8. Zhao, Z.; Ma, X.; Kasik, A.; Li, Z.; Lin, Y. S., *Ind. Eng. Chem. Res.* **2013,** *52*, 1102-1108.

9. Van de Voorde, B.; Bueken, B.; Denayer, J.; De Vos, D., *Chem. Soc. Rev.* **2014,** *43*, 5766-5788.

10. *SAINT Plus*, (Version 7.03); Bruker AXS Inc.: Madison, WI, **2004**.

11. Sheldrick, G. M. *SHELXTL*, *Reference Manual*: version 5.1: Bruker AXS; Madison, WI, **1997**.

12. Sheldrick, G. M. *Acta Crystallogr. Sect. A* **2008**, 112-122.

13. WINGX version 1.80.05 Louis Farrugia, University of Glasgow.

14. Spek, A. L. PLATON, *A Multipurpose Crystallographic Tool*, Utrecht University, Utrecht, The Netherlands, **2005**.

15. Grant Glover, T.; Peterson, G. W.; Schindler, B. J.; Britt, D.; Yaghi, O., *Chem. Eng. Sci.* **2011,** *66*, 163-170.

16. Calleja, G.; Sanz, R.; Orcajo, G.; Briones, D.; Leo, P.; Martínez, F., *Catal. Today* **2014,** *227*, 130-137.

17. Bloch, E. D.; Murray, L. J.; Queen, W. L.; Chavan, S.; Maximoff, S. N.; Bigi, J. P.; Krishna, R.; Peterson, V. K.; Grandjean, F.; Long, G. J.; Smit, B.; Bordiga, S.; Brown, C. M.; Long, J. R., *J. Am. Chem. Soc.* **2011,** *133*, 14814-14822.

18. Cozzolino, A. F.; Brozek, C. K.; Palmer, R. D.; Yano, J.; Li, M.; Dincă, M., *J. Am. Chem. Soc.* **2014,** *136*, 3334-3337.

19. Zhang, Z.; Zhao, Y.; Gong, Q.; Li, Z.; Li, J., *Chem. Commun.* **2013,** *49*, 653-661.

20. Zhang, Z.; Yao, Z.-Z.; Xiang, S.; Chen, B., *Energy Environ. Sci.* **2014,** *7*, 2868-2899.

21. Li, J.-R.; Ma, Y.; McCarthy, M. C.; Sculley, J.; Yu, J.; Jeong, H.-K.; Balbuena, P. B.; Zhou, H.-C., *Coord. Chem. Rev.* **2011,** *255*, 1791-1823.

22. Li, J.-R.; Sculley, J.; Zhou, H.-C., *Chem. Rev.* **2012,** *112*, 869-932.

23. Hu, Z.; Deibert, B. J.; Li, J., *Chem. Soc. Rev.* **2014,** *43*, 5815-5840.

24. Nagarkar, S. S.; Joarder, B.; Chaudhari, A. K.; Mukherjee, S.; Ghosh, S. K., *Angew. Chem. Int. Ed.* **2013,** *52*, 2881-2885.

25. Huxford, R. C.; Della Rocca, J.; Lin, W., *Curr. Opin. Chem. Biol.* **2010,** *14*, 262-268.

26. Horcajada, P.; Gref, R.; Baati, T.; Allan, P. K.; Maurin, G.; Couvreur, P.; Férey, G.; Morris, R. E.; Serre, C., *Chem. Rev.* **2012,** *112*, 1232-1268.

27. Lee, J.; Farha, O. K.; Roberts, J.; Scheidt, K. A.; Nguyen, S. T.; Hupp, J. T., *Chem. Soc. Rev.* **2009,** *38*, 1450-1459.

28. Gascon, J.; Corma, A.; Kapteijn, F.; Llabrés i Xamena, F. X., *ACS Catal.* **2014,** *4*, 361-378.

29. Suh, M. P.; Park, H. J.; Prasad, T. K.; Lim, D.-W., *Chem. Rev.* **2012,** *112*, 782-835.

30. Rowsell, J. L. C.; Yaghi, O. M., *Microporous Mesoporous Mater.* **2004,** *73*, 3-14.

31. Rosseinsky, M. J., *Nat Mater* **2010,** *9*, 609-610.

32. Mukherjee, S.; Joarder, B.; Desai, A. V.; Manna, B.; Krishna, R.; Ghosh, S. K., *Inorg. Chem.* **2015,** *54*, 4403-4408.

33. Mukherjee, S.; Joarder, B.; Manna, B.; Desai, A. V.; Chaudhari, A. K.; Ghosh, S. K., *Sci. Rep.* **2014,** *4*, 5761.

34. Kang, Z.; Xue, M.; Fan, L.; Huang, L.; Guo, L.; Wei, G.; Chen, B.; Qiu, S., *Energy Environ. Sci.* **2014,** *7*, 4053-4060.

35. Li, B.; Wen, H.-M.; Wang, H.; Wu, H.; Tyagi, M.; Yildirim, T.; Zhou, W.; Chen, B., *J. Am. Chem. Soc.* **2014,** *136*, 6207-6210.

36. Li, B.; Wen, H.-M.; Zhou, W.; Chen, B., *J. Phys. Chem. Lett.* **2014,** *5*, 3468-3479.

37. Senkovska, I.; Kaskel, S., *Chem. Commun.* **2014,** *50*, 7089-7098.

38. Herm, Z. R.; Bloch, E. D.; Long, J. R., *Chem. Mater.* **2014,** *26*, 323-338.

39. Herm, Z. R.; Wiers, B. M.; Mason, J. A.; van Baten, J. M.; Hudson, M. R.; Zajdel, P.; Brown, C. M.; Masciocchi, N.; Krishna, R.; Long, J. R., *Science* **2013,** *340*, 960-964.

40. Bai, Y.; Qian, J.; Zhao, Q.; Xu, Y.; Ye, S., *J. Appl. Polym. Sci.* **2006,** *102*, 2832-2838.

41. Shimomura, S.; Horike, S.; Matsuda, R.; Kitagawa, S., *J. Am. Chem. Soc.* **2007,** *129*, 10990-10991.

42. Zhang, J.-P.; Chen, X.-M., *J. Am. Chem. Soc.* **2008,** *130*, 6010-6017.

43. Dong, H.; Yang, X.; Yue, G.; Cao, W.; Zhang, J., *J. Chem. Eng. Data* **2011,** *56*, 2664-2668.

44. Takahashi, A.; Yang, R. T., *AIChE J.* **2002,** *48*, 1457-1468.

45. Barthomeuf, D.; Ha, B.-H., *J. Chem. Soc. Faraday Trans.* **1973,** *69*, 2147-2157.

46. Jeong, B.-H.; Hasegawa, Y.; Sotowa, K.-I.; Kusakabe, K.; Morooka, S., *J. Membr. Sci.* **2003,** *213*, 115-124.

47. Lin, J.-B.; Zhang, J.-P.; Zhang, W.-X.; Xue, W.; Xue, D.-X.; Chen, X.-M., *Inorg. Chem.* **2009,** *48*, 6652-6660.

48. Yang, R.; Li, L.; Xiong, Y.; Li, J.-R.; Zhou, H.-C.; Su, C.-Y., *Chem. Asian J.* **2010,** *5*, 2358-2368.

49. Shimomura, S.; Matsuda, R.; Kitagawa, S., *Chem. Mater.* **2010,** *22*, 4129-4131.

50. Hijikata, Y.; Horike, S.; Sugimoto, M.; Sato, H.; Matsuda, R.; Kitagawa, S., *Chem. Eur. J.* **2011,** *17*, 5138-5144.

51. Ren, G.; Liu, S.; Ma, F.; Wei, F.; Tang, Q.; Yang, Y.; Liang, D.; Li, S.; Chen, Y., *J. Mater. Chem.* **2011,** *21*, 15909-15913.

52. Joarder, B.; Mukherjee, S.; Chaudhari, A. K.; Desai, A. V.; Manna, B.; Ghosh, S. K., *Chem. Eur. J.* **2014,** *20*, 15303-15308.

53. Ren, C.-X.; Cai, L.-X.; Chen, C.; Tan, B.; Zhang, Y.-J.; Zhang, J., *J. Mater. Chem. A* **2014,** *2*, 9015-9019.

54. Karmakar, A.; Desai, A. V.; Manna, B.; Joarder, B.; Ghosh, S. K., *Chem. Eur. J.* **2015,** *21*, 7071-7076.

55. Cheng, J.-Y.; Wang, P.; Ma, J.-P.; Liu, Q.-K.; Dong, Y.-B., *Chem. Commun.* **2014,** *50*, 13672-13675.

56. Hu, T.-L.; Wang, H.; Li, B.; Krishna, R.; Wu, H.; Zhou, W.; Zhao, Y.; Han, Y.; Wang, X.; Zhu, W.; Yao, Z.; Xiang, S.; Chen, B., *Nat Commun* **2015,** *6*.

57. He, Y.; Zhang, Z.; Xiang, S.; Fronczek, F. R.; Krishna, R.; Chen, B., *Chem. Commun.* **2012,** *48*, 6493-6495.

58. Xiang, S.-C.; Zhang, Z.; Zhao, C.-G.; Hong, K.; Zhao, X.; Ding, D.-R.; Xie, M.-H.; Wu, C.-D.; Das, M. C.; Gill, R.; Thomas, K. M.; Chen, B., *Nat Commun* **2011,** *2*, 204.

59. Sun, D.; Ma, S.; Ke, Y.; Petersen, T. M.; Zhou, H.-C., *Chem. Commun.* **2005**, 2663-2665.

60. Sun, D.; Ma, S.; Ke, Y.; Collins, D. J.; Zhou, H.-C., *J. Am. Chem. Soc.* **2006,** *128*, 3896-3897.

61. Sun, D.; Ke, Y.; Collins, D. J.; Lorigan, G. A.; Zhou, H.-C., *Inorg. Chem.* **2007,** *46*, 2725-2734.

62. Ma, S.; Sun, D.; Ambrogio, M.; Fillinger, J. A.; Parkin, S.; Zhou, H.-C., *J. Am. Chem. Soc.* **2007,** *129*, 1858-1859.

63. Ren, H.; Ben, T.; Wang, E.; Jing, X.; Xue, M.; Liu, B.; Cui, Y.; Qiu, S.; Zhu, G., *Chem. Commun.* **2010,** *46*, 291-293.

64. Buckingham, A. D.; Disch, R. L., *Proc. R. Soc. A* **1963,** *273*, 275-289.

65. Millward, A. R.; Yaghi, O. M., *J. Am. Chem. Soc.* **2005,** *127*, 17998-17999.

66. Couck, S.; Denayer, J. F. M.; Baron, G. V.; Rémy, T.; Gascon, J.; Kapteijn, F., *J. Am. Chem. Soc.* **2009,** *131*, 6326-6327.

67. Demessence, A.; D'Alessandro, D. M.; Foo, M. L.; Long, J. R., *J. Am. Chem. Soc.* **2009,** *131*, 8784-8786.

68. McDonald, T. M.; D'Alessandro, D. M.; Krishna, R.; Long, J. R., *Chem. Sci.* **2011,** *2*, 2022-2028.

69. Shimogaki, T.; Dei, S.; Ohta, K.; Matsumoto, A., *J. Mater. Chem.* **2011,** *21*, 10730-10737.

70. Horike, S.; Shimomura, S.; Kitagawa, S., *Nat Chem* **2009,** *1*, 695-704.

71. Serre, C.; Millange, F.; Thouvenot, C.; Noguès, M.; Marsolier, G.; Louër, D.; Férey, G., *J. Am. Chem. Soc.* **2002,** *124*, 13519-13526.

72. Dubbeldam, D.; Krishna, R.; Snurr, R. Q., *J. Phys. Chem. C* **2009,** *113*, 19317-19327.

73. Serre, C.; Bourrelly, S.; Vimont, A.; Ramsahye, N. A.; Maurin, G.; Llewellyn, P. L.; Daturi, M.; Filinchuk, Y.; Leynaud, O.; Barnes, P.; Férey, G., *Adv. Mater.* **2007,** *19*, 2246-2251.

74. Yue, Y.; Rabone, J. A.; Liu, H.; Mahurin, S. M.; Li, M.-R.; Wang, H.; Lu, Z.; Chen, B.; Wang, J.; Fang, Y.; Dai, S., *J. Phys. Chem. C* **2015,** *119*, 9442-9449.

75. Krishna, R., *RSC Adv.* **2015,** *5*, 52269-52295.

76. Webster, C. E.; Drago, R. S.; Zerner, M. C., *J. Am. Chem. Soc.* **1998,** *120*, 5509-5516.

77. Kitagawa, S.; Kitaura, R.; Noro, S.-i., *Angew. Chem. Int. Ed.* **2004,** *43*, 2334-2375.

78. Ameloot, R.; Vermoortele, F.; Vanhove, W.; Roeffaers, M. B. J.; Sels, B. F.; De Vos, D. E., *Nat Chem* **2011,** *3*, 382-387.

79. Pachfule, P.; Shinde, D.; Majumder, M.; Xu, Q., *Nat Chem* **2016,** *8*, 718-724.

80. Chen, Y.-Z.; Wang, C.; Wu, Z.-Y.; Xiong, Y.; Xu, Q.; Yu, S.-H.; Jiang, H.-L., *Adv. Mater.* **2015,** *27*, 5010-5016.

81. Bloch, W. M.; Babarao, R.; Hill, M. R.; Doonan, C. J.; Sumby, C. J., *J. Am. Chem. Soc.* **2013,** *135*, 10441-10448.

82. Qin, J.; Ye, Q.; Xiong, X.; Li, N., *Ind. Eng. Chem. Res.* **2013,** *52*, 10754-10766.

83. Yin, W.; Ding, S.; Xia, S.; Ma, P.; Huang, X.; Zhu, Z., *J. Chem. Eng. Data* **2010,** *55*, 3274-3277.

84. Rosi, N. L.; Kim, J.; Eddaoudi, M.; Chen, B.; O'Keeffe, M.; Yaghi, O. M., *J. Am. Chem. Soc.* **2005,** *127*, 1504-1518.

85. Dietzel, P. D. C.; Morita, Y.; Blom, R.; Fjellvåg, H., *Angew. Chem. Int. Ed.* **2005,** *44*, 6354-6358.

86. Dietzel, P. D. C.; Johnsen, R. E.; Blom, R.; Fjellvåg, H., *Chem. Eur. J.* **2008,** *14*, 2389-2397.

87. Caskey, S. R.; Wong-Foy, A. G.; Matzger, A. J., *J. Am. Chem. Soc.* **2008,** *130*, 10870-10871.

88. Queen, W. L.; Hudson, M. R.; Bloch, E. D.; Mason, J. A.; Gonzalez, M. I.; Lee, J. S.; Gygi, D.; Howe, J. D.; Lee, K.; Darwish, T. A.; James, M.; Peterson, V. K.; Teat, S. J.; Smit, B.; Neaton, J. B.; Long, J. R.; Brown, C. M., *Chem. Sci.* **2014,** *5*, 4569-4581.

89. Bloch, E. D.; Queen, W. L.; Krishna, R.; Zadrozny, J. M.; Brown, C. M.; Long, J. R., *Science* **2012,** *335*, 1606-1610.

90. Bao, Z.; Alnemrat, S.; Yu, L.; Vasiliev, I.; Ren, Q.; Lu, X.; Deng, S., *Langmuir* **2011,** *27*, 13554-13562.

91. Britt, D.; Furukawa, H.; Wang, B.; Glover, T. G.; Yaghi, O. M., *Proc. Natl. Acad. Sci. U.S.A.* **2009,** *106*, 20637-20640.

92. Bae, Y.-S.; Lee, C. Y.; Kim, K. C.; Farha, O. K.; Nickias, P.; Hupp, J. T.; Nguyen, S. T.; Snurr, R. Q., *Angew. Chem. Int. Ed.* **2012,** *51*, 1857-1860.

93. He, Y.; Krishna, R.; Chen, B., *Energy Environ. Sci.* **2012,** *5*, 9107-9120.

94. Hou, X.-J.; He, P.; Li, H.; Wang, X., *J. Phys. Chem. C* **2013,** *117*, 2824-2834.

95. Kim, H.; Park, J.; Jung, Y., *Phys. Chem. Chem. Phys.* **2013,** *15*, 19644-19650.

96. F. A. Cotton, G. Wilkinson, P. L. Gaus in *Basic Inorganic Chemistry*, (Eds: John Wiley and Sons, Inc.) 3rd Ed., **1994**.

97. https://www.ionicviper.org/class-activity/polarizing-power-cations

98. Mahadevi, A. S.; Sastry, G. N., *Chem. Rev.* **2013,** *113*, 2100-2138.

99. Dougherty, D. A., *Acc. Chem. Res.* **2013,** *46*, 885-893.

100. Lee, K.; Howe, J. D.; Lin, L.-C.; Smit, B.; Neaton, J. B., *Chem. Mater.* **2015,** *27*, 668-678.

101. Yi, H.-B.; Lee, H. M.; Kim, K. S., *J. Chem. Theory Comput.* **2009,** *5*, 1709-1717.

102. Henkelman, G.; Arnaldsson, A.; Jónsson, H., *Comput. Mater. Sci.* **2006,** *36*, 354-360.

103. Myers, A. L.; Prausnitz, J. M., *AIChE J.* **1965,** *11*, 121-127.

Chapter 4

An Ultrahydrophobic Fluorous MOF Derived Recyclable Composite As a Promising Platform to Tackle Marine Oil Spills

4.1. Introduction:

Oil and petroleum-based industrial hydrocarbon by-products are one of the exigent energy sources in today's world. The steadily escalating risk concerning the uncontrolled release of toxic pollutants into the environment, particularly involving oil spills, leaks of harmful industrial toxins, is a pressing issue of great concern, since the omnipresent facets of transportation, storage and usage of oil encompass huge clean-up costs worldwide.[1] Remediation of this major environmental issue necessitated the expensive use of large amounts of porous adsorbent materials such as activated carbons, organoclays, cotton fibres, sand, and zeolites.[2-4] Moreover, fabricated functional materials have been found important for preparing efficient oil-absorbing materials, such as mesh/membrane,[5] sponges,[6-8] graphene,[9] microporous polymers,[7] macroporous gels,[10] and cross-linked polymer gels.[6] However, the efficiency of most of these adsorbents is by and large limited by the common issue of moisture-affinity, merged with aqueous instability. Therefore, the quest for highly hydrophobic new-generation porous sorbent materials to be employed as apposite stopgap for tackling detrimental organic spills is regarded as one top-notch agenda with supreme importance.

Over the last two decades, the field of Metal–organic frameworks (MOFs), or Porous coordination polymers (PCPs)[11-13] have witnessed huge strides of constructive development to get established as one of the most promising materials possessing immense practical potential in view of serving a spectra of diverse applications,[14-16] such as gas storage,[17-20] chemical separation,[21-27] sensing,[28, 29] drug delivery,[30, 31] proton conductivity,[32, 33] and catalysis,[34, 35] to name a few. The unmatched popularity of a vast array of such functionalized crystalline porous MOFs stems from their intrinsic long-range order, high surface area, and thermal stability coupled with tunable guest-accessible channel dimension and surface properties.[36-38] The coherent control of the surface properties can be judiciously achieved by rational modulation of the employed linkers and metal nodes or clusters, which eventually serve as constituents of the MOFs.[39, 40] Among the various methods of managing the aforementioned control, linker pre-functionalization approach has been established as one of the key factors behind the modulation of guest-accessible surface properties for MOFs, since the desired affinity between the targeted adsorbed guests and the host framework channels could be astutely tuned with retention of intrinsic crystallinity of the concerned nanoporous MOF materials.[41] Nevertheless, the

advantageous structural features of even some of the best-performing benchmark MOFs readily undergo deterioration, chiefly due to their high moisture-sensitivity and aqueous instability,[42-44] eventually restricting their practical applications. Regarding the attainment of this crucial aspect of moisture-stability, MOFs which feature very strong metal–ligand bonds those are not readily hydrolyzed, or which contain organic struts bearing hydrophobic groups have posed as the most sought-after materials.[45-51]

In general, the major challenge behind serving direct usage-based oil/water separation frontiers lies associated with the inherent difficulty to transfer and recycle the bulk phase adsorbent materials, subsequent to each separation cycle.[52, 53] The necessity to fabricate such superhydrophobic particles/powders on some appropriate substrates, which are recyclable and easily transferable in nature, becomes highlighted in the present scenario. Henceforth, superhydrophobic MOF-coated membranes are anticipated to be exploited owing to the unique convergence of multiple key factors *viz.*, linker-derived superhydrophobicity and oleophilicity characteristics in porous domain, leading to excellent absorption capacity of oil with ample reusability traits (**Scheme 4.1**).

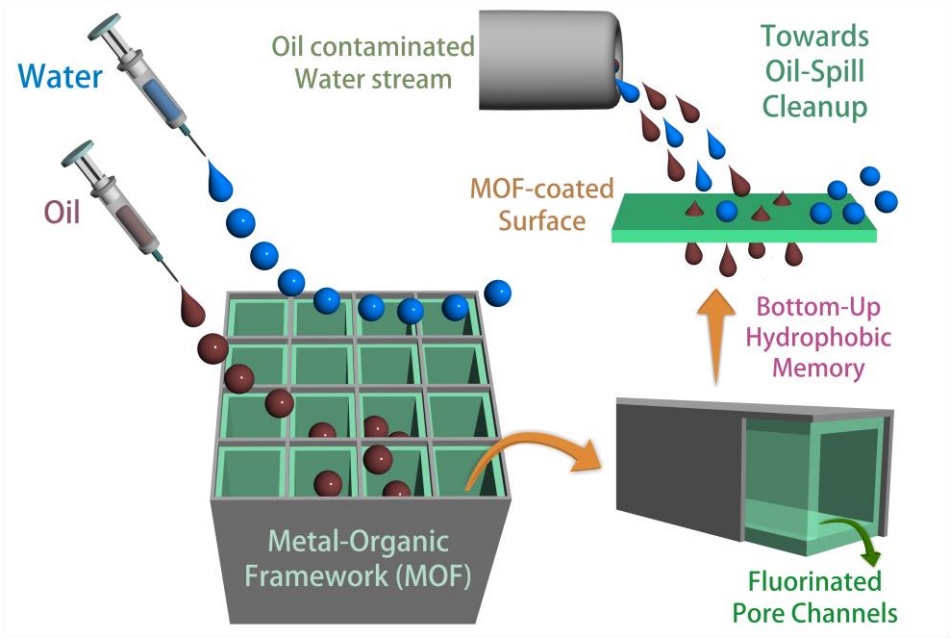

Scheme 4.1. Schematic illustration of fluorinated linker-based predesigned pore surface corrugations, exploited as a potential way-out to render ultrahydrophobicity in MOFs.

The ideal blueprint behind the systematic synthesis of new functionalized MOFs requires careful initial choice of the organic linker component, due to its momentous influence over controlling the chemical and structural properties of the resultant material. Low-symmetry linkers possessing an approximate molecular diameter ~1 nm,[54] are of particular interest because of their well-known role behind forming highly anisotropic networks containing dominant crystal planes, presenting a major contribution of functionalized organic surfaces with nanoscale periodicity. Smaller organic struts often result into porous networks with excellent periodicities in the order of several angstroms (<1 nm), which would eventually lead to surface corrugations, periodic enough to leave a vital impact on the materials contact surface traits with liquid water. If these crucial aspects can be rationally infused into some predesigned fluorinated linker platform, such as, 4,4'-((3,5-bis(trifluoromethyl)phenyl)azanediyl)dibenzoic acid (H_2L, **Appendix 4.1**), it might serve as an ideal candidate for purposefully leading to unprecedented hydrophobic features of the resultant MOF; owing to its low symmetry, molecular dimensions and most undeniably, the tactically introduced fluorinated moieties. Subsequent to a simple two-step synthesis of this new dicarboxylic acid linker, reactivity-based screening with a variety of transition metal ions were performed, which ended up in the synthesis of a typically anticipated highly hydrophobic MOF (hereinafter, denoted as **UHMOF-100**) with stunning surface properties, as revealed in the ensuing discussion. Apart from registering the highest recorded water contact angle in MOF regime (~176°) (**Appendix table 4.1**), it has been proficiently fabricated to a reusable membrane form by spray-coating the MOF crystallites over an inexpensive polypropylene (PP) polymeric support. Due to its strong water-repellent nature, **UHMOF-100** presents high alcohol-water separation performance, validated from its vapor sorption isotherms for the mentioned adsorptives. Much intriguingly, This is the first report of an ultrahydrophobic MOF being exploited in the form of MOF coated hydrophobic polymeric membrane (**UHMOF-100/PDMS/PP**), which exhibits excellent oil absorption capacities and reusability features.

4.2. Experimental Section:

4.2.a. Materials and measurements:

Unless otherwise noted, all the reagents and solvents were commercially available and used without further purification. Solvothermal syntheses were carried out in a Binder

programmable temperature oven (Model: FDL 115), using glass vials sealed with Teflon-lined lids. Powder X-ray diffraction (PXRD) patterns were measured on Bruker D8 Advanced X-Ray diffractometer at room temperature using Cu-Kα radiation (λ= 1.5406 Å) with a scan speed of 0.5° min^{-1} and a step size of 0.01° in 2 theta. Thermogravimetric analysis results were obtained in the temperature range of 30-600 ºC on Perkin-Elmer STA 6000 analyzer under N_2 atmosphere, at a heating rate of 10 ºC min^{-1}. The Fourier transform (FT-IR) infra-red spectra were recorded on NICOLET 6700 FT-IR Spectrophotometer using KBr Pellets. The morphology of the crystalline **UHMOF-100** material was recorded with Zeiss Ultra Plus field-emission scanning electron microscopy (FESEM)-Ultra Plus Field Emission Scanning Electron Microscope with integral charge compensator and embedded EsB and AsB detectors [Oxford X-max instruments 80mm^2. (Carl Zeiss NTS, Gmbh), Imaging conditions: 2 kV, WD = 2mm, 200 kX, Inlens detector]. Contact angles on the **UHMOF-100** pellet and **UHMOF-100/PDMS/PP** fabric (and that of an uncoated PP fabric) were measured by using a contact angle meter (model ID: HO-IAD-CAM-01; Holmarc Opto-Mechatronics Pvt. Ltd.), followed by LBADSA drop analysis (ImageJ software), which is based on the fitting of the Young-Laplace equation to the image data.

4.2.b. X-ray Structural Studies:

Single-crystal X-ray data of compound **UHMOF-100a** was collected at 140K on a Bruker KAPPA APEX II CCD Duo diffractometer (operated at 1500 W power: 50 kV, 1 mA) using graphite-monochromated Cu Kα radiation (λ = 1.5418 Å), mounting on nylon CryoLoop (Hampton Research) with Paraton-N (Hampton Research) oil. The data integration and reduction were processed with SAINT[55] software. A multi-scan absorption correction was applied to the collected reflections. The structure was solved by the direct method using SHELXTL[56] and was refined on F^2 by full-matrix least-squares technique using the SHELXL-97[57] program package within the WINGX[58] programme. All non-hydrogen atoms were refined anisotropically. All hydrogen atoms were located in successive difference Fourier maps and they were treated as riding atoms using SHELXL default parameters. The structure was examined using the *Adsym* subroutine of PLATON[59] to assure that no additional symmetry could be applied to the model.

Crystal data for UHMOF-100a: Formula $C_{109}H_{93}N_{11}O_{23}F_{24}Cu_4$, triclinic, space group *P -1*, *a* = 15.774 (2) Å, *b* = 16.545(2) Å, *c* = 23.383(3) Å, α = 80.170(9), β = 71.168(9), γ =75.394(9), *V* = 5562.6(13) $Å^3$, *Z* = 2, *T* = 140(2) K, *R* = 0.1714, wR_2 = 0.4459, GOF = 1.757. CCDC-1434995 contains the supplementary crystallographic data for this chapter. This data can be obtained free of charge from The Cambridge Crystallographic Data Centre via www.ccdc.cam.ac.uk/data_request/cif

4.2.c. Low Pressure Gas and Solvent Sorption Measurements:

Low pressure gas and solvent sorption measurements were performed using BELSORP-max and BELSORP-aqua3 adsorption analyzers (BEL Japan, Inc.) respectively, both equipped with constant temperature bath. All the gases used were of 99.999% purity, and solvents adhering to HPLC grade. MeCN-exchanged crystals of compound **UHMOF-100** were heated at 85 °C under vacuum for 6 h, to get guest-free crystals of compound **UHMOF-100**. Prior to adsorption measurement, the guest free sample **UHMOF-100** was again pre-treated at 100 °C under vacuum for 4h, using BelPrepvacII, and purged with He on cooling. All solvent sorption measurements were recorded at 298K.

4.2.d. Solvent exposure study:

Crystalline solid powder of compound **UHMOF-100** taken in smaller glass vials were kept open inside larger capped closed glass vials containing different guest solvents (benzene, toluene, ethyl benzene and *p*-xylene respectively) over a period of 72h to allow vapor-phase exposure of solvents and characterized by PXRD.

4.2.e. Membrane-based Experiment; Materials and Methods:

The polymer reactants hydroxy terminated poly(dimethylsiloxane) (HPDMS) of 18,000-22,000 cSt viscosity, polymethylhydrosiloxane (PMHS) of 12-45 cSt viscosity, catalyst dibutyltindilaurate as employed in the cross-linking processes, along with hexadecane were directly procured from Sigma-Aldrich Chemical Co. The other solvents used were obtained from Merck-Chem. Ltd., India. The used PP is commercially available non-woven polypropylene fabric film (Viledon novatexx 2432 ND) of 110 μm thickness. All the chemicals were of analytical reagent grade and used without any further purification.

4.2.e.1. Preparation of polymeric solution:

For the preparation of polymeric solution, the aforementioned reagents HPDMS and PMHS were mixed in toluene solvent. The ratio of the reactants HPDMS and PMHS dissolved in toluene for the cross-linking process was 10:1 (w/w), while 3% (w/w) of catalyst (with respect to total polymer weight) was added in the above solution during the mixing process. The total polymer concentration of the coating solution 1% (w/w) was used to undergo cross-linking reaction in order to form membrane films over a porous polypropylene (PP) support.

4.2.e.2. Preparation of UHMOF-100/PDMS/PP membrane

The polymeric solution and **UHMOF-100** were mixed well, ultrasonicated till 1 hour and allowed to complete cross-linking at 40°C over a span of 45 minutes. An 1:1 (w/w) **UHMOF-100** was taken, with respect to HPDMS. The resulting cross-linked solution was deposited over polypropylene fabric by spray coating technique. Approximately 5ml of the polymeric solution was carefully and homogeneously sprayed over the fabric, followed by immediate evaporation of the extra solvent. In totality, 20 ml of the polymeric solution was gently sprayed over the fabric by repeating the experiment four times, and the sample was dried by keeping it overnight at room temperature in air. Finally, tight cross-linked coating on PP was achieved by heating the coated fabric at 80°C curing for an hour. The schematic representation for the protocol followed herein to prepare **UHMOF-100/PDMS/PP** membrane has been presented in the **Scheme 4.2**.

4.2.e.3. Contact Angle Measurement and AFM

Contact angles on the **UHMOF-100** pellet and **UHMOF-100/PDMS/PP** fabric (and that of an uncoated PP fabric) were measured by using a Contact Angle Meter (Model ID: HO-IAD-CAM-01; Holmarc Opto-Mechatronics Pvt. Ltd.), followed by LBADSA drop analysis (ImageJ software), which is based on the fitting of the Young-Laplace equation to the image data.

The **UHMOF-100/PDMS** was coated over PP by spray coating technique, the formation of cross-linked structured of **UHMOF-100/PDMS** on PP fabric was confirmed by SEM analysis. **Appendicees 4.25A** and **4.25B** shows the SEM images of PP before coating and after coating of **UHMOF-100/PDMS** respectively. From **Appendix 4.25B**, it is evident that the PDMS cross-

linked solution was employed as a binding agent for **UHMOF-100** on PP fabric and extra space on PP fabric was also filled by the PDMS solution to form a cross-linked network.

To check out the hydrophobicity of the prepared membrane sample **UHMOF-100/PDMS/PP**, contact angle (CA) measurements were carried out. For these measurements, a 3×3 cm^2 uniform area of fabric was accurately cut, and gently stuck to a glass plate. The amount of water dispersion on the sample surface was around 4 μl per droplet. The CA measurements were recorded for six consecutive times from different areas of the sample, following which the average CA value was calculated. Similarly, AFM experiment was carried out to check surface roughness of the sample. The average roughness and root mean square roughness (RMS) were calculated using Nova_P9_Ntegra_2.1.0.800 software. For AFM analysis 1×1 cm^2 was cut and dried in a vacuum chamber at 60˚ C for 1 hour. The sample was immediately tested for analysis (results described in **Appendix 4.26** and **Appendix table 4.3**).

4.2.e.4. Sorption Experiment and reusability

Sorption experiments were carried out to check the absorption capacity of different organic solvents such as hexadecane, CCl_4, Bio-diesel, Crude oil and toluene in case of **UHMOF-100/PDMS/PP**. For experiment purpose, coated fabric samples were cut in square shape-uniform units of ~2×2 cm^2, and the initial weight (W_0) were noted (in each of the respective organic solvent-mediated experiments). These were then dipped in the specific solvent for 1 h, after which each of their wet weight (W) values was recorded. The samples in each of the cases were washed thoroughly with acetone, and dried at 60°C under vacuum for 1 h to make them suitable for subsequent use. Recycle tests were carried out for 10 times each to evaluate the reusability of samples. The absorption capacity of pristine **UHMOF-100** was also measured by dispersing the powder in appropriate organic solvent and allowed it to sediment for half an hour. The extra solvent was decanted from the beaker, and the settled wet powder was transferred in clean Petri dish. The wet weight of powder (W) was measured by weight balance. The wet powder was allowed to dry at 80°C for 2 h in oven, and finally, the dry weight (W_0) of powder was measured. The sorption capacity (S) of the sample was calculated by the following equation:

$$S = \frac{(W - W_0) \times 100}{W}$$

Figure 4.4e shows the absorption capacity of **UHMOF-100/PDMS/PP** sample in some typically hydrophobic organic solvents viz. CCl_4, hexadecane, toluene, crude oil, biodiesel. The absorption capacities for crude oil and bio-diesel were found to be around 72 and 51% respectively while CCl_4, hexadecane and toluene came up with absorption capacities of 50, 45 and 41% respectively. The absorption capacity achieved by the MOF-coated fabric sample shows quite a high value as compared to some reported literature reported values. The details of its absorption capacity result, in comparison with other fabric based materials have been provided in the **Appendix table 4.2**. From recycle study as shown in **Figure 4.4f**, it was found that the sample is stable, reusable and oil-absorption capacity of the sample differs slightly even after ten cycles of oil absorption.

4.2.e.5. Oil-water separation experiment

For oil-water separation, the **UHMOF-100/PDMS** coated PP fabric was used as the membrane. A mixture of 10 ml of Hexadecane and 10 ml of water (already coloured with a pinch of methyl orange) were taken in the separating funnel (as shown in the video S2).[60] To further enhance the separation rate, low vacuum (~650 torr) was applied aimed at fast separation. The flux was calculated as according to consider the effective area of membrane around ~8.5 cm^2. Similarly, Toluene/water and Chloroform/water separation was carried out.

As shown in the video S2,[60] the **UHMOF-100/PDMS/PP** membrane could easily separate the organics (all possessing diverse hydrophobicity) from water mixture. The mixture of hexadecane and water were poured on top of the membrane surface. This pouring resulted into the entire hexadecane getting penetrated through the membrane and flowing down to the collection flask underneath, whereas all the water fraction was retained on surface of the membrane. After filtration, no water was found at the collection reservoir, while only clear, transparent oil was visible at the same. This indicates the excellent oil-water separation efficiency of the **UHMOF-100/PDMS/PP**.

Moreover, the membrane retains their high oil-water separation efficiency even after ten consecutive cycles of oil-water separation. 10 ml of hexadecane was separated from 10 mL water within a short span of 1 hour by applying 650 torr vacuum, while with-out vacuum it took 2 hours for attaining such complete separation. The flux of hexadecane/water, toluene/water and CCl_4/water was around 12±1, 75±2 and 85±5 L/(m^2.s) respectively without applying vacuum on the down side.

To test water-in-oil emulsion separation, the water-in-oil emulsions (namely, dichloromethane, toluene and hexadecane separately) were prepared by mixing water and oil in 1:9 v: v, with triton-x 100 surfactant (0.1-0.4 $g.L^{-1}$) and sonicated for 2h in order to prepare white milky emulsion (for all three solvents). The permeate flux (productivity flux in volume/area/time) of water-in-oil emulsions were around 30 ± 2, 115 ± 3 and 172 ± 2 L/(m^2.s) for hexadecane, toluene and DCM respectively in water-oil emulsion.

4.2.f. Simulation details:

The ESP charges for the system were calculated for a small segment of the crystal structure using Hartree-Fock theory with 6-31G* basis set using Gaussian 09[61] program package. Dreiding force field[62] parameters and GROMACS[63] software packages have been used for running the simulations. The crystal structure coordinates were used at the starting of the simulation and the structure was solvated using TIP4P/2005[64] water model. The box dimensions were chosen in such a way that there was a 10 Å layer of water around the crystal structure. We have kept the Cu and oxygen atoms of the crystal structure frozen during the simulation in order to maintain same distances between these atoms. The system was energy minimized using steepest descent method[65] followed by heating up to 300 K using Berendsen thermostat[66] with a coupling constant of 0.2 ps. The system was equilibrated for 1 ns at constant temperature 300 K and constant pressure 1bar using Nosé-Hoover thermostat[67, 68] and Parrinello-Rahman barostat[69] with a coupling constant of 0.2 ps for each. Electrostatic interactions were treated using PME electrostatics[70] with 10 Å cut-off. Van der Waals cut-off was set to 10 Å. A final molecular dynamics run of 2 ns was carried out for the system under NVT condition with similar treatment of temperature, electrostatics and vdW as in final equilibration.

Analysis details: For the snapshot, we have taken a slice of our whole simulation box so that the location of the water molecules can be compared before and after the equilibration. For calculation of the number density around a particular group, we have used the method for calculating radial distribution function. In our case, the system is not spherical and has modifications at the terminals, hence we used the method for calculating proximal radial distribution function (PRDF)[71] of water molecules around different sites. This method measures water distribution perpendicular to the local surface of a site.[72] For our purpose, we have selected the more exposed $–CF_3$ groups atoms and the inner atoms separately and calculated the PRDFs by utilising a faster grid-based algorithm proposed by Makarov *et al.*[73] By multiplying the PRDF value with the value for bulk water number density, we get the number density of water around these groups.

4.3. Synthetic Protocol:

4.3.a. Synthesis of Intermediate L':

3,5-bis(trifluoromethyl)aniline (5 g, 22 mmol), 4-fluorobenzonitrile (6.1 g, 50 mmol) and cesium fluoride (~10 g, 66 mmol) were refluxed at 170 °C in N, N-dimethylformamide (DMF) (250 mL) for a span of 48 h. After cooling the reaction mixture to r.t., it was poured into ~500 mL ice-cold water, which yielded light brown-colored precipitation. This was filtered under vacuum, washed well with water, and this crude product was recrystallized from methanol to obtain the brown-colored intermediate compound L'. Yield: 7.6 g, ~81%.^{1}H NMR (400 MHz, DMSO-d_6) (**Appendix 4.3**): δ 7.0 (s, 1H), 6.9 (m, 6H), 6.3 (m, 4H); ^{13}C NMR (100 MHz, DMSO-d_6) (**Appendix 4.4**): δ 149.0, 146.7, 134.0, 132.1, 131.8, 131.5, 126.1, 124.1, 123.9, 121.4, 118.6, 106.1; HRMS (**Appendix 4.2**): Calc. for $C_{22}H_{11}F_6N_3$ $[M+H]^+$: 432.0935; Found: 432.948. Elemental Analysis: Anal. Calcd for $C_{22}H_{11}F_6N_3$: C, 61.26; H, 2.57; N, 9.74. Found: C, 61.19; H, 2.60; N, 9.69.

4.3.b. Synthesis of Ligand LH_2:

A mixture of L' (7.5 g, 17 mmol) (**Appendix 4.1**) and potassium hydroxide (3.82 g, 68 mmol) was refluxed in 200 mL water/ ethanol (1:1) solvent mixture for 24 h. After the reaction mixture was allowed to cool to r.t., it was acidified by dil. HCl keeping on an ice bath till pH ~5.

The precipitated product LH_2 was conveniently filtered out, followed by thorough washing with cold water. Yield: 5.88 g, ~72%. ^{1}H NMR (400 MHz, DMSO-d_6) (**Appendix 4.6**): δ 7.9 (m, 4H), 7.8 (s, 1H), 7.6 (s, 2H), 7.2 (m, 4H); ^{13}C NMR (100 MHz, DMSO-d_6) (**Appendix 4.7**): δ 166.6, 149.3, 147.9, 131.9, 131.7, 131.3, 126.5, 124.3, 123.8, 121.6. HRMS (ESI) (**Appendix 4.5**): Calc. for $C_{22}H_{13}F_6NO_4$ $[M+H]^+$: 470.0826; Found: 470.0819. Elemental Analysis: Anal. Calcd for $C_{22}H_{13}F_6NO_4$: C, 56.30; H, 2.79; N, 2.98. Found: C, 55.96; H, 2.84; N, 3.02.

4.3.c. Synthesis of $[\{Cu_4L_4(DMF)_4\}.(DMF)_3]_n$ (UHMOF-100a):

A mixture of H_2L (23 mg, 0.05 mmol), $Cu(NO_3)_2.3H_2O$ (12.1 mg, 0.05 mmol), DMF (2 mL) and water (1 mL) was placed in a teflon capped glass vial. This was heated at 90 °C for 48h and then slowly cooled to room temperature over the next 24h. Growth of green, block-shaped crystals was observed upon cooling to RT, the desired product $[Cu_4L_4(DMF)_4]$ (**UHMOF-100a**) appeared in ~76% yield (with respect to metal). Elemental analyses: Anal. Calcd (found) for compound **UHMOF-100a** ($C_{109}H_{93}Cu_4F_{24}N_{11}O_{23}$): C, 49.69 (49.27); N, 5.85 (6.02); H, 3.56 (3.59).

4.3.d. Synthesis of guest-free phase (UHMOF-100):

Slightly pale green polycrystalline phase **UHMOF-100** were obtained on heating the MeCN-exchanged (exchanged twice a day, over a period of 7days) phase of **UHMOF-100a** at 85 °C under reduced pressure for ~6h. Elemental analyses: Anal. found for compound **UHMOF-100**: C, 49.82; N, 2.59; H, 2.14. Anal. Calcd for DMF-removed predicted formula $[\{Cu_4L_4\}_n]$: C, 49.78; N, 2.64; H, 2.09.

4.4. Result and discussions:

Crystalline compound $[\{Cu_4L_4(DMF)_4\}.(DMF)_3]_n$ (**UHMOF-100a**) was synthesized by the solvothermal reaction of $Cu(NO_3)_2{\bullet}3H_2O$ with fluorinated H_2L (syntheses and characterization: **Appendices 4.1-4.7**) (**Appendices 4.8** and **4.9**). Single-crystal X-ray diffraction (SC-XRD) studies disclosed that the solvated framework **UHMOF-100a** possesses an archetypal

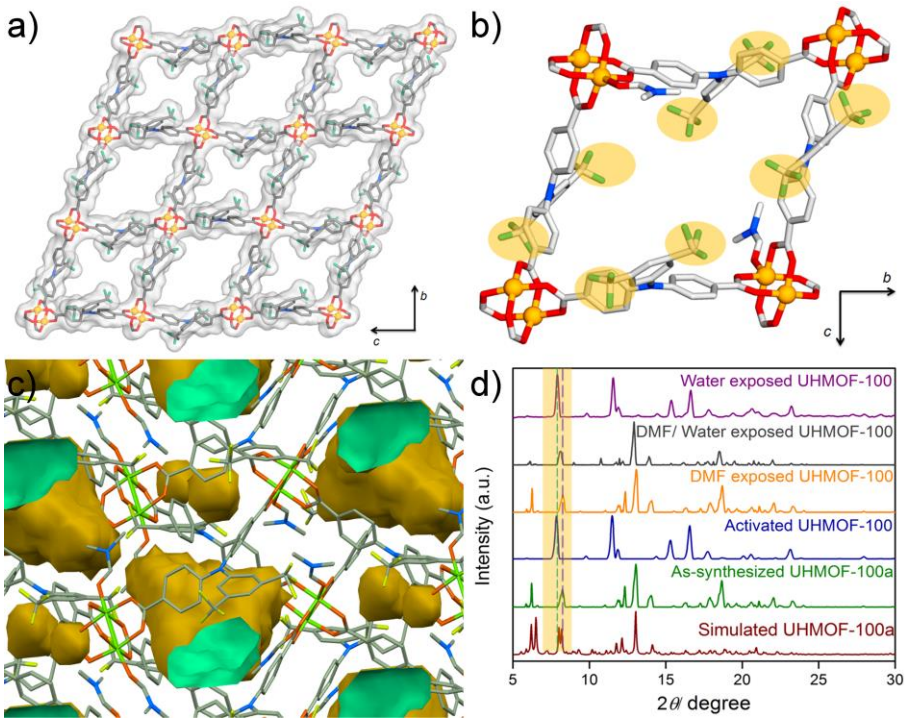

Figure 4.1. a) Orthographic surface view of as-synthesized **UHMOF-100a**; b) single fluorous pore of **UHMOF-100**; c) decorated fluorous voids' connolly surface; d) PXRD profiles for different phases of **UHMOF-100**, validating soft porous crystallinity and water stability.

two-dimensional layered structure (**Appendices 4.17-4.19**) (**Appendix Table 4.4**), with typical paddle-wheel motifs. Analysis of each of the individual layers of the 2D-sheet framework structure revealed periodic arrangement of nanopores (~7.2 × 6.7 $Å^2$; considering a single net) along crystallographic *a*-axis (**Figures 4.1a**, **4.1b**, and **Appendices 4.17-4.19**) with the bis(trifluoromethyl) moieties well-decorating the porous channels. Such fluorine-rich arrangement in the nanospace should ideally facilitate strong interactions with the hydrophobic guests and parallely impart strong water-repellent surface corrugations. The phase purity for the as-synthesized phase was established from the PXRD analysis (**Figure 4.1d**) along with the SC-XRD-based unit cell examination of randomly selected crystals (**Appendix 4.9**).

Although the individual layers are relatively dense (**Appendices 4.18**, **4.19**), the voids (10.6% of unit cell volume; ~591 $Å^3$, considering probe radius 1.2 Å and grid spacing ~0.7 Å) produced between the parallely running layers seem adequately large to accommodate the desired guest species (**Figure 4.1c**). Thermogravimetric analysis profile (**Appenidix 4.10**) for

this as-synthesized phase suggests that coordinated and free DMF guest molecules occluded inside **UHMOF-100a** (**Appendix 4.9a**) can be removed by MeCN-exchange protocol, followed by heating (see **Appendix section**), to obtain the slightly pale green desolvated crystals of compound **UHMOF-100** (**Appenidix 4.9b**). This activated guest-free phase (**Appendix 4.10**) with high crystallinity and thermal stability, recorded a distinct PXRD profile (**Figure 4.1d** and **Appendix 4.15**) relative to the pristine MOF. Such framework dynamism might be attributed to the phase shift concurrent with the loss of coordinating DMF molecules, leading to the generation of coordinatively unsaturated Cu(II) open metal sites (OMS), accompanied with quite an anticipable slippage of the constituent 2D layers (**Appendix 4.16**). Interestingly, the claimed generation of OMS perfectly corroborates with the PXRD for DMF exposed phase of **UHMOF-100**, which in fact, entirely reverts back to the **UHMOF-100a** PXRD, validating reversible framework dynamism.[74-77] In spite of prolonged water and steam exposure to **UHMOF-100**, the PXRD patterns for water-soaked **UHMOF-100** (**Figure 4.1d**, **Appenidix 4.12**) is found precisely identical to the water untreated sample. This indicates that **UHMOF-100** entirely retains framework-integrity post-water treatment, leading to concomitant absence of any dynamic phase shift, as observed in the cases of DMF and DMF/water (1:1) (**Figure 4.1d**).

Permanent porosity of activated **UHMOF-100** was confirmed by N_2 adsorption–desorption isotherms at 77 K which show a reversible type-I isotherm (**Figure 4.2a**). The calculated Langmuir and Brunauer–Emmett–Teller (BET) surface area based on the low-pressure region (P/P_0 = 0.05–0.2) N_2 adsorption dataset are 660.1 and 469.2 m^2g^{-1} respectively, while the total pore volume calculated from the N_2 isotherms is 1.07 cm^3g^{-1} with an effective pore diameter of ~5.9 Å (Inset: **Figure 4.2a**). Even the low pressure CO_2 adsorption isotherm recorded at 195K showed a steady type-I uptake of ~411 mLg^{-1} (**Appendix 4.13**), thus indicating that **UHMOF-100** has modest porosity and guest-accessible voids (**Figure 4.2c**) available for guest inclusion. The permanent porosity of **UHMOF-100** permits potential access to an entire array of organic vapor molecules, particularly the most common oil components embodied by C_6–C_8 hydrocarbons like benzene (BZ), ethyl benzene (EB), toluene (TL), and *p*-xylene (PX).[78] The mentioned vapor adsorptives sorption isotherms were recorded at 298 K, as shown in **Figure 4.2b**, featuring stepwise uptake for each of these hydrophobic solvents. On the contrary, water adsorption isotherm showed no uptake at all. While the high hydrophobic solvent species' uptake

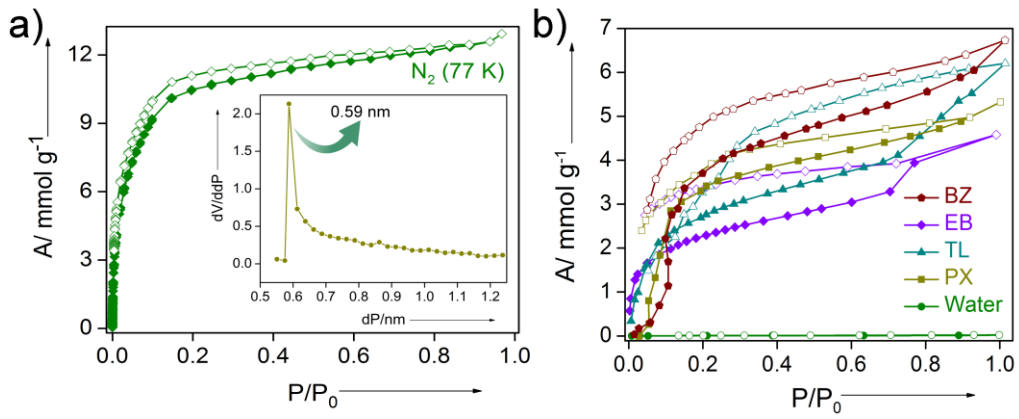

Figure 4.2. a) Type-I N_2 adsorption isotherm recorded at 77K indicating nanoporous nature of the adsorbent (Inset: pore size distribution plot); b) oil's constituent hydrocarbon vapors' sorption isotherms plotted in comparison to water sorption profile.

poses as a sign of strong host–guest interactions through confinement effects for aromatic adsorbates, the contrasting nature of water sorption highlighted extreme water-repellent nature of the voids. Similar trend was also noted in case of coordinating guest adsorptive species like methanol and ethanol, which show quite high saturation uptakes (**Appendix 4.14**), on the contrary to water uptake. Again, this might be attributed to the hydrophobic pore surface characteristics of **UHMOF-100**.

Notably enough, the pristine linker (H_2L) surface registered a moderately high WCA ~136° (**Appendix 4.21**). To examine the influence of such distinct pore surface hydrophobicity on the actual surface property of bulk crystalline phase, contact angle(CA) measurements were performed on **UHMOF-100** (in pellet form), which reproducibly registered an unprecedented high value of WCA ~176° (**Figure 4.4b**, and **Appendices 4.22-4.23**); even higher than the only few recent reports on superhydrophobic MOFs (**Appendix table 4.1**),[45, 47, 49, 79-82] with petite WCA hysteresis (difference between the advancing and receding contact angles) of ~2-4°], therefore marking it as the first ultrahydrophobic MOF. Furthermore, analogous CA measurement with an oil droplet carefully incident on **UHMOF-100** presented CA ~0° (**Appendix 4.22**), indicating superoleophilicity, as a coexisting property with ultrahydrophobicity. The unprecedented water-repellent characteristics could be better realized when water droplets were attempted to be carefully cast on the solid MOF surface, resulting in

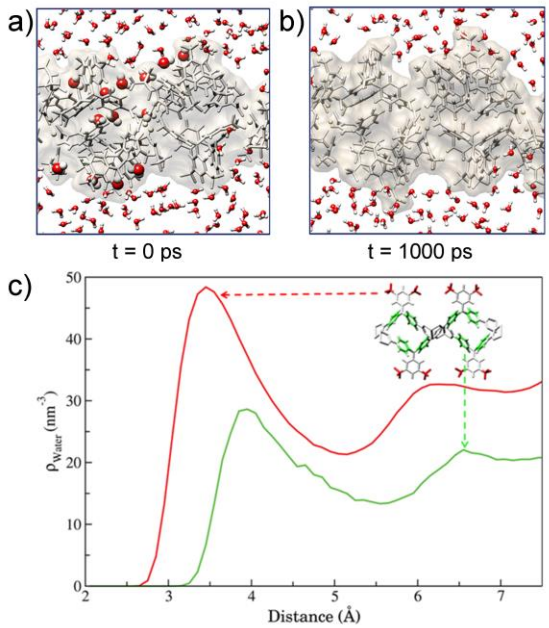

Figure 4.3. Snapshots for simulation system of **UHMOF-100** at two different times: a) at the beginning of simulation; b) at the end of 1000 ps equilibration. Water molecules inside the voids are shown bigger, while other water molecules are shown by ball and stick model; c) water number density plot around the simulated system: red line indicates water number density around the $–CF_3$ groups (red), while green line indicates water number density around the carbon atoms (green).

immediate jumping away of the same (attached video S1).[60] To the best of our knowledge, such extreme repercussion of MOF surface to incident water droplets suggestive of remarkably low surface free energy is not yet reported in literature, and leaves enough scopes of further development.[83]

To gain an even better insight into the remarkable water-repellent surface characteristics, and to also find out the precise behavior of water molecules in the close proximity of the bis(trifluoromethyl)-decorated porous voids of **UHMOF-100**, between water molecules and **UHMOF-100**; all atom MD simulation with a small section of the total structure has been performed. The initial coordinates were taken from the crystal structure and the end portion of our structure was terminated by replacing the carboxyl groups with hydrogen atoms. (Other simulation details are provided in the experimental section). It has been found that although few water molecules initially (at 0 ps) remain inside the cavities of the system, after 1000 ps of simulation under NPT condition, these water molecules leave entirely, since the inner

trifluoromethyl-decorated void nanospace comes up with complete absence of water molecules as shown in **Figures 4.3a** and **4.3b**. To investigate the water arrangement near the system, the number densities of water in the vicinity of different groups of atoms have been calculated. Since the concerned simulated system herein, is not a continuous one and has been modified at the terminals, the calculation solely considers water density near the $–CF_3$ groups (labeled red) and the inner carbon atoms (labeled green) shown in **Figure 4.3c**, which represents the water molecules present near the more exposed fluorine atoms on the surface and the inner carbon atoms of the ligand. It is observed that the maximum value for water density near the $–CF_3$ group is similar to the literature-reported values near hydrophobic self-assembled monolayers,[84] but the density near the inner atoms has been found to be significantly smaller compared to the exposed atoms. This evidently indicates that the $–CF_3$ groups on the surface prevent water molecules to enter inside the voids of **UHMOF-100**, resulting in the strikingly lower water density around the aforementioned inner atoms.

Enthused from all these revelations, a first-of-its kind approach was introduced to fabricate an ultrahydrophobic MOF material into a recyclable coated membrane form by virtue of spray-coating technique (**Scheme 4.2**). PP fabric, a kind of soft and flexible inexpensive polymer material, is also considered as a good candidate for oil/water separation after various post-treatments and its native porosity ensures the free passage of liquids.[85-87] **UHMOF-100** was well-dispersed in PDMS cross-linked solution and it was successfully fabricated on polypropylene support by spray coating technique (**Scheme 4.2**). Herein, The PDMS cross-linked solution was employed as a binding agent for **UHMOF-100** on PP fabric. The prepared **UHMOF-100/PDMS** coated PP fabric, hereinafter denoted as **UHMOF-100/PDMS/PP** (**Figures 4.4c**, **4.4d**), was used for the targeted real time oil/water separation (see video S2 file),[60] with excellent recyclability and absorption capacity. (The exact details of sample preparation and characterization are elaborately provided in the experimental section).

The prepared **UHMOF-100/PDMS/PP** membrane recorded WCA ~135˚ (**Appendix 4.24**), which indicates substantially high hydrophobic nature of the fabricated MOF membrane. Generally, PDMS film (**Appendix 4.24**) shows CA around 109˚,[88] while the enhancement in WCA for **UHMOF-100/PDMS/PP** sample can be ascribed to the addition-mediated coating of **UHMOF-100** in PDMS matrix. While SEM analyses on this water-repulsive membrane

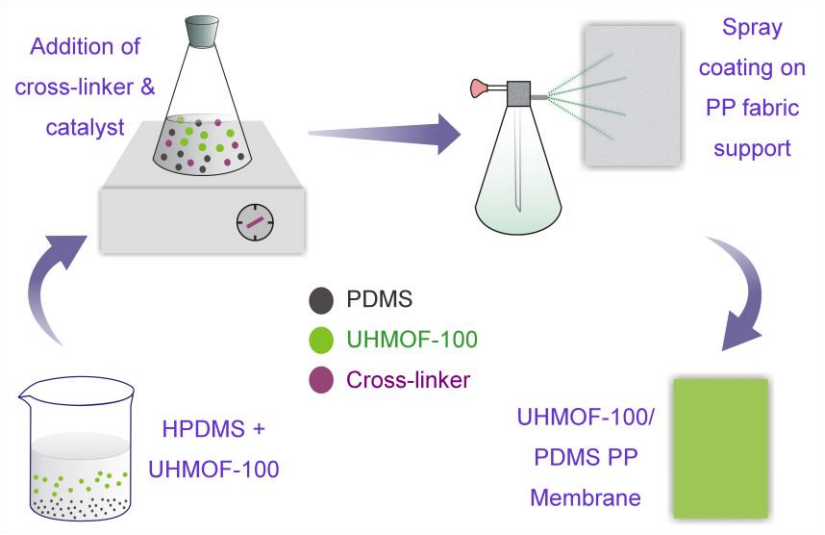

Scheme 4.2. Schematic illustration of the fabrication protocol followed during the coating of **UHMOF-100** onto PP fabric, to lead to the reusable form **UHMOF-100** coated membrane **UHMOF-100/PDMS/PP**.

(**Appendix 4.25**) reveal cross-linked hierarchical microstructures, AFM measurements divulge the surface roughness values for the **UHMOF-100** coated membrane surface (two different areas) (**Appendix table 4.3**); quite likely pointing out to a smooth "reentrant texture" coated fibre surface, with the mentioned values falling in nanometer scale (**Appendix 4.26**). **UHMOF-100/PDMS/PP** membrane was tested for determining the absorption capacities of different organic solvents, particularly hydrophobic ones, well-recognized as oil constituents', such as hexadecane, CCl_4, bio-diesel, crude oil and toluene. The sample was also tested for real time volumetric oil/water (1:1) separation, which showed its excellent oil-water separation capacity (see video S2 file).[60] Owing to its intrinsic water-repellency, the entire water portion (colored with methyl orange) was retained at the top of the filtering **UHMOF-100/PDMS/PP** membrane; while the whole oil fraction from initial 1:1 oil/water mixture passed quantitatively through the membrane within a short span of 1.5 h, even in the absence of any externally applied vacuum. It was verified that the prepared **UHMOF-100/PDMS/PP** membrane is air-stable, moisture insensitive, reusable and oil-absorption capacity of the sample differs almost negligibly (**Figures 4.4e** and **4.4f**), even after ten consecutive cycles of oil absorption. To the best of our knowledge, this marks the first report of any super/-ultrahydrophobic MOF based composite material being exploited for oil/water separation purpose.[89] The recorded absorption capacity (~40-70 wt%)

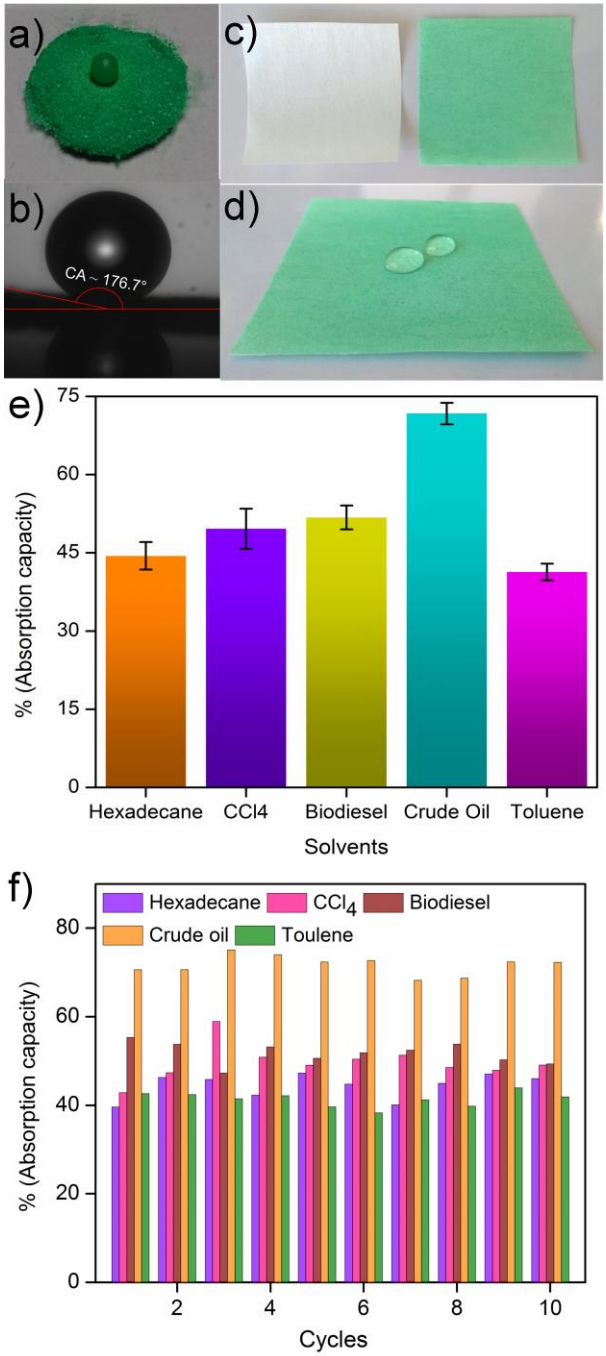

Figure 4.4. Water droplet suspended on **UHMOF-100** crystallites: naked eye proof of ultrahydrophobicity; b) image of a water drop slowly cast on the water-repellent surface of **UHMOF-100** pellet with CA ~176°, resembling mercury-like droplets; c) photographs of PP (white) and **UHMOF-100/PDMS/PP** (green); d) water droplets drop-casted on **UHMOF-100/PDMS/PP**; e) and f) bar diagram representation of the absorption capacities and recycle tests on **UHMOF-100/PDMS/PP**.

and flux (85±5 $Lm^{-2}s^{-1}$) ranks **UHMOF-100/PDMS/PP** among the best membrane/fabric based materials known for oil–water separation (**Appendix table 4.2**).[3] To test the water-in-oil emulsion separation capability of **UHMOF-100/PDMS/PP**, a series of water-in-oil emulsions prepared in different types of solvents, viz. DCM, toluene, and hexadecane were prepared. The water-in-oil emulsion was prepared by using triton X-100 surfactant, with uniform size of emulsion droplets in micro meter scale (**Appendix 4.27**). The as-prepared emulsions werepoured onto upper side of the **UHMOF-100/PDMS/PP** membrane. Oil components immediately permeated through the membrane; meanwhile, emulsion droplets demulsified on merely touching the membrane, while water was wholly retained above (see video S3 for observing the demulsification process of the emulsion on the **UHMOF-100/PDMS** coated PP membrane).[60] The water-in-oil emulsion separation process is totally driven by gravity without any external force, and is recyclable in nature.

4.5. Conclusion:

In a nutshell, apart from achieving extreme ultrahydrophobic features, like the highest water contact angle coupled with the intriguing aspects of stern water-repellence and contrasting water/hydrocarbon, water/alcohol vapor sorption isotherms; the bis(trifluoromethyl)-based linker derived fluorous coordination nanospace of **UHMOF-100** has been exploited for achieving oil/water separation, with substantial oil (hexadecane, bio-diesel, toluene, CCL_4 and crude oil) absorption capacities and recyclability traits. Such recyclable, reusable, ultrahydrophobic MOF adsorbent coated membrane has been fabricated for the first time, and has also been cogently investigated for oil/water separation possibilities.[90-94] This report might indeed prove crucial behind the development of new-generation, commercially viable inroads through the direct utilization of water-repellent super-/ultrahydrophobic MOF materials, behind addressing the globally challenging issue of marine oil spills.

4.6. Appendix Section:

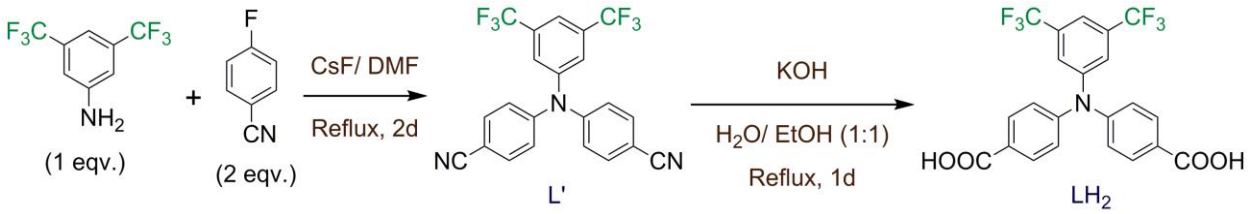

Appendix 4.1. Synthesis of dicarboxylic acid ligand LH_2 via intermediate L'.

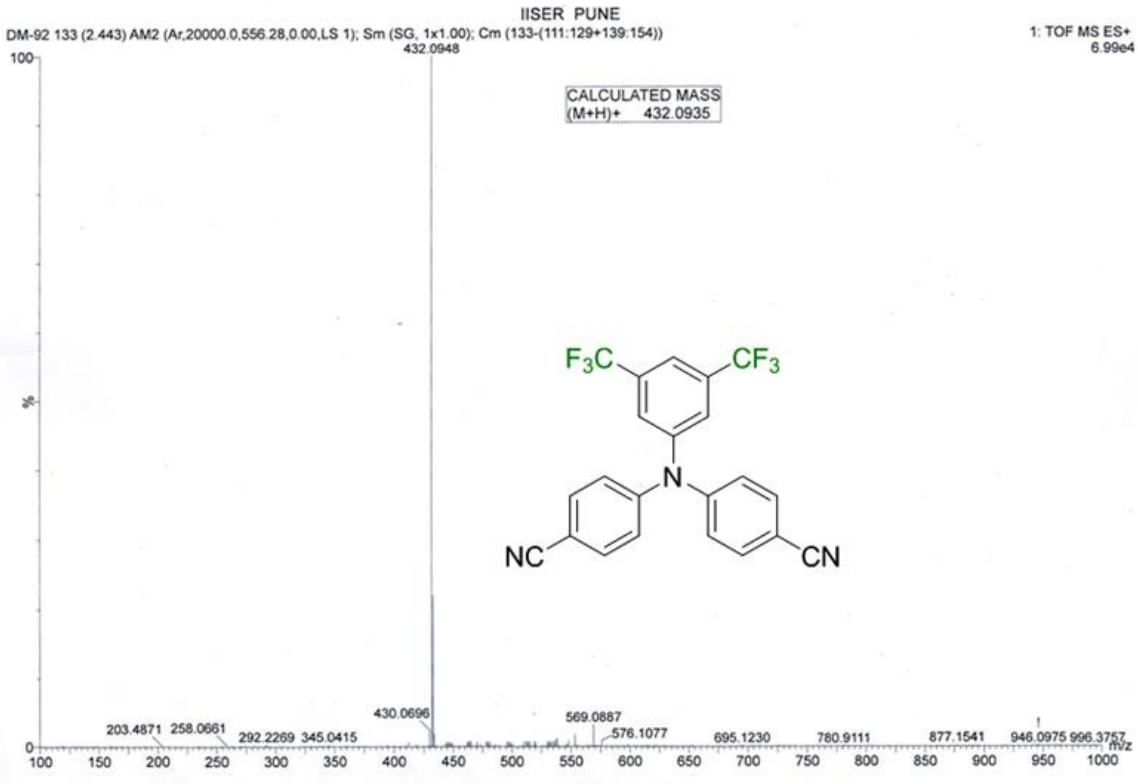

Appendix 4.2. HRMS spectra for linker L'.

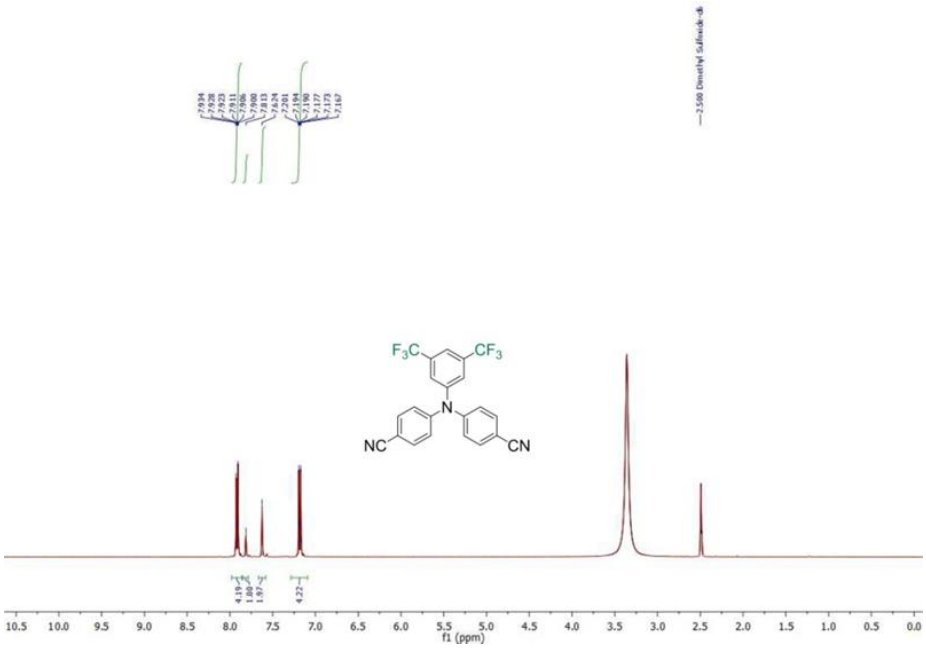

Appendix 4.3. ^{1}H NMR spectra for linker L'.

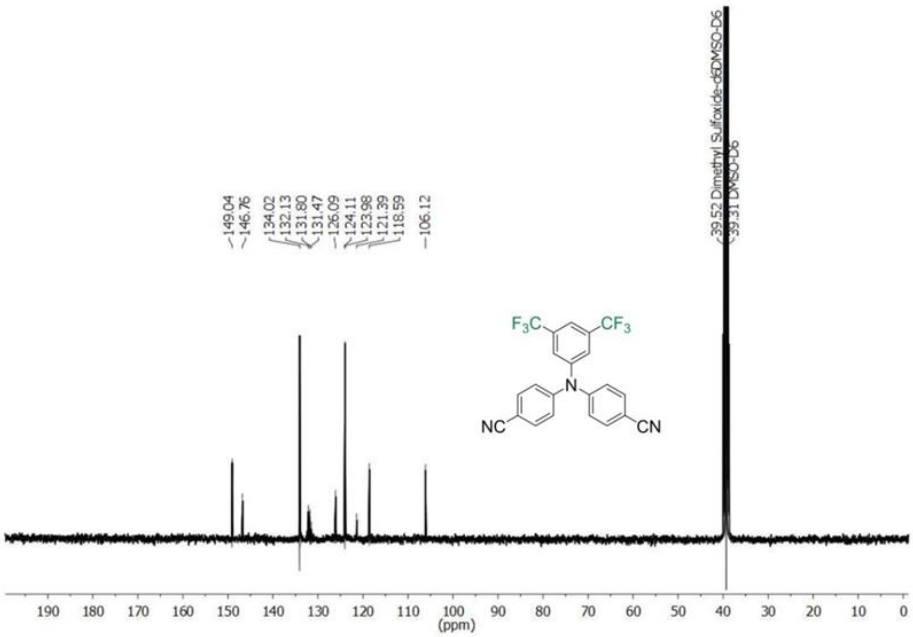

Appendix 4.4. ^{13}C NMR spectra for linker L'.

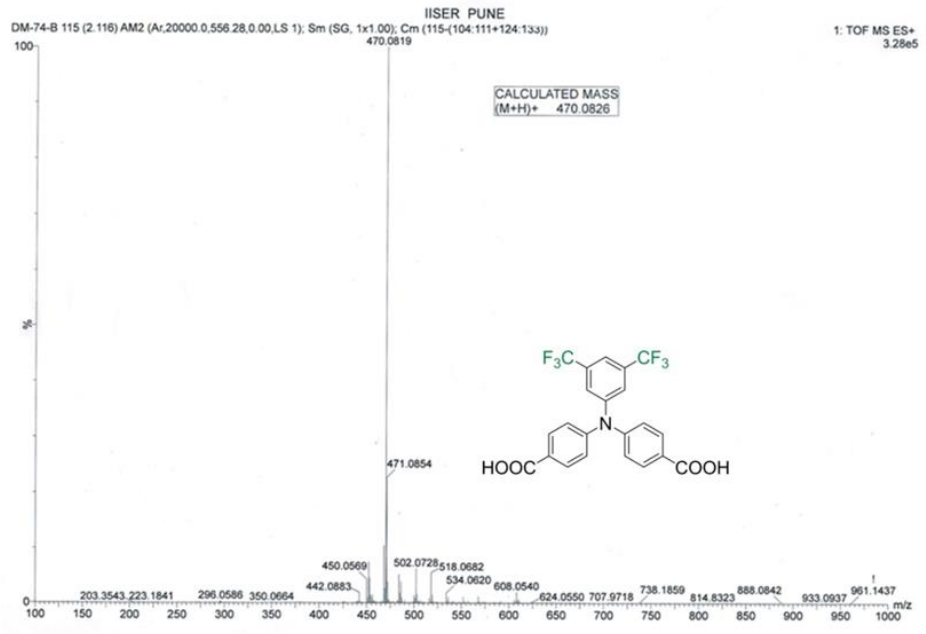

Appendix 4.5. HRMS spectra for linker LH_2.

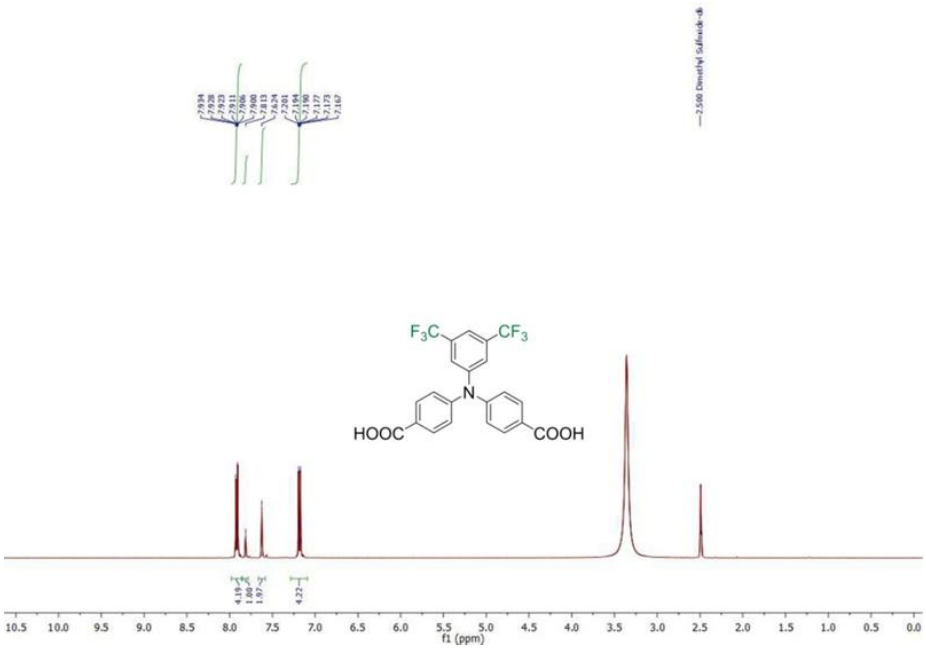

Appendix 4.6. ^{1}H NMR spectra for linker LH_2.

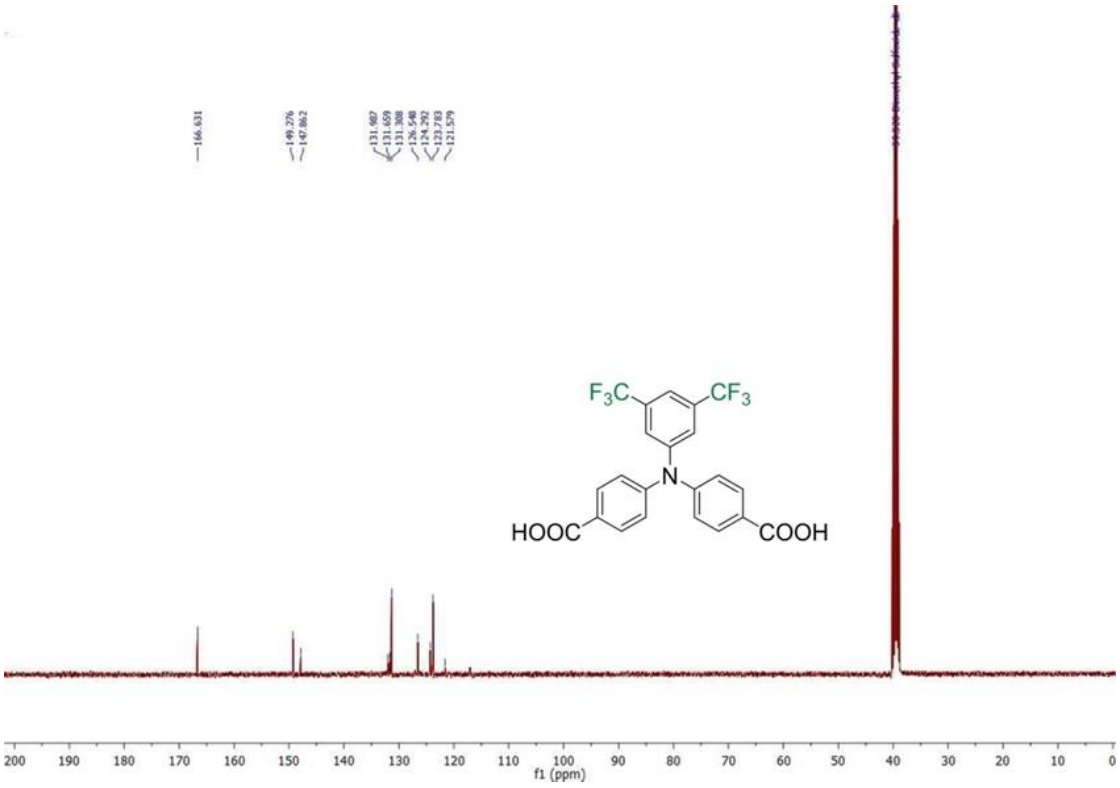

Appendix 4.7. ^{13}C NMR spectra for linker LH_2.

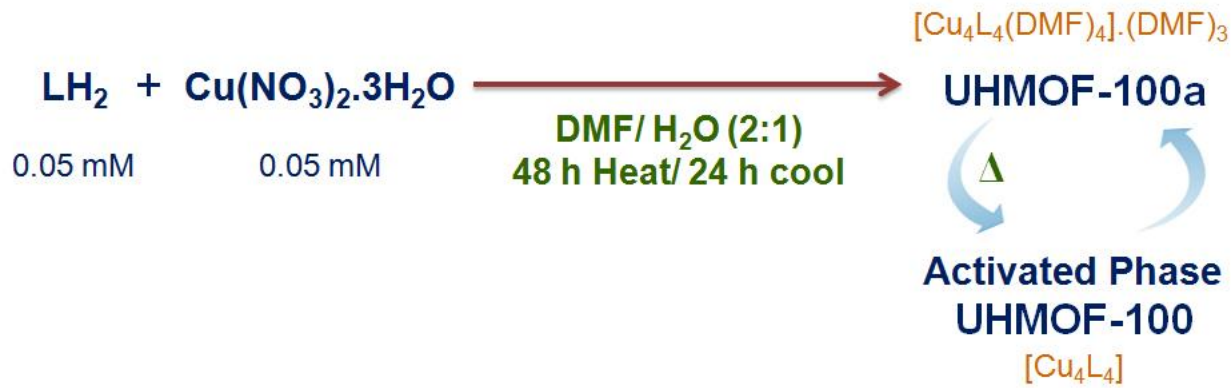

Appendix 4.8. Reaction Protocol to obtain the studied ultrahydrophobic crystalline **UHMOF-100**.

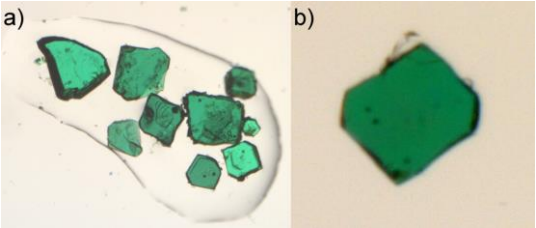

Appendix 4.9. a) Zoomed Microscopy images of the green crystals obtained for the different crystalline phases: a) compound **UHMOF-100a** (as-synthesized), b) compound **UHMOF-100** (desolvated).

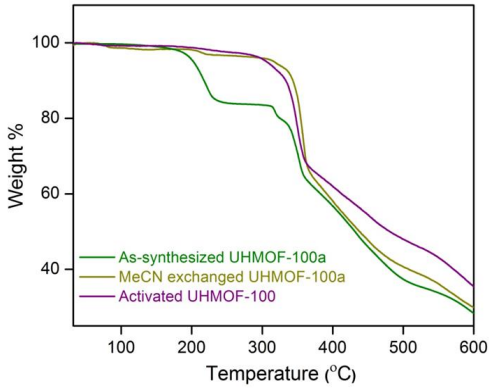

Appendix 4.10. Thermogravimetric analysis profiles for the three phases of the **UHMOF-100**: as-synthesized **UHMOF-100a**, MeCN exchanged **UHMOF-100a**,, and guest-free activated phase **UHMOF-100**, plotted together.

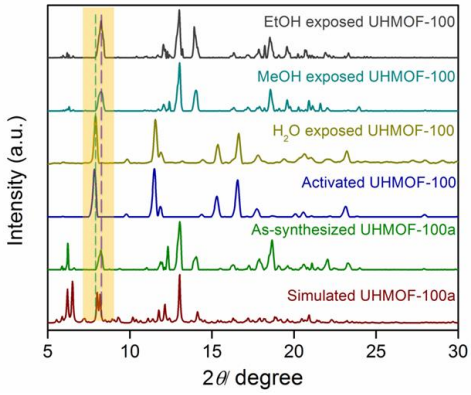

Appendix 4.11. PXRD patterns for compounds **UHMOF-100a** (simulated), **UHMOF-100a** (as-synthesized), **UHMOF-100** (activated), three different phases of **UHMOF-100** obtained on water exposure, MeOH exposure, and EtOH exposure experiments respectively.

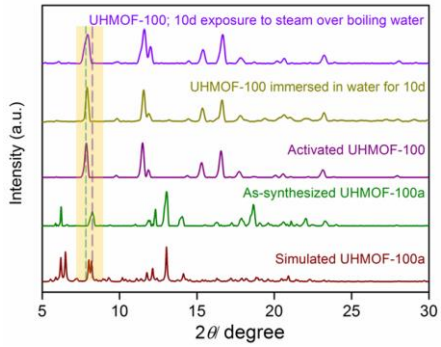

Appendix 4.12. PXRD patterns for compounds **UHMOF-100a** (simulated), **UHMOF-100a** (as-synthesized), **UHMOF-100** (activated), two phases of **UHMOF-100**: a) phase obtained on water immersion over 10d, b) phase obtained after steam exposure over 10 days (on boiling water).

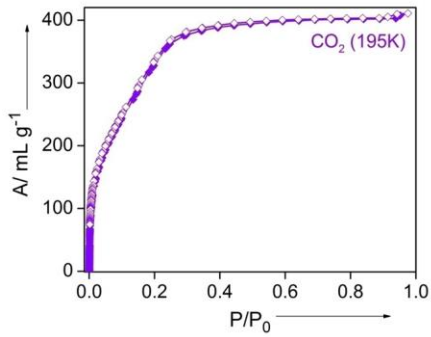

Appendix 4.13. Single component adsorption isotherm (Type-I nature) of **UHMOF-100** for CO_2 recorded at 195K, in terms of adsorptive loading against increasing relative pressure (P/P_0).

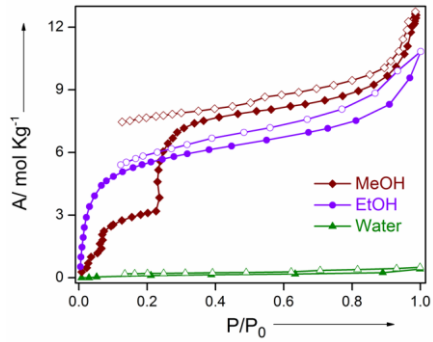

Appendix 4.14. Contrasting natures of alcohol sorption isotherms as compared to that of water for **UHMOF-100**, suggesting its potential alcohol-water separation efficiency.

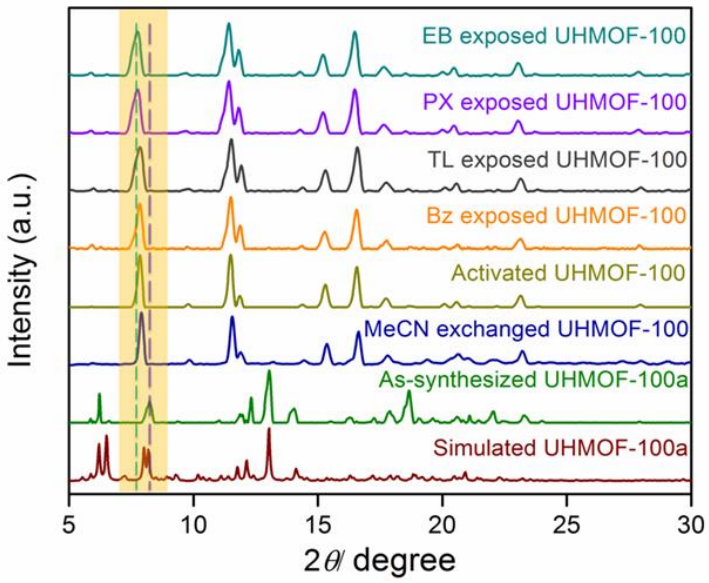

Appendix 4.15. PXRD patterns for compounds **UHMOF-100a** (simulated), **UHMOF-100a** (as-synthesized), **UHMOF-100** (MeCN-exchanged), **UHMOF-100** (activated), four different phases of **UHMOF-100** obtained on Benzene (Bz) exposure, Toluene (TL) exposure, *p*-xylene (PX) and Ethyl Benzene (EB) exposure experiments respectively.

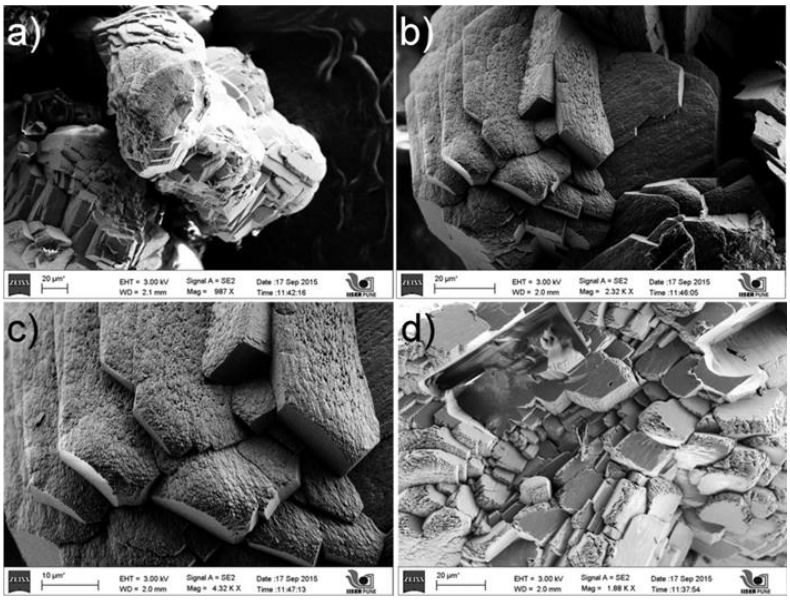

Appendix 4.16. 2D-plate like crystalline architectures of **UHMOF-100** as represented by the FE-SEM images.

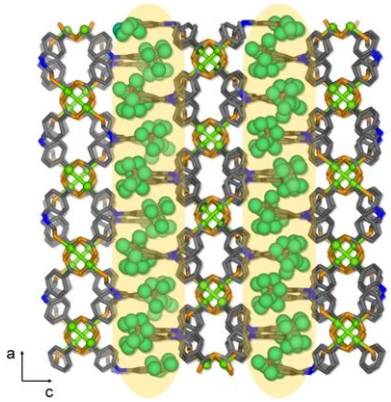

Appendix 4.17. Fluorine-rich 1D channels of **UHMOF-100a**, viewed along crystallographic *b*-axis.

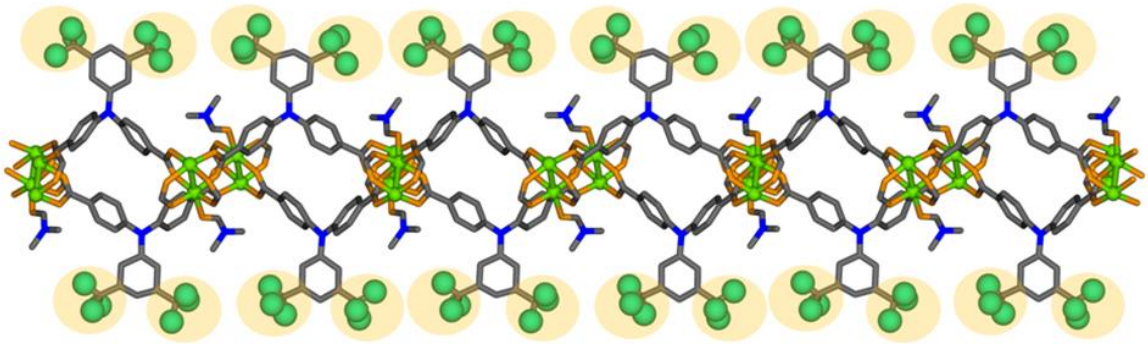

Appendix 4.18. Progression of a single 2D-sheet (along *b*-axis) for the phase **UHMOF-100a**.

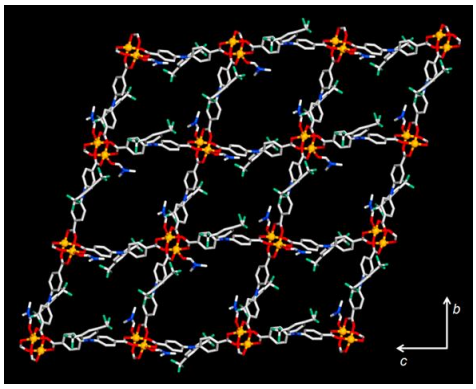

Appendix 4.19. Perspective view of the framework **UHMOF-100a**, along crystallographic *a*-axis.

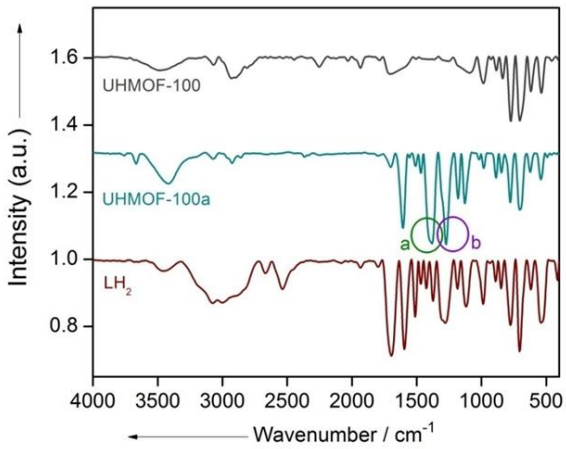

Appendix 4.20. IR spectra of solid LH_2**, UHMOF-100a** (as-synthesized), **UHMOF-100** (desolvated) phases, wherein the labelled peaks [a: C-N stretching (DMF); b: C-H rocking (in DMF, $–CH_3$)] refer to the presence of N.N.-dimethyl formamide (DMF) molecules exclusively within **UHMOF-100a**, while the mentioned peaks are absent in **UHMOF-100** owing to the absence of DMF molecules.

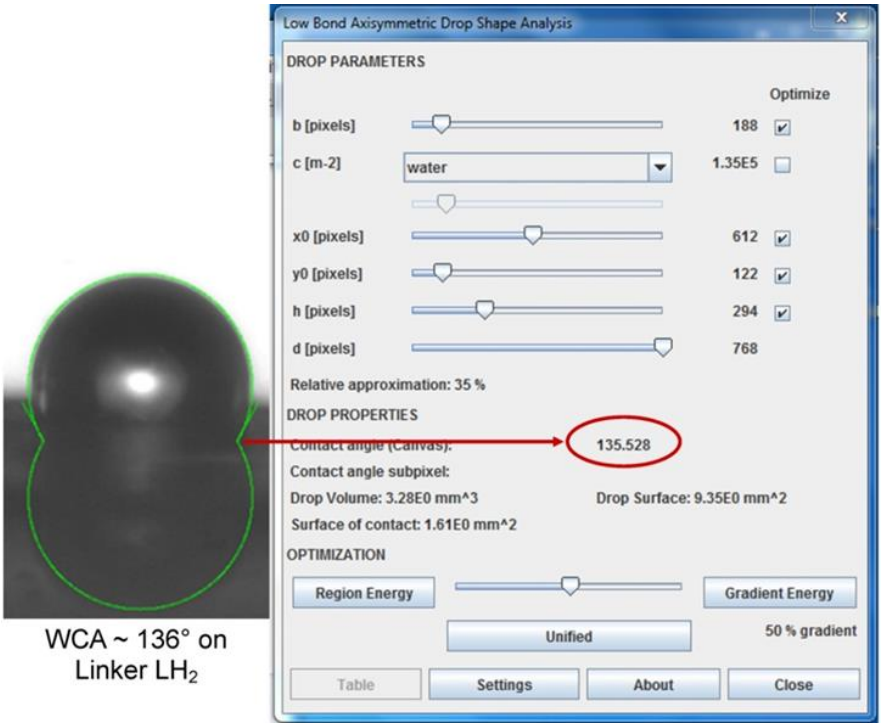

Appendix 4.21. Measured WCA (~136°) as recorded on **LH_2** (linker) pellets (by circle fitting mode).

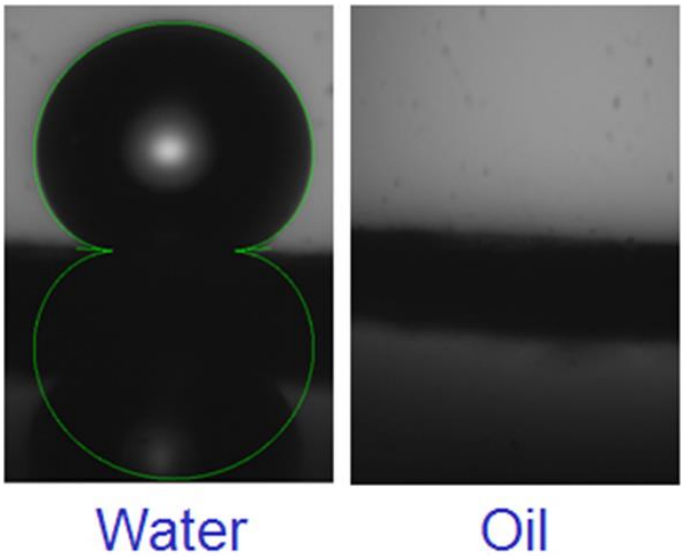

Appendix 4.22. The contact angles recorded for water (left) (CA ~176°) and oil (right) (CA ~0°), suggesting ultrahydrophobicity and superoleophilicity respectively.

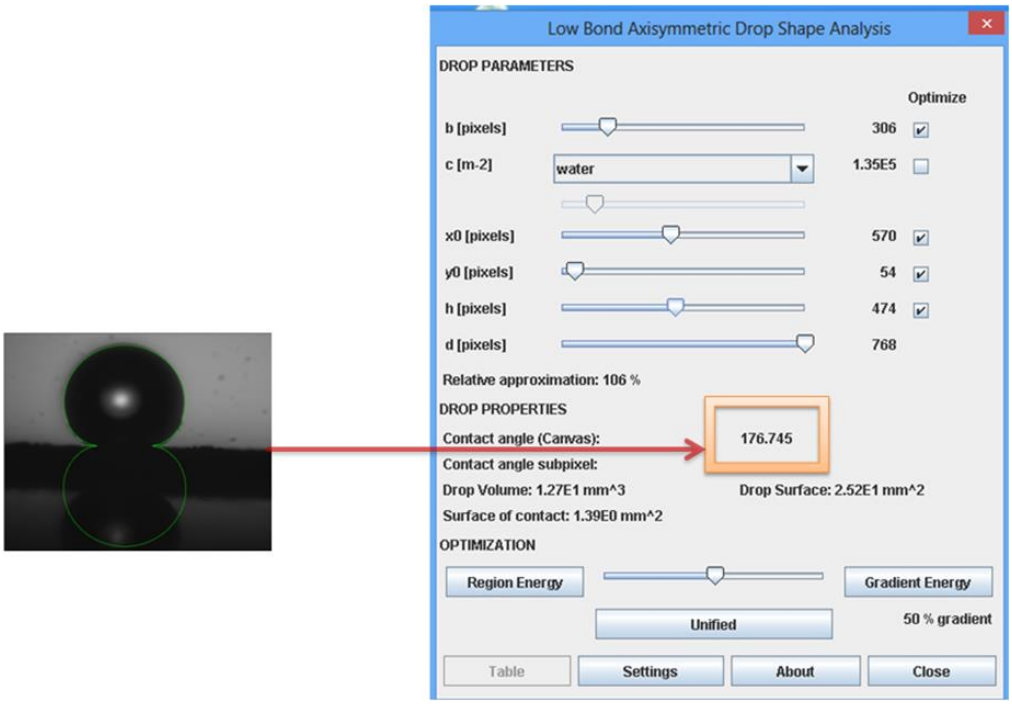

Appendix 4.23. Measurement of water contact angle on **UHMOF-100** pellet by circle fitting mode.

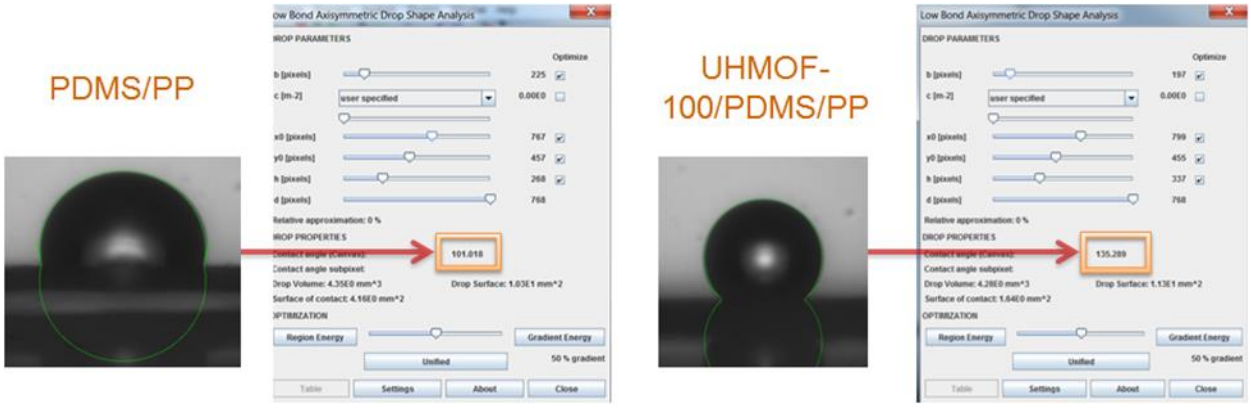

Appendix 4.24. The measured contact angle value of ~101° for PDMS membrane increased to much higher contact angle value of ~135.3° for **UHMOF-100/PDMS/PP** membrane; this increase in recorded C.A. value attributed to the spray-coating of fluorinated **UHMOF-100** material on the very less hydrophobic PDMS/PP membrane, rendering it highly hydrophobic.

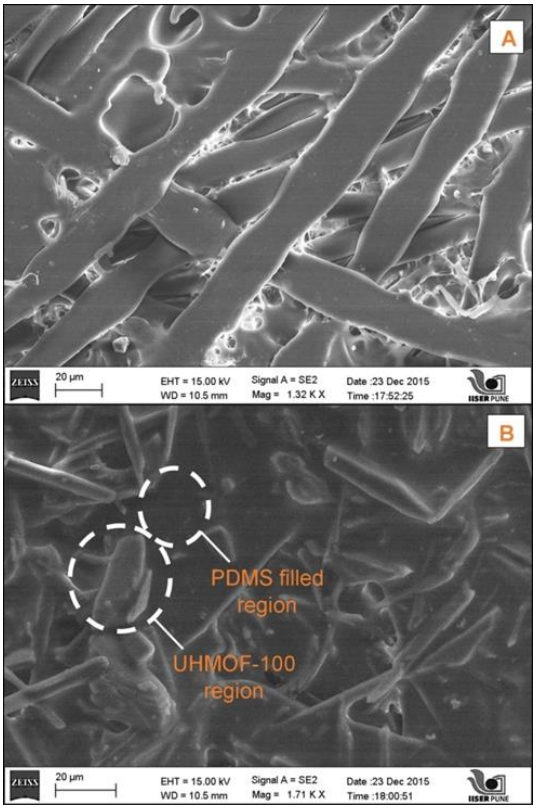

Appendix 4.25. SEM images of the uncoated PP fabric and **UHMOF-100/PDMS** coated PP fabric.

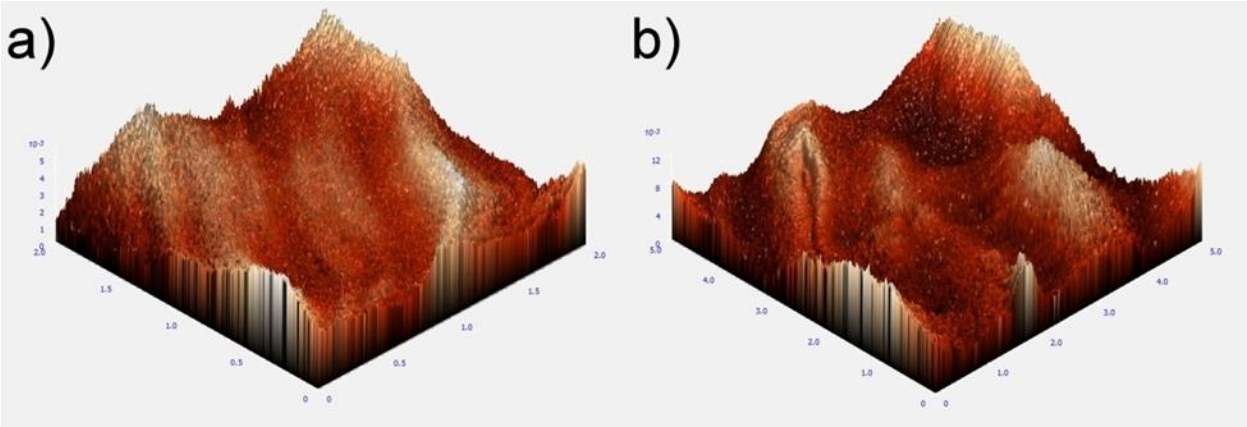

Appendix 4.26. AFM images of the coated membrane sample, the surface being scanned from two different areas (a) Scanned area: 2 μm (b) Scanned area: 5 μm.

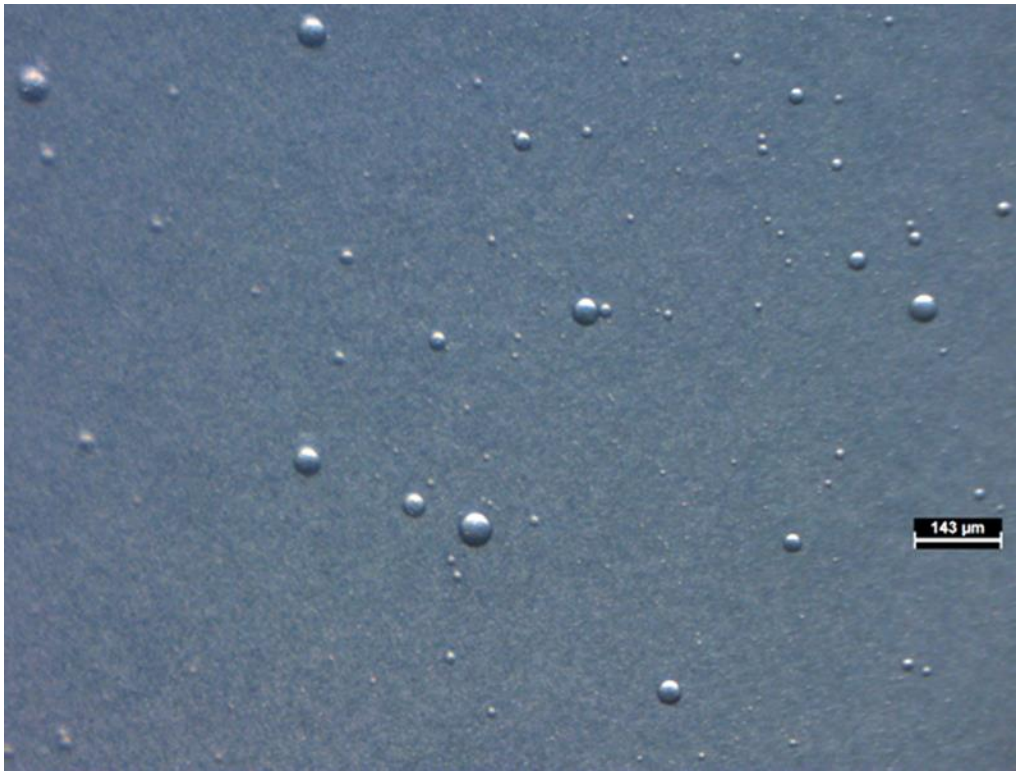

Appendix 4.27. Optical microscope image of emulsion droplets, the approximate droplets size was found in micro metre scale.

Appendix Table 4.1: Comparative analysis of contact angles of ultrahydrophobic MOF **UHMOF-100**, with only few literature reports on superhydrophobic MOFs.

MOF/ PCP	Investigated Form	WCA (in air) (°)	Genesis of Surface modification	References
UHMOF-100	Desolvated crystalline powder	**~176**	bis(trifluoromethyl) functionalized aromatic linker	Our study
HFGO@ZIF-8 composite	Composite material pellet	~162	highly fluorinated graphene oxide (HFGO)	Ref. 80
NMOF-1	Coated glass substrates	160-162	*oligo*-(*p*-phenyleneethynylene) dicarboxylate with alkoxyoctadecyl (C_{18}) chains (OPE-C18)	Ref. 82
PESD-1	single crystal powder (as-synthesized); powder(desolvated)	152; >150	Aromatic hydrocarbon linker	Ref. 49
MOFF-2	pressed crystals	151±1	Perfluorinated aromatic ring	Ref. 45
SIM-2(C12)/Al_2O_3	film on Al_2O_3 support	>150	alkyl chain (C_{12})	Ref. 48
MIL-53(Al)-AM6	Powder	>150	alkyl chain (C_6)	Ref. 79
MIL-53(Al)-AM4	Powder	>150	alkyl chain (C_4)	Ref. 79

Appendix Table 4.2: Performance evaluation of **UHMOF-100/PDMS/PP** membrane in comparison with the non-MOF based oil-water separating fabric materials.

Oil/water separation materials	Preparation methods	WCA (in air) (°)	Separation or absorption substances	Oil-Absorption Capacities, (g/g)	Recycle	Flux, L/(m^2.s)	References
UHMOF-100/PDMS Coated PP fabric (UHMOF-100/PDMS/PP)	**Spray coating**	**135.3**	**Hexadecane, toluene, crude oil, CCl_4, Bio-diesel**	**2-4**	**10**	**85±5**	**Our study**
UHMOF-100		**176**	**Hexadecane, toluene, crude oil, CCl_4, Bio-diesel**	**2.5-4.3**	**3**	**-**	**Our study**
Superhydrophobic polyester material	Dip-Coating	>150	Petrol, diesel, crude-oil	2-3	10	-	Wu, L. *et al.*[95]
Superhydrophobic cigarette filters	One step fabrication	158	Heptane, Hexane, Lubricating oil	4-5	10	-	Liu, C. *et al.*[96]
Superhydrophobic PP fabric	Recrystallization	155	chloroform	-	-	76.4±5	Zhu, T. *et al.*[97]
Superhydrophobic cotton fabrics	Sonochemical irradiation	159	kerosene	-	-	16	Li, J. *et al.*[98]
USTC-6@GO@sponge	Fabrication	121	diverse oils and organic solvents	(wt% ~ 1200 to 4300)	-	-	Jiang, Z.-R. *et al.*[89]

Appendix Table 4.3: AFM results of **UHMOF-100/PDMS/PP** sample.

Sample Area, µm	Peak to Peak, sy, nm	Roughness average, sa, nm	Root mean square (RMS), sq
2	5.61	0. 518	0. 667
5	12.8	1.56	1.94

Appendix Table 4.4: Crystal data and structure refinement for compound **UHMOF-100a**.

Crystal data: Compound **UHMOF-100a**	
Chemical formula	$C_{109}H_{93}Cu_4F_{24}N_{11}O_{23}$
M_r	2635.10
Crystal system, space group	Triclinic, *P*-1
Temperature (K)	140
a, *b*, *c* (Å)	15.774 (2), 16.545 (2), 23.383 (3)
α, β, γ (°)	80.170 (9), 71.168 (9), 75.394 (9)
V (Å^3)	5562.6 (13)
Z	2
Radiation type	Cu *K*α
μ (mm^{-1})	1.89
Crystal size (mm)	0.22 × 0.20 × 0.18
Data collection	
Diffractometer	Bruker *APEX*-II CCD diffractometer
Absorption correction	Multi-scan Bruker *SADABS*
T_{min}, T_{max}	0.692, 0.737
No. of measured, independent and observed [$I > 2\sigma(I)$] reflections	160284, 15866, 11220
R_{int}	0.159
θ_{max} (°)	60.3
$(\sin \theta/\lambda)_{max}$ (Å^{-1})	0.563
Refinement	
$R[F^2 > 2\sigma(F^2)]$, $wR(F^2)$, S	0.176, 0.487, 1.96
No. of reflections	15866
No. of parameters	1527
No. of restraints	461
H-atom treatment	H-atom parameters constrained
$\Delta\rho_{max}$, $\Delta\rho_{min}$ (e Å^{-3})	3.67, −1.14

4.7. References:

1. Kontovas, C. A.; Psaraftis, H. N.; Ventikos, N. P., *Marine Poll. Bull.* **2010,** *60*, 1455-1466.

2. Adebajo, M. O.; Frost, R. L.; Kloprogge, J. T.; Carmody, O.; Kokot, S., *J. Porous Mater.* **2003,** *10*, 159-170.

3. Wang, B.; Liang, W.; Guo, Z.; Liu, W., *Chem. Soc. Rev.* **2015,** *44*, 336-361.

4. Jiang, T.; Guo, Z.; Liu, W., *J. Mater. Chem. A* **2015,** *3*, 1811-1827.

5. Zhang, J.; Seeger, S., *Adv. Funct. Mater.* **2011,** *21*, 4699-4704.

6. Zhang, L.; Zhang, Z.; Wang, P., *NPG Asia Mater* **2012,** *4*, e8.

7. Li, A.; Sun, H.-X.; Tan, D.-Z.; Fan, W.-J.; Wen, S.-H.; Qing, X.-J.; Li, G.-X.; Li, S.-Y.; Deng, W.-Q., *Energy Environ. Sci.* **2011,** *4*, 2062-2065.

8. Gui, X.; Wei, J.; Wang, K.; Cao, A.; Zhu, H.; Jia, Y.; Shu, Q.; Wu, D., *Adv. Mater.* **2010,** *22*, 617-621.

9. Sohn, K.; Joo Na, Y.; Chang, H.; Roh, K.-M.; Dong Jang, H.; Huang, J., *Chem. Commun.* **2012,** *48*, 5968-5970.

10. Hayase, G.; Kanamori, K.; Fukuchi, M.; Kaji, H.; Nakanishi, K., *Angew. Chem. Int. Ed.* **2013,** *52*, 1986-1989.

11. James, S. L., *Chem. Soc. Rev.* **2003,** *32*, 276-288.

12. Long, J. R.; Yaghi, O. M., *Chem. Soc. Rev.* **2009,** *38*, 1213-1214.

13. Kitagawa, S.; Kitaura, R.; Noro, S.-i., *Angew. Chem. Int. Ed.* **2004,** *43*, 2334-2375.

14. Kuppler, R. J.; Timmons, D. J.; Fang, Q.-R.; Li, J.-R.; Makal, T. A.; Young, M. D.; Yuan, D.; Zhao, D.; Zhuang, W.; Zhou, H.-C., *Coord. Chem. Rev.* **2009,** *253*, 3042-3066.

15. Kitagawa, S.; Matsuda, R., *Coord. Chem. Rev.* **2007,** *251*, 2490-2509.

16. Moon, H. R.; Lim, D.-W.; Suh, M. P., *Chem. Soc. Rev.* **2013,** *42*, 1807-1824.

17. Xiang, S.; He, Y.; Zhang, Z.; Wu, H.; Zhou, W.; Krishna, R.; Chen, B., *Nat Commun* **2012,** *3*, 954.

18. Mason, J. A.; Veenstra, M.; Long, J. R., *Chem. Sci.* **2014,** *5*, 32-51.

19. Li, B.; Wen, H.-M.; Zhou, W.; Chen, B., *J. Phys. Chem. Lett.* **2014,** *5*, 3468-3479.

20. Kumar, A.; Madden, D. G.; Lusi, M.; Chen, K.-J.; Daniels, E. A.; Curtin, T.; Perry, J. J.; Zaworotko, M. J., *Angew. Chem. Int. Ed.* **2015,** *54*, 14372-14377.

21. Zhang, Z.; Zhao, Y.; Gong, Q.; Li, Z.; Li, J., *Chem. Commun.* **2013,** *49*, 653-661.

22. Zhang, Z.; Yao, Z.-Z.; Xiang, S.; Chen, B., *Energy Environ. Sci.* **2014,** *7*, 2868-2899.

23. Nugent, P.; Belmabkhout, Y.; Burd, S. D.; Cairns, A. J.; Luebke, R.; Forrest, K.; Pham, T.; Ma, S.; Space, B.; Wojtas, L.; Eddaoudi, M.; Zaworotko, M. J., *Nature* **2013,** *495*, 80-84.

24. Duan, J.; Higuchi, M.; Krishna, R.; Kiyonaga, T.; Tsutsumi, Y.; Sato, Y.; Kubota, Y.; Takata, M.; Kitagawa, S., *Chem. Sci.* **2014,** *5*, 660-666.

25. Bloch, W. M.; Babarao, R.; Hill, M. R.; Doonan, C. J.; Sumby, C. J., *J. Am. Chem. Soc.* **2013,** *135*, 10441-10448.

26. Mukherjee, S.; Joarder, B.; Desai, A. V.; Manna, B.; Krishna, R.; Ghosh, S. K., *Inorg. Chem.* **2015,** *54*, 4403-4408.

27. Mukherjee, S.; Joarder, B.; Manna, B.; Desai, A. V.; Chaudhari, A. K.; Ghosh, S. K., *Sci. Rep.* **2014,** *4*, 5761.

28. Nagarkar, S. S.; Joarder, B.; Chaudhari, A. K.; Mukherjee, S.; Ghosh, S. K., *Angew. Chem. Int. Ed.* **2013,** *52*, 2881-2885.

29. Hu, Z.; Deibert, B. J.; Li, J., *Chem. Soc. Rev.* **2014,** *43*, 5815-5840.

30. Della Rocca, J.; Liu, D.; Lin, W., *Acc. Chem. Res.* **2011,** *44*, 957-968.

31. Horcajada, P.; Chalati, T.; Serre, C.; Gillet, B.; Sebrie, C.; Baati, T.; Eubank, J. F.; Heurtaux, D.; Clayette, P.; Kreuz, C.; Chang, J.-S.; Hwang, Y. K.; Marsaud, V.; Bories, P.-N.; Cynober, L.; Gil, S.; Ferey, G.; Couvreur, P.; Gref, R., *Nat Mater* **2010,** *9*, 172-178.

32. Ramaswamy, P.; Wong, N. E.; Shimizu, G. K. H., *Chem. Soc. Rev.* **2014,** *43*, 5913-5932.

33. Sadakiyo, M.; Yamada, T.; Kitagawa, H., *J. Am. Chem. Soc.* **2014,** *136*, 13166-13169.

34. Lee, J.; Farha, O. K.; Roberts, J.; Scheidt, K. A.; Nguyen, S. T.; Hupp, J. T., *Chem. Soc. Rev.* **2009,** *38*, 1450-1459.

35. Gascon, J.; Corma, A.; Kapteijn, F.; Llabrés i Xamena, F. X., *ACS Catal.* **2014,** *4*, 361-378.

36. Horike, S.; Dincă, M.; Tamaki, K.; Long, J. R., *J. Am. Chem. Soc.* **2008,** *130*, 5854-5855.

37. Higuchi, M.; Nakamura, K.; Horike, S.; Hijikata, Y.; Yanai, N.; Fukushima, T.; Kim, J.; Kato, K.; Takata, M.; Watanabe, D.; Oshima, S.; Kitagawa, S., *Angew. Chem. Int. Ed.* **2012,** *51*, 8369-8372.

38. Chaudhari, A. K.; Han, I.; Tan, J.-C., *Adv. Mater.* **2015,** *27*, 4438-4446.

39. Furukawa, H.; Cordova, K. E.; O'Keeffe, M.; Yaghi, O. M., *Science* **2013,** *341*.

40. Wilmer, C. E.; Leaf, M.; Lee, C. Y.; Farha, O. K.; Hauser, B. G.; Hupp, J. T.; Snurr, R. Q., *Nat Chem* **2012,** *4*, 83-89.

41. Chen, T.-H.; Popov, I.; Kaveevivitchai, W.; Miljanić, O. Š., *Chem. Mater.* **2014,** *26*, 4322-4325.

42. Kaye, S. S.; Dailly, A.; Yaghi, O. M.; Long, J. R., *J. Am. Chem. Soc.* **2007,** *129*, 14176-14177.

43. Greathouse, J. A.; Allendorf, M. D., *J. Am. Chem. Soc.* **2006,** *128*, 10678-10679.

44. De Toni, M.; Jonchiere, R.; Pullumbi, P.; Coudert, F.-X.; Fuchs, A. H., *ChemPhysChem* **2012,** *13*, 3497-3503.

45. Chen, T.-H.; Popov, I.; Zenasni, O.; Daugulis, O.; Miljanic, O. S., *Chem. Commun.* **2013,** *49*, 6846-6848.

46. Yang, C.; Kaipa, U.; Mather, Q. Z.; Wang, X.; Nesterov, V.; Venero, A. F.; Omary, M. A., *J. Am. Chem. Soc.* **2011,** *133*, 18094-18097.

47. Serre, C., *Angew. Chem. Int. Ed.* **2012,** *51*, 6048-6050.

48. Aguado, S.; Canivet, J.; Farrusseng, D., *J. Mater. Chem.* **2011,** *21*, 7582-7588.

49. Rao, K. P.; Higuchi, M.; Sumida, K.; Furukawa, S.; Duan, J.; Kitagawa, S., *Angew. Chem. Int. Ed.* **2014,** *53*, 8225-8230.

50. Padial, N. M.; Quartapelle Procopio, E.; Montoro, C.; López, E.; Oltra, J. E.; Colombo, V.; Maspero, A.; Masciocchi, N.; Galli, S.; Senkovska, I.; Kaskel, S.; Barea, E.; Navarro, J. A. R., *Angew. Chem. Int. Ed.* **2013,** *52*, 8290-8294.

51. Chen, T.-H.; Popov, I.; Kaveevivitchai, W.; Chuang, Y.-C.; Chen, Y.-S.; Jacobson, A. J.; Miljanić, O. Š., *Angew. Chem. Int. Ed.* **2015,** *54*, 13902-13906.

52. Akhavan, B.; Jarvis, K.; Majewski, P., *ACS Appl. Mater. Interfaces* **2013,** *5*, 8563-8571.

53. Wang, X.-S.; Liu, J.; Bonefont, J. M.; Yuan, D.-Q.; Thallapally, P. K.; Ma, S., *Chem. Commun.* **2013,** *49*, 1533-1535.

54. Schnobrich, J. K.; Lebel, O.; Cychosz, K. A.; Dailly, A.; Wong-Foy, A. G.; Matzger, A. J., *J. Am. Chem. Soc.* **2010,** *132*, 13941-13948.

55. *SAINT Plus*, (Version 7.03); Bruker AXS Inc.: Madison, WI, **2004**.

56. Sheldrick, G. M. *SHELXTL*, *Reference Manual*: version 5.1: Bruker AXS; Madison, WI, **1997**.

57. Sheldrick, G. M. *Acta Crystallogr. Sect. A* **2008**, 112-122.

58. WINGX version 1.80.05 Louis Farrugia, University of Glasgow.

59. Spek, A. L. PLATON, *A Multipurpose Crystallographic Tool*, Utrecht University, Utrecht, The Netherlands, **2005**.

60. Mukherjee, S.; Kansara, A. M.; Saha, D.; Gonnade, R.; Mullangi, D.; Manna, B.; Desai, A. V.; Thorat, S. H.; Singh, P. S.; Mukherjee, A.; Ghosh, S. K., *Chem. Eur. J.* **2016,** *22*, 10937-10943.

61. M. J. Frisch *et al.*, Gaussian 09, revision B.01; Gaussian, Inc.: Wallingford, CT, **2010**.

62. Mayo, S. L.; Olafson, B. D.; Goddard, W. A., *J. Phys. Chem.* **1990,** *94*, 8897-8909.

63. Hess, B.; Kutzner, C.; van der Spoel, D.; Lindahl, E., *J. Chem. Theory Comput.* **2008,** *4*, 435-447.

64. Abascal, J. L. F.; Vega, C., *J. Chem. Phys.* **2005,** *123*, 234505.

65. T. Schlick, *Molecular Modeling and Simulation: An Interdisciplinary Guide*. 2nd ed.; Springer: New York, **2010**.

66. Berendsen, H. J. C.; Postma, J. P. M.; van Gunsteren, W. F.; DiNola, A.; Haak, J. R., *J. Chem. Phys.* **1984,** *81*, 3684-3690.

67. S. Nosé, *Mol. Phys.* **1984**, *52*, 255-268.

68. Hoover, W. G., *Phys. Rev. A* **1985,** *31*, 1695-1697.

69. Parrinello, M.; Rahman, A., *J. Appl. Phys.* **1981,** *52*, 7182-7190.

70. Darden, T.; York, D.; Pedersen, L., *J. Chem. Phys.* **1993,** *98*, 10089-10092.

71. Mehrotra, P. K.; Beveridge, D. L., *J. Am. Chem. Soc.* **1980,** *102*, 4287-4294.

72. Lounnas, V.; Pettitt, B. M., *Proteins: Struct., Funct., Bioinf.* **1994,** *18*, 133-147.

73. Makarov, V. A.; Andrews, B. K.; Pettitt, B. M., *Biopolymers* **1998,** *45*, 469-478.

74. Horike, S.; Shimomura, S.; Kitagawa, S., *Nat Chem* **2009,** *1*, 695-704.

75. Sato, H.; Kosaka, W.; Matsuda, R.; Hori, A.; Hijikata, Y.; Belosludov, R. V.; Sakaki, S.; Takata, M.; Kitagawa, S., *Science* **2014,** *343*, 167-170.

76. Henke, S.; Schneemann, A.; Wütscher, A.; Fischer, R. A., *J. Am. Chem. Soc.* **2012,** *134*, 9464-9474.

77. Henke, S.; Li, W.; Cheetham, A. K., *Chem. Sci.* **2014,** *5*, 2392-2397.

78. U.S. Department of Labor, Petroleum Refining Process, https://www.osha.gov/dts/osta/otm/otm_iv/otm_iv_2.html (accessed on 24-08-2016).

79. Nguyen, J. G.; Cohen, S. M., *J. Am. Chem. Soc.* **2010,** *132*, 4560-4561.

80. Jayaramulu, K.; Datta, K. K. R.; Rösler, C.; Petr, M.; Otyepka, M.; Zboril, R.; Fischer, R. A., *Angew. Chem. Int. Ed.* **2016,** *55*, 1178-1182.

81. He, C.-T.; Jiang, L.; Ye, Z.-M.; Krishna, R.; Zhong, Z.-S.; Liao, P.-Q.; Xu, J.; Ouyang, G.; Zhang, J.-P.; Chen, X.-M., *J. Am. Chem. Soc.* **2015,** *137*, 7217-7223.

82. Roy, S.; Suresh, V. M.; Maji, T. K., *Chem. Sci.* **2016,** *7*, 2251-2256.

83. Miljkovic, N.; Preston, D. J.; Enright, R.; Wang, E. N., *Appl. Phys. Lett.* **2014,** *105*, 013111.

84. Acharya, H.; Vembanur, S.; Jamadagni, S. N.; Garde, S., *Farad. Discuss.* **2010,** *146*, 353-365.

85. Zhao, J.; Xiao, C.; Xu, N., *Environ. Sci. Pollut. Res.* **2013,** *20*, 4137-4145.

86. Yang, H.-C.; Liao, K.-J.; Huang, H.; Wu, Q.-Y.; Wan, L.-S.; Xu, Z.-K., *J. Mater. Chem. A* **2014,** *2*, 10225-10230.

87. K. Liao, X.-Y. Ye, P.-C. Chen, Z.-K. Xu, *J. Appl. Polym. Sci.* **2014**, *131*, 39897

88. Jadav, G. L.; Aswal, V. K.; Singh, P. S., *J. Mater. Chem. A* **2013,** *1*, 4893-4903.

89. Jiang, Z.-R.; Ge, J.; Zhou, Y.-X.; Wang, Z. U.; Chen, D.; Yu, S.-H.; Jiang, H.-L., *NPG Asia Mater* **2016,** *8*, e253.

90. Ge, J.; Ye, Y.-D.; Yao, H.-B.; Zhu, X.; Wang, X.; Wu, L.; Wang, J.-L.; Ding, H.; Yong, N.; He, L.-H.; Yu, S.-H., *Angew. Chem. Int. Ed.* **2014,** *53*, 3612-3616.

91. Shang, L.; Bian, T.; Zhang, B.; Zhang, D.; Wu, L.-Z.; Tung, C.-H.; Yin, Y.; Zhang, T., *Angew. Chem. Int. Ed.* **2014,** *53*, 250-254.

92. Wang, L.; Zhao, Y.; Tian, Y.; Jiang, L., *Angew. Chem. Int. Ed.* **2015,** *54*, 14732-14737.

93. Gupta, D.; Sarker, B.; Thadikaran, K.; John, V.; Maldarelli, C.; John, G., *Science Advances* **2015,** *1*.

94. Huang, G.; Yang, Q.; Xu, Q.; Yu, S.-H.; Jiang, H.-L., *Angew. Chem. Int. Ed.* **2016,** *55*, 7379-7383.

95. Wu, L.; Zhang, J.; Li, B.; Wang, A., *J. Colloid Interface Sci.* **2014,** *413*, 112-117.

96. Liu, C.; Chen, B.; Yang, J.; Li, C., *J. Adhes. Sci. Technol.* **2015,** *29*, 2399-2407.

97. Zhu, T.; Cai, C.; Duan, C.; Zhai, S.; Liang, S.; Jin, Y.; Zhao, N.; Xu, J., *ACS Appl. Mater. Interfaces* **2015,** *7*, 13996-14003.

98. Li, J.; Yan, L.; Zhao, Y.; Zha, F.; Wang, Q.; Lei, Z., *Phys. Chem. Chem. Phys.* **2015,** *17*, 6451-6457.

Chapter 5

Summary and Perspectives

To sum it up (the entire work done in the thesis) in a concise nutshell seems a real tricky one, since it brings in the inevitable probabilities of overgeneralization of the actual findings encompassed throughout the period of research work. However, rather than providing a fairly plain conclusion over a single focussed project, it would be judicious to convene a few take-home messages together, in a comprehensive manner.

On a frank note, to address the aspect of challenging separation of chemical species ubiquitously poses a daunting task in view of the crucial cornerstones convoluted from the industrial standpoint. These issues do not seem to get entirely solved as a wholesome problem, but would always continue to come up with new advancement steps for easing out the prevalent bottlenecks. Therefore, new-generation advanced porous materials are imperative to be aptly designed, since their germane implementation subsequent to syntheses-driven experimental analyses are anticipated to result in great improvement of the actual knowhow of chemical separation-governed intricacies.

The key aspects of recyclability and sustainability principally drive the relentlessly intensifying research efforts put together in the fascinating domain of novel materials-based permanently porous adsorbent materials. To invoke the two aforementioned facets, development of coherent strategic design principles for the upcoming materials science-based research is an absolute necessity. Recent years of intense research activities on miscellaneous porous polymers like MOFs, COFs, HOFs, PAFs, PCPs, PPNs, CTFs, POFs (see glossary of acronyms section), particularly the colossal achievements garnered in the field of metal-organic framework sorbents have distinctly focused on the ease of bed restoration and aqueous stability traits along with the usage of environment-friendly greener protocols employed during syntheses. Taking into account the rapid growth in this domain, it seems only a matter of time until the dually decisive aspects of sustainability and energy-economy can be addressed. To astutely tackle the omnipresent situation of carrying out the balancing act amongst energy and economical tailbacks, it seems vibrant to move the present research forward in the right direction by adopting the path of using sustainable, energy-economic processes like adsorptive separation and therein, to discover better benchmark sorbents with enhanced efficiency.

As a vital take-home message from this thesis work, the influence of appending diverse pore surface functionalization to the ensuing pore channels/surfaces of the ensuing coordination

polymers/MOFs have been expansively evaluated, in terms of achieving a few critical separation deliverables. Notwithstanding with accomplishing merely the sorption oriented industrially relevant hydrocarbon separation deliverables such as, C_6 and C_8 isomeric or azeotropic vapor species' adsorptive separation phenomena; environmentally pertinent, real-time oil/water separation by a reusable, uniformly MOF-fabricated polymer membrane has been proficiently demonstrated. If such novel approaches can be appropriately infused with further understandings and rational insights already documented in the domain of pre-functionalized and post-synthetically functionalized porous materials and the future keynote discernments, a lot of targeted scientific advancements will not be a thing of distant future.

Keeping the principal research-focus of discovering innovative practical aspects for porous materials pretty streamlined, the next years of research with functionalized MOFs will hopefully help the entire scientific community at large, to progress in the best possible way, giving way to some innovative ideas and their apt validations with the aid of my own experimental efforts, described in this thesis.